Electronic and magnetic properties of single molecule magnets on surfaces

Dissertation submitted for the degree of
Doctor of Natural Sciences

Presented by
Philipp Erler

at the

Universität Konstanz

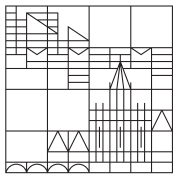

Faculty of Sciences
Department of Physics

Date of the oral examination: May 20, 2016
First referee: Apl. Prof. Dr. Mikhail Fonin
Second referee: Prof. Dr. Elke Scheer

Zusammenfassung

Einzelmolekülmagnete (engl. single molecule magnets, SMMs) spielen im Bereich der molekularen Spintronik eine Schlüsselrolle. Ein vielversprechender Ansatz zur Nutzung des Spin-Zustands einzelner SMMs ist die Organisation dieser Moleküle in zwei-, ein- oder null-dimensionalen Strukturen auf Oberflächen. Dabei stellen sich im Wesentlichen zwei Herausforderungen: Zum einen wird eine Deposition intakter SMMs durch die häufig komplexe Struktur dieser Moleküle erschwert. Zum anderen kann die Wechselwirkung der Moleküle mit dem Substrat zu einem Verlust ihrer funktionalen magnetischen Eigenschaften führen.

Die vorliegende Arbeit ist eine experimentelle Untersuchung von SMMs auf metallischen und nichtmetallischen Oberflächen. Ein besonderes Interesse liegt dabei auf der strukturellen Organisation der SMMs, sowie auf dem Einfluss der Oberfläche auf die elektronischen und magnetischen Eigenschaften. Zur Deposition der Moleküle wird das Verfahren der Elektrospray-Deposition im Ultrahochvakuum angewandt, das eine nahezu zerstörungsfreie Abscheidung selbst komplexer und nicht flüchtiger Verbindungen ermöglicht. Die anschließende Charakterisierung der molekularen Eigenschaften erfolgt durch Rastertunnelmikroskopie und -spektroskopie (engl. scanning tunneling microscopy and spectroscopy, STM/STS), sowie durch oberflächenempfindliche röntgenbasierte Messmethoden.

Im ersten Teil der Arbeit wird der zur Elektrospray Deposition verwendete experimentelle Aufbau detailliert beschrieben. Die vielseitigen Einsatzmöglichkeiten des Depositionsverfahrens werden am Beispiel verschiedener molekularer Verbindungen demonstriert, unter anderem an Eisen-Phthalocyanin (FePc), einem sternförmigen Polyfluoren Polymer und einem Triazatruxen (TAT) Derivat. Durch eine Deposition dieser Verbindungen auf Edelmetall-Oberflächen und eine anschließende Untersuchung der Oberflächenbeschaffenheit mittels STM werden Informationen über die Unversehrtheit der Moleküle, deren Wachstumsverhalten, sowie die Anzahl an Verunreinigungen auf der Probenoberfläche gewonnen.

Im zweiten Teil der Arbeit wird der Einzelmolekülmagnet Mn_{12}-ac untersucht, der als typischer Vertreter dieser Klasse von Molekülen gilt. Als Substrat für die Deposition wurden Au(111) und Ag(111) Oberflächen, sowie eine einatomige Lage von Graphen auf Ir(111) verwendet. STM Messungen bestätigen eine Abscheidung von

strukturell intakten Mn_{12} Molekülen. Jedoch führt die Wechselwirkung zwischen Mn_{12} und dem Substrat im Fall der Edelmetall-Oberflächen zu einer Reduktion der Mangan-Ionen, die über Röntgen-Photoelektronenspektroskopie nachgewiesen werden kann, sowie zu einer Verbreiterung der molekularen Zustände in STS Messungen. Im Gegensatz dazu zeigen STS Messungen an Mn_{12} auf Graphen/Ir(111) scharfe Leitfähigkeitsmaxima, die auf eine elektronische Entkopplung der Moleküle vom metallischen Substrat hinweisen.

Im dritten Teil der Arbeit wird die Untersuchung von SMMs auf Oberflächen auf den vierkernigen Eisen(III) Komplex Fe_4 erweitert. Durch eine gezielte Modifizierung der organischen Liganden-Hülle der Verbindung, sowie durch die Verwendung von hexagonalem Bornitrid auf Rh(111) und Graphen auf Ir(111) als geeignete Substrate wird die erste erfolgreiche Organisation von Fe_4 SMMs in hoch-geordneten periodischen Oberflächenstrukturen demonstriert. Hochaufgelöste STM Messungen zeigen, dass die einfache magnetische Achse der Moleküle auf beiden Substraten entlang der Oberflächennormalen ausgerichtet ist. Die Anisotropiekonstante ist im Falle einer Deposition auf Graphen unverändert gegenüber kristallinem Material, was über eine Messung des zirkularen magnetischen Röntgendichroismus nachgewiesen wird. Um zusätzliche Informationen über die intramolekulare Austauschwechselwirkung in Fe_4 auf der Graphen-Schicht zu gewinnen, wird die Energie von Spin-Anregungen in einzelnen Molekülen mittels inelastischer Tunnelspektroskopie gemessen.

Summary

Single molecule magnets (SMMs) play a key role in the upcoming field of molecular spintronics. A possible route to the utilization of the spin state of individual SMMs is the organization of these molecules in two-, one- or zero-dimensional structures on surfaces. However, the deposition of intact SMMs is often hindered by the large and complex molecular structure of these compounds and the interaction of the molecules with the substrate can result in a loss of their magnetic functionality.

In this thesis, we study the organization of SMMs on metallic and non-metallic surfaces and investigate whether and to what extend the proximity of the SMMs to the surface is changing their electronic and magnetic properties. For the deposition of the SMMs, we use electrospray deposition (ESD) in ultra-high vacuum, which is capable of bringing complex and nonvolatile molecules onto surfaces with only minor fragmentation. In order to address the properties of the SMMs on the single-molecule level, we use low temperature scanning tunneling microscopy and spectroscopy (STM/STS). In addition, we utilize X-ray based techniques to obtain surface-sensitive spectroscopic information averaged over a large number of molecules.

In the first part of the thesis, the implementation of the ESD setup is described in detail, as it has been a substantial part of this work. The design of the individual setup components is discussed and the relevant deposition parameters are characterized. In order to demonstrate the capabilities of the setup, we investigate the deposition of several exemplary compounds on noble metal surfaces, including iron phthalocyanine (FePc), a polyfluorene star polymer and a triazatruxene (TAT) derivative. STM images obtained on the samples after deposition provide insight into the integrity of the molecules, their growth behavior and the amount of contaminations present on the sample surface.

In the second part, we perform a study of the archetypical SMM Mn_{12}-ac on three different substrates: Au(111), Ag(111) and graphene on Ir(111). Our STM measurements indicate that structurally intact Mn_{12} clusters are present on all of these surfaces after deposition. However, the interaction between Mn_{12} and the noble metal surfaces results in a broadening of the molecular states as obtained from STS measurements, as well as in a reduction of the manganese ions observed

in X-ray photoelectron spectroscopy (XPS). In contrast, sharp resonances are observed in STS measurements performed on Mn_{12}-ac on graphene/Ir(111), indicating that the molecules can be electronically decoupled from the metallic substrate by a monatomic layer of graphene.

Finally, we extend our investigation of surface-supported SMMs to a tetranuclear iron(III) complex known as Fe_4. By modifying the organic ligand shell of the compound and using hexagonal boron nitride (h-BN) on Rh(111) and graphene on Ir(111) as growth templates, we demonstrate for the first time that Fe_4 can be organized in highly periodic two-dimensional structures. Based on high resolution STM images, we show that the molecules adsorb on both substrates in a well defined geometry with their magnetic easy-axis being oriented along the surface normal. Furthermore, by means of X-ray magnetic circular dichroism (XMCD) measurements, we demonstrate that the magnetic anisotropy constant of Fe_4 is unaffected upon the deposition on graphene. To obtain information on the intramolecular exchange coupling in Fe_4 on the graphene layer, we measure the energy of spin-flip excitations in individual molecules via inelastic electron tunneling spectroscopy (IETS).

Contents

Introduction

The enormous performance improvement of integrated circuits over the last 50 years mainly resulted from the ongoing miniaturization of their basic electronic components. As of 2016, complementary metal–oxide–semiconductor (CMOS) technology is produced in the 14 nm fabrication node and the typical feature size of a single transistor in end-user devices is well below 100 nm. Many technical hurdles have been overcome to reach this state, disproving the predicted end of Moore's scaling law over and over again. However, there is an inevitable limit of how small a transistor can get and this limit will probably be reached within the next two decades.

Considering the amount of research and development that has been placed in over a long period of time, the current CMOS technology is unlikely to be replaced anytime soon. Possible alternatives are still on the stage of fundamental research and are far from entering everyday applications. Nevertheless, the elaboration of new concepts is unavoidable to maintain the development of electronic devices on a long-term scale.

A perspective to surpass the limits of silicon-based technology is provided by molecular electronics, i.e. the use of molecular building blocks for the fabrication of electronic components. Going back to a proposal of Aviram and Ratner in 1974 that a single molecule could be used as a rectifier [1], molecular electronics provide several advantages that cannot be achieved by conventional top-down fabrication methods. As the smallest functional unit occurring in nature, a single molecule represents the ultimate limit of miniaturization. Unlike metallic and semiconducting nanostructures, molecules offer a precise control of the exact spatial position and binding configuration of every single atom. They are not subject to dispersion in size and shape and therefore have predictable and reproducible properties. The chemical functionality of most molecules can be tailored by means of established wet-chemical methods, allowing for an adaption to different environments. Furthermore, molecular devices may facilitate a cost-effective production process by utilizing molecular self-assembly.

Going one step further, non-diamagnetic molecules offer the possibility to exploit both the electronic and spin degrees of freedom, which is the basic concept of a discipline called spintronics. In the field of data storage, spintronic components,

such as spin-valves, already found their way into everyday technology. Furthermore, spin-based logic devices have been proposed for future applications [2]. Combining the ideas of spintronics and molecular electronics, a class of molecules which is particularly promising are single molecule magnets (SMMs). The striking property of these compounds is their magnetic hysteresis of purely molecular origin, meaning that the spin state of a single molecule – at low temperature – remains stable in zero magnetic field over a long period of time. Due to this unique magnetic behavior, SMMs were proposed as candidates for spintronics [3], magnetic data storage [4] and quantum computing [5] applications. Moreover, SMMs have attracted considerable attention in fundamental research, since they allow for a macroscopic observation of quantum mechanical effects, such as quantum tunneling of magnetization [6, 7] and berry phase oscillations [8].

The perspective to use SMMs as building blocks in molecular spintronics is the main motivation for this work. Here, we present a study of two specific molecules. One of them, Mn_{12}, is the first discovered SMM [9, 10] and is widely considered as the archetype of this class of molecules. The other one, Fe_4, comprises a more simple and highly symmetric molecular structure and has raised great interest due to its remarkable chemical stability [11]. In order to contact the individual molecules, we use the tip of a scanning tunneling microscope (STM), which enables an unprecedented control of the junction geometry, including a precise knowledge of the electrode structure and molecule orientation. Insight into the elastic and inelastic charge transport properties of the molecules is obtained by recording the current-voltage characteristics of the tunnel junction, which is also known as scanning tunneling spectroscopy (STS).

A prerequisite for STM measurements and a requirement for any possible application is the deposition of the molecules on a substrate. In the field of SMMs, progress has been hindered for a long time by the difficulty to find suitable deposition procedures. Thermal sublimation in vacuum is not possible for most SMMs, as the large size of these molecules results in low vapor pressures. Other methods, such as drop-casting or wet-chemical grafting, suffer from poor sample quality and are difficult to combine with the demands of STM and STS. In this work, we utilize electrospray deposition (ESD) in ultra-high vacuum (UHV), which is a recently advanced technique allowing for an *in situ* deposition of nonvolatile molecules with well controllable surface coverage and with only little restrictions in choice of the substrate. The construction and characterization of a UHV-ESD setup has been an essential part of this work.

The content of this thesis is organized in three major parts. The first part, comprising chapters 1 to 4, outlines the basics of SMMs, ESD and STM/STS. Additional experimental methods that were applied in this work, such as low energy electron

diffraction (LEED), X-ray photoelectron spectroscopy (XPS) and superconducting quantum interference device (SQUID) magnetometry, are briefly introduced. The second part, including chapters 5 to 7, mainly deals with the experimental equipment and preparation routines. Special emphasis is placed here on the description of the utilized ESD setup, as it is crucial for the preparation process. Finally, the third part presents and discusses the performed experiments. Chapter 8 first gives a brief overview of the capabilities and limitations of the ESD setup by showing several experimental examples. Subsequently, the main study of Mn_{12} and Fe_4 compounds is presented in chapters 9 and 10, respectively.

Part I

Basics

1 | Single-Molecule Magnets

A single-molecule magnet (SMM) is a molecular material in which the individual molecule can be considered as a tiny magnet, meaning that its magnetic moment is stable over a certain period of time at low temperatures. It therefore exhibits a slow relaxation of magnetization of purely molecular origin, which is in contrast to conventional magnetic materials whose magnetism is a collective phenomenon that is based on the interaction of a large number of particles. The preservation of magnetic hysteresis in the case of non interacting molecules has been confirmed experimentally by various studies, such as measurements on frozen diluted solutions of Mn_{12} [12–14] and on diluted crystals of Fe_4, in which the spin carrying molecules are embedded in a crystalline matrix of their diamagnetic Ga_4 analogue [15]. This formation of magnetic order on the molecular level does not only give rise to the great interest in SMMs as molecular building blocks for possible applications, but is also the origin of fascinating quantum size effects that are reflected in their magnetic behavior. It is the goal of this chapter to introduce the main theoretical concepts that are widely used in order to describe magnetic relaxation in SMMs and to give insight into their unique magnetic properties. The content will be discussed in a rather general manner, since specific examples of SMMs can be found in later chapters that describe the materials used within this work in detail.

1.1 The Spin Hamiltonian Approach

Heisenberg Hamiltonian

The magnetic moment of a SMM is in general carried by a number of transition metal, lanthanide or actinide ions that are interlinked with each other by their coordinating ligands. Although single ion SMMs are known today [16], this number is typically significantly larger than one. The spins of the individual metal centers are not independent of each other, but are exchange coupled by indirect interactions, such as superexchange or double exchange. If only the isotropic contribution of these interactions is taken into account and if all non-nearest-neighbor terms are neglected,

the exchange coupling can be described by the Heisenberg Hamiltonian

$$\mathcal{H}_{\mathrm{ex}} = -\sum_{i<j} J_{ij} \boldsymbol{S}_i \cdot \boldsymbol{S}_j, \tag{1.1}$$

where the sum is evaluated over all pairs of spins $\boldsymbol{S}_i$ of the cluster. J_{ij} are called the exchange coupling constants and can be positive or negative in sign, depending on whether the interaction is ferromagnetic or antiferromagnetic, respectively.

Although (1.1) is a considerable simplification of the complicated processes that are responsible for the exchange interaction and that take place in the spatial domain rather than in spin space, utilizing it is often inconvenient. Even for moderate cluster sizes, numerical diagonalization of (1.1) can be extremely time consuming, since the dimension of the Hilbert space grows exponentially with the number of spin centers. Furthermore, the parameter space built up by all different coupling constants often is too large to be determined by experiment.

Giant Spin Approximation

The complexity of the problem is significantly reduced, when the isotropic exchange coupling is the dominating term in the overall spin Hamiltonian and when the system is studied at low temperatures, so that only the ground spin state S of (1.1) is occupied. In this so called strong exchange limit, the system can be described by a single giant spin $\boldsymbol{S}$ of spin quantum number S. For the cluster to behave as a SMM rather than a paramagnetic molecule, it is necessary that this giant spin is subject to a magnetic anisotropy. The microscopic origin of magnetic anisotropy in SMMs is based on various contributions, the most important ones being related to the crystal field of the coordination environment of the individual metal centers and to the magnetic dipole-dipole interaction between all spins within one molecule [17]. In first approximation, the anisotropic term in the Hamiltonian is a quadratic form of the spin operators and it is convenient[1] to write it as

$$\mathcal{H}_{\mathrm{an}} = DS_z^2 + E(S_x^2 - S_y^2). \tag{1.2}$$

The two constants D and E account for the axial and the transverse contribution to the anisotropy, respectively. They are restricted by the condition $|E/D| \leq 1/3$, since larger $|E/D|$ ratios would be equivalent to renaming the coordinate axes. In some cases, e.g. when $E = 0$ due to symmetry reasons, it might be necessary to include higher order anisotropy terms. In general, only even order terms up to order $2S$ have to be taken into account. A useful method that takes advantage of the molecular

[1] A more obvious choice of a quadratic form of the spin operators would be $\mathcal{H}_{\mathrm{an}} = D_{xx}S_x^2 + D_{yy}S_y^2 + D_{zz}S_z^2$. By using the relation $S_x^2 + S_y^2 + S_z^2 = S(S+1)$, it can be easily shown that this term differs from (1.2) only by a constant when the anisotropy parameters fulfill the relations $D = D_{zz} - \frac{1}{2}(D_{xx} + D_{yy})$ and $E = \frac{1}{2}(D_{xx} - D_{yy})$.

point group symmetry is to write the anisotropic term as a sum of so called Stevens operators [18]. In the important case of tetragonal symmetry, the lowest order terms are given by [19]

$$\mathcal{H}_{\mathrm{an}} = DS_z^2 + \frac{B}{2}(S_x^4 + S_y^4). \tag{1.3}$$

In addition to the exchange interaction (1.1) and the magnetic anisotropy (1.2) or (1.3), the effect of an external magnetic field $\boldsymbol{H}$ can be taken into consideration. This is done by adding a Zeeman term

$$\mathcal{H}_{\mathrm{Z}} = g\mu_{\mathrm{B}}\boldsymbol{S}\cdot\boldsymbol{H} \tag{1.4}$$

to the spin Hamiltonian, where g denotes the g-factor of the total spin.

1.2 Thermally Activated Magnetic Relaxation

Ising Type Magnetic Anisotropy

In many cases, the lowest order transverse anisotropy term is small compared to the axial one. In a first approximation, we will therefore neglect the transverse term in (1.2) or (1.3). Furthermore, we will assume that the external magnetic field is applied in direction of the anisotropy axis, i.e. $\boldsymbol{H} = H\boldsymbol{e}_z$, so that we have to consider the Hamiltonian

$$\mathcal{H}_0 = DS_z^2 + g\mu_{\mathrm{B}}HS_z. \tag{1.5}$$

Because $\mathcal{H}_0$ and S_z commute, the eigenstates $|m\rangle$ of S_z, defined by $S_z|m\rangle = m|m\rangle$, are also eigenstates of $\mathcal{H}_0$ and the corresponding eigenvalues are obviously given by

$$\mathcal{H}_0|m\rangle = E_m|m\rangle\,,\ E_m = Dm^2 + g\mu_{\mathrm{B}}Hm. \tag{1.6}$$

Since the term Dm^2 in (1.6) lifts the degeneracy of the spin $2S+1$ multiplet even for $H = 0$, the constant D is also called zero field splitting (ZFS) parameter. In the following, we will assume $D < 0$, so that the anisotropy is characterized by an easy axis of magnetization in z-direction. This situation is depicted in Figure 1.1 for the example of an $S = 10$ state. The energy levels are forming a double potential well, in which the two lowest lying states $|m\rangle = |\pm S\rangle$ are separated by an energy barrier of

$$\Delta E = |D|(S^2 - m_0^2), \tag{1.7}$$

where m_0 is 0 for integer S and $\frac{1}{2}$ for half-integer S.

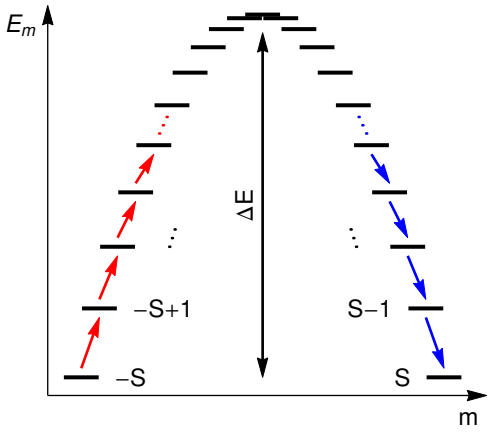

Figure 1.1 | Energy levels of a SMM with an easy axis of magnetization in zero magnetic field, depicted for an exemplary $S = 10$ ground spin state. Red and blue arrows illustrate stepwise excitation and relaxation by adsorption and emission of phonons, respectively.

Arrhenius Law

The occurrence of slow magnetic relaxation in SMMs is related to the time scale, on which the system is able to overcome this energy barrier. To illustrate this, one might consider the situation that all the spins initially occupy the same side of the double well, which can be realized by first saturating the magnetization of the sample in a strong magnetic field and then driving the field quickly back to zero. In thermal equilibrium, both sides of the double well will be equally occupied, meaning that no magnetization of the sample is present in zero magnetic field. However, transition into equilibrium requires the spins to climb up the ladder of states $|m\rangle$ and subsequently relax into the lower lying levels of the opposite well. This stepwise excitation and relaxation process takes place by adsorption and emission of phonons via spin-phonon coupling and will therefore strongly depend on temperature.

In general, the convergence of the magnetization M to its equilibrium value M_{eq} will follow an exponential time evolution

$$M(t) - M_{\mathrm{eq}}(H) \propto \exp(-t/\tau), \tag{1.8}$$

which defines a relaxation time τ. As for many other processes in nature that require an energy barrier to be overcome by thermal excitation, the temperature dependence of the relaxation time is described by a so called Arrhenius law

$$\tau = \tau_0 \exp \frac{\Delta E}{k_{\mathrm{B}} T}. \tag{1.9}$$

The reciprocal of the prefactor τ_0 is also called attempt frequency. Experimental values of τ_0 can differ by several orders of magnitude and are typically in the range of 10^{-6}–10^{-11} s [20]. An analytical expression of τ_0 was derived by Villain *et al.* [21], stating that

$$\tau_0 \propto \frac{\rho c_s^5}{|V_{m_0+1,m_0}|^2} \frac{S^6}{\Delta E^3}, \tag{1.10}$$

where ρ is the mass density, c_s is the velocity of sound (assumed to be the same for all acoustic modes) and V_{m_0+1,m_0} is the matrix element of the spin-phonon interaction for the last transition in climbing up the ladder, i.e. $|m_0+1\rangle \rightarrow |m_0\rangle$[2].

The Arrhenius law (1.9) implicates that magnetic hysteresis in SMMs can only be observed at low temperatures. When the temperature rises, the relaxation time becomes small compared to the time required for a measurement, meaning that the sample will behave like a paramagnetic ensemble of spins with large quantum number S in thermal equilibrium. Such a behavior is known as superparamagnetic and has been observed on ferromagnetic single-domain particles and granular ferromagnetic alloys long before the discovery of the first SMM [22–24]. The transition between both regimes takes place at the so called blocking temperature T_B, which marks the point where relaxation occurs on the time scale of the experiment[3].

The need of applications for high blocking temperatures did motivate the search for SMMs with ever larger values of ΔE and S, resulting in a record energy barrier of $\Delta E = 938\,\mathrm{K}$ for a mononuclear Tb complex [25] and a record ground spin state of $S = 83/2$ in a ferromagnetically coupled Mn_{19} aggregate [26]. However, it must be observed that the increase of T_B achieved within more than two decades of research did not meet the expectations. To the knowledge of the author, the SMM which represents the strongest magnet-like behavior to this day is a radical-bridged Dy_2 compound that shows hysteresis up to 8.3 K in magnetometric measurements recorded at conventional sweep rates [27]. The reason of this shortcoming is a second relaxation process, that will be discussed in the next chapter.

1.3 Quantum Tunneling of Magnetization

At very low temperatures, the relaxation time τ of a SMM deviates from the temperature dependence predicted by the Arrhenius law. Instead of further increasing with falling temperature, it approaches a constant level, as shown in Figure 1.2a for the archetypical Mn_{12}-ac cluster. Furthermore, it is observed that the relaxation time oscillates with the magnetic field, reaching minima at almost equally distanced values, which is in contradiction to the monotone field dependence of the energy barrier in (1.9) (see Figure 1.2b).

[2]The exclusive dependence of τ_0 on the specific matrix element V_{m_0+1,m_0} reflects the small number of phonons available at low energies. The transition with the smallest energy difference is the slowest one and therefore determines the attempt frequency of the whole relaxation process.

[3]Depending on the experimental technique (i.e. DC magnetometry, AC magnetometry, Mößbauer spectroscopy), the relevant time scale can vary by many orders of magnitude. Therefore, the value of T_B is always related to the method used for its measurement.

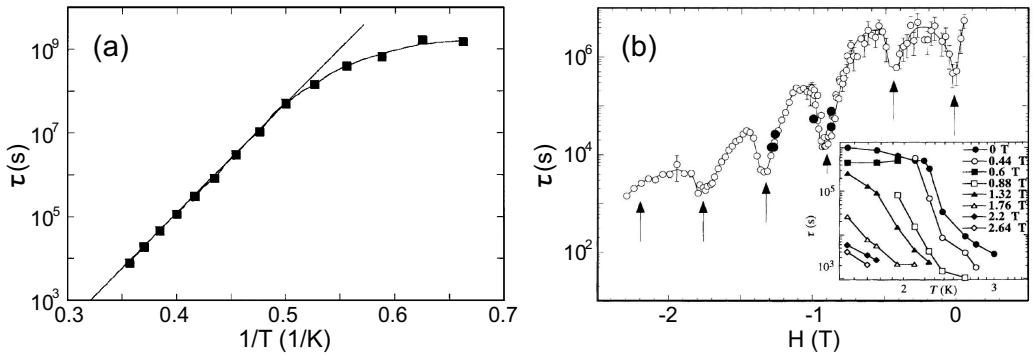

Figure 1.2 | Relaxation time of Mn_{12}-ac. **(a)** Arrhenius plot of the temperature dependence in zero magnetic field (adapted from [28]). **(b)** Plot as a function of the longitudinal magnetic field at $T = 2.10\,\mathrm{K}$ (adapted from [6]).

Perturbation Approach

The origin of the remarkable low temperature behavior lies in the transverse terms of the spin Hamiltonian that have been neglected in the discussion so far. Since these terms do not commute with S_z, the eigenstates of the Hamiltonian are a superposition of different states $|m\rangle$. Valuable insight into the problem is provided by perturbation theory, when the transverse terms are considered as a disturbance $\delta\mathcal{H}$ of the unperturbed Hamiltonian $\mathcal{H}_0$, given by (1.5). To first order of perturbation theory, the admixture of a state $|m'\rangle$ to an eigenstate $|m\rangle$ of $\mathcal{H}_0$ is given by

$$\frac{\langle m'|\,\delta\mathcal{H}\,|m\rangle}{E_m^{(0)} - E_{m'}^{(0)}}, \tag{1.11}$$

where $E_m^{(0)} = \langle m|\,\mathcal{H}_0\,|m\rangle$ denotes the zero order eigenvalue of a state $|m\rangle$. Although (1.11) is valid only when $|m\rangle$ and $|m'\rangle$ are not degenerate, it can be deduced that the impact of the transverse terms on the eigenstates is strongest when the unperturbed states are close or identical in energy. Degeneracy of the unperturbed states occurs if

$$E_m^{(0)} - E_{m'}^{(0)} = 0 \tag{1.12}$$

and it can be easily shown that this condition is met when the external magnetic field is given by

$$H^{(mm')} = \frac{|D|}{g\mu_\mathrm{B}}(m + m'). \tag{1.13}$$

It should be noted that (1.13) implies that all pairs of states (m, m') with the same sum $m + m'$ are degenerate simultaneously[4].

[4]This is only valid when higher order terms of axial anisotropy are neglected.

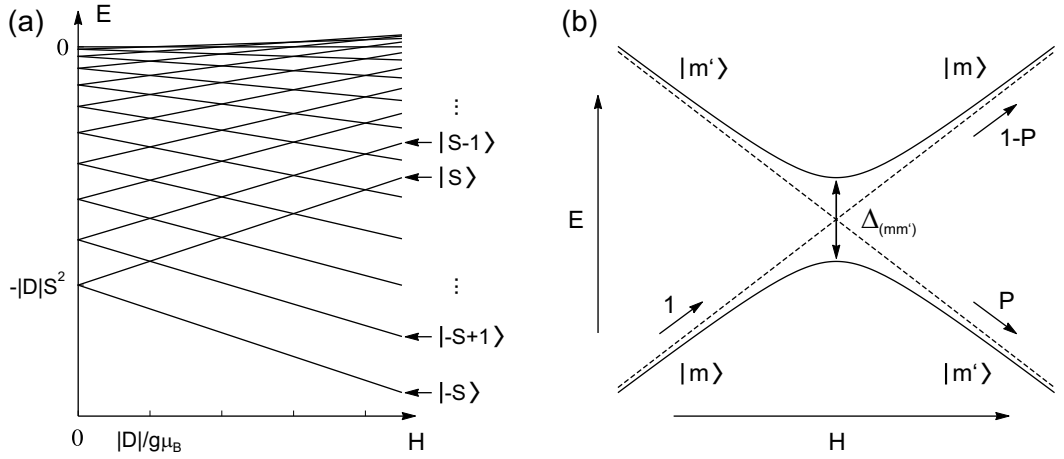

Figure 1.3 | **(a)** Longitudinal field Zeeman splitting calculated based on the unperturbed Hamiltonian (1.5) for an exemplary $S = 10$ state. **(b)** Transverse anisotropy terms cause a splitting of the eigenvalues originating from $|m\rangle$ and $|m'\rangle$ at the level crossing field $H \approx H^{(mm')}$.

Level Anticrossing and Pure Quantum Tunneling

When H is far away from $H^{(mm')}$, admixture of states can be neglected and it is reasonable to write the eigenstates of the Hamiltonian as $|m\rangle$, although strictly speaking m is not a good quantum number anymore. On the other hand, the states $|m\rangle$ and $|m'\rangle$ will be strongly admixed when $H \approx H^{(mm')}$ and the notation of the eigenstates as m and m' will become meaningless in this case. In general, it is observed that the original degeneracy of the eigenstates at $H^{(mm')}$ is lifted by the influence of the transverse terms. Instead, the two eigenvalues of the perturbed Hamiltonian are separated by an energy difference which is called tunnel splitting and denoted $\Delta_{(mm')}$ or $2\hbar\omega_{\mathrm{T}}^{(mm')}$, where $\omega_{\mathrm{T}}^{(mm')}$ is referred to as the tunnel frequency[5]. This effect is also known as anticrossing and is depicted in Figure 1.3.

It can be shown that significant admixing of states around $H^{(mm')}$ only appears in a field interval of width $\delta H^{(mm')}$ in which the energy difference between the unperturbed states is of the order of the tunnel splitting, i.e.

$$g\mu_{\mathrm{B}}|m' - m|\delta H^{(mm')} \approx \hbar\omega_{\mathrm{T}}^{(mm')}. \tag{1.14}$$

Within this interval, the delocalization of the eigenstates over both wells can enable a direct transition between $|m\rangle$ and $|m'\rangle$. This process, known as quantum tunneling of magnetization (QTM), provides an alternative relaxation mechanism besides thermally excited crossing of the energy barrier and therefore results in a reduction of the

[5]The introduction of a tunnel frequency refers to the theoretical scenario of a SMM that is perfectly isolated from its environment. In this case, transverse anisotropy leads to an oscillation of the spin between $|m\rangle$ and $|m'\rangle$ with angular frequency $\omega_{\mathrm{T}}^{(mm')}$ at at $H = H^{(mm')}$, which is called resonant quantum tunneling [19].

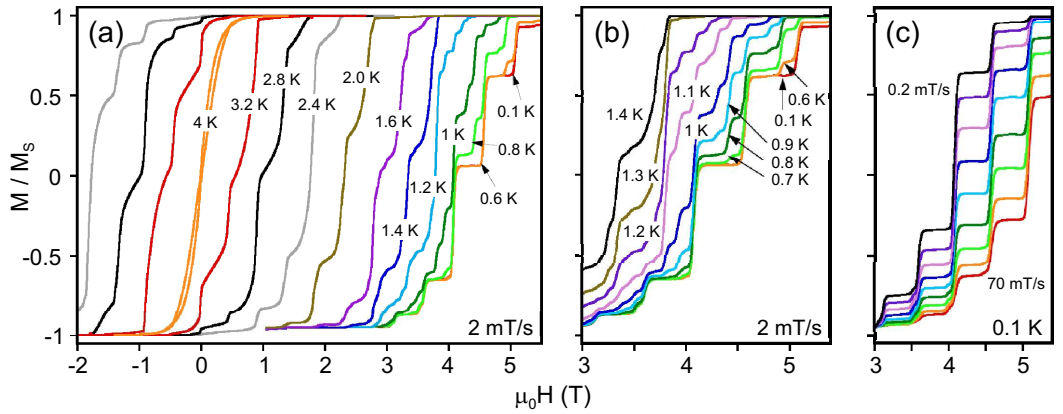

Figure 1.4 | QTM observed in Mn_{12}-*t*BuAc. **(a,b)** Hysteresis loops at different temperatures and constant field sweep rate. The curves become temperature independent below 0.6 K, indicating pure quantum tunneling from the ground state. **(c)** Hysteresis at different field sweep rates and at $T = 0.1$ K, demonstrating that the transition probability in the temperature independent regime is a function of the sweep rate. Adapted from [32].

relaxation time. When the system is initially in state $|m\rangle$ and the field H is ramped over the level crossing $H^{(mm')}$ with a sweep rate $\mathrm{d}H/\mathrm{d}t$, a transition into $|m'\rangle$ will take place with a certain probability P that depends only on $\Delta_{(mm')}$ and $\mathrm{d}H/\mathrm{d}t$ and that can be described by a formula first derived by Landau, Zener and Stückelberg in 1932 [29–31]. Magnetic hysteresis curves of SMMs therefore become temperature independent at very low temperatures, while steps appear at well defined field values $H^{(mm')}$ (Figure 1.4). These steps, widely considered as the fingerprint of QTM in SMMs, were first observed on Mn_{12}-ac in 1996 [6, 7].

Thermally Assisted Quantum Tunneling

When magnetization curves are recorded at intermediate temperatures, the process of magnetization reversal can include both thermal excitation and QTM. While the tunnel frequencies $\omega_{\mathrm{T}}^{(mm')}$ can be extremely small for tunneling from the ground state $m = \pm S$, they might be of considerable size for smaller values of m and m'. Therefore, quantum tunneling might take place from a higher spin state after thermal excitation, provided that the timescale of the tunneling transition is reasonably short compared to the lifetime of the excited state. The mechanism of this process, which is called thermally assisted QTM, is sketched in Figure 1.5. It is the dominating relaxation path at intermediate temperatures, but can extend to very low temperatures in some cases. A prominent example is Mn_{12}-ac: Although steps in magnetization curves can already be observed at several Kelvin, the hysteresis stays temperature dependent down to 59 mK [33] and pure QTM with temperature independent hysteresis could only be observed in other compounds, such as Mn_{12}-*t*BuAc [32] and Fe_8 [8, 34].

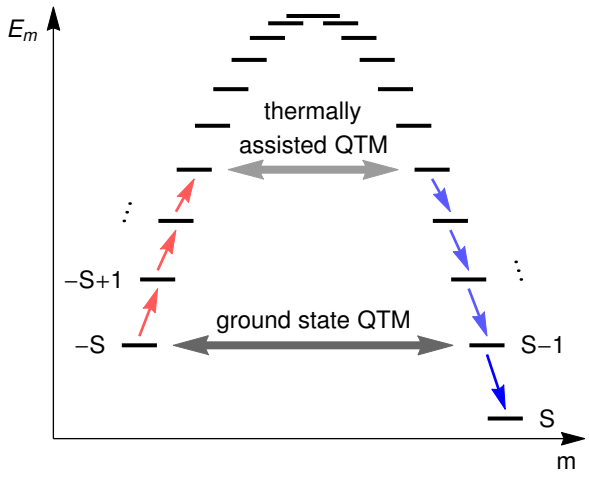

Figure 1.5 | Energy levels of an $S = 10$ spin state subject to a longitudinal magnetic field $H = H^{(-S,S-1)}$. Thermally assisted QTM is possible when the system is first excited into a state with smaller quantum number m.

An important consequence of thermally assisted QTM is that the effective height of the energy barrier is reduced by bypassing the upmost energy levels. For this reason, it is generally observed that the value of ΔE extracted from a fit of experimental relaxation time data to the Arrhenius law is significantly smaller than a calculation of the full barrier height (1.7) based on a magnetometric or electron paramagnetic resonance (EPR) spectroscopy measurement of S and D.

Symmetry Related Selection Rules

From a theoretical point of view, QTM is not possible between arbitrary states, but underlies selection rules that are related to symmetry. Since tunneling between two states $|m\rangle$ and $|m'\rangle$ is only allowed when the transition matrix element $\langle m'|\,\delta\mathcal{H}\,|m\rangle$ appearing in (1.11) is not zero, a tunneling resonance only exists when the transverse anisotropy Hamiltonian contains terms of the spin ladder operators $S_\pm = S_x \pm iS_y$ of order $|\Delta m| = |m' - m|$. In the case of high symmetry molecules, this leads to a restriction of the allowed tunneling transitions. It can be easily shown that, e.g., the transverse term in (1.3) only allows $|\Delta m| = 4$ and that, more generally, molecules with S_4 symmetry (tetragonal crystal system) are subject to the transition rule $|\Delta m| = 4n$, where n is an integer [19].

However, the existence of selection rules is in contradiction to almost all experiments on SMMs, where usually all QTM transitions are found regardless of the molecular symmetry. In fact, an experimental manifestation of selection rules was not observed until 2009 [35]. There are many possible reasons for this violation, such as local symmetry reduction due to crystalline disorder or theoretical shortcomings of the giant spin approximation. The interested reader is referred to [35] for further information.

2 | Electrospray Ionization

The atomization of electrically conductive liquids into charged droplets by high electric fields is a phenomenon that has been known for a long time. First reports on the subject were published by Zeleny as early as 1914 [36,37]. Since then, the so-called electrospray effect found its way into various applications of aerosol generation, such as crop spraying, ink-jet printing, fuel atomization and air cleaning [38].

The idea that electrospraying could also be used to produce intact gas phase ions from large and complex species in solution was first introduced by Dole *et al.* in 1968 [39, 40]. The pioneering work of Dole was motivated by the expectation that this technique, called electrospray ionization (ESI), could be used to perform mass spectrometry on macromolecules that tend to fragment when ionized by conventional methods. However, the original setup used by Dole had some technical drawbacks and it was finally up to Fenn and coworkers in 1984 to provide convincing experimental evidence of electrospray ionization mass spectrometry (ESI-MS) [41, 42].

In contrast to other so-called soft ionization techniques[1] that are capable of producing mass spectra with only little content of fragmentation, ESI-MS offers a number of unique advantages. Since ionization is performed from solution, an electrospray mass spectrometer can be directly coupled to a high performance liquid chromatography (HPLC) system, which allows for a high throughput analysis of complex analyte mixtures. Furthermore, ESI is capable of producing strong multiple charging of heavy molecules, which effectively extends the mass range accessible in mass spectrometry. Conventional mass analyzers are typically limited to mass-to-charge ratios m/z of some thousand Th – a range which is well covered by ESI. Among the species that have been successfully investigated by ESI-MS are large organic polymers [42] and biological macromolecules like proteins [42], DNA [43] and even viruses [44]. The molecular mass of the latter ones is in the range of 10^7 Da and there is yet no evidence of an upper limit.

Besides mass spectrometry, another steadily growing field of electrospray ionization is the surface deposition of nonvolatile materials, whose sublimation in vacuum is prevented by low vapor pressures and thermal instability. In the most simple case, electrospray deposition (ESD) is performed under ambient conditions, which allows

[1] Besides ESI, most importantly matrix assisted laser desorption/ionization (MALDI) is to be mentioned.

for a growth of thick film material [45–48]. Soft-landing of mass selected ions onto solid and liquid surfaces in vacuum was performed with the aim of preparative mass spectrometry [49–52]. More recently, a number of groups did build up experiments for the in-situ investigation of electrospray-deposited molecules in submonolayer coverage, making use of the powerful and highly surface sensitive methods that are available in ultrahigh vacuum (UHV) technology [53–59]. Alternative techniques for the UHV deposition of nonvolatile compounds, such as pulsed valves [60] or stamping techniques [61], are often easier to implement, but cannot reach the high degree of control of surface coverage and purity that is achieved by ESD.

Within this work, electrospray generation and ionization was utilized in multiple ways. On the one hand, thick films and submonolayers of molecular materials were prepared by ESD at atmospheric pressure and in UHV, respectively. On the other hand, ESI-MS was implemented as a part of sample analysis. The experimental details of these procedures are described in chapters 5 and 6. The scope of this chapter is to introduce the physical fundamentals behind electrospray ionization and to review the properties of ions produced by ESI.

2.1 The Mechanism of Electrospray Ionization

The principle setup used for electrospray ionization is depicted in Figure 2.1. A solution containing the analyte is pushed through a hollow metallic needle, called emitter, at a certain volume flow rate F. By applying a high voltage V_e between the emitter and a counter electrode, a strong electric field is generated at the apex of the emitter, which leads to an accumulation of excess charge at the surface of the liquid. The polarity of the voltage can be both positive or negative. In the following, only the more commonly used positive ion mode will be considered.

2.1.1 Creation of Charged Droplets

When the electric field at the liquid surface reaches a critical value, the liquid meniscus acquires a conical shape, also known as Taylor cone. The deformation typically takes place at voltages V_e of several kV, with the exact value depending on the electrode geometry and liquid surface tension [62]. In his original work, Taylor did show that an equilibrium between all forces acting on the liquid surface[2] theoretically requires an opening angle of the cone of $\alpha_\mathrm{T} = 98.6°$ [62]. In practice, opening angles deviating from this value are observed since the system is not in a static condition.

From the apex of the cone, a jet is emerging, which breaks up into charged droplets after short time due to Plateau–Rayleigh instability. The diameter of the jet D_j critically depends on the volume flow rate F and liquid conductivity K. In

[2] A description of the shape of the liquid surface must include the electrostatic pressure, the surface tension, the internal pressure of the liquid and the external pressure of the surrounding gas.

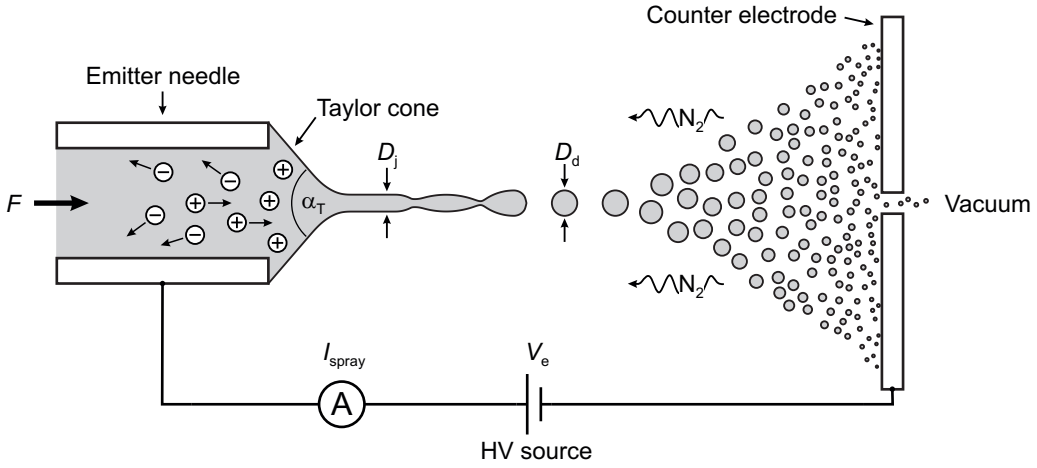

Figure 2.1 | Principle setup used for electrospray ionization, containing an emitter needle and a counter electrode, the latter one having an entrance orifice to a vacuum region.

the regime of highly conducting liquids, the functional dependence is described by the scaling law

$$D_\mathrm{j} \propto (\epsilon F/K)^{1/3}\,, \tag{2.1}$$

where ϵ is the dielectric constant of the solution [63]. The same law holds for the initial droplet diameter D_d, since the most probable size of the droplets is given by the ratio $D_\mathrm{d}/D_\mathrm{j} \approx 1.89$, well known from the breakup of jets without electric charge [64].

Typical initial droplet diameters of conventional electrospray sources using flow rates of several μl/min are in the range of 1–3 μm [65,66]. Significantly smaller initial droplet sizes can be achieved by reducing the flow rate to the nl/min range, which gave rise of the construction of so called nanoelectrospray sources that offer very high ionization efficiencies [66–68]. It should be noted, however, that stable working conditions at low flow rates require small inner diameters of the emitter needle [64], which makes the operation of such spray sources challenging. Furthermore, it should be stated that F and K can not be chosen independently of each other. The appearance of a stable Taylor cone emitting a single jet (a so-called cone-jet mode) can only be observed in a narrow domain of the F-V_e space and it generally holds that the higher the conductivity K is, the smaller are the allowed values of liquid flow rates F [64]. Fine droplets are therefore generally created from highly conducting liquids and in the case of liquid metals, the jet diameter can even become atomically small [63].

The electric current I_spray that is transported by the jet depends on the liquid

flow rate and conductivity as well. For highly conducting liquids, the scaling law

$$I_{\text{spray}} \propto (\gamma F K)^{1/2} \tag{2.2}$$

is found, where γ is the surface tension of the solution [63]. High spray currents can therefore be achieved by using high analyte concentrations, resulting in high conductivities K. However, due to decreasing ionization efficiencies, signal intensities observed in ESI-MS typically approach a plateau value at concentrations of around 10^{-5}–10^{-4} M, which settles the upper concentration limit commonly used in electrospray ionization mass spectrometry [69].

2.1.2 Desolvation and Formation of Gas Phase Ions

In the electric field that is generated by V_{e}, the charged droplets created from the liquid meniscus are accelerated towards the counter electrode. On their way, the droplets are reduced in size due to solvent evaporation. A rapid decrease in droplet temperature due to evaporative cooling is compensated by the interaction of the droplets with the surrounding gas [39]. The electrospray generation therefore needs to be performed at high enough (atmospheric) pressure and the evaporation is often further supported by a counter flow of hot nitrogen gas.

During the evaporation process, the charge density at the surface of the droplets is continuously increasing. When the Coulomb repulsion between the charges exceeds the surface tension of the liquid, the spherical shape of the droplet becomes unstable. It was first shown by Lord Rayleigh [70] that the critical diameter of a droplet carrying a charge Q is given by

$$D_{\text{crit}} = \left(\frac{Q^2}{8\pi^2 \epsilon_0 \gamma} \right)^{1/3}, \tag{2.3}$$

where ϵ_0 is the permittivity of the surrounding medium. Notably, equation (2.3) states that the distribution of a given charge over several small droplets is more stable than a single large droplet of the same volume. Reaching of the Rayleigh limit therefore leads to a disintegration of the droplet into smaller entities, which is known as Coulomb fission [65, 71] (see Figure 2.2a). Since the satellite droplets created during disintegration are again subject to solvent evaporation, further reduction of the droplet size rapidly takes place by a cascade of desolvation and Coulomb fission processes.

The mechanism for the final formation of gas phase ions has been the subject of a long lasting and still ongoing controversy, that did revolve around two alternative models (see Figure 2.2b). The so-called charge residue model (CRM) [39] assumes that desolvation and Coulomb fission processes continue until droplets containing only a single charged particle are created. Further evaporation of the solvent then

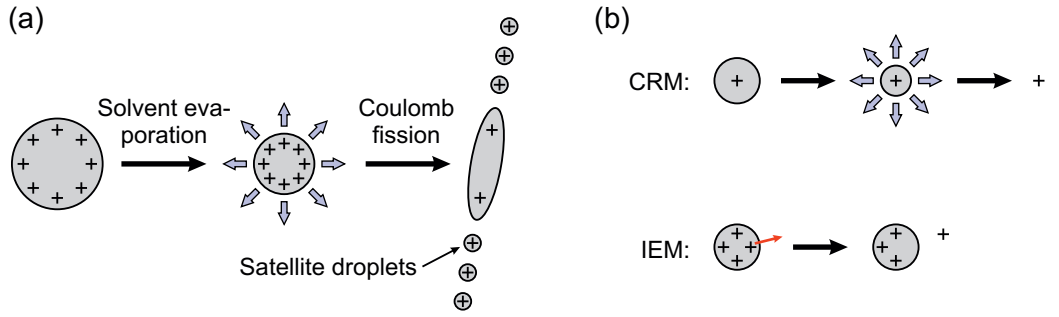

Figure 2.2 | **(a)** Schematic representation of droplet size reduction due to solvent evaporation and Coulomb fission. The fission process takes place by ejection of small satellite droplets, that are carrying only a few percent of the total liquid mass, but a significant fraction of the total charge [65]. **(b)** Formation of gas phase ions as proposed by CRM and IEM.

leaves behind the gas phase ion as a residue. The alternative ion evaporation model (IEM) [72] proposes that individual ions can separate ("evaporate") from charged droplets when they are close to being unstable. Ion evaporation therefore has to be thought of as a process that is competing with Coulomb fission and it is predicted based on theoretical calculations that the ejection of individual ions rather then charged droplets is dominating when the droplets reach sizes of the order of 10 nm [72].

Regardless of the model, it should be noted that only a fraction of the particles present in the original solution are ionized and brought into gas phase during the electrospray process. The counter electrode is therefore reached by a mixture of gas phase ions, solvent molecules and droplets containing charged as well as uncharged particles. The efficiency of ion detection or deposition is further reduced by losses that occur during ion transfer into vacuum, as it will be discussed in the next section.

2.1.3 Transfer into Vacuum

For the purpose of mass spectrometry and UHV surface deposition, a transfer of the ions created by ESI into vacuum is mandatory. A vacuum chamber is connected to the atmospheric pressure region of the electrospray source by a small leak in the counter electrode. In practice, the leak is realized either as an orifice, or by using a several cm long capillary, the latter one being easier to implement from a technical point of view.

By adapting the inner diameter of the entrance hole and the pumping speed of the vacuum pumping system, a pressure drop of around 3–5 orders of magnitude can be achieved. Under these conditions, the expansion of the mixture of gas, droplets and gas phase ions into vacuum becomes supersonic, which has important implications for the properties of the created ion beam. Since a fluid traveling at supersonic speed is not affected by changes of state appearing in downstream direction, the

expansion of the jet takes place as if it entered a perfect vacuum. It is accompanied by a transformation of particle movement from random to directed motion, which results in a substantial cooling of the jet. Noteworthy, the jet is supersonic primarily because of its cooling, resulting in a local decrease in speed of sound, rather than because of the increase in velocity.

An adjustment to the local boundary conditions of the vacuum chamber takes place by formation of a shock wave, in which the jet particles undergoe collisions with the warm background gas, resulting in a back transformation of particle movement from directed flow to random motion (see Figure 2.3a). At moderate chamber pressures (of the order of 1 mbar), the shock wave is thick enough to prevent a penetration of the background gas into the region of free expansion [73, 74]. The location of the shock wave, which is called Mach disk in flow direction, is an important design consideration for the construction of supersonic jet sources. It can be estimated from the empirical law

$$x_{\mathrm{M}} = 0.67 d_{\mathrm{i}} \sqrt{\frac{p_0}{p_1}}, \tag{2.4}$$

where x_{M} is the distance between Mach disk and entrance opening, d_{i} is the internal diameter of the entrance opening and p_0 and p_1 correspond to the pressures of the atmospheric region and the vacuum chamber, respectively [75].

A conical opening to a lower pressure region, also called skimmer, is placed upstream of the Mach disk in order to retain the directed motion of the jet particles (see Figure 2.3b). To avoid scattering on an additional shock wave forming at the entrance of the skimmer, it is important that the edge of the opening is as sharp as possible [40]. Furthermore, it was found that maximum values for beam intensity are achieved when the skimmer angle is in the range of 50–60° [73, 76].

The velocity of the beam downstream of the skimmer is determined by the properties of the carrier-gas. Macroions that are diluted in the carrier-gas are accelerated to a velocity equal to that of the gas itself by undergoing collisions with the carrier-gas molecules [39]. A theoretical estimation of the terminal velocity that is approached during the free jet expansion is given by

$$v_\infty = \sqrt{\frac{2k_{\mathrm{B}}}{m}\left(\frac{\gamma}{\gamma - 1}\right) T_0}. \tag{2.5}$$

Here, m is the mass of a carrier-gas molecule, $\gamma = C_{\mathrm{p}}/C_{\mathrm{V}}$ is the heat capacity ratio of the carrier-gas, which is assumed to be independent of temperature ($\gamma = 7/5$ for ideal diatomic gases), and T_0 is the temperature of the carrier-gas in the atmospheric pressure region [75].

A major disadvantage of the nozzle-skimmer design described here is the significant loss in ion intensity that appears in the first differential pumping stage of the

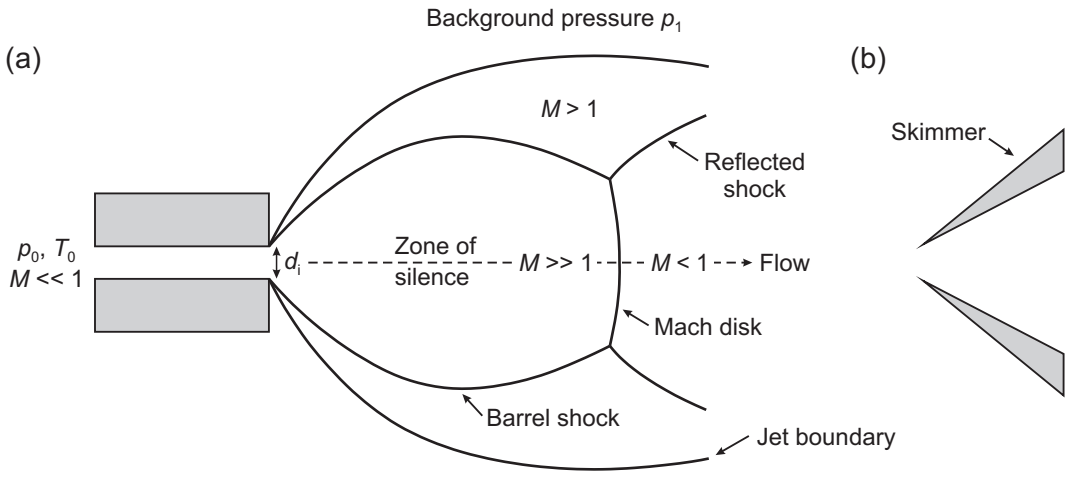

Figure 2.3 | **(a)** Sketch of the main features present in a supersonic expansion. M indicates the Mach number, defined as the ratio of flow velocity to the local speed of sound. The region of free expansion, also called zone of silence, is delimited by a shock wave, which is divided into Mach disk and Barrel shock. Shock wave structure redrawn from [75]. **(b)** A skimmer is used for sampling of the jet.

vacuum system, owing to the fact that a only small part of the supersonic jet is sampled by the skimmer. A substantially higher ion transmission can be achieved by implementing a so called ion funnel, which consists of a series of ring electrodes of progressively smaller internal diameter, used for focusing of the ions onto the entrance of the second pumping stage [77–79]. However, the construction and operation of an ion funnel means a much larger effort compared to the use of a standard nozzle-skimmer interface and it was therefore not taken into consideration for the experimental setup used within this work.

2.2 Ions Produced by an Electrospray Source

Many analytes that are dissolved for the purpose of mass spectrometry or surface deposition are originally present as neutral species. Their ionization pathway strongly depends on the chemical properties of the analyte molecules, and is further influenced by the composition of the solution and the parameters used for operation of the electrospray source. Both positive and negative ions can be produced by electrospray ionization, with the sign of charge being defined by the polarity of the emitter voltage V_e. In accordance with the previous section, only the positive ion mode will be considered in the following discussion.

Analyte molecules containing basic groups can be charged by protonation in a chemical acid-base reaction. An important example is the amino group, which is present in many biological macromolecules, most famously in proteins. Since the protonation equilibrium depends on the pH, the ionization efficiency can be increased by adding volatile acids to the solution. Formic acid and acetic acid are widely used

additives in electrospray mass spectrometry.

A similar charging mechanism is the formation of adducts with ions that are present in solution either as contaminations, or as part of a salt that is added to the solution on purpose. Na^+ ions can derive from contact with glassware and are found in concentrations of around 10^{-6} M even in analytical grade solvents [80]. Other alkali and alkaline earth metal ions such as Li^+, K^+, Mg^{2+} and Ca^{2+} are typically present as impurities to a smaller extend. Adduct formation plays an important role for polar analyte molecules, that do not contain any basic functional group. It is not limited to neutral species, but can also affect the formation of gas phase ions from ionic molecules.

As the opposite of adduct formation, charging can also take place by fragmentation. When a part of the analyte molecule is split off by heterolytic cleavage of a chemical bond, two fragments of opposite charge are formed, one of which can occur in the electrospray, depending on the sign of the ion mode. Although ESI is generally known as a soft ionization method, fragmentation can not be excluded. It should be considered especially in analytes that contain non-covalent bonds, such as the coordinate bonds that are typically present in single-molecule magnets. In fact, fragmentation of SMMs has regularly been observed in the ESI-MS spectra measured within this thesis.

Finally, uncharged molecules can also be ionized by undergoing an electrochemical reaction. Oxidation of the analyte is then caused by the high electric field that is generated at the gas-liquid interface. In contrast to protonation, the molecular mass remains the same within the process, which enables an unambiguous identification in mass spectrometry.

3 | Scanning Tunneling Microscopy and Spectroscopy

The development of the scanning tunneling microscope by Binnig and Rohrer in 1982 [81,82] represents a milestone in surface physics and nanotechnology. The utility of the new technique was demonstrated for the first time just one year later, when the observation of the 7×7 reconstruction on Si(111) in real space put an end to a long-lasting and controversial debate about an ever-increasing number of models of this structure [83]. The real capabilities of scanning tunneling microscopy (STM) however go far beyond resolving surface structures. Due to its ability to image, manipulate and spectroscopically investigate matter at the atomic level, STM has become an indispensable tool for scientists in various fields of research.

Figure 3.1 shows the principle setup used in STM. A fine metallic tip, usually made of W or PtIr alloy, is attached to a piezoelectric scanner that can be moved in all spatial directions x, y and z with sub-nm precision. The tip is brought in close vicinity to the sample, meaning that the distance d between tip apex and sample surface is in the range of around 0.5–1 nm. When a bias voltage V is applied between tip and sample, a tunneling current I is generated due to the overlap of tip and sample wave functions. Common values of V are between a few mV and several V, while I typically ranges from a few pA up to several ten nA.

The key property of the tunneling current $I \propto e^{-2\kappa d}$ is its exponential dependence on the tip-sample distance d. As a rule of thumb, typical values of the decay constant are around $\kappa \approx 11\,\mathrm{nm}^{-1}$, meaning that I decays by one order of magnitude when d is increased by 1 Å [86]. The drastic distance dependence of the tunneling current is taken advantage of by the two principle operating modes of STM. In the so called constant current mode, the height z of the tip is adjusted by a feedback loop in order to keep I at a preset level, while the tip is scanning the surface along its lateral coordinates (x, y). In this way, a three-dimensional data set $(x, y, z(x, y))$ is received, which is called topographic image. In the less frequently used constant height mode, the tip is moved on a plane parallel to the surface and the lateral dependence of the tunneling current is recorded, yielding an image of the surface in form of a data set $(x, y, I(x, y))$. This mode, however, is only appropriate for atomically flat surfaces and is therefore of no importance for the present thesis.

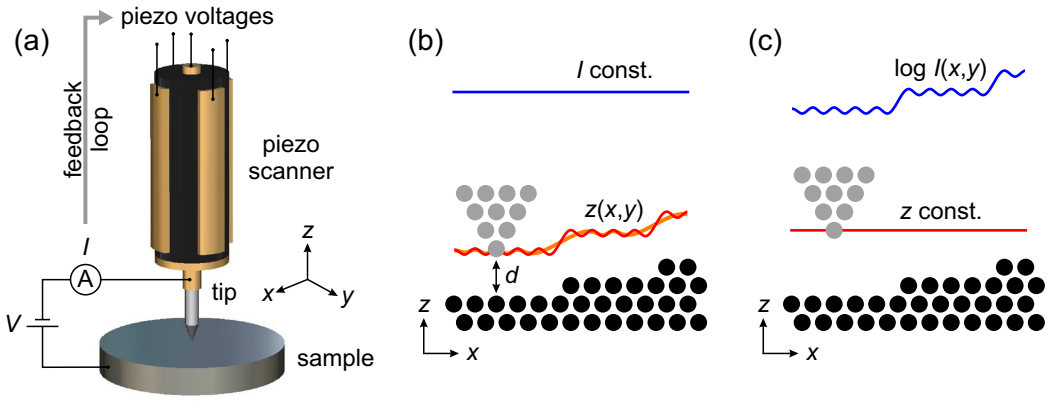

Figure 3.1 | Functional principle of STM. **(a)** Sketch of the integral parts of an STM setup. **(b)** Constant current mode. Red and orange line profiles correspond to different response times (gain settings) of the feedback loop. **(c)** Constant height mode. Images adapted from [84, 85].

3.1 Theory of Electron Tunneling

The theoretical background of STM is nowadays described in several textbooks, for example the monographs of C. J. Chen [86] and R. Wiesendanger [87] and the collective work edited by J. A. Stroscio and W. J. Kaiser [88]. For a detailed introduction into the topic, the reader is referred to the mentioned references. The aim of this chapter is to give a brief overview of the fundamental aspects that are needed for a comprehension of the main results presented in this work.

3.1.1 Bardeen Theory of Tunneling

The foundation for a theoretical treatment of electron tunneling in STM goes back to a work of Bardeen published in 1961 [89], long before the invention of the scanning tunneling microscope. Bardeen's idea was to provide a solid explanation of a pioneering experiment carried out by Giaever, who showed that the bandgap of a superconducting material is reflected in the conductivity of a metal–insulator–superconductor [90] or superconductor–insulator–superconductor [91] tunnel junction. The original calculation of Bardeen was carried out in one dimension in order to match the planar junction geometry used by Giaever. However, Bardeen's formalism can easily be extended to three dimensions, enabling a treatment of the asymmetric tip-sample interface present in STM.

The idea of Bardeen's calculation resembles first order perturbation theory, although being different from the standard perturbation approach of quantum mechanics. Instead of solving the Schrödinger equation of the combined system of both electrodes, Bardeen starts by considering the solutions of the two electrodes separately. Since the wave functions of each electrode overlap with the other electrode, none of the solutions of the individual subsystems also fulfills the combined

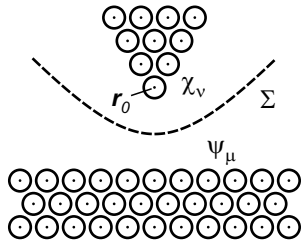

Figure 3.2 | Definition of Bardeen's tunneling matrix element. The surface integral (3.2) is calculated on an arbitrary separation surface Σ.

Schrödinger equation. Therefore, when an electron is initially in an eigenstate ψ_μ of electrode A (say the sample), there is a finite probability for it to be in a state χ_ν of electrode B (say the tip) at a later point of time. Bardeen did show that the transition rate (probability per time) between both states is given by

$$\lambda_{\mu\nu} = \frac{2\pi}{\hbar}|M_{\mu\nu}|^2\delta(E_\mu - E_\nu). \tag{3.1}$$

Equation (3.1) implies elastic tunneling, i.e. transitions can only take place between states of equal energy $E_\mu = E_\nu$. The so called tunneling matrix element is defined as

$$M_{\mu\nu} = \frac{\hbar^2}{2m}\int_\Sigma (\psi_\mu \nabla\chi_\nu^* - \chi_\nu^*\nabla\psi_\mu)\cdot \mathrm{d}\boldsymbol{S}, \tag{3.2}$$

where the integration has to be carried out on an arbitrary separation surface Σ that is located inside of the tunneling barrier (see Figure 3.2). The exact position and shape of Σ is not important for the result of integral [86].

By summing up the transition rates of all pairs of states, an expression for the tunneling current I is obtained:

$$\begin{aligned} I &= -e\sum_{\mu,\nu}\big(f(E_\mu - E_\mathrm{F}^\mathrm{s})[1 - f(E_\nu - E_\mathrm{F}^\mathrm{t})]\cdot\lambda_{\mu\nu} \\ &\qquad - f(E_\nu - E_\mathrm{F}^\mathrm{t})[1 - f(E_\mu - E_\mathrm{F}^\mathrm{s})]\cdot\lambda_{\nu\mu}\big) \\ &= \frac{2\pi e}{\hbar}\sum_{\mu,\nu}[f(E_\nu - E_\mathrm{F}^\mathrm{t}) - f(E_\mu - E_\mathrm{F}^\mathrm{s})]\cdot|M_{\mu\nu}|^2\delta(E_\mu - E_\nu). \end{aligned} \tag{3.3}$$

Here, E_F^s denotes the Fermi energy of the sample, $E_\mathrm{F}^\mathrm{t} = E_\mathrm{F}^\mathrm{s} + eV$ is the Fermi energy of the tip and $f(\epsilon) = 1/(1 + e^{\epsilon/k_\mathrm{B}T})$ is the Fermi distribution function, giving the probability of a state to be occupied at an energy ϵ relative to the local Fermi level.

3.1.2 Tersoff-Hamann Model

The main task in the application of Bardeen's theory of tunneling to STM is to find a solution of the matrix element (3.2). While the aim of an STM experiment typically is to explore the electronic states ψ_μ of the sample, a central difficulty in the interpretation of measurement data is that little is known about the states χ_ν

of the tip. In general, the spatial dependence of the tip wave functions inside the vacuum gap can be extended in a series of spherical harmonics $Y_{lm}(\theta, \phi)$ around the center of the apex atom $\boldsymbol{r}_0$. In a simple model, Tersoff and Hamann [92,93] did only take the $l = 0$ term of the series into account (s-wave tip states). Based on this approximation, they did find

$$M_{\mu\nu} \propto \psi_\mu(\boldsymbol{r}_0). \tag{3.4}$$

Influence of Energy and Momentum

For a periodic sample surface, a general expression of the wave function within the vacuum region is given by [92]

$$\psi_\mu = \sum_{\boldsymbol{G}} a_{\boldsymbol{G}} \exp\big(-\sqrt{k^2 + |\boldsymbol{k}_\parallel + \boldsymbol{G}|^2}\, z\big) \exp\big(i(\boldsymbol{k}_\parallel + \boldsymbol{G}) \cdot \boldsymbol{r}\big). \tag{3.5}$$

Here $k = \sqrt{2m|E_\mu|}/\hbar$ results from the energy eigenvalue E_μ (measured relative to the vacuum level), $\boldsymbol{k}_\parallel$ is the parallel component of the Bloch wave vector of the sample state and $\boldsymbol{G}$ is a surface reciprocal-lattice vector.

The slowest decay in z-direction occurs for the $\boldsymbol{G} = 0$ term, which is therefore dominating the distance dependence of the tunneling rate. Based on (3.4), one obtains

$$|M_{\mu\nu}|^2 \propto e^{-2\kappa d}, \ \kappa = \sqrt{k^2 + \boldsymbol{k}_\parallel^2}. \tag{3.6}$$

Equation (3.6) implies that tunneling is most effective for sample states with high energy (note that $E_\mu < 0$) and small $|\boldsymbol{k}_\parallel|$, i.e. at the upper boundary of the energy interval contributing to charge transport and in the center of the surface Brillouin zone.

Interpretation of Topographic STM Images

The result of Tersoff and Hamann becomes particularly illustrative when the tunneling process is considered in the limit of small bias voltage and low temperature. In this regime, the general formula of the tunneling current (3.3) is simplified to

$$I \approx \frac{2\pi e^2}{\hbar} V \sum_{\mu,\nu} |M_{\mu\nu}|^2 \delta(E_\mu - E_\mathrm{F}) \delta(E_\nu - E_\mathrm{F}), \tag{3.7}$$

where $E_\mathrm{F} = E_\mathrm{F}^\mathrm{s} \approx E_\mathrm{F}^\mathrm{t}$. Substituting expression (3.4) for $M_{\mu\nu}$ into equation (3.7), one obtains for the tunneling conductance

$$I/V \propto \rho_\mathrm{t}(0) \rho_\mathrm{s}(0, \boldsymbol{r}_0). \tag{3.8}$$

Here $\rho_\mathrm{t}(\epsilon) = \sum_\nu \delta(E_\nu - E_\mathrm{F}^\mathrm{t} - \epsilon)$ is the density of states (DOS) of the tip at energy ϵ relative to the tip Fermi level and $\rho_\mathrm{s}(\epsilon, \boldsymbol{r}_0) = \sum_\mu |\psi_\mu(\boldsymbol{r}_0)|^2 \delta(E_\mu - E_\mathrm{F}^\mathrm{s} - \epsilon)$ is the local density of states (LDOS) of the sample at the position of the tip apex $\boldsymbol{r}_0$ and at energy ϵ relative to the sample Fermi level. Therefore, a topographic STM image measured in constant current mode represents a surface of constant sample LDOS, with the value of the LDOS on the surface (i.e. the distance of the iso-surface from the sample) being defined by the ratio I/V.

3.1.3 Extension to Finite Bias Voltage

Extending the low voltage limit of the tunneling conductance (3.8) derived by Tersoff and Hamann to finite values of V is not a trivial task. A fundamental problem of such a generalization is the first order perturbative nature of Bardeen's tunneling theory that assumes the states of tip and sample to be unaffected by the electric field building up inside of the vacuum gap. While this is a reasonable assumption for the mV range used in the experiments of Giaever [90, 91] that were originally addressed by Bardeen, it is not appropriate for bias voltage values of up to several V that are often used in STM.

Instead of rigorously treating the problem by calculating the tip and sample wave functions at finite bias voltage, Selloni *et al.* [94] proposed that the result of Tersoff and Hamann could be qualitatively generalized by introducing an energy and voltage dependent transmission coefficient $T(\epsilon, eV)$ that accounts for the voltage drop in the vacuum region. Motivated by equations (3.3) and (3.8), the tunneling current is then written as

$$I \propto \int_{-\infty}^{+\infty} \Big[f(\epsilon - eV) - f(\epsilon) \Big] \rho_\mathrm{s}(\epsilon) \rho_\mathrm{t}(\epsilon - eV) T(\epsilon, eV) \, \mathrm{d}\epsilon \tag{3.9}$$

(see Figure 3.3). Using the semiclassical Wentzel–Kramers–Brillouin (WKB) approximation for tunneling through a trapezoidal potential barrier, the transmission coefficient is given by [87]

$$T(\epsilon, eV) = \exp\left(-2\frac{\sqrt{2m}}{\hbar} d \left(\frac{\phi_\mathrm{t} + \phi_\mathrm{s}}{2} + \frac{eV}{2} - \epsilon \right)^{1/2} \right), \tag{3.10}$$

where ϕ_t and ϕ_s denote the work functions of tip and sample, respectively (see Figure 3.4). It should be mentioned that expression (3.10) is derived for a planar junction geometry (one-dimensional case) and is therefore neglecting the dependence of the tunneling probability on the parallel momentum. Furthermore, image potential effects arising from electron-electron interaction are not taken into account by the trapezoidal shape of the barrier [87].

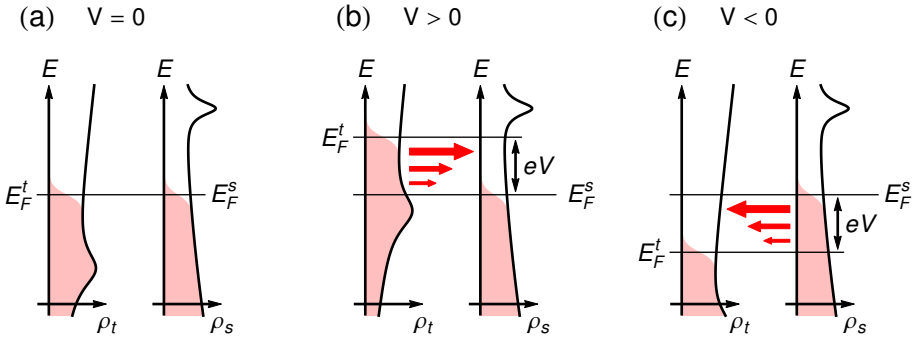

Figure 3.3 | Tunneling process in the regime of finite bias voltages, depicted for $V = 0$ **(a)**, $V > 0$ **(b)** and $V < 0$ **(c)**. Tip and sample DOS are arbitrary, consisting of a smooth background and a peak. Shaded areas represent occupied states and the size of the red arrows corresponds to the contribution of the electrons at the given energy to the tunneling current.

3.1.4 Beyond Tersoff-Hamann

The limitations of the Tersoff-Hamann approximation were already pointed out by the original authors [92, 93]. When the lateral size of a feature is of the order of 0.3 nm or smaller, the tunneling matrix element will in general be dominated by $l \neq 0$ contributions to the tip wave function [86]. As a result, the Tersoff-Hamann model is unable to describe the appearance of atomic-scale STM images. In particular, the experimental achievement of atomic resolution on close-packed metal surfaces is in contradiction to the small atomic corrugations predicted by the spatial dependence of their LDOS.

An extension of the model to nonspherical tip states was performed by Chen [95, 96]. The result can be summarized in the so called derivative rule. When the angular dependence of the tip wave function in the vacuum region is described by a spherical harmonic of order $l > 0$, Bardeen's matrix element (3.2) will be related to a spatial derivation of the sample wave function at the position of the tip apex in a very simple way. A p_z tip state for example will result in a matrix element $M_{\mu\nu} \propto \frac{\partial}{\partial z}\psi_\mu(\boldsymbol{r}_0)$, while a d_{xy} tip state gives $M_{\mu\nu} \propto \frac{\partial^2}{\partial x \partial y}\psi_\mu(\boldsymbol{r}_0)$. Compared to the s-wave form (3.4), these matrix elements are enhanced for states at the border of the surface Brillouin zone. This intuitively explains the increased lateral resolution accessible with tips made of W or PtIr alloy, whose DOS at the Fermi level is dominated by d-electrons [95].

3.2 Scanning Tunneling Spectroscopy

In the previous section, it was shown that the voltage dependence of the tunneling current is related to the local electronic properties of the sample. Therefore, recording the current-voltage characteristic $I(V)$ at a specific position of the sample allows

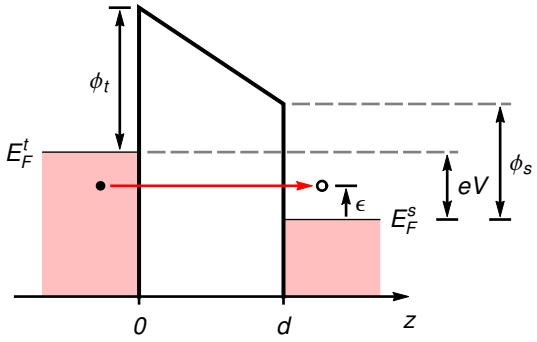

Figure 3.4 | Definition of the one-dimensional tunneling barrier, used for deriving expression (3.10) of the transmission coefficient $T(\epsilon, eV)$ within WKB approximation. The shape of the barrier is trapezoidal due to the bias voltage drop in the vacuum region as well as the work function difference between tip and sample.

to extract spectroscopic information of high spatial resolution. In the following, different techniques of data acquisition and data analysis will be introduced that are applicable for different experimental situations.

3.2.1 Fixed Separation Measurements

The most common way of performing a so called scanning tunneling spectroscopy (STS) measurement is to keep the tip-sample separation constant, while ramping the voltage V over a specified interval $[V_1, V_2]$. This requires the feedback loop to be opened at a certain set point I_s and V_s of tunneling current and bias voltage, respectively, which defines the tip-sample distance of the measurement. Treatment of the data mainly depends on the magnitude of V_1 and V_2.

Low Bias Voltage Regime

When the applied bias voltages $e|V|$ are small compared to the work functions ϕ_t and ϕ_s of tip and sample, the energy and voltage dependence of the transmission coefficient $T(\epsilon, eV)$ can be neglected. If in addition the measurement is performed at low temperature (i.e. $k_\mathrm{B}T$ is small compared to the energy scale on which variations in the DOS occur) and if the tip DOS is assumed to be featureless in the relevant interval of energy $[eV_1, eV_2]$, the general formula of the tunneling current (3.9) is simplified to

$$I \propto \rho_\mathrm{t}(0) T(0,0) \int_0^{eV} \rho_\mathrm{s}(\epsilon)\, \mathrm{d}\epsilon. \tag{3.11}$$

By differentiation of the above expression, one obtains

$$\frac{\mathrm{d}I}{\mathrm{d}V} \propto \rho_\mathrm{s}(eV). \tag{3.12}$$

Therefore, the voltage dependence of the differential conductance offers a direct measure of the energy dependence of the sample DOS.

High Bias Voltage Regime

For STS measurements performed in the range of up to several volts, the impact of the transmission coefficient on the tunneling current cannot be neglected anymore. Since electrons tunneling from higher energy levels feel a reduced barrier height compared to electrons that occupy lower states in energy, the tunneling current is dominated by the contribution of the upper states within the allowed energy interval (see Figure 3.3). As a result, the differential conductance $\frac{\mathrm{d}I}{\mathrm{d}V}$ mainly probes the unoccupied states of the sample at energy $E_\mathrm{F}^\mathrm{s} + e|V|$ for positive bias voltage, while it is most sensitive to the unoccupied states of the tip at energy $E_\mathrm{F}^\mathrm{t} + e|V|$ for negative bias voltage.

A quantitative estimation of this effect can be obtained based on equation (3.10). Assuming $e|V|$ to be small compared to the average work function $\overline{\phi} = (\phi_\mathrm{t} + \phi_\mathrm{s})/2$, which is a reasonable approximation for most experiments even in the high bias voltage regime, the energy dependence of the transmission coefficient is given by

$$T(\epsilon, eV) \approx T(0,0) \exp\left(\frac{\kappa_0 d}{\overline{\phi}}\left(\epsilon - \tfrac{eV}{2}\right)\right), \tag{3.13}$$

where $\kappa_0 = \sqrt{2m\overline{\phi}}/\hbar$ is the vacuum decay constant of a state at the Fermi level. Typically, the work function of a metal surface is about 5 eV and the tip-sample distance is of the order of 1 nm, which results in $\kappa_0 d/\overline{\phi} \approx 2.3\,\mathrm{eV}^{-1}$. Therefore, the transmission coefficient is increased by about one order of magnitude, when the energy is increased by 1 eV.

An additional implication of equation (3.13) is that the strength of the mentioned effect critically depends on the tip-sample separation d. Therefore, $I(V)$ curves measured at different tip-sample separations can differ significantly in shape, as it is shown in Figure 3.5a. This is in clear contrast to the low bias voltage regime, where the tip-sample distance affects the current-voltage characteristic as a mere prefactor[1].

It was proposed by Feenstra, Stroscio and coworkers [97,98] that the exponential energy and distance dependence of the transmission probability can be canceled out to a large extent by normalizing the differential conductance $\frac{\mathrm{d}I}{\mathrm{d}V}$ to the total conductance $\frac{I}{V}$, i.e. by calculating the ratio $\frac{\mathrm{d}I}{\mathrm{d}V}/\frac{I}{V} = \frac{\mathrm{d}\ln I}{\mathrm{d}\ln V}$. A close correspondence of the normalized conductance to features in the DOS was first demonstrated in theoretical calculations by Lang [99]. An experimental application of the procedure is shown in Figure 3.5b, confirming that multiple $I(V)$ data measured at different tip-sample separations indeed collapse onto a single curve after normalization.

The cancellation can be seen from the theoretical expression of the tunneling current (3.9). Neglecting again the influence of temperature and tip DOS, we can

[1] Note that the term $T(0,0)$ in equation (3.11) depends on the tip-sample separation.

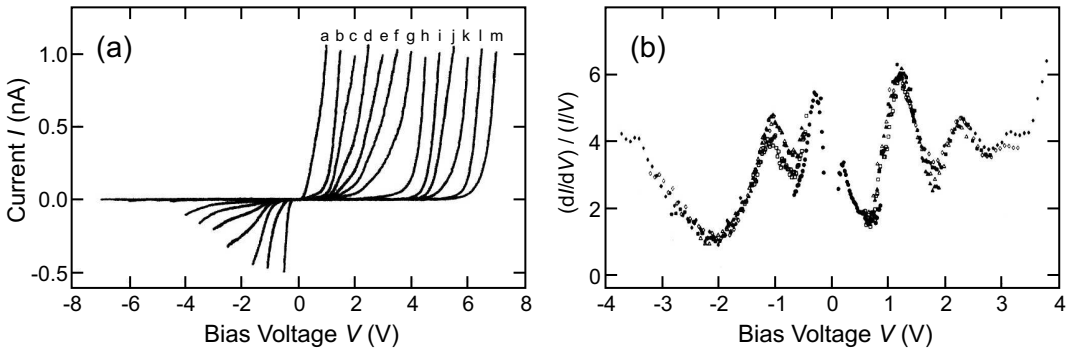

Figure 3.5 | STS measurement of the Si(111) 2×1 surface. **(a)** $I(V)$ curves at different tip-sample separations d, increasing from curve a (7.8 Å) to m (19.5 Å). **(b)** Ratio of differential to total conductance. The circles, open squares, filled triangles, open triangles, filled squares, open lozenges and filled lozenges refer to curves a–g, respectively. Adapted from [97].

write the current as

$$I \propto \int_0^{eV} \rho_\mathrm{s}(\epsilon) T(\epsilon, eV) \mathrm{d}\epsilon. \tag{3.14}$$

Differentiation of this equation results in an expression of the differential conductance:

$$\frac{\mathrm{d}I}{\mathrm{d}V} \propto e\rho_\mathrm{s}(eV)T(eV, eV) + e\int_0^{eV} \rho_\mathrm{s}(\epsilon) \frac{\mathrm{d}}{\mathrm{d}(eV)} T(\epsilon, eV)\, \mathrm{d}\epsilon. \tag{3.15}$$

Thus, we find for the normalized spectrum

$$\frac{\mathrm{d}I/\mathrm{d}V}{I/V} = \frac{\rho_\mathrm{s}(eV) + \displaystyle\int_0^{eV} \frac{\rho_\mathrm{s}(\epsilon)}{T(eV, eV)} \frac{\mathrm{d}}{\mathrm{d}(eV)} T(\epsilon, eV)\, \mathrm{d}\epsilon}{\dfrac{1}{eV}\displaystyle\int_0^{eV} \rho_\mathrm{s}(\epsilon) \frac{T(\epsilon, eV)}{T(eV, eV)}\, \mathrm{d}\epsilon}. \tag{3.16}$$

According to equation (3.13), we can make the approximation $\frac{\mathrm{d}}{\mathrm{d}(eV)} T(\epsilon, eV) \propto T(\epsilon, eV)$. Therefore, the integrals in the second term of the numerator and in the denominator provide a similar voltage dependence, meaning that their ratio does not depend on the voltage at all. Furthermore, the denominator has the form of an arithmetic average over the interval $[0, eV]$, which results in a relatively smooth voltage dependence compared to the first term in the numerator. As a result, the voltage dependence of the ratio $\frac{\mathrm{d}I}{\mathrm{d}V} / \frac{I}{V}$ mainly reflects the energy dependence of the sample DOS.

3.2.2 Variable Separation Measurements

The dynamic range of an STS measurement can be increased when the tip-sample separation d is varied as a function of the bias voltage V. This is particularly important for the investigation of semi-conductive or insulating materials (such as the molecular compounds studied within this work), where the presence of a band gap results in a variation of the tunneling conductance over many orders of magnitude.

Typically, a linear functional dependence $d(V) = d_0 - \alpha|V|$ is used for the separation, where d_0 is the distance at zero voltage and α is commonly in the range of 0.5–1 Å/V [88]. The measured tunneling current $I(d(V), V)$ then reflects both the intrinsic and the distance related variation with the bias voltage. Calculation of the actual spectrum from the current is not possible, since numerical differentiation gives a total derivative

$$\frac{\mathrm{d}I}{\mathrm{d}V} = \frac{\partial I}{\partial V}\Big|_d + \frac{\partial I}{\partial d}\Big|_V \frac{\mathrm{d}d}{\mathrm{d}V}, \tag{3.17}$$

which has no simple relationship to the DOS. The differential conductance at fixed separation $\frac{\partial I}{\partial V}|_d$ therefore needs to be acquired separately by means of a modulation technique, which is described in detail in section 3.2.5. For the sake of simplicity, the differential conductance at fixed separation will be denoted $\frac{\mathrm{d}I}{\mathrm{d}V}$ in the following course of this work.

In order to remove the influence of the varied separation on the spectrum, it is mandatory to perform a subsequent data transformation. An overview of different transformation procedures is given in [88]. A simple and reliable method is to cancel the separation dependence by using the normalization procedure described in the previous section, i.e. by calculating $\frac{\mathrm{d}I}{\mathrm{d}V} / \frac{I}{V}$.

Unfortunately, a normalization to I/V cannot be applied directly when a band gap is present at small voltage, since both the differential and the total conductance become zero in the band gap region, resulting in an ill-defined and diverging behavior of the normalized conductance. The problem itself is not limited to variable separation measurements, but also occurs in the normalization of fixed separation curves. As pointed out by Mårtensson and Feenstra [100], the origin of the problem is related to the role of I/V in the normalization procedure. While I/V usually provides as estimation of $T(\epsilon, eV)$, the method breaks down in the band gap region, where the transmission coefficient itself does not approach zero.

Mårtensson and Feenstra proposed that the divergence in the normalized conductance could be avoided when I/V is broadened via convolution with a suitable function [100]. When the line width ΔV of the function is of the order of the gap width, I/V becomes non zero in the band gap region, while its overall shape will not change significantly (see Figure 3.6). An alternative procedure, which is advan-

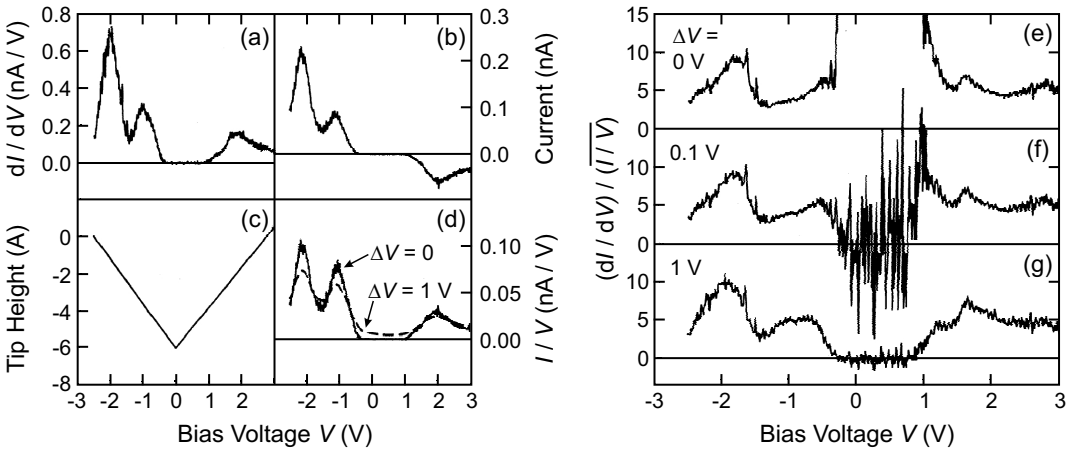

Figure 3.6 | Variable separation measurement on a monolayer of Sb on GaAs(110). The left panel shows the raw data of the differential conductance at fixed separation **(a)**, the tunneling current **(b)**, the variation in the tip-sample separation **(c)** and the total conductance **(d)**. In the right panel, the normalized conductance is plotted for different broadening widths ΔV of the I/V curve. A reasonable signal-to-noise ratio in the band gap region is achieved for $\Delta V = 1\,\mathrm{V}$. Adapted from [100].

tageous for wide band gap materials, was proposed by Prietsch *et al.* [101]. Here, the zeros of the denominator are removed by replacing I/V with $\sqrt{(I/V)^2 + c^2}$, where c is a small offset constant.

Whether the method of Mårtensson and Feenstra or of Prietsch *et al.* is more favorable depends on the shape of the I/V curve, as well as on the width of the band gap. Both methods define an additional parameter (ΔV or c), which must be chosen as large as necessary (to get a reasonable signal-to-noise ratio in the band gap), but as small as possible (to minimize the deviation from the original I/V curve outside the band gap).

3.2.3 Measurements on Molecular Adsorbents

When STS measurements are performed on molecular adsorbents, the electronic states of the molecules can in general not be simply ascribed to the sample DOS. Instead, the molecule has to be viewed as a system on its own, which is coupled to the surrounding tip and sample electrodes. The positions of the molecular orbitals are defined with respect to the local vacuum level E_{vac}. In particular, the difference of E_{vac} to the energy of the highest occupied molecular orbital (HOMO) is given by the ionization potential *IP*, whereas the position of the lowest unoccupied molecular orbital (LUMO) is determined by the electron affinity *EA*. Due to the coupling to the electrodes, the lifetime τ of the molecular states is finite, which implies an energy broadening $\Gamma = \hbar/\tau$ that can be used to indicate the coupling strength. Considering both electrodes separately, the coupling to tip and substrate is denoted as Γ_{t} and Γ_{s}, respectively, and the total broadening of the state is given by $\Gamma = \Gamma_{\mathrm{t}} + \Gamma_{\mathrm{s}}$.

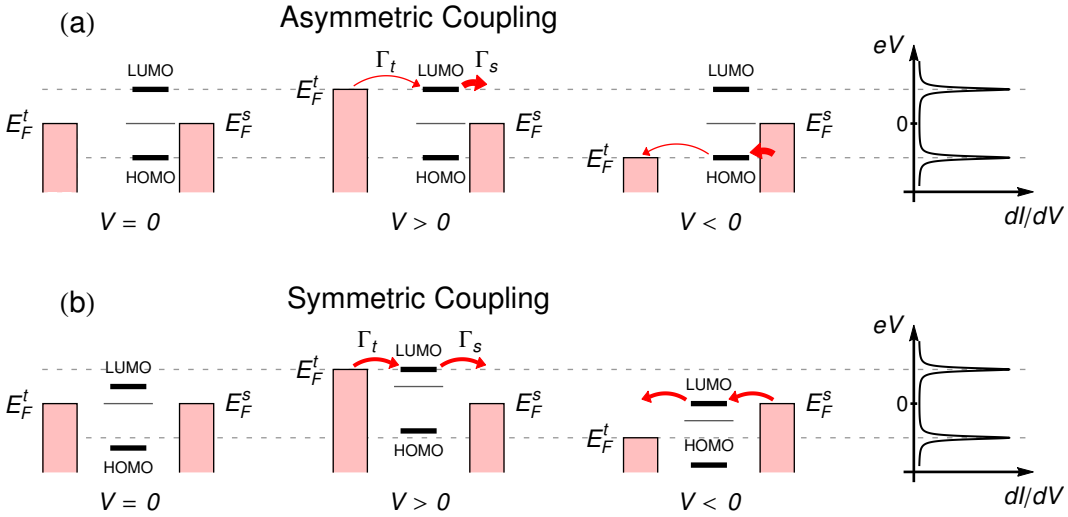

Figure 3.7 | Schematic illustration of charge transport through a molecule coupled to tip and substrate, shown for the case of **(a)** asymmetric coupling $\Gamma_s \gg \Gamma_t$ and **(b)** completely symmetric coupling $\Gamma_s = \Gamma_t$. A tunneling current occurs when a molecular orbital aligns to the Fermi level of one of the electrodes. The energies of the molecular orbitals have been chosen so that features in the dI/dV curves appear at identical positions in (a) and (b). Note that a direct extraction of the HOMO and LUMO energy from the dI/dV curve is only possible in the asymmetric coupling regime.

The interpretation of features in molecular STS spectra depends on the ratio Γ_s/Γ_t. Since the distance of the molecule from the tip is typically larger than its separation from the substrate, it is often save to assume an asymmetric coupling $\Gamma_s \gg \Gamma_t$. In this case, the positions of the molecular orbitals are fixed with respect to the Fermi level of the substrate, as shown in Figure 3.7a. The differential conductance will consequently reflect the molecular DOS, meaning that features appearing at positive and negative bias voltage are interpreted in terms of LUMO and HOMO, respectively. As it will be discussed later, this is the situation which is assumed for the spectra taken within this work.

However, it should be kept in mind that also more symmetric coupling conditions $\Gamma_s \approx \Gamma_t$ can be the case, especially in systems where the molecule is decoupled from the substrate by an insulating layer. The molecular states are then shifted with respect to the Fermi levels of both tip and substrate when a bias voltage V is applied. As a result, resonances at both positive and negative bias voltage can be related to the same molecular orbital, as depicted in Figure 3.7b for the case of LUMO-mediated transport. For an introduction into the topic, the reader is referred to [102]. A more comprehensive review of the rich variety of physical effects that can be observed in molecular junctions is given in [103, 104].

3.2.4 Inelastic Electron Tunneling Spectroscopy

Inelastic processes can give rise to an additional contribution to the tunneling current that has not been considered in the discussion so far. Features in $I(V)$ curves which originate from this contribution can be related to characteristic excitation energies, which is the idea of inelastic electron tunneling spectroscopy (IETS). Early experiments on planar tunnel junctions were already performed in the 1960s, where the conductance was reported to change on the order of 1 % when vibrational modes are excited in molecules that are embedded in the metal–oxide interface [105, 106]. The bonding structure and environment of the buried molecules however remain unclear in these experiments and the taken spectra are an average over at least 10^9 molecules, so that individual differences in the vibration energies are effectively washed out [107].

The invention of the scanning tunneling microscope paved the way for an extension of IETS to the level of individual atoms or molecules in a well defined sample geometry. Theoretical calculations dealing with the possibility to measure vibrational excitations in STM were reported soon after its invention by several groups [108–111]. Successful experiments, however, where hindered for a long time by the small cross sections of the underlying excitation processes, resulting in high demands on the mechanical stability of the tunneling gap. An experimental observation of vibrational excitations in STM was therefore not demonstrated until the pioneering work of Ho *et al.* in 1998 [112]. Later on, it was shown by Heinrich *et al.* [113–115] that STM-IETS is not limited to the measurement of vibrational modes, but can also be applied to detect spin-flip excitations in magnetic structures. The observation of such spin-flip excitations in individual single-molecule magnets has been one of the main motivations of this work.

The process of inelastic tunneling and its effect on the spectroscopic signal are illustrated in Figure 3.8. When the excess kinetic energy $e|V|$ of the tunneling electrons is higher than the energy difference eV_0 between two discrete internal states of an object placed within the tunneling barrier, a fraction of the electrons will be able to excite the respective object by losing a part of their kinetic energy. Since this opens up a new tunneling channel in addition to the elastic transition, the differential conductance $\mathrm{d}I/\mathrm{d}V$ increases step-wise at $|V| = V_0$ and the second derivative $\mathrm{d}^2I/\mathrm{d}V^2$ consequently presents a peak at this voltage. It should be noted that the direction of current flow doesn't play a role for the excitation process, meaning that inelastic features symmetrically appear at both polarities of the bias voltage.

The exact voltage and temperature dependence of the inelastic contribution I_i to the tunneling current can be easily calculated when it is assumed that the lifetime τ of the excited state is much smaller than the average time between two tunneling

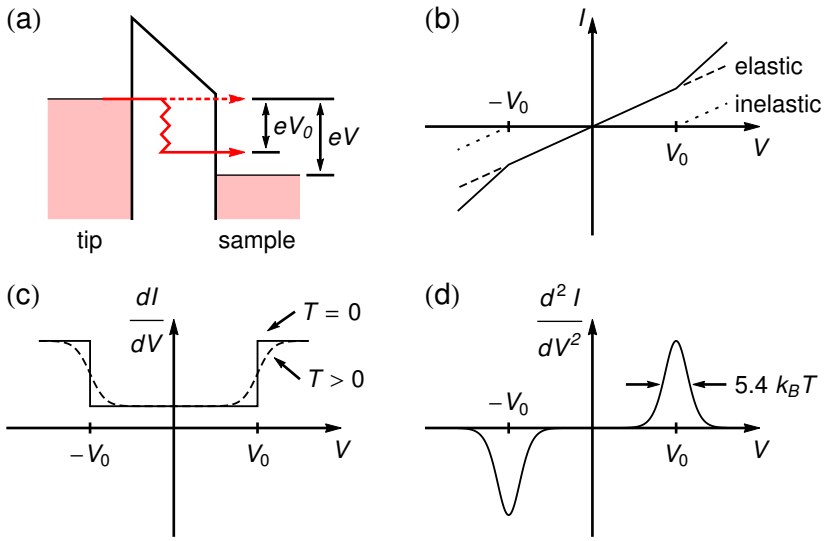

Figure 3.8 | **Principle of STM-IETS. (a)** Schematic illustration of elastic (dashed arrow) and inelastic tunneling (solid arrow) between tip and sample. **(b-d)** Resulting voltage dependence of the tunneling current I and its first and second derivative. While elastic tunneling is possible for all values of V, an additional inelastic transport path opens up at $|V| \geq V_0$.

processes[2], i.e. $\tau \ll e/I$. Neglecting the energy dependence of the transmission coefficient and of tip and sample DOS[3], one can write

$$I_\mathrm{i} \propto \int_{-\infty}^{+\infty} \Big(f(\epsilon - eV)\big[1 - f(\epsilon - eV_0)\big] - f(\epsilon)\big[1 - f(\epsilon - eV - eV_0)\big] \Big)\, \mathrm{d}\epsilon. \tag{3.18}$$

The integral can be solved analytically, yielding

$$I_\mathrm{i} \propto g(V) - g(-V), \quad \text{with} \quad g(V) \coloneqq e(V - V_0) \frac{\exp\left(\frac{e(V-V_0)}{k_\mathrm{B}T}\right)}{\exp\left(\frac{e(V-V_0)}{k_\mathrm{B}T}\right) - 1}. \tag{3.19}$$

Differentiation of this expression results in the curves plotted in Figure 3.8c,d. The full width at half maximum (FWHM) of the peak in $\mathrm{d}^2I/\mathrm{d}V^2$ can be estimated to be $5.4\, k_\mathrm{B}T$ [106].

3.2.5 Lock-In Technique

Experimentally, the differential conductance $\mathrm{d}I/\mathrm{d}V$ is not obtained by numerical differentiation of the taken $I(V)$ curve, but is measured simultaneously by means of

[2]This assumption ensures that a tunneling electron always finds the system in its ground state. Saturation effects can lead to a drastic change of the obtained spectra [116].

[3]Typical spin-flip excitation energies in SMMs are of the order of a few meV. One can therefore restrict the calculation to the low bias voltage regime.

a lock-in amplifier. While this generally results in a better signal-to-noise ratio, it is moreover a mandatory requirement for the measurement of the spectroscopic signal in variable separation experiments (see section 3.2.2).

The technique is generally based on the principle of signal modulation, meaning that a small sinusoidal voltage $\hat{V}_{\mathrm{mod}} \sin \omega t$ is added to the bias voltage V. This results in a modulation of the tunneling current $I(V + \hat{V}_{\mathrm{mod}} \sin \omega t)$ with the same base frequency, as can be seen from a Taylor expansion:

$$I(V + \hat{V}_{\mathrm{mod}} \sin \omega t) = I(V) + \frac{\mathrm{d}I}{\mathrm{d}V}(V)\, \hat{V}_{\mathrm{mod}} \sin \omega t + \mathcal{O}((\hat{V}_{\mathrm{mod}} \sin \omega t)^2). \tag{3.20}$$

The modulation frequency $f = \omega/2\pi$ has to be set to a value higher than the regulation speed of the feedback loop in order to prevent a crosstalk to the piezo movement, but must be lower than the bandwidth of the STM preamplifier to allow for a measurement of the modulation of the tunneling current. Due to the capacitance C of the wiring, an additional capacitive current

$$I_{\mathrm{c}}(t) = C \frac{\mathrm{d}}{\mathrm{d}t}(\hat{V}_{\mathrm{mod}} \sin \omega t) = \omega C \hat{V}_{\mathrm{mod}} \cos \omega t \tag{3.21}$$

is caused by the modulation, which appears at the same frequency, but is phase shifted relative to the tunneling current by 90°. The total (measured) current I_{tot} can therefore be written as

$$I_{\mathrm{tot}}(t) = I(V + \hat{V}_{\mathrm{mod}} \sin \omega t) + I_{\mathrm{c}}(t) + N(t), \tag{3.22}$$

where $N(t)$ denotes the noise of the current measurement. The lock-in amplifier can now be thought of as a filter which is selective with respect to both frequency and phase. When the transmission of the filter is restricted to a narrow bandwidth around the modulation frequency f and to the phase of the tunneling current I, the first harmonic of the tunneling current $\propto \frac{\mathrm{d}I}{\mathrm{d}V}(V)$ can be separated from the rest of the signal.

Technically, the filtering is achieved by first multiplying the measured signal I_{tot} with the original sinusoidal modulation phase shifted by an adjustable parameter φ and then integrating the result by means of a low-pass filter with cutoff frequency $f_{\mathrm{c}} \ll f$ (see Figure 3.9b). In the limit of large integration times $\tau \propto 1/f_{\mathrm{c}}$, the output can be written as

$$\lim_{\tau \to \infty} \frac{1}{\tau} \int_{-\tau/2}^{\tau/2} I_{\mathrm{tot}}(t) \cdot \sin(\omega t + \varphi_{\mathrm{ref}} + \varphi)\, \mathrm{d}t, \tag{3.23}$$

where the phase φ_{ref} takes into account that the measured signal in general is phase shifted with respect to the reference modulation due to the impact of the STM

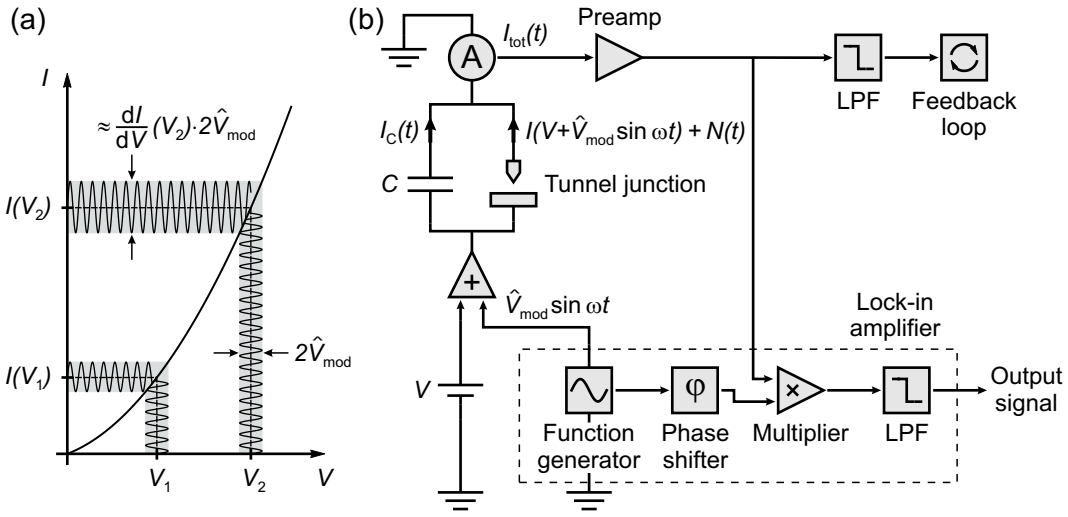

Figure 3.9 | **Lock-in detection. (a)** A small modulation of the bias voltage V results in an oscillation of the tunneling current I that is proportional to the slope of the $I(V)$ curve in first order of approximation. **(b)** Schematic representation of a lock-in amplifier implemented in an STS experiment. The reaction speed of the feedback loop can be slowed down by an additional low pass filter (LPF) with cutoff frequency below f.

preamplifier. The integration effectively cancels out every term in I_{tot} that is oscillating with an angular frequency different from ω. This also applies to the current noise $N(t)$, which is assumed not to be correlated to the reference modulation. Calculation of the integral can be carried out by substituting equations (3.20) to (3.22) into (3.23). In the limit of small modulation amplitudes $\hat{V}_{\mathrm{mod}} \to 0$, one obtains the result

$$\frac{1}{2}\frac{\mathrm{d}I}{\mathrm{d}V}\hat{V}_{\mathrm{mod}}\cos(\varphi_{\mathrm{ref}}+\varphi)+\frac{1}{2}\omega C\hat{V}_{\mathrm{mod}}\sin(\varphi_{\mathrm{ref}}+\varphi). \tag{3.24}$$

The phase therefore has to be adjusted to $\varphi = -\varphi_{\mathrm{ref}}$ in order to eliminate the capacitive contribution to the signal. This is realized in experiment by retracting the tip by several nm, meaning that the tunneling term in (3.24) vanishes ($\frac{\mathrm{d}I}{\mathrm{d}V} \to 0$), and subsequently setting the phase φ to the value that minimizes the remaining capacitive signal $\propto \sin(\varphi_{\mathrm{ref}}+\varphi)$.

A complete elimination of the noise, as implied by (3.24), is not possible in experiment, since large integration times are slowing down the response of the lock-in amplifier to changes of the input signal. In general, τ should be multiple times smaller than the amount of time needed for the measurement of a single point in the spectrum, which itself is limited by the temporal stability of the tunneling contact. A measurement example is shown in Figure 3.10.

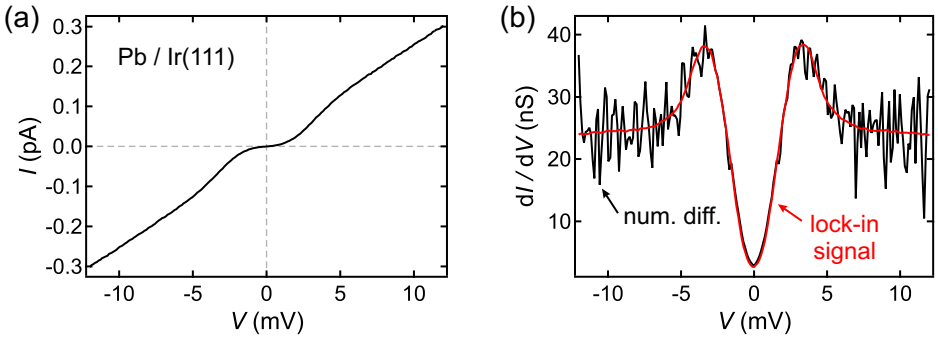

Figure 3.10 | **Example of a lock-in measurement. (a)** $I(V)$ curve obtained on a superconducting Pb cluster on Ir(111). **(b)** Comparison of the numerical derivative of the curve shown in (a) (black) and the simultaneously measured lock-in signal (red). Parameters for spectroscopy: $V_\mathrm{s} = 12\,\mathrm{mV}$, $I_\mathrm{s} = 300\,\mathrm{pA}$, $V_\mathrm{mod} = 0.5\,\mathrm{mV}$, $f = 614.3\,\mathrm{Hz}$, $\tau = 30\,\mathrm{ms}$, $T = 1.9\,\mathrm{K}$. Measurement performed together with Lars Müller and Samuel Bouvron [117, 118].

Energy Resolution

The linear dependence of the lock-in signal (3.24) on the differential conductance $\frac{\mathrm{d}I}{\mathrm{d}V}$ was derived on the assumption of small modulation amplitudes, i.e. by neglecting higher order terms in the Taylor expansion (3.20) of the tunneling current. For finite values of $\hat{V}_\mathrm{mod}$, it can be shown by variable substitution that the general expression (3.23) of the lock-in output is of the form [118]

$$\frac{1}{2\pi\hat{V}_\mathrm{mod}} \int_{-\hat{V}_\mathrm{mod}}^{\hat{V}_\mathrm{mod}} \frac{\mathrm{d}I}{\mathrm{d}V}(V+x)\sqrt{\hat{V}_\mathrm{mod}^2 - x^2}\,\mathrm{d}x, \tag{3.25}$$

provided that the phase φ is adjusted correctly. The result can be read as a convolution of the differential conductance and a semicircle of width $2\,\hat{V}_\mathrm{mod}$ and FWHM $\Delta_\mathrm{mod} = \sqrt{3}\,\hat{V}_\mathrm{mod} \approx 1.7\,\hat{V}_\mathrm{mod}$, meaning that the measurement signal is smeared out within a small window around the bias voltage V (see Figure 3.11b). The correct choice of the modulation amplitude therefore is a trade-off between signal strength and energy resolution.

The ability of an STS measurement to resolve energetically sharp features in the DOS however is not restricted by the lock-in technique alone, but is also limited by the temperature broadening of the Fermi edge. The influence of a finite temperature T on the spectroscopic signal so far has only been considered in the case of IETS, while a temperature of zero has been assumed in the discussion of elastic tunneling. An extension of expression (3.12) for elastic STS in the low bias voltage regime[4] to

[4] In the high bias voltage regime, thermal broadening is typically small compared to the intrinsic width of spectroscopic features and can therefore be neglected.

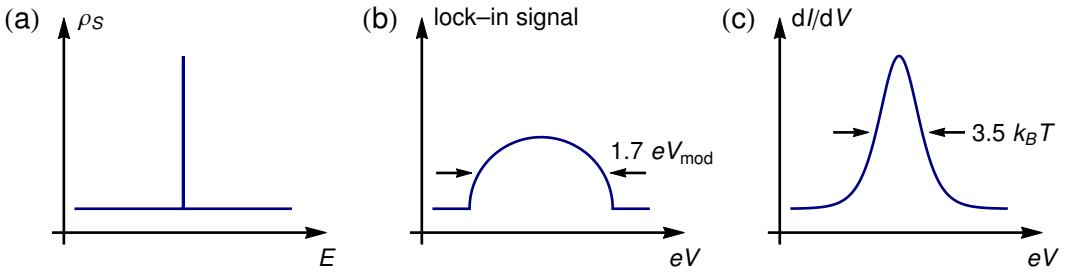

Figure 3.11 | **Energy resolution in elastic STS.** An infinitely sharp peak in the sample DOS **(a)** is broadened to a semicircle due to the modulation voltage V_{mod} of the lock-in amplifier **(b)** and to the derivative of the Fermi distribution function due to the finite measurement temperature T **(c)**.

finite temperatures is given by

$$\frac{\mathrm{d}I}{\mathrm{d}V} \propto -\int_{-\infty}^{\infty} \frac{\mathrm{d}f(\epsilon)}{\mathrm{d}\epsilon} \rho_{\mathrm{s}}(\epsilon + eV)\,\mathrm{d}\epsilon. \tag{3.26}$$

The differential conductance therefore is a convolution of the sample DOS and the first derivative of the Fermi distribution function $\frac{\mathrm{d}f}{\mathrm{d}\epsilon}$, which is a Gaussian-like peak of FWHM $\Delta_{\mathrm{T}} = 3.5\,k_{\mathrm{B}}T$ (see Figure 3.11c). Note that the temperature induced line width of elastic tunneling spectroscopy is smaller than the value of $5.4\,k_{\mathrm{B}}T$ derived for IETS, which is due to the fact that inelastic features result from tunneling between electronic states that are located at the Fermi edge on both sides of the tunneling barrier.

Combining lock-in and temperature broadening, the measurement signal in general must be written as a convolution of the sample DOS with both broadening functions. A simple estimation of the resulting energy resolution ΔE is obtained by assuming a Gaussian-like sum rule of the individual line widths $\Delta E^2 \approx \Delta_{\mathrm{T}}^2 + \Delta_{\mathrm{mod}}^2$. Substituting the modulation amplitude with the more convenient root mean square (rms) value $V_{\mathrm{mod}} = \hat{V}_{\mathrm{mod}}/\sqrt{2}$, the result is given by

$$\Delta E \approx \sqrt{(3.5 k_{\mathrm{B}}T)^2 + (2.4 e V_{\mathrm{mod}})^2}. \tag{3.27}$$

4 | Additional Experimental Methods

Besides scanning tunneling microscopy and spectroscopy, a number of additional experimental techniques has been used for sample characterization within this thesis. The basics of these methods will be briefly discussed in the following sections.

4.1 X-ray Photoelectron Spectroscopy (XPS)

X-ray photoelectron spectroscopy (XPS) is a surface-sensitive technique based on the photoemission of electrons from occupied sample-states due to illumination with X-ray radiation. It allows for a determination of the type and chemical state of different elements present on the sample surface.

The essential components of an XPS setup are depicted in Figure 4.1a. An X-ray source generates photons of energy $h\nu$, to which the sample is exposed. A fraction of the emitted photoelectrons is collected by electrostatic lenses and filtered by an energy analyzer. Those electrons whose kinetic energy E_{kin} is close to a preset value are able to pass the analyzer and get subsequently detected by an electron multiplier. The photoelectron spectrum is then acquired as the number of electrons $N(E_{\mathrm{kin}})$ counted within a certain time interval as a function of kinetic energy.

Due to energy conservation, the kinetic energy of the photoelectrons can be related to the binding energy E_{B} of their initial state. The corresponding relation is given by

$$E_{\mathrm{kin}} = h\nu - E_{\mathrm{B}} - \Phi, \tag{4.1}$$

where Φ denotes the work function of the energy analyzer. Since the binding energies of core electrons are characteristic for different elements, XPS spectra can be used to identify the elemental composition of the sample. Even more important, subtle shifts of the binding energies can arise depending on the chemical bonding of the elements, meaning that XPS spectra also provide information about the local chemical environment. Comprehensive spectroscopic data of reference materials are available in literature and can be used for comparison [119].

The information depth of XPS data is determined by the mean free path of the excited photoelectrons. Within the energy range relevant for most photoemission

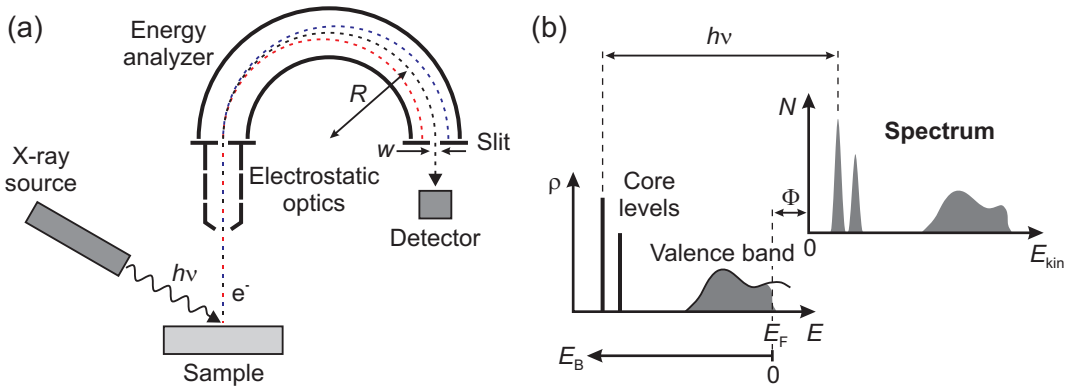

Figure 4.1 | **(a)** Schematic illustration of the experimental setup used for XPS. Dashed lines visualize photoelectron paths for zero incidence angle and kinetic energy values which are equal (black), larger (blue) or smaller (red) than the pass energy of the electron analyzer. **(b)** Exemplary sample density of states $\rho(E)$ consisting of core level and valence band contributions, together with the corresponding photoelectron spectrum $N(E_{\mathrm{kin}})$.

experiments (10–2000 eV), the mean free path of the photoelectrons is of the order of a few monolayers, which renders XPS a highly surface sensitive technique [120]. A reliable and reproducible measurement of XPS data therefore demands for ultrahigh vacuum (UHV) conditions during sample preparation and data acquisition.

Whether a spectroscopic feature can be resolved by XPS depends on several contributions: the resolution of the energy analyzer, the spectral line width of the photon source and the thermally broadened intrinsic line widths of the electronic levels, which are usually dominated by the finite lifetime of the excited ionic states. Typically, the analyzer resolution is set to a value slightly below the line width of the X-ray source, which in most cases limits the overall resolution of the measurement. For a hemispherical analyzer, the energy resolution is given approximately by [121]:

$$\Delta E = E_{\mathrm{p}} \left(\frac{w}{2R} + \frac{\alpha^2}{4} \right). \tag{4.2}$$

Here, E_{p} is the pass energy of the analyzer, w is the effective combined width of entrance and exit slit, R is the mean radius of the hemispheres and α is the angular divergence of the electrons at the entrance slit (see Figure 4.1a).

It should be noted that the relaxation of the system into its electronic ground state after excitation of a core electron can be accompanied by the Auger effect, which gives rise to the emission of additional electrons contributing to the spectrum. In contrast to the photoelectric effect, Auger electrons appear at characteristic values of the kinetic energy rather than the binding energy. A discrimination between Auger electrons and photoelectrons is therefore possible by recording spectroscopic data at

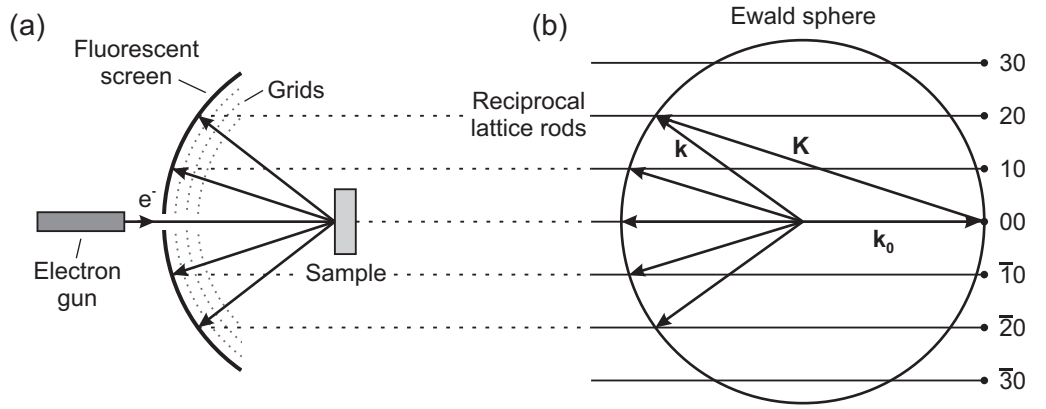

Figure 4.2 | Low energy electron diffraction. (a) Principle experimental setup, containing the sample, an electron source and a fluorescent detector. The detector is usually surrounded by three or four concentric grids, which are used to screen the electric field generated by the high detector potential and to suppress the homogeneous background signal caused by inelastically scattered electrons. **(b)** Ewald construction for a 2D lattice.

different photon energies.

4.2 Low Energy Electron Diffraction (LEED)

Low energy electron diffraction (LEED) is a standard UHV analysis technique used for investigating the surface structure of crystalline materials [122,123]. The principle setup is depicted in Figure 4.2a. A collimated beam of monochromatic electrons with a kinetic energy typically in the range of 20–300 eV is directed at the sample surface. Those electrons which are elastically backscattered from the surface are observed on a hemispherical fluorescent screen. Since the de Broglie wavelength $\lambda = h/p$ of the electrons is of the order of interatomic distances, diffraction patterns of periodic surfaces comprise well separated spots.

For a qualitative understanding of the essential features of a LEED pattern, kinematic scattering theory is sufficient, i.e. multiple and inelastic scattering can be neglected. Due to the small mean free path of low energy electrons, scattering mainly takes place within a few atomic layers of the sample surface. In first approximation, the sample can therefore be treated as a 2D lattice, meaning that the scattering condition becomes [122]

$$\boldsymbol{K}_{\parallel} \coloneqq \boldsymbol{k}_{\parallel} - \boldsymbol{k}_{0,\parallel} = \boldsymbol{G}_{\parallel}. \tag{4.3}$$

Here, $\boldsymbol{k}_{0,\parallel}$ and $\boldsymbol{k}_{\parallel}$ refer to the in plane wave vector components of incident and backscattered electrons, respectively, and $\boldsymbol{G}_{\parallel}$ is a 2D reciprocal lattice vector.

The solutions of (4.3) can be visualized by means of an Ewald construction (see Figure 4.2b). According to the experimental geometry, the wave vector $\boldsymbol{k}_0$ is

positioned with its end on the (00) reciprocal lattice point and a sphere of radius $|\boldsymbol{k}_0| = \sqrt{2m_e E}/\hbar$ is drawn around its starting point. In order to account for the infinitely large inter-layer distance of the real space structure, the 2D reciprocal lattice must be extended into three dimensions as rods pointing perpendicular to the reciprocal lattice plane. The scattering condition is fulfilled for all intersections between these rods and the Ewald sphere. Consequently, the diffraction pattern observed on a hemispherical screen directly reproduces the symmetry of the 2D reciprocal lattice. The highest order of diffraction which is visible on the fluorescent screen depends on the radius of the Ewald sphere and therefore on the energy of the incoming electrons. When the energy is increased, all diffraction spots move towards the (00) reflex, while higher order reflexes appear at the edge of the screen.

4.3 Superconducting Quantum Interference Device (SQUID) Magnetometry

A superconducting quantum interference device (SQUID) is a highly sensitive magnetic field sensor. It can be considered as a flux-voltage converter, which turns a small magnetic flux into a measurable voltage signal. Every physical property which is related to a magnetic flux can be measured by means of a SQUID sensor. In particular, this applies to the magnetic moment, which is measured in SQUID magnetometry.

The integral part of a SQUID sensor is a superconducting ring, which is interrupted by either one (radio frequency (rf) SQUID) or two (direct current (dc) SQUID) weak links. A weak link can be realized either as a thin barrier made of insulating or normal-conducting material, or as a physical constriction that diminishes the superconductivity at a specific point (i.e. a grain boundary in a high temperature superconductor). Together with the surrounding superconducting material, each of the weak links forms a so called Josephson junction, which underlies specific relations between the supercurrent, the voltage drop and the superconducting phase parameter. For a detailed discussion of the physical fundamentals and technical subtleties of SQUID measurements, the reader is referred to the available literature [124, 125]. Here, only a brief insight into SQUID operation will be given. In accordance with the experimental setup (see chapter 5.2), the discussion will be limited to the rf SQUID type operated in the so called hysteretic regime.

Figure 4.3a shows a schematic drawing of the electric circuit used for rf SQUID operation. The superconducting loop containing the Josephson junction is inductively coupled to a tank circuit that is driven by an oscillating current $I_{\mathrm{rf}} \sin \omega_{\mathrm{rf}} t$ at a frequency $\omega_{\mathrm{rf}}/2\pi$ in the range of around 20 MHz to 10 GHz [125]. The external flux Φ_{ext} in the SQUID loop – which is to be measured – is therefore superimposed by an oscillating flux Φ_{rf} generated by the current in the inductor of the tank circuit.

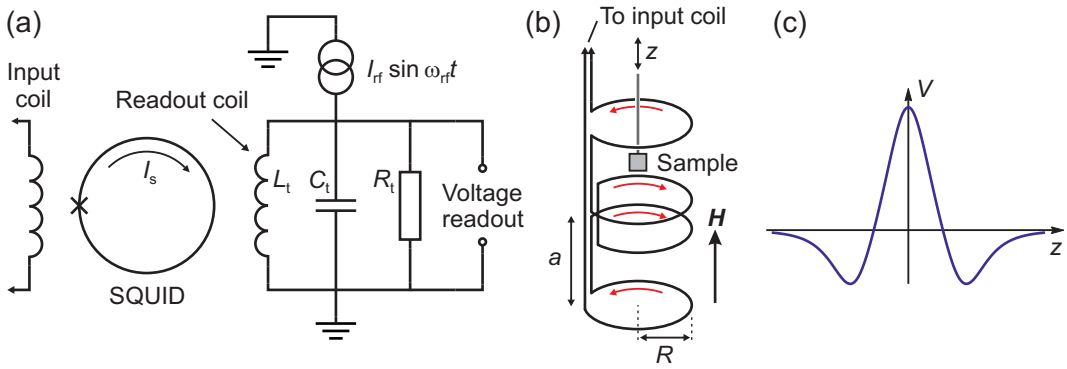

Figure 4.3 | SQUID magnetometry. (a) Schematic representation of the rf SQUID with tank circuit and input coil. **(b)** Structure of a superconducting detection coil which is configured as a second order gradiometer. The sample is moved along the axial position z in the applied magnetic field $\boldsymbol{H}$. **(c)** Shape of the SQUID response curve $V(z)$ according to equation (4.4).

Since the total magnetic flux in a superconducting ring must be a multiple of the flux quantum $\Phi_0 = h/2e \approx 2 \times 10^{-15}$ Wb, a screening current I_s must flow in the SQUID loop in order to increase or decrease the flux to next integral number of Φ_0. When the system is designed properly, energy is dissipated in the Josephson junction with a rate that depends on I_s and that is therefore a periodic function of Φ_{ext} with a period of Φ_0. This in turn affects the damping of the tank circuit, so that the rf voltage amplitude across the circuit – the actual output signal – is a periodic function of Φ_{ext} as well. In order to achieve a linear response of the SQUID to the applied flux, the sensor might be operated within a small flux range (a small fraction of Φ_0) around the steepest point of the periodic transfer function. A much larger dynamic range, however, can be attained when the SQUID is operated in a so called flux-locked feedback-loop (see [124] for details).

Within a magnetometer, the SQUID sensor is typically not directly exposed to the flux of the sample, but is inductively coupled to a superconducting detection coil. In the used experimental setup, the detection coil is configured as a second order gradiometer, comprising four loops, two of which are wound clockwise and two counter-clockwise (see Figure 4.3b). This configuration has the advantage that it is not sensitive to temporal changes in magnetic fields which are homogenous or linear in space and is therefore reducing background noise and drift effects in the SQUID detection caused by fluctuations and drifts in the large magnetic field of the superconducting magnet. For a measurement of the magnetic moment, the sample is moved along the axial coordinate z of the detection coil. The change in the position of the sample causes a change in the flux of the detection coil and is therefore changing the current flowing in the detection circuit. Since the circuit is superconducting, this current does not decay and can therefore be measured as a position dependent voltage signal $V(z)$ by means of the inductively coupled SQUID

sensor. For a sample that is approximated as an ideal point dipole, it can be shown that the SQUID response is of the form [126]:

$$V(z) = X_1 + X_2 \cdot \Big(2[R^2 + z^2]^{-3/2} - [R^2 + (z+a)^2]^{-3/2} - [R^2 + (z-a)^2]^{-3/2}\Big). \tag{4.4}$$

Here, R is the detection coil radius, a is the longitudinal coil separation and X_1 and X_2 are parameters accounting for signal offset and amplitude. The typical shape of the response curve is plotted in Figure 4.3c. Calculation of the magnetic moment from the response curve is possible by fitting (4.4) to the $V(z)$ measurement and extracting the value of the magnetic moment from the best fit value of X_2.

4.3.1 Subtracting the Sample Holder Background

A SQUID magnetometric measurement performed on a sample is always superimposed by the signal of the sample holder. In order to eliminate this contribution, a reference measurement is performed on the empty sample holder. Usually, the magnetic moments of both measurements are first determined by fitting (4.4) to the corresponding $V(z)$ raw data. The two moments are then subtracted from each other, yielding the moment of the sample alone. However, this procedure might fail in certain situations. While the sample usually fulfills the point dipole approximation with adequate accuracy, i.e. its lateral dimensions are small compared to the detection coil, the sample holder often does not. As a result, the $V(z)$ raw data of both measurements will deviate from the functional dependence predicted by (4.4), making an accurate calculation of the separate magnetic moments impossible.

The same problem arises when there is a spatial offset between both response curves along the axis of the magnet. In this case, the superposition of sample and sample holder will not have the ideal dipole pattern, even though both of them on their own might have. This issue becomes particularly problematic in the case of diluted samples and thin films with only weak magnetic moment, for which the diamagnetic background of the sample holder can be of the same order as the moment of the sample. For para- and ferromagnetic samples, typically both moments cancel each other out at a certain magnetic field within an $M(H)$ measurement (since the moment of the sample saturates while the diamagnetic background is linear in H) or at a certain temperature within an $M(T)$ measurement (since the moment of the sample follows a Curie or Curie-Weiss law while the diamagnetic background is temperature independent). Around these points, the fitting procedure totally breaks down, resulting in strong artifacts of the measurement. An example of such a case is shown Figure 4.4.

The problem can be solved by subtracting the $V(z)$ response curves of both measurements rather their magnetic moments. Special care must be taken that the

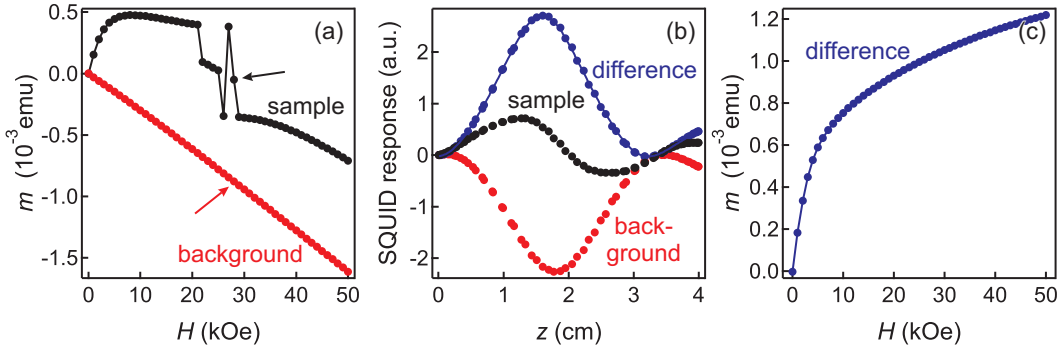

Figure 4.4 | SQUID measurement of a film of Fe_4H SMMs on a sapphire substrate taken at 1.8 K, together with a reference measurement of the background signal (substrate + sample holder). **(a)** Magnetic moments m as calculated automatically by the SQUID measurement software from a fit of the $V(z)$ response curves. Strong artifacts distort the measurement of the sample, as the moments of film and background almost cancel each other out. **(b)** $V(z)$ response curves corresponding to the points measured at 28 kOe (marked by arrows in (a)). The response curve of the sample strongly deviates from the ideal dipole pattern. Subtracting both signals yields the response curve of the film alone (blue points). The solid line is a fit to the curve based on (4.4). **(c)** Magnetic moment of the film alone as calculated from the subtracted response curves.

empty sample holder is placed at exactly the same position as in the measurement of the sample. The resulting difference of both curves then resembles the dipole form and can therefore be fitted based on (4.4), yielding the magnetic moment of the sample (see Figure 4.4b,c).

4.3.2 Pascal's Constants

A quantitative analysis of paramagnetic behavior often requires a correction of the diamagnetic contribution that is inherent in all atoms. This applies in particular to single molecule magnets, whose magnetic moment is carried by an overall small number of atoms in the molecular compound. While the diamagnetic contribution of these materials may be negligible at low temperatures, it can account for several percent of the total magnetization at room temperature, making a diamagnetic correction neccessary.

A rough estimate of the molar diamagnetic susceptibility χ_D is given by

$$\chi_D \approx -\frac{M}{2} 10^{-6} \,\mathrm{emu\,mol^{-1}}, \tag{4.5}$$

where M is the molecular mass of the compound in multiples of atomic mass units [127]. A more accurate calculation must take into account the contributions of the individual atomic species present in the material and their chemical bonds. Diamagnetic susceptibility values of a broad variety of atoms and bonds are tabulated

in literature as so called Pascals's constants. All diamagnetic corrections performed within this work are based on the values listed in [127].

Part II

Experimental Setups and Sample Preparation

5 | Setups Used for Sample Characterization

5.1 Ultra High Vacuum Setups

Unless otherwise stated, surface sensitive measurements were carried out on two different ultra high vacuum (UHV) systems from Omicron Nanotechnology, which comprise a variable temperature (VT) STM/AFM and a Cryogenic STM, respectively. Both systems are composed of two separate chambers that offer base pressures below 1×10^{-10} mbar. They are equipped with identical tools for *in situ* tip and sample preparation, including an Ar^+ sputter gun for surface cleaning, a resistive heater for annealing of samples to intermediate temperatures, flashing stations for heating of tips and samples to high temperatures via electron bombardment, effusion cells and electron beam evaporators for material deposition and leak valves for controlled gas admission. Furthermore, both setups include LEED optics, allowing for a quick sample surface characterization.

All STM measurements reported in this thesis were carried out using electrochemically etched polycrystalline tungsten tips, cleaned in UHV by flash annealing, or grinded and polished PtIr tips (Nanoscore GmbH).

5.1.1 VT STM/AFM Setup

The Omicron VT STM/AFM (Figure 5.1) is capable of STM and atomic force microscopy (AFM) measurements at variable temperatures down to 25 K. Vibration isolation of the system is achieved by means of an eddy current damped suspension. Within this thesis, the VT STM/AFM was operated exclusively in the STM mode and at room temperature.

The setup also contains instrumentation for XPS measurements, including an Omicron EA 125 hemispherical electron energy analyzer equipped with a seven channel electron multiplier (CEM) detector and a twin-anode X-ray source supplied with Aluminum (Al K_α, $h\nu = 1486.6$ eV) and Magnesium (Mg K_α, $h\nu = 1253.6$ eV) anodes. The line widths of the Al and Mg K_α emission lines are around 0.85 and 0.70 eV, respectively. The analyzer was operated in constant analyzer energy mode.

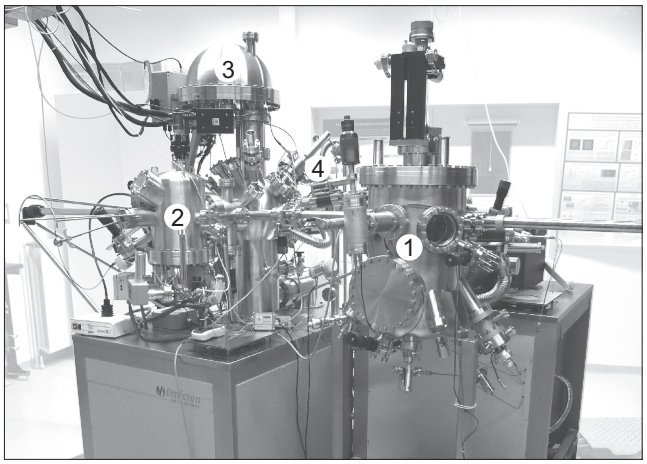

Figure 5.1 | Photograph of the **VT STM/AFM setup**. Labels correspond to the preparation chamber (1), the STM (2), the hemispherical electron energy analyzer (3) and the X-ray source (4).

According to equation (4.2), pass energy, slit widths and angular divergence were typically chosen to achieve an overall energy resolution of around 1.0 eV.

5.1.2 Cryogenic STM Setup

The Omicron Cryogenic STM (Figure 5.2) enables low noise STM and STS measurements at low temperatures and in high magnetic fields. It is based on a ^{4}He evaporation cryostat which can be continuously operated at sample temperatures ranging from around 1.6 K to 300 K. The cryostat is equipped with a 3D vector field superconducting magnet that provides maximum magnetic field values of 6 T perpendicular to the sample surface and 1 T in in-plane direction. In order to reduce mechanical noise, the system is installed on a separate foundation (35 t concrete slab) within a low noise laboratory environment that contains an isolated accommodation for the ^{4}He and UHV backing pumps and a vibration-free air conditioning system. Transmission of vibrations to the STM is further reduced by a passive pneumatic damping system. More detailed information about the setup can be found in the thesis of S. Bouvron [118].

All $\mathrm{d}I/\mathrm{d}V$ spectra presented within this thesis were acquired at the Cryogenic STM setup by modulating the bias voltage and using a Stanford Research Systems SR 830 DSP lock-in amplifier for detection. The modulation frequency was typically set to values of 600–700 Hz in order to comply with the limits imposed by the 800 Hz bandwidth of the STM preamplifier and the 300 Hz cutoff frequency of the STM feedback loop. The value of the modulation amplitude is stated separately for each individual measurement.

5.2 SQUID Magnetometry Setup

Magnetic characterization of samples was performed using a Quantum Design MPMS XL5 SQUID magnetometer. The setup is based on an rf SQUID sensor coupled to a

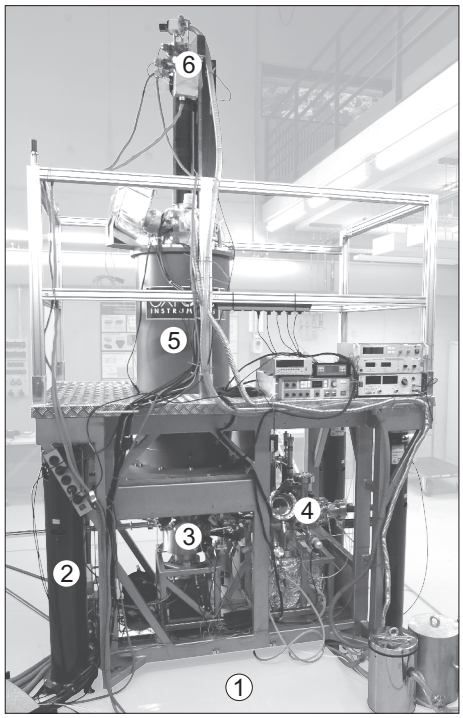

Figure 5.2 | Photograph of the **Cryogenic STM setup**. Labels correspond to the separate foundation (1), the pneumatic damping system (2), the UHV system comprising STM chamber (3) and preparation chamber (4), the ^{4}He cryostat (5) and the STM preamplifier (6).

second order gradiometer detection coil. It allows for a measurement of the magnetic moment at temperatures ranging from 1.8 K to 400 K and in external magnetic fields of up to 5 T.

Different types of sample holders were used in order to achieve both a low background signal and a solid sample mounting. Single crystal samples were glued to plastic straws, using small amounts of instant glue. Polycrystalline powder samples were mounted either within straw hold gelatine capsules, or by using Quantum Design VSM sample holders, which consist of a plastic capsule that is press fit into a brass trough. Thin films were grown on sapphire substrates purchased from CrysTec GmbH, which provide low amplitude diamagnetic background signals. In order to allow for a film growth by means of electrospray deposition, the sapphire substrates were covered with a 50–100 nm thick layer of Au prior to preparation.

All measurements performed on thin films and VSM sample holders were background corrected using the procedure described in chapter 4.3.1.

5.3 ESI-MS Setups

Mass spectra were recorded on a Bruker micrOTOF II and a Bruker amaZon SL system, operated by the group of Prof. Marx at the university of Konstanz. Both setups rely on the electrospray effect for analyte ionization. Solutions were directly injected into the ESI interface, i.e. the HPLC system was bypassed. Typical operating parameters of the electrospray source were as follows: source temperature 180 °C, desolvation gas flow 6–10 l/min, nebulizing gas pressure 0.5–1.2 bar.

6 | Design and Characterization of a Setup for Electrospray Deposition

The construction and characterization of a setup for electrospray deposition (ESD) of nonvolatile compounds in ultra-high vacuum has been a key aspect of this work. The setup was specifically designed for the preparation of samples that are suited for STM and STS measurements, but it is also capable of growing films that can be investigated by means of bulk sensitive methods. The demands on the preparation are quite different in both cases: STM studies require a fine control over the surface coverage with typical values ranging from a few hundred molecules per μm^2 up to a complete monolayer. They need to be performed on samples of high purity in order to assure an adequate stability of the tunneling contact, which presupposes that sample preparation takes place *in situ*. Furthermore, the deposition method should not restrict the choice of substrate, in order to ensure that the molecule-substrate interaction can be adjusted with the greatest possible flexibility. In contrast, a certain amount of impurities can be tolerated in film samples, provided that the method of investigation is not sensitive to them. However, film thicknesses in the range of some tens of nanometers up to several micrometers are often required to achieve sufficient signal strength, which demands for high beam intensities in order to achieve reasonable deposition times.

Figure 6.1 schematically shows the concept of the ESD setup. The construction is based on the commercially available 'UHV4' system from Molecularspray Ltd. It features a compact design, allowing for a direct attachment of the system to one of the available UHV setups via a standard CF40 flange. In order to improve performance, reproducibility and ease of operation, parts of the original UHV4 setup were extended, modified or even redesigned from scratch. In the following, the design and performance of the setup will be described in detail.

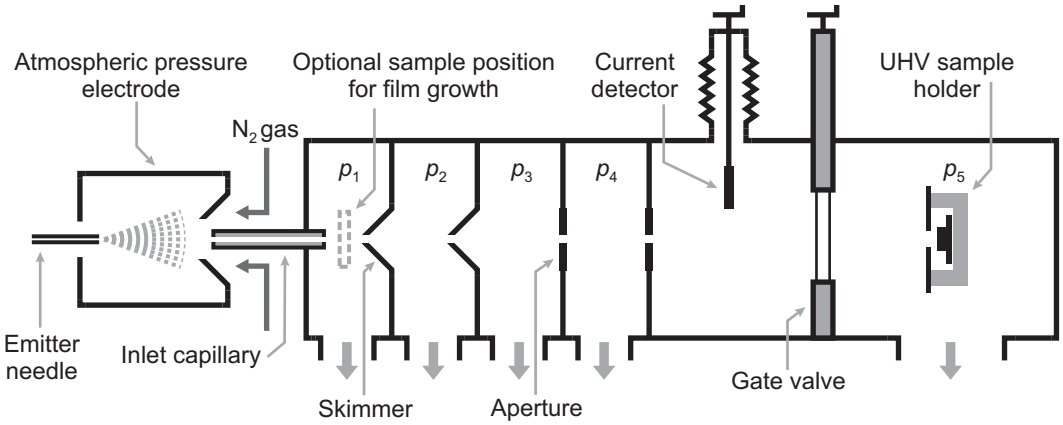

Figure 6.1 | Schematic diagram of the electrospray deposition setup. Values of the pressures $p_1 - p_5$ are given in the text.

6.1 Design of the Setup Components

6.1.1 The Electrospray Ion Source

The electrospray source used for ion generation is depicted in Figure 6.2. Sample solutions enter the source through a stainless-steel emitter needle (Metal Taper-Tip, inner diameter (i.d.) 100 μm, New Objective Inc.) at a flow rate of typically 1.5 μl/min. Constant and reproducible flow rates are achieved by using a syringe pump (Legato 180, KD Scientific Inc.). The exact position of the emitter needle can be adjusted by means an XYZ-manipulator. During operation, the emitter is placed at a distance of 2–3 mm from the vacuum entrance capillary, which is forming the interface between the electrospray ion source and the vacuum system.

The reference potential of the emitter needle apex can be adapted by an atmospheric pressure electrode (APE) which is surrounding the emitter. In order to generate an electrospray plume, a voltage of around 1–3 kV with respect to the APE is applied to the emitter needle via a metal pin that is immersed into the sample solution. Increasing the voltage applied to the APE results in a focusing of the electrospray plume onto the vacuum inlet, which is increasing the ion beam intensity. A review of the APE performance is given in section 6.2.1. The vacuum entrance capillary is in electrical contact to the vacuum chamber and therefore at ground potential.

Desolvation of the generated droplets can be supported by heating the entrance capillary up to a temperature of 150 °C. For this purpose, a 65 W coil heater is wrapped around the capillary mounting, which is thermally decoupled from the vacuum chamber by a PEEK spacer. In addition, the electrospray plume can be exposed to a counter-flow of hot nitrogen gas (max. 130 °C). Typical counter-gas flow rates for stable spray operation are of the order of 2 l/min.

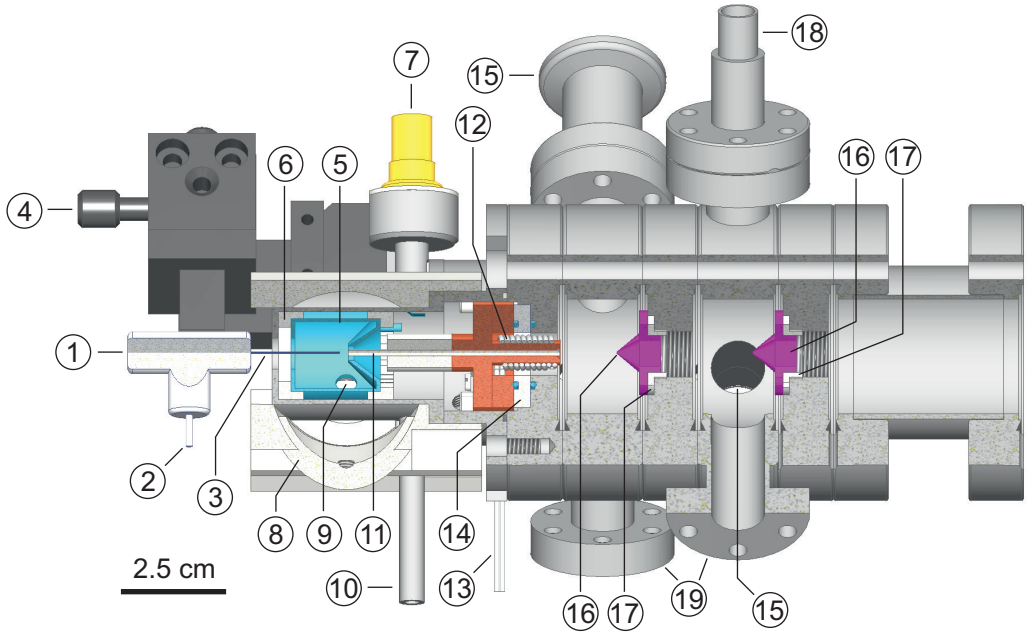

Figure 6.2 | Sectional drawing of the electrospray ion source and the first two differential pumping stations: (1) Connection to syringe, (2) plug for emitter needle voltage, (3) emitter needle, (4) XYZ manipulator, (5) APE, (6) electrical insulation of APE, (7) plug for APE voltage, (8) microscope mounting, (9) opening for light source, (10) inlet for counter gas flow, (11) vacuum entrance capillary, (12) capillary heater, (13) plug for capillary heater voltage, (14) thermal insulation of capillary heater, (15) connection to vacuum pumps, (16) skimmer, (17) electrical insulation of skimmer, (18) electrical feedthrough for skimmer current, (19) connection to Pirani gauges.

Optical control of the electrospray plume during operation is achieved by illuminating the spray region with a light source and using a video camera equipped microscope (SKS 25x, Peak Optics) for observation. A free line of sight to the spray region is realized by openings in the sidewall of the APE. Indirect light which is reflected from the inner surface of the APE can significantly hamper the spray monitoring, as it leads to a considerable background brightness in the microscope image. The stainless-steel surface of the APE was therefore treated by a bluing process, resulting in high light absorption while retaining high electrical conductivity and high resistance against the solvents used in the electrospray process.

6.1.2 The Differential Pumping System

In order to maintain a ratio of 11–12 orders of magnitude in pressure between the electrospray ion source and the UHV chamber, a differential pumping system comprising four separate stages is used. The geometry of the first three pumping stages is adopted from the original UHV4 setup.

A 12 m^3/h rotary vane pump (RV12, Edwards) evacuates the first chamber to a

pressure of $p_1 = 1.3\,\text{mbar}$, overcoming the $4\,\text{mbar}\,\text{l/s}$ leak rate through the entrance capillary (5 cm length, 0.25 mm i.d., stainless-steel). The same rotary vane pump is used to back a 10 l/s turbo pump[1] (HiPace 10, Pfeiffer) which is attached to the second pumping stage. Separation between the first two stages is realized by an electroformed skimmer (0.4 mm i.d.), which is placed at a distance of 13 mm from the entrance capillary, resulting in a pressure within the second stage of $p_2 = 4 \times 10^{-2}\,\text{mbar}$. Since gas dynamics at this pressure are still within the viscous flow regime, a second skimmer with larger opening (0.6 mm i.d.) is placed between the second and third stage.

The third and fourth chamber are both pumped by 67 l/s turbo pumps (HiPace 80, Pfeiffer). No direct measurement of the pressure is performed in these stages. However, according to the manufacturer of the UHV4 system, the pressure in the third chamber is of the order of $p_3 \approx 1 \times 10^{-5}\,\text{mbar}$, meaning that gas dynamics in the third and fourth chamber are described by free molecular flow. Simple apertures with 1.5 and 2.5 mm i.d. are therefore used to separate the third stage from the fourth one and the fourth stage from the UHV chamber, respectively.

The differential pumping system is separated from the UHV chamber by a gate valve. In order to reduce vibrations during STM measurements, all pumps are stopped and the differential pumping system is vented after sample preparation. No bakeout of the differential pumping system is performed in advance of a preparation. With the gate valve opened but in absence of an electrospray, the pressure in the UHV chamber is $p_5 \sim 4 \times 10^{-9}\,\text{mbar}$. During the deposition process, the pressure is rising to $p_5 \sim 8 \times 10^{-9}\,\text{mbar}$ with the additional pressure being caused by solvent molecules.

A careful alignment of all skimmers and apertures is crucial to achieve high deposition rates. The backlash of the CF flanges which are separating the pumping stages can be used to adjust the position of each orifice. A laser is utilized to ensure that all openings are centered on a straight line. Practice has shown that good results can only be achieved when the position of the entrance capillary is included into the adjustment procedure.

6.1.3 Sample Holders

Depending on the desired coverage, sample holders at different stages of the setup can be utilized for deposition.

Preparation of (sub)monolayers is carried out with the sample being placed inside the UHV chamber. The available UHV setups were equipped with sample holders that comprise an aperture of 4 mm diameter in front of the sample (Figure 6.3). Both sample and aperture are electrically insulated from ground and contacted separately

[1] Alternatively, evacuation of the second pumping stage can be performed by a two stage rotary vane pump with a pumping speed of around $10\,\text{m}^3/\text{h}$.

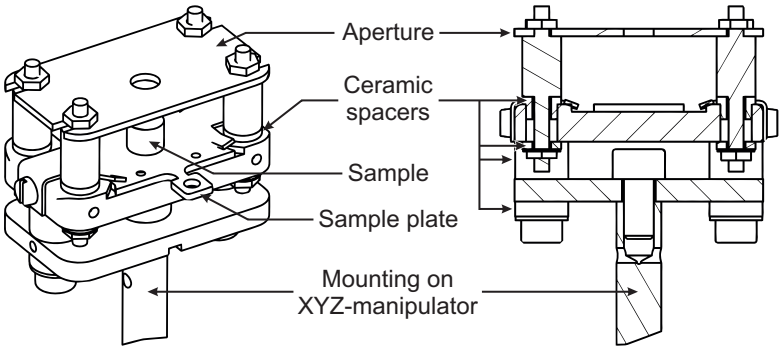

Figure 6.3 | Schematic drawing and cross section of the UHV sample holder used for electrospray deposition in the VT-STM setup. A similar sample holder is implemented in the preparation chamber of the Cryogenic STM. Sample and sample plate are omitted in the cross section.

by shielded coaxial cables. This allows for a direct measurement of the sample current without distorting contributions from ions that are hitting the sample plate.

In order to allow for an adjustment of the sample position with respect to the ion beam, the UHV sample holder is mounted on a manipulator. Optimization of the sample position is performed by maximizing the sample current. As an alternative, replacing the entrance capillary by a viewport and determining the sample position with the help of a laser was found to be highly reliable.

Film samples can be grown by placing the substrate in front of the skimmer inside of the first differential pumping stage. In order to achieve higher deposition rates, the entrance capillary is then replaced by a capillary with 0.5 mm i.d., resulting in a rise in pressure to $p_1 \approx 3.7\,\mathrm{mbar}$.

Alternatively, the substrate can be placed directly in front of the electrospray emitter tip at ambient conditions. By moving the emitter tip along a raster pattern parallel to the substrate, the deposited material can be spread over a large area. Furthermore, deposition at ambient conditions yields higher grow rates, which is achieved, however, at the expense of a reduced droplet desolvation. For the preparation of the film samples presented in this thesis, both low vacuum and atmospheric pressure deposition was applied.

6.1.4 Current Measurement

During operation of the electrospray source, currents can be measured on various electrodes for different purposes. While some electrodes are permanently monitored during deposition, others are only used for alignment and cleaning of the differential pumping system.

The total current I_{spray} that is carried by the charged droplets of the electrospray plume is determined by measuring the voltage drop across a shunt R_{s} that is placed in series between the HV power supply and the electrospray emitter tip. Considering

Electrode	Chamber	Typical Current
Emitter needle	Air	10–100 nA
LV sample holder	1st stage	5–30 nA*
First skimmer	1st stage	0.2–2 nA
Second skimmer	2nd stage	0.1–1 nA
First aperture	3rd stage	50–400 pA
Second aperture	4th stage	10–150 pA
Current detector	Behind 4th stage	10–150 pA
UHV sample holder	UHV chamber	10–150 pA

Table 6.1 | Typical electrode currents observed in the ESD setup. Exact current values generally depend on several factors, including the solution used for the electrospray process, the adjustment of the skimmers and apertures and the amount of contaminations present on the skimmer surfaces. *Value refers to 0.5 mm i.d. entrance capillary.

that emitter voltages are usually in the range of 1–3 kV and that total spray currents rarely exceed 100 nA, the shunt was chosen to have a resistance of $R_s = 100\,\mathrm{k\Omega}$. The voltage readout is opto-coupled to an AD-converter and transferred to a PC via USB interface, where it is converted to the corresponding current value by a LabVIEW program.

Currents on vacuum electrodes are measured with a Keithley 6517A electrometer that is capable of detecting signals down to the sub-pA range. Besides the sample and the aperture of the UHV sample holder, all skimmers and apertures of the differential pumping system are electrically insulated from ground, allowing for a determination of the ion loss in each individual pumping stage. Furthermore, a plate connected to a linear translator that can be moved into the ion beam enables an estimation of the sample current in advance of a deposition, i.e. with the gate valve to the UHV chamber being closed (see Figure 6.1). Typical current values for all electrodes are summarized in Table 6.1.

6.2 Setup Performance and Ion Beam Characterization

6.2.1 Performance of the Atmospheric Pressure Electrode

The efficiency of ESD and ESI-MS is generally hampered by ion losses appearing at the interface between the atmospheric pressure region and the vacuum system. As it can be seen from Table 6.1, in case of the setup used in this work, only around 1 % of the total current created by the electrospray ion source is transmitted into the first differential pumping stage. In principle, ion transmission into the vacuum system can be improved by using large entrance openings. This, however, places high demands on the pumping speed of the system, which not only is a cost issue, but also is in contradiction to the requirement of a compact setup design we are facing

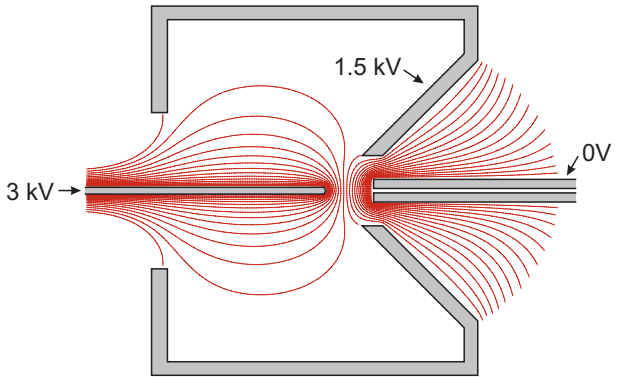

Figure 6.4 | Optimized geometry of the atmospheric pressure electrode. Equipotential lines were calculated with SIMION 8.0. APE and emitter needle potentials are stated in the figure. The separation between adjacent equipotential lines is 100 V.

here[2].

Since the current transmitted into the vacuum system depends on both the gas throughput and the charge density, another approach to increase sampling efficiency is to focus the charge cloud generated by the electrospray ion source on the vacuum system opening. Two different possibilities are available for doing so: On the one hand, enhanced ion intensities can be achieved when ion motion is influenced by atmospheric pressure electrodes (APEs) [68, 128, 129]. On the other hand, ion focusing at atmospheric pressure can also be realized by utilizing gas flow, which was successfully demonstrated by the use of Venturi devices [130, 131]. In the setup used here, an atmospheric pressure electrode (APE) was integrated into the electrospray ion source.

Design Issues

Optimization of the electrode geometry was carried out by simulating the electric field within the ion source for different electrode configurations. SIMION 8.0 from Scientific Instrument Services (Ringoes, USA) was utilized for the calculations. The optimized result is shown in Figure 6.4, together with a set of equipotential lines calculated for typical APE and electrospray emitter voltages.

The effect of the electrode on the motion of charged particles was simulated within SIMION by using the atmospheric pressure extension of Appelhans and Dahl [132]. However, such simulations cannot take into account the spatially dependent distribution of particle sizes in the electrospray plume and are therefore only of qualitative nature. Regardless of this shortcoming, the focusing effect of the electrode can be estimated based on the convex form of the equipotential lines around the vacuum entrance capillary, which is clearly visible in Figure 6.4. The conical shape of the APE has almost no influence on the shape of the equipotential lines in this region, but is simplifying the optical control of the electrospray plume.

[2]Note that a pump with pumping speed S that is connected to a vacuum system via a conductance C generates an effective volume flow S_{eff} which is given by $1/S_{\text{eff}} = 1/S + 1/C$. High pumping speeds therefore require a high conductance between pump and vacuum system, i.e. large dimensions of the vacuum chamber.

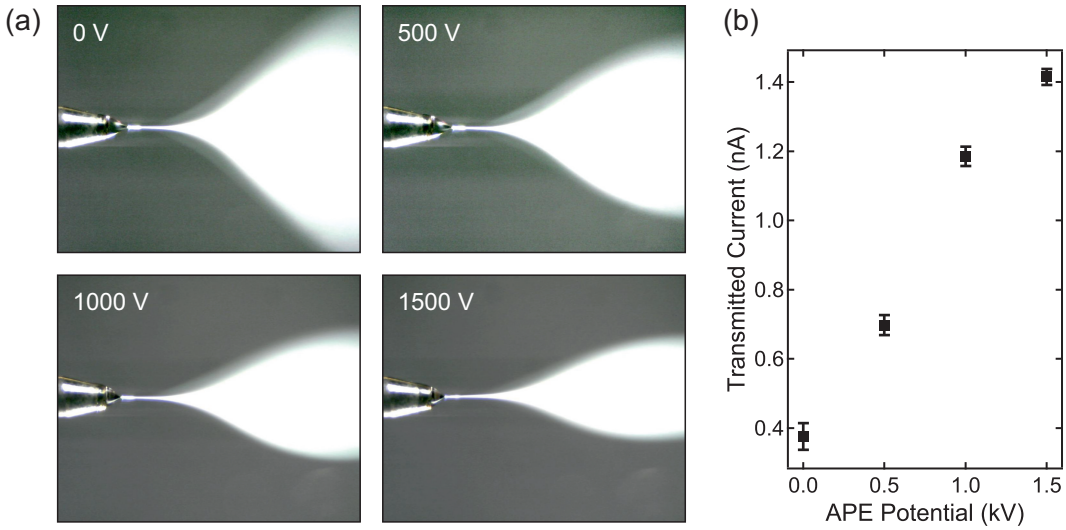

Figure 6.5 | Performance of the atmospheric pressure electrode. **(a)** Photographs of the electrospray plume for different APE voltages. **(b)** Measurement of the ion current transmitted through the entrance capillary as a function of APE potential.

APE Performance

In order to test the performance of the APE, measurements were carried out on a 5×10^{-4} M solution of NaCl in a mixture of water and methanol (volume ratio 1:1). The position of the emitter needle was optimized for zero APE voltage and subsequently kept constant during the measurement. Steady ionization conditions at the emitter apex were ensured by adapting the emitter voltage according to the APE potential with a fixed difference between emitter and APE of 1.55 kV. All measurements were performed in a 2.5 l/min counter flow of N_2 gas.

Figure 6.5a shows a series of photographs of the electrospray plume taken at different APE potentials in the range of 0 to 1.5 kV. The apparent divergence of the charge cloud on its way from the emitter to the entrance capillary is caused by Coulomb repulsion. Clearly, the cross section of the spray plume becomes smaller with increasing APE potential, demonstrating the APE's focusing capability. The impact of this effect on the transmission of ions from atmospheric pressure to vacuum was evaluated by summing up the currents over all vacuum electrodes, yielding an estimate of the total current transmitted into the vacuum system. Figure 6.5b shows the transmitted current as a function of APE potential. By increasing the voltage applied to the APE from 0 to 1.5 kV, the current conducted through the entrance capillary is rising from 0.38(4) to 1.41(2) nA, resulting in an almost fourfold enhancement in ion beam intensity. Taking into account that a value of $I_{\mathrm{spray}} = 53$ nA was simultaneously measured for the total spray current, this corresponds to an increase of ion transmission through the capillary from 0.71(7) to 2.67(4) %.

Limitations Imposed by Ion Losses in the Entrance Capillary

A significant enhancement in ion transmission via focusing at atmospheric pressure cannot be achieved in every case. Practical application of the APE has shown that the impact on ion transmission can strongly vary, depending on the properties of the analyte solution and the operational parameters of the electrospray ion source. Generally, a decrease of APE efficiency is observed for large ion currents. The effect of the APE potential on the transmission becomes negligible, when the current transmitted into the vacuum system is of the order or greater than 3 nA.

The current dependence of the APE efficiency can be explained by considering the mechanism of ion transport through the entrance capillary. Ion loss to the walls is generally caused by diffusion and space-charge expansion, the latter one being the dominant process in the initial segment of the capillary, where the charge density is the highest. As stated by Lin and Sunner [133], the space-charge driven development of the charge density $\rho(t)$ of an ion cloud generated by electrospray ionization is given by the unipolar formula

$$\frac{1}{\rho(t)} = \frac{1}{\rho(0)} + \frac{\kappa}{\epsilon}t, \tag{6.1}$$

where t is the time, κ is the ion mobility and ϵ is the electric permittivity. The time zero can be arbitrarily chosen and is here referring to the time when the charge cloud enters the capillary. Focusing of the ions on the capillary entrance results in an increase in the initial charge density $\rho(0)$. However, according to (6.1), the charge density becomes independent of its initial value in the limit $\rho(0) \to \infty$, meaning that ion losses in the capillary impose a limit to the transmission improvement achievable by ion focusing at atmospheric pressure.

6.2.2 Ion Energy Distribution

The kinetic energy of particles in the ion beam is determined by the supersonic expansion inside the first vacuum chamber. In good approximation, the velocity that is reached by the expansion is equal to the theoretical maximum v_∞, which is given by equation (2.5). As already pointed out in chapter 2.1.3, the value of v_∞ depends on the properties of the carrier gas alone, meaning that the velocity is the same for all particles. The energy of a particle is therefore proportional to its mass M and the distribution of kinetic energies directly reflects the mass spectrum of the ion beam. Indeed, the idea that ESI-MS can be performed by a simple measurement of kinetic particle energies was already utilized in the pioneering work of Dole *et al.* in 1968 [39].

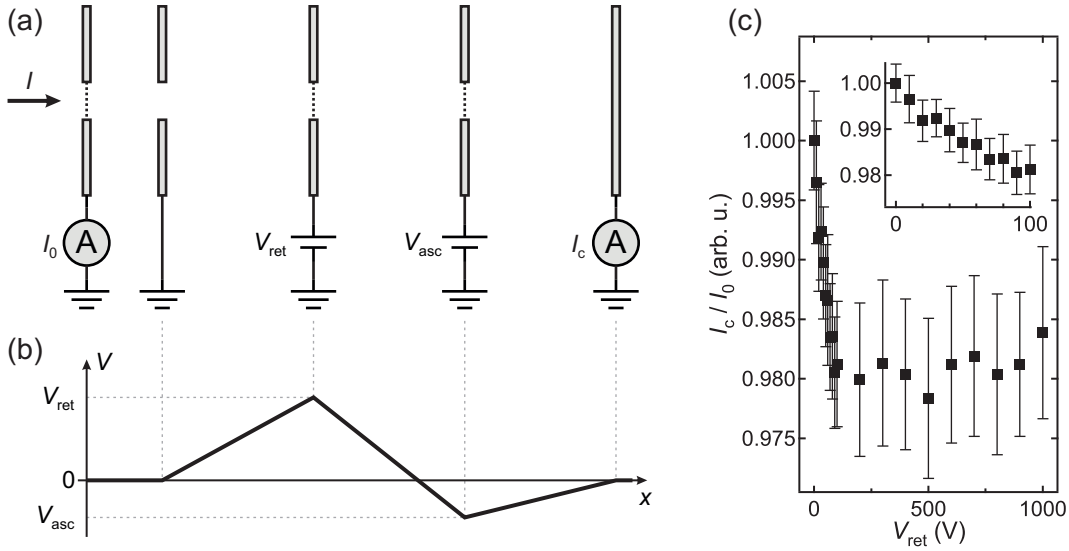

Figure 6.6 | **(a)** Schematic diagram of the constructed retarding field energy analyzer. **(b)** Idealized shape of the electrostatic potential $V(x)$ along the analyzer axis. **(c)** Ion transmission as a function of the retarding potential V_{ret}, measured on a NaCl solution. V_{asc} was set to a constant value of $-100\,\mathrm{V}$. The inset shows the low energy region in more detail.

Energy Analyzer Setup

Measurements of the energy distribution were carried out with a retarding field energy analyzer[3] that was positioned behind the last aperture of the differential pumping system. Figure 6.6a shows the schematic construction of the device. A retarding potential V_{ret} is applied to an electrode placed in between a charge collector and an I_0 grid. The ratio of the currents I_{c}/I_0 measured on the collector and on the grid gives the fraction of ions whose energy $E > zeV_{\mathrm{ret}}$ is sufficient to overcome the retarding field, with ze being the ion charge. In order to prevent a falsification of I_0 by low energy ions reflected from the retarding potential plate, a grounded shield is introduced directly behind the I_0 grid. Furthermore, a fourth electrode lying on a constant negative potential V_{asc} is placed in between the retarding electrode and the collector. The function of this electrode is to reject secondary electrons emitted from the collector which otherwise would cause an increase of the ratio I_{c}/I_0 with increasing V_{ret}[4].

Sodium Chloride Solution

As a test bed, ionization was performed from a solution of NaCl with identical solvent and NaCl concentration as in section 6.2.1. Figure 6.6c shows a measurement of the

[3] Technical aspects of retarding field energy analyzers are reviewed in [134].

[4] An alternative to the implementation of a fourth electrode is to use a Faraday cup as current collector.

$z = 1$			$z = 2$		
n	M [u]	E/z [eV]	n	M [u]	E/z [eV]
0	22.99	0.074	11	688.82	1.112
1	81.43	0.263	12	747.26	1.206
2	139.87	0.452	13	805.70	1.301
3	198.31	0.640	14	864.14	1.395
4	256.75	0.829	15	922.58	1.489
5	315.19	1.018	16	981.02	1.584

Table 6.2 | Mass M and expected kinetic energy E of NaCl clusters $[\mathrm{Na_z(NaCl)_n}]^{z+}$.

energy distribution up to a maximum retarding potential of $V_{\mathrm{ret}} = 1\,\mathrm{kV}$. In the range $V_{\mathrm{ret}} \lesssim 100\,\mathrm{V}$, the ratio I_c/I_0 continuously decreases to around 98 % of its starting value. A further increase of the retarding potential up to the maximum value has no significant effect on the transmitted current anymore. Similar results were achieved with solutions of other materials.

The result of the measurement is surprising at first sight. Solutions of NaCl are known to form singly and multiply charged clusters of formula $[\mathrm{Na_z(NaCl)_n}]^{z+}$ ($z = 1, 2, \dots$) in electrospray ionization [135–137]. Possible cluster sizes n depend on the charge number z, with values of $n \geq 0$ observed for $z = 1$ and $n \geq 11$ for $z = 2$. Discrete steps are expected to appear in the measurement at retarding voltages $V_{\mathrm{ret}} = E/ze$, where $E = \frac{1}{2}Mv_\infty^2$ depends on the cluster mass $M = (n + z)\,M(\mathrm{Na^+}) + n\,M(\mathrm{Cl^-})$. According to (2.5), the value of the terminal velocity is calculated to be $v_\infty = 789.3\,\mathrm{m/s}$. Table 6.2 summarizes the step positions that are expected for the smallest singly and doubly charged NaCl clusters.

Notably, energy per charge ratios of typical cluster sizes are of the order of 1 eV. This is in clear contradiction to the observation that the current ratio I_c/I_0 is almost unaffected by the retarding potential up to values of $V_{\mathrm{ret}} = 1\,\mathrm{kV}$. In fact, the measurement shows that the ion beam is mainly composed of particles with mass-to-charge ratios far greater than what is expected for ionized clusters or molecules. The only type of particle that comes into consideration for this mass-to-charge range are charged droplets arising from incomplete desolvation.

It is interesting to estimate a lower limit of the droplet size from the maximum retarding voltage used in the measurement. In general, the charge Q carried by a droplet must be smaller than the Rayleigh limit (2.3). Therefore, it can be calculated that the fraction of around 98 % of the ion current with energy-to-charge ratios above 1 kV must be carried by droplets with diameters greater than around 90 nm. Assuming typical analyte concentration of 10^{-5}–$10^{-4}\,\mathrm{M}$, this corresponds to a number of around 2–20 analyte units that are at least solved in a single droplet.

The Role of Collisions with the Background Gas

Although it is clear that not every droplet created in the electrospray ion source is completely desolvated, the predominant abundance of droplets in the ion beam seems to be unexpected. The observation that only a small fraction of the ion current is carried by gas phase ions can be explained by a discrimination of small particles during the transition from ambient conditions to ultra high vacuum. Several reasons are responsible for this discrimination. First, the opening of the skimmer in the first pumping stage is not located inside the region of free supersonic expansion. According to equation (2.4), the length of the free expansion zone up to the Mach disk is $x_{\mathrm{M}} = 4.6\,\mathrm{mm}$, which is several times smaller than the distance of 13 mm between skimmer and entrance capillary. Therefore, ions undergo heavy collisions with the background gas before they can enter the second pumping stage. Furthermore, the pressure in the second pumping stage is still within the vicious flow regime, meaning that collisions with the background gas also play a crucial role in this part.

The impact that collisions have on the particle motion can be estimated by means of kinetic gas theory. We consider a beam of ions with mass M, radius R and initial energy $E_0 = \frac{1}{2}Mv_\infty^2$, moving in a background gas of particles with mass m and radius r. Density and thermal motion of the gas are characterized by its temperature T and pressure p. In order to simplify the calculation, collisions between the ion beam and the background gas are described on the assumption that the background gas is at rest[5]. The mean free path, defined as the average distance an ion can travel between two successive collisions, is then given by

$$\lambda = (n\sigma)^{-1}. \tag{6.2}$$

Here, $n = \frac{p}{k_{\mathrm{B}}T}$ is the number of gas particles per unit volume and $\sigma = \pi(r^2 + R^2)$ is the collision cross section of the hard sphere model.

Calculating the change in ion energy that is caused by a collision is not possible without knowledge of the exact collision parameters. It is therefore useful to calculate the maximum ratio of the ion energy before (E_1) and after (E_2) a collision, which is given by the kinematic factor [54]

$$\kappa = \frac{E_2}{E_1} = 1 - \frac{m}{m+M}. \tag{6.3}$$

After k collisions, the energy of the ion is reduced to a value greater than $E(k) = E_0\kappa^k$. When the kinetic energy becomes smaller than the average energy stored in the thermal movement of a single particle, i.e. $E(k) \leq \frac{3}{2}k_{\mathrm{B}}T$, the motion of the particle is considered to be transformed from directed flow to random movement.

[5] Note that this is a rough approximation, considering that the average velocity $\overline{v} = \sqrt{8k_{\mathrm{B}}T/\pi m}$ of nitrogen at room temperature is 476 m/s, which is only around a factor of 2 smaller than v_∞.

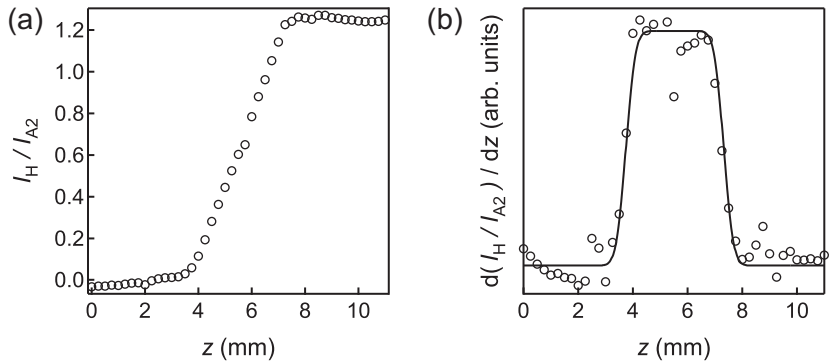

Figure 6.7 | Ion beam profile. **(a)** Current on the aperture plate of the UHV sample holder I_H as a function of the sample holder position z. **(b)** Derivative of the curve in (a). The solid line is a fit to the data, taking a convolution between a rectangular profile and a Gaussian as model function.

The number of collisions that is at least required to reach this limit is given by

$$k = \log_\kappa \frac{3k_B T}{2E_0}. \tag{6.4}$$

To illustrate the meaning of equations (6.2) – (6.4), we consider an ion of mass $M = 1000\,u$ and radius $R = 1\,\text{nm}$. Taking N_2 as background gas, the mean free path in the first pumping stage is around $9\,\mu\text{m}$, while it takes ca. 160 collisions before the directed motion of the ion is stopped. Most likely, the ion will not be able to pass the first differential pumping stage. The situation, however, becomes different for heavy particles, since the initial ion energy $E_0 \propto R^3$ grows faster than the number of collisions $\lambda^{-1} \propto R^2$. A droplet of 90 nm diameter, for example, will undergo around 2×10^6 collisions in the first two pumping stages, while it takes more than 10^8 collisions to reduce its energy below the thermal limit.

The observation that molecules are deposited from sub-μm sized droplets rather than as gas phase ions can have important implications on the growth behavior, as will be seen in the later course of this work. Furthermore, it should be noted that charged droplets are not considered as *ions*, according to the exact definition of the term. The deposition method used here is therefore referred to as electrospray deposition (ESD) and should not be confused with the term electrospray ion beam deposition (ESIBD), which is used for deposition of real gas phase ions [54]. However, for the sake of simplicity, the beam created by the ESD setup is denoted as ion beam in this thesis.

6.2.3 Deposition Spot Profile

The diameter of the deposition spot was measured by driving the edge of the aperture plate of the UHV sample holder across the profile of the ion beam and simultaneously

measuring the current on the plate I_{H} as a function of the position z. In order compensate for fluctuations of the ion beam intensity, the signal is normalized to the current on the second aperture I_{A2}. The result of the measurement is shown in Figure 6.7a.

The spatial dependence of the ion beam intensity can be extracted from the measurement by calculating the derivative $\frac{\mathrm{d}}{\mathrm{d}z}(I_{\mathrm{H}}/I_{\mathrm{A2}})$. The corresponding curve exhibits a surprisingly flat profile with a FWHM of around 3.6 mm (Figure 6.7b). Taking into account the distance between UHV sample holder and second aperture, the opening angle of the beam is calculated to be 0.4°.

7 | Substrates Used for Deposition

Substrates for deposition were prepared by means of standard UHV techniques. Unless otherwise stated, the preparation was performed at one of the UHV setups described in chapter 5.1. Cut and polished single crystals were purchased from Mateck GmbH (Jülich, Germany) or SPL (Zaandam, Netherlands). All crystals were mounted on molybdenum or tungsten sample holders.

7.1 Single Crystal Noble Metal Surfaces: Au(111), Ag(111) and Cu(111)

The (111) surfaces of Au, Ag and Cu can be considered as standard substrates for the investigation of atomic and molecular assemblies. They were widely used within this thesis as supports for ESD and wet chemical preparation procedures.

Preparation

Cleaning of the crystal surfaces was performed by repeated cycles of Ar^+ sputtering (Ag: 800 eV, Au & Cu: 1000–1500 eV) and subsequent annealing to high temperature (Ag: 550 °C, Au & Cu: 600 °C). The surface quality was occasionally checked by means of STM and XPS measurements.

The Au(111) Surface Reconstruction

Gold is the only fcc metal that exhibits a reconstruction of the close-packed (111) surface [138–140]. As the topmost atomic layer is contracted along the $[1\bar{1}0]$ directions, periodic transitions between regions of fcc and hcp stacking occur with a periodicity of 22 bulk atomic distances. The corresponding height variation is visible in STM topographic images as characteristic lines propagating along the $[11\bar{2}]$ directions, which are often referred to as herringbone structure (see Figure 7.1a,b). Typical STM corrugations are in the range of 10–20 pm. At the boundary between domains of different (crystallographically equivalent) contraction orientations, so called elbow sites are formed, which provide nucleation centers for the growth of atomic and molecular adsorbates.

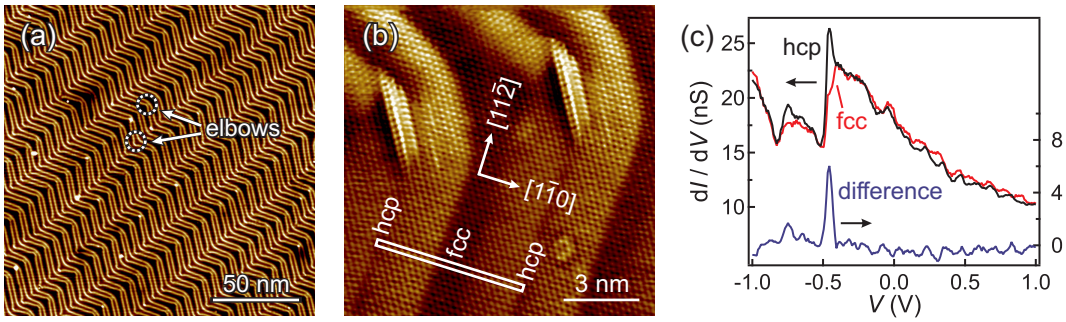

Figure 7.1 | STM and STS measurements on Au(111). (a) Large scale image showing the herringbone pattern of the surface reconstruction. **(b)** Close up image with atomic resolution. Regions with fcc and hcp stacking and crystallographic orientations are indicated. The white rectangle marks the $(22 \times \sqrt{3})$ reconstruction unit cell. **(c)** STS spectra recorded on fcc and hcp sites of the surface reconstruction. Scanning parameters: (a) $V = 0.1\,\mathrm{V}$, $I = 950\,\mathrm{pA}$, $T = 15.8\,\mathrm{K}$, (b) $V = 0.1\,\mathrm{V}$, $I = 3.2\,\mathrm{nA}$, $T = 10.0\,\mathrm{K}$. Parameters for spectroscopy: $V_\mathrm{s} = 200\,\mathrm{mV}$, $I_\mathrm{s} = 3\,\mathrm{nA}$, $V_\mathrm{mod} = 10\,\mathrm{mV}$.

Surface States

The electronic density of states of all three substrates comprises a surface state in the vicinity of E_F, which is reflected in STS measurements as a step-like increase in differential conductivity. Since the onset energies of the surface states are well known [141–143], they can be used as a spectroscopic reference when performing STS measurements on not yet characterized adsorbates. Figure 7.1c shows the appearance of the surface state in an STS measurement on Au(111). In accordance with the literature, the surface state band edge is located at around $-0.5\,\mathrm{eV}$, coinciding with the minimum energy of the parabolic surface state dispersion. As first reported by Crommie *et al.* [141], a slight difference in spectroscopic shape is observed between measurements performed on fcc and hcp sites of the Au(111) surface reconstruction.

7.2 NaCl(100) on Au(111)

Ultrathin insulating layers on metallic substrates facilitate the investigation of asorbates on insulator surfaces with scanning tunneling microscopy. A possible approach is to use multi-layered NaCl islands, which have been successfully grown on a variety of different crystalline metal surfaces [144–151].

Preparation

Preparation of NaCl on Au(111) was performed by thermal sublimation of a NaCl single crystal at around 500 °C. The substrate was kept at room temperature during the deposition process. Before each preparation, the temperature of the evaporator

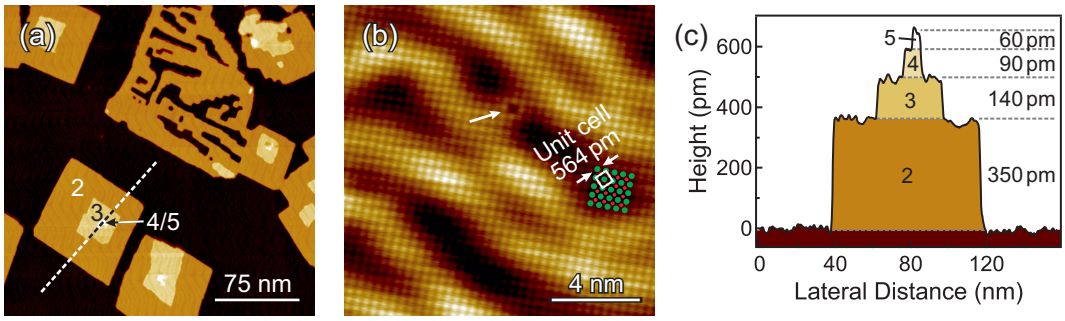

Figure 7.2 | STM measurement of NaCl(100) on Au(111). (a) Large scale image of several NaCl islands. Numbers indicate the amount of layers. **(b)** Close up image showing the atomically resolved NaCl lattice superimposed to the Au(111) herringbone reconstruction. Green and red circles indicate the positions of Cl^- and Na^+ ions, respectively. A point defect of the NaCl lattice is visible in the upper part (arrow). **(c)** Height profile along the dashed line in (a). Scanning parameters: (a) $V = -2.5\,\mathrm{V}$, $I = 10\,\mathrm{pA}$, room temperature, (b) $V = -2\,\mathrm{V}$, $I = 150\,\mathrm{pA}$, $T = 7.5\,\mathrm{K}$.

was fine adjusted using a quartz crystal microbalance to achieve deposition rates in the range of 1–2 Å/min. Typical coverages are between 2 and 4 Å.

Properties

NaCl on Au(111) grows epitaxially as islands with (100) orientation [144, 145]. The first plateau is formed by an atomic double layer – single layered islands are not observed. Further layers start growing before the first double layer is completed.

An STM image of NaCl islands comprising up to 5 layers is shown in Figure 7.2a. The first NaCl double layer forms straight edges in 90° angles to each other. Edges of higher layers exhibit an increased roughness.

The apparent height of NaCl in STM is generally smaller than the physical height, owing to the insulating nature of the material. Bulk NaCl crystallizes in fcc structure with a lattice constant of 564 pm [144], corresponding to the physical height of two atomic layers. As it can be seen in Figure 7.2c, the apparent height of the first double layer of around 350 pm is already well below this value. Furthermore, the apparent height of each additional layer is successively reduced, making STM measurements on multi-layered islands increasingly difficult. For the comparable system NaCl(100)/Cu(111), it was reported that tunneling is possible through up to five layers of NaCl, provided that tunneling currents of only a few pA are used [152]. It should be noted that the apparent height of the first double layer, while being smaller than the physical height of two layers, is still larger than the physical height of a single layer. This verifies that the first plateau of NaCl on Au(111) is indeed formed by more than one atomic layer.

An atomically resolved STM image of NaCl is shown in Figure 7.2b. The atomic corrugation exhibits a square lattice with a lattice constant of around 400 pm, super-

imposed to the Au(111) surface reconstruction. Since the periodicity coincides with the closest separation between ions of the same species, it is concluded that only one of the two element sublattices is imaged in STM. According to [144], protrusions in the STM topography are attributed to Cl^- anions.

7.3 Graphene on Ir(111)

The self-limited growth of two dimensional materials on catalytic surfaces offers another possibility to decouple adsorbates from the impact of the metallic substrate. Graphene, a monatomic layer of carbon atoms arranged in a honeycomb lattice, is probably the most prominent example of such a system. Using low pressure chemical vapor deposition (CVD), high quality epitaxial graphene can be grown on the surfaces of various transition metals, including Ni, Cu, Pt, Ir, Rh and Ru [153]. The procedure applied during the CVD process is the following: While the substrate is kept at high temperature, it is exposed to an atmosphere of a carbonic precursor. After catalytic decomposition of the precursor molecules on the hot metal surface, the graphene layer is formed from small building blocks, which in turn are composed of precursor fragments. Since the catalytic effect of the substrate is passivated once it is completely covered, the process stops abruptly after the first layer is formed.

Preparation

Cleaning of the Ir(111) substrate was performed by repeated cycles of Ar^+ sputtering (2 kV), heating in O_2 atmosphere (5×10^{-7} mbar, 850–1150 °C) and flash annealing in UHV (1600 °C). Subsequently, graphene was prepared by keeping the substrate at a temperature of 1230–1270 °C while exposing it to an ethylene pressure of 1×10^{-7} mbar for 20 min.

Properties

Graphene on Ir(111) most often grows in the so called R0 phase, corresponding to a parallel alignment between the C zigzag directions and the crystallographic $\langle 1\bar{1}0 \rangle$ orientations of Ir. Based on a graphene lattice constant of 2.46 Å and an Ir(111) nearest-neighbor distance of 2.715 Å [154], the lattice mismatch of the graphene layer with respect to the substrate is around 9.4 %. The superposition of both lattices gives rise to an incommensurate moiré superstructure with a periodicity of around 2.53 nm [154, 155]. Sites of high local symmetry in the moiré unit cell are denoted here referring to the center positions of the carbon hexagons. Configurations in which the hexagon centers are placed on top of an Ir atom of the first, second or third layer are therefore referred to as atop, hcp and fcc, respectively. As an illustration, Figure 7.3 shows the moiré unit cell of the closest matching commensurate superstructure, which spans (10×10) C rings placed on (9×9) Ir atoms.

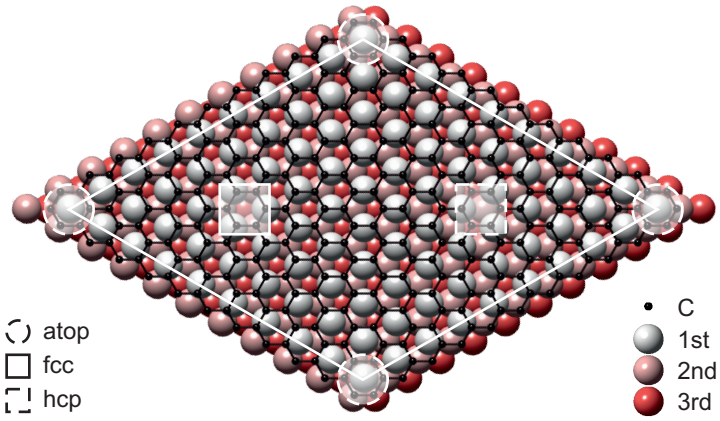

Figure 7.3 | Structure model of a commensurate moiré superstructure formed by (10×10) graphene unit cells on a (9×9) Ir(111) slab. The moiré unit cell and several high symmetry sites are highlighted.

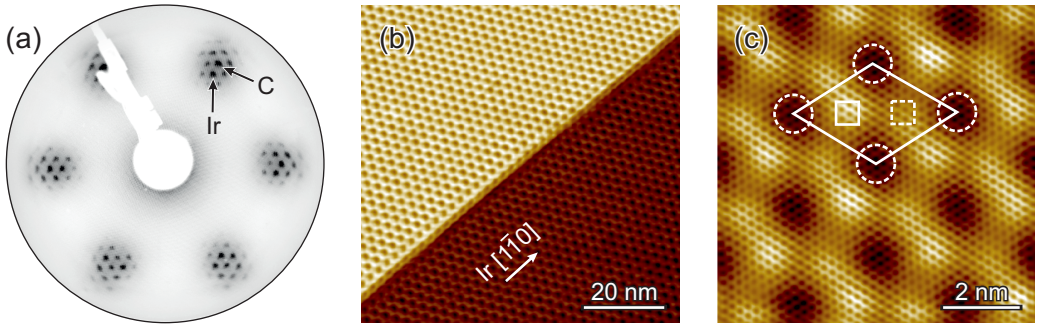

Figure 7.4 | **Graphene on Ir(111). (a)** LEED pattern measured at 75 eV. **(b)** Large scale STM image of the moiré superstructure. The graphene layer expands over Ir step edges in a carpet-like manner. **(c)** Atomically resolved STM image with dark-atop contrast. The moiré unit cell and high symmetry sites are indicated according to Figure 7.3. Scanning parameters: (a) $V = 42\,\text{mV}$, $I = 16\,\text{nA}$, (b) $V = 13\,\text{mV}$, $I = 21\,\text{nA}$, both at room temperature. STM data acquisition performed by A. Zusan.

LEED measurements were routinely performed after graphene/Ir(111) preparation in order to verify the sample quality. An example of a LEED pattern is shown Figure 7.4a. Outer and inner first order spots are attributed to the graphene honeycomb lattice and the Ir substrate, respectively, based on the values of their real space lattice constants. The first order C spots are surrounded by satellite spots which reflect the long-range periodicity of the moiré superstructure. Additional sets of first order C spots which are rotated with respect to the Ir spots and which are considerably weaker in intensity were occasionally observed for some of the samples, indicating that rotated graphene domains are present on the sample besides the most abundant R0 phase. However, such rotated domains occur so rarely that they were never observed in STM images.

The continuous shift of the C atoms with respect to the substrate results in a variation of binding energies over the moiré unit cell and therefore in a topographic buckling of the graphene layer. Density functional theory (DFT) calculations indicate that the separation between graphene and Ir is the highest on atop sites and the lowest in the hcp regions. The real topographic corrugation predicted by DFT is 0.35 Å [156]. STM images of the moiré superstructure generally give no realistic measure of the topographic corrugation, since they also reflect electronic variations within the moiré unit cell. Most often, atop regions are imaged as dark depressions in STM topography (see Figure 7.4b,c). Spontaneous inversions of the contrast can be observed, depending on the bias voltage and the tip state [84].

7.4 Hexagonal Boron Nitride on Rh(111)

A single layer of hexagonal boron nitride (*h*-BN) is an isoelectronic structure analogue to graphene, consisting of equal numbers of boron and nitrogen atoms. In contrast to freestanding graphene which behaves as a zero bandgap semiconductor, BN polymorphs including *h*-BN are wide-bandgap electric insulators. In recent years, an increasing interest in single layer *h*-BN on metal surfaces, in particular on Rh(111), emerged because of its ability to act as a nano-template for the growth of atoms [157, 158], clusters [159] and molecules [157, 160–163].

Preparation

Preparation of *h*-BN/Rh(111) was performed as follows: The Rh(111) substrate was cleaned by several cycles of Ar^+ sputtering (2 kV), heating in oxygen atmosphere (5×10^{-7} mbar, 650–900 °C) and annealing in UHV (1100 °C). For the formation of the *h*-BN layer, the substrate was kept at 800 °C while it was exposed to a borazine ($B_3N_3H_6$) vapor pressure of 1×10^{-7} mbar for 26 min. The borazine precursor was purified prior to preparation by several freeze-pump-thaw cycles.

Properties

Hexagonal boron nitride on Rh(111) forms a highly regular hexagonal superstructure with a periodicity of around 3.2 nm, which is often referred to as *nanomesh*. The term goes back to an early work which suggested a two layer model of *h*-BN/Rh(111), in which the formation of each BN layer is incomplete [160]. Considering the necessarily large number of broken B-N bonds, this model turned out to be not realistic and consensus is reached today that *h*-BN forms a single, complete layer on Rh(111) with a highly corrugated moiré pattern [164, 165].

LEED measurements confirm that *h*-BN/Rh(111) preferably grows in R0 orientation (see Figure 7.5a). The moiré superstructure is reflected by a hexagonal pattern of satellite spots accompanying the principal substrate reflexes. Based on

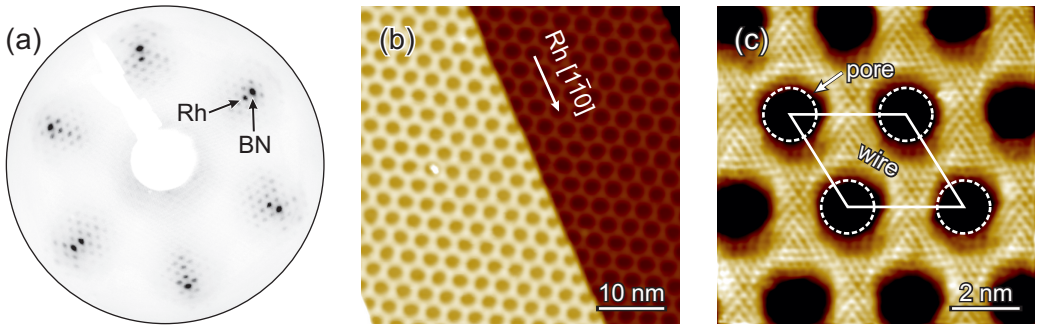

Figure 7.5 | **Hexagonal boron nitride on Rh(111). (a)** LEED pattern recorded with an electron energy of 63 eV. **(b)** Large scale STM image of the *h*-BN moiré superstructure. **(c)** Atomically resolved close up image. The moiré unit cell as well as pore and wire sites are indicated. Scanning parameters: (b) $V = -1.1$ V, $I = 500$ pA, $T = 6.1$ K, (c) $V = 70$ mV, $I = 2$ nA, $T = 7.8$ K.

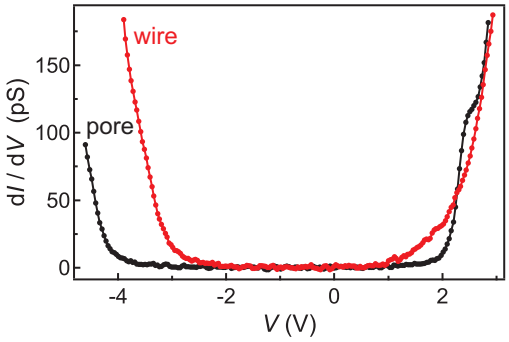

Figure 7.6 | Site resolved STS spectra, recorded on pore and wire regions of the *h*-BN superstructure. A wide conduction gap around E_F reflects the insulating nature of the *h*-BN layer. Parameters: $V_s = 3$ V, $I_s = 100$ pA, $V_{mod} = 40$ mV, $T = 1.9$ K.

the distances between the substrate and *h*-BN primary spots, a real space lattice ratio between *h*-BN and the metal substrate of 12:13 is deduced, corresponding to a moiré unit cell which contains (13×13) *h*-BN units on (12×12) Rh atoms [166].

A peculiarity of the *h*-BN/Rh(111) moiré pattern is the relatively abrupt transition between regions of low and high corrugation. In STM images, strongly bound areas ('pores') appear as relatively flat holes of ca. 2 nm diameter, which are separated from elevated regions ('wires') by an almost stepwise change in height (see Figure 7.5b). The unique structure is well reproduced by DFT calculations, which predict a corrugation of around 0.55 Å, the *h*-BN layer being closest to the metal surface in regions where B and N atoms are close to fcc and atop sites, respectively [164]. While atomic resolution on the wire sites is routinely achieved in STM, no structure is usually visible inside the pore regions (see Figure 7.5c). Adjacent atomic protrusions on the wire sites are measured to be separated by about 2.50 Å. According to DFT, only N atoms are probed by STM in the vicinity of E_F [165].

An intriguing question is whether the boron nitride layer remains an electric insulator on the Rh surface. Insight into the local electronic structure can be obtained based on STS measurements. Spectra taken at different sites of the *h*-BN moiré pattern are shown in Figure 7.6. A band gap of around 6 eV is observed on the pore

regions, while a smaller gap of ca. 4 eV is visible in curves taken on wire sites. STS data reported in literature [159] show slightly larger band gap values, but are in overall good agreement with the measurement performed here.

Part III

Results and Discussion

8 | Electrospray Deposition: Application Examples

This chapter provides several examples of molecular compounds that were deposited by means of ESD in the course of this thesis. The aim is to briefly demonstrate the capabilities as well as the limitations of the ESD setup, without going into details concerning the physical properties of the systems.

8.1 Fe-Phthalocyanine

Metal phthalocyanines (MPcs) are planar coordination complexes with a single metal ion M, located at the center of an aromatic macrocycle that is formed by alternating carbon and nitrogen atoms. The structure of the molecule shows a remarkable thermal and chemical stability, which enables deposition of MPcs onto surfaces by means of thermal sublimation in UHV. Since MPcs are utilized in a wide field of industrial applications, most importantly in dyeing, they are commercially available in huge amounts and in high purity. All these aspects – combined with a great interest in the electronic properties of MPcs in fundamental research [167–170] – have led to a vast amount of literature that is available on MPcs on surfaces today [171]. Therefore, MPcs an ideal test bed for verifying the ESD setup functionality. Here, M = Fe was chosen as central metal ion. The structure of the FePc complex is shown in Figure 8.1a.

FePc was purchased from Sigma-Aldrich as FePcCl powder (95 % purity). The chloride salt rather than the neutral complex was used due to the generally bad solubility of phthalocyanines in polar organic solvents. Electrospray deposition of the compound was performed on Au(111), using a 2×10^{-5} M solution in pure methanol.

Typical STM images of the surface after deposition are shown in Figure 8.1b,c. Most of the molecules occur as individual objects that preferably occupy the elbow sites of the Au(111) herringbone reconstruction. A clear intramolecular structure is resolved in the STM topography, reflecting the fourfold symmetry of the molecule with the four benzene rings appearing as well-separated lobes and the Fe center appearing as a small protrusion. It is therefore be concluded that the molecules lay

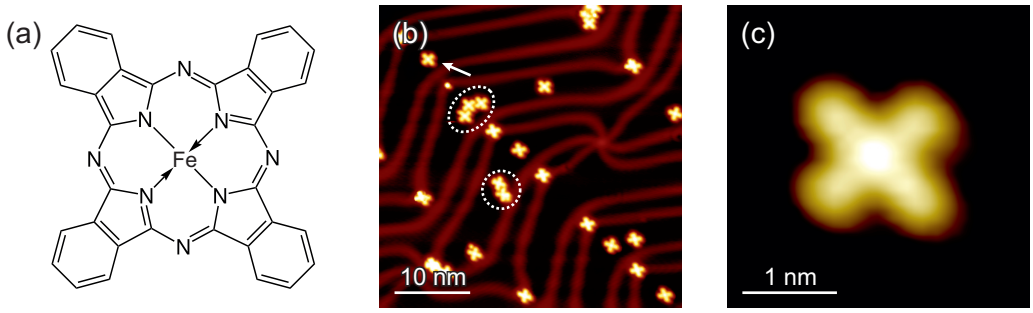

Figure 8.1 | **(a)** Molecular structure of FePc. **(b)** STM image showing the Au(111) surface after electrospray deposition of FePc molecules. Dashed circles indicate formation of multimers. **(c)** Magnification of the molecule marked by an arrow in (b). Scanning parameters: $V = 1\,\mathrm{V}$, $I = 400\,\mathrm{pA}$, $T = 9.8\,\mathrm{K}$.

on the substrate in a flat geometry. Besides individual molecules, also formation of dimers and trimers is observed (see Figure 8.1b).

By comparing our results to other STM studies of FePc on Au(111) [172,173], we find that the sample quality provided by the ESD process is equal to that of thermal sublimation. In particular, no residuals of the solvent and only small amounts of impurities are found in large scale STM images. The intramolecular structure resolved in STM topography provides no evidence for molecular fragmentation. Furthermore, the adsorption behavior of the molecules is the same as reported in [172,173]. These findings demonstrate the high potential for an application of ESD in the field of ultra-high vacuum scanning tunneling microscopy.

8.2 Four-Armed Polyfluorene Star Polymer

A polymer with star-like configuration [174] is among the biggest molecules that have been deposited by means of the ESD setup so far. Figure 8.2a shows the molecular structure of the complex, which is referred to as TDI-star-PF. It comprises a terrylene diimide core with four polyfluorene arms. The average number n of fluorene units in each arm is determined by the parameters of the polymerization process. The measurements reported here were conducted on a complex with $n \approx 5$.

Chemical synthesis of the material was performed by C. S. Fischer in the group of Prof. Mecking (Department of Chemistry, University of Konstanz). For the electrospray process, the polymer was dissolved in a mixture of dichloromethane and methanol (volume ratio 5:2) at a concentration $3 \times 10^{-5}\,\mathrm{M}$. Au(111) was used as substrate for deposition.

STM images of the TDI-star-PF on Au(111) are depicted in Figure 8.2b,c. Isolated molecules are mainly found at step edges with a part of their polyfluorene arms oriented along the edge direction. The individual fluorene units of the arms are clearly resolved in the STM topography. At higher coverage, networks of molecules

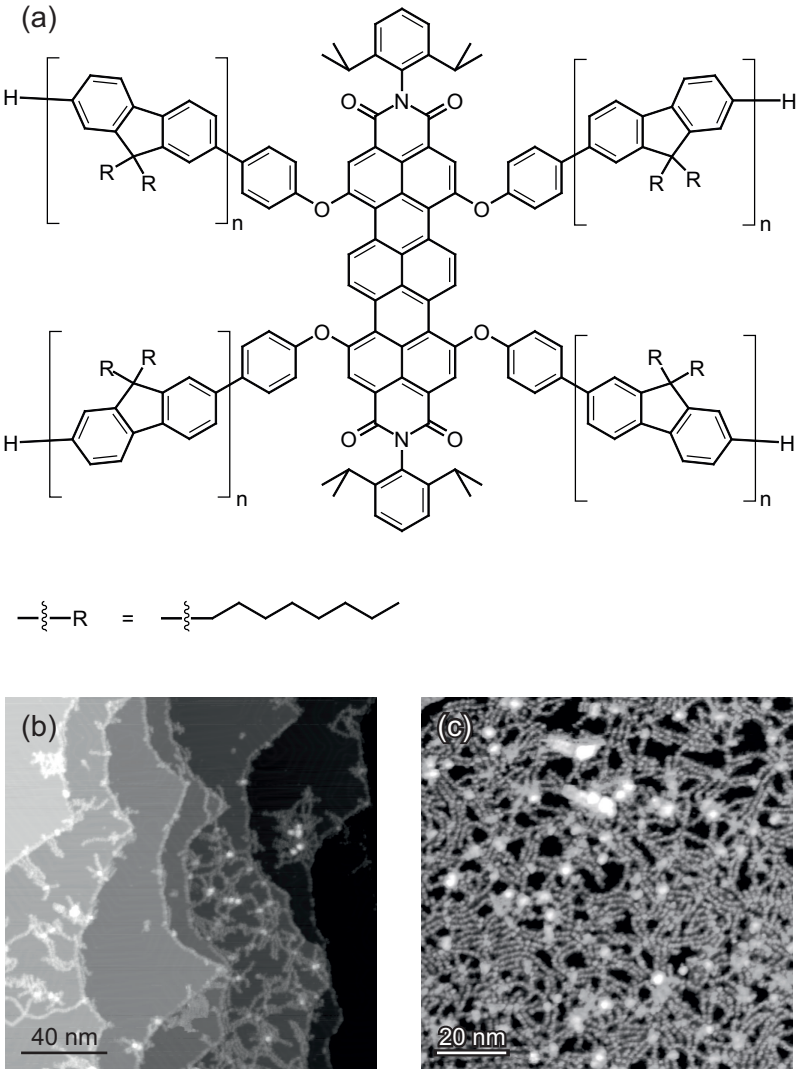

Figure 8.2 | **(a)** Molecular structure of the TDI-star-PF. **(b,c)** STM images showing the arrangement of TDI-star-PF molecules after deposition on Au(111). Scanning parameters: $V = 2\,\mathrm{V}$, $I = 25\,\mathrm{pA}$, $T = 8.1\,\mathrm{K}$.

are formed in which adjacent polymers tend to align their arms parallel to each other (Figure 8.2c). The formation of such structures demonstrates the importance of van-der-Waals interactions between the unpolar arms of the polymers.

8.3 Triazatruxene

STM measurements on triazatruxenes were performed in the course of a current project, aiming at the realization of different charge states of molecules on surfaces and the control of these states on the single molecule level. Triazatruxenes (TATs) are planar, triangular molecules that comprise three interconnected indole rings. The TAT core is electroactive and can be easily oxidized in two reversible redox-steps, making it a suitable candidate for the planned measurements. Furthermore, the

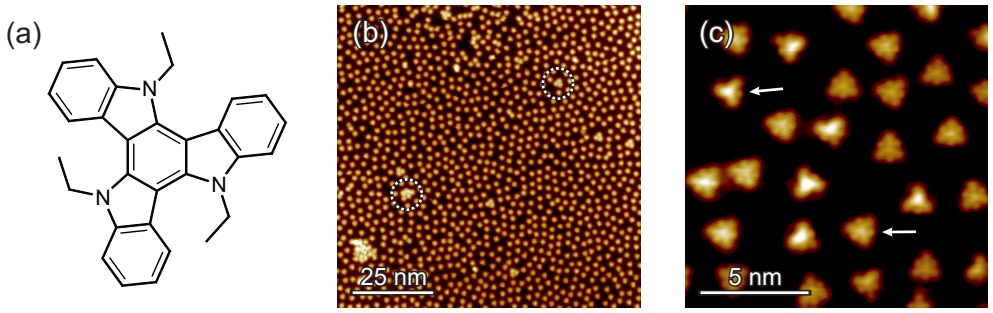

Figure 8.3 | **(a)** Molecular structure of the investigated TAT derivative. **(b)** Large scale STM image of TAT on Ag(111) at 0.3 ML coverage. Dashed circles mark the formation of a trimer and pentamer. **(c)** Magnified view with intramolecular resolution. Arrows indicate examples of molecules with retained and broken C_3 symmetry. Data acquisition by F. Singer. Scanning parameters: (b) $V = 1\,\mathrm{V}$, $I = 50\,\mathrm{pA}$, $T = 7.8\,\mathrm{K}$, (c) $V = 0.3\,\mathrm{V}$, $I = 300\,\mathrm{pA}$, $T = 7.2\,\mathrm{K}$.

possibility to modify the outer phenyl rings of the structure with up to six peripheral substitutes opens the way for synthesizing highly functionalized compounds that incorporate the TAT core as a building block [175].

The structure of the TAT derivative used here is shown in Figure 8.3a. Chemical systhesis was performed by M. Meier in the group of Prof. Winter (Department of Chemistry, University of Konstanz). The complex was dissolved in a mixture of dichloromethane and methanol (volume ratio 4:1, concentration $2 \times 10^{-4}\,\mathrm{M}$) and subsequently electrospray deposited from solution on a Ag(111) surface.

The adsorption behavior of TAT at around 0.3 ML coverage is shown in Figure 8.3b,c. Although formation of multimers is observed, most of the molecules are present as individual objects. As can be seen from Figure 8.3b, the spatial distribution of isolated molecules favors a uniform intermolecular distance, indicating a repulsive molecule-molecule interaction. The origin of this phenomenon is not fully understood at the current point and is still under investigation.

High resolution images of intact molecules reveal a clear intramolecular structure with threefold rotational symmetry (Figure 8.3c). In addition, objects with reduced symmetry are present on the surface, which are possibly explained by the occasional loss of one or several indolic alkyl groups during the electrospray ionization process.

At higher surface coverage, the TAT molecules start to organize in self-assembled periodic structures. The coexistence of at least three different molecular arrangements was observed at a coverage of 0.7 ML. STM images of all three structure types are shown in Figure 8.4a-d. Structure models derived from the STM images are presented in Figure 8.4e-g. A detailed discussion of the structures is beyond the scope of this chapter. It should be noted however that one of the structures is described by a honeycomb lattice.

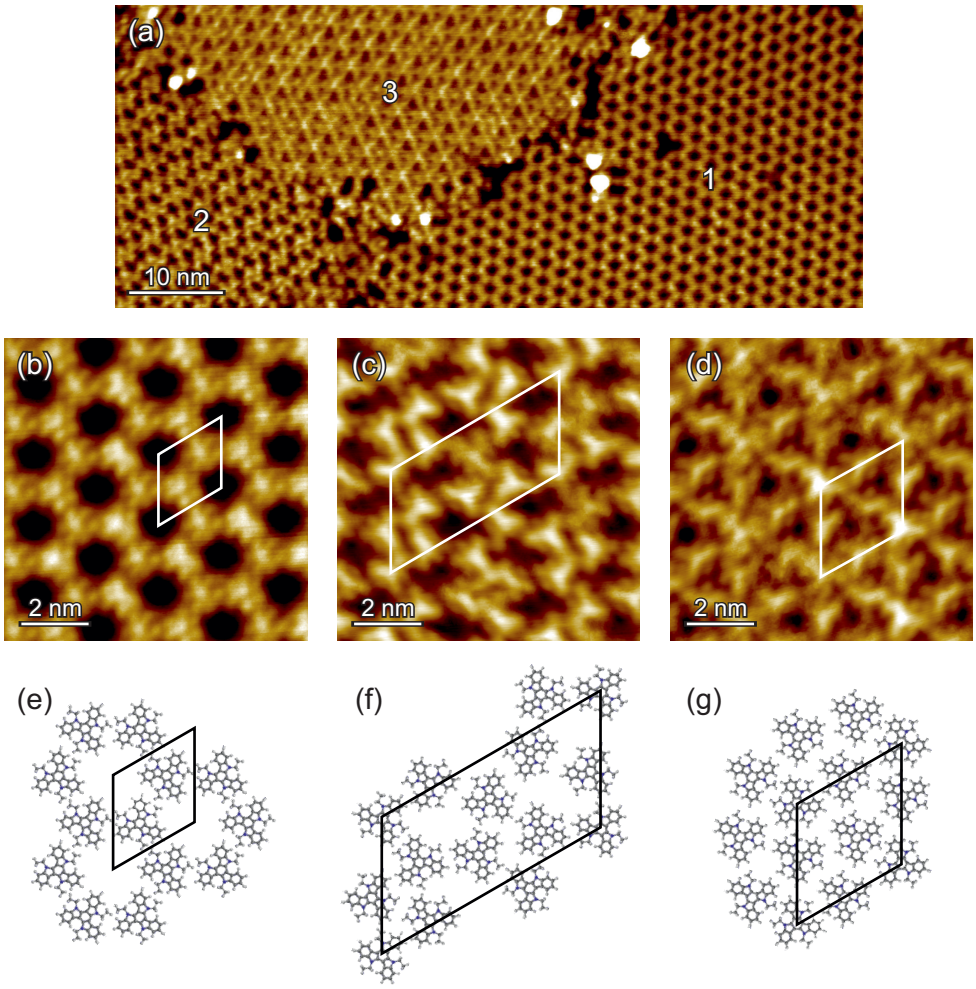

Figure 8.4 | **Molecular self-assembly of TAT on Ag(111). (a)** STM image of an area comprising three domains with different self-assembled structures. **(b-d)** Detailed view of the structures corresponding to the domains 1–3, respectively. The unit cells are marked by white parallelograms. Data acquisition by F. Singer. **(e-g)** Structure models deduced from STM images. Scanning parameters: (a) $V = 1\,\mathrm{V}$, $I = 100\,\mathrm{pA}$, $T = 7.5\,\mathrm{K}$, (b) $V = 1\,\mathrm{V}$, $I = 300\,\mathrm{pA}$, $T = 7.5\,\mathrm{K}$, (c,d) $V = 0.5\,\mathrm{V}$, $I = 200\,\mathrm{pA}$, $T = 7.5\,\mathrm{K}$.

8.4 Limitations Imposed by Solvent Effects

A major advantage of ESD compared to wet chemical preparation schemes is the relatively free choice of the substrate. Deposition procedures in which the substrate is directly immersed into solution typically rely on a specific molecule-substrate interaction and can therefore only be used with one particular surface. One of the most prominent examples is the strong interaction between sulfur and gold, that is widely used to anchor molecular compounds containing thiol groups on gold surfaces [176]. ESD is not restricting the choice of substrate in a comparable way. However, it should be kept in mind that the sample is exposed to the solvent during the ESD

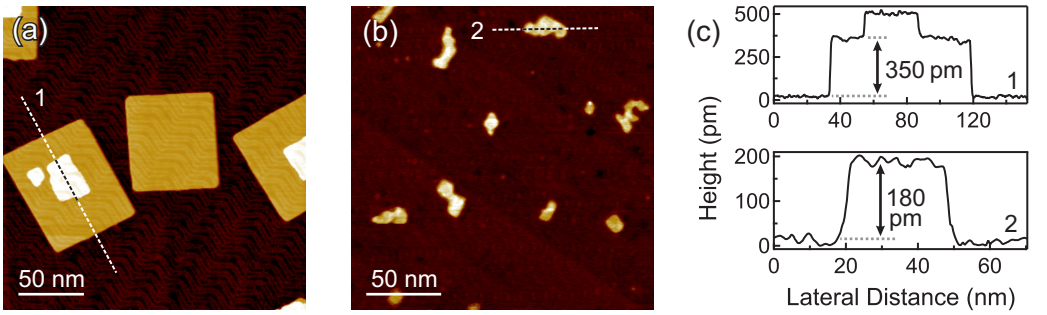

Figure 8.5 | **Solvent effects in ESD. (a)** STM image of NaCl islands on Au(111) before the ESD process. **(b)** Image of the same sample after 90 min exposure to the ESD beam. **(c)** Height profiles along the lines marked in (a) and (b). Scanning parameters: $V = -2.8\,\mathrm{V}$, $I = 10\,\mathrm{pA}$, room temperature.

process, which rules out substrates that are not inert to solvent effects.

In the following, it will be shown that NaCl islands grown on Au(111) are affected by ESD when methanol is part of the solution. The deposition of NaCl on Au(111) was performed as described in section 7.2. After preparation, the quality of the NaCl/Au(111) sample was first verified by means of STM. Subsequently, the sample was exposed to the ESD beam over a period of 90 minutes, before the surface was finally checked with STM again. In order to ensure that any effect on the substrate is caused by the solvent alone, the electrospray source was operated with pure methanol.

Figure 8.5 compares STM images measured before and after the ESD process. Before exposure to the ESD beam, NaCl islands with lateral dimensions of around 50–100 nm are observed (Figure 8.5a). As already described in chapter 7.2, the first NaCl double layer forms rectangular islands with an apparent height of ca. 350 nm. The formation of a third layer is observed on a part of the islands. After the ESD process, the condition of the surface is significantly changed. The lateral size of the NaCl islands is strongly reduced to around 5–30 nm. The form of the islands clearly deviates from their original rectangular appearance and their apparent height at identical scanning parameters is almost halved to ca. 180 nm. In addition, the surface roughness of both the islands and the substrate is significantly increased, rendering the Au(111) surface reconstruction almost not visible anymore.

The exact mechanism of the changes observed after the ESD process is not known. However, it appears likely that NaCl gets dissolved when the islands are in contact to the methanol droplets deposited on the surface. After evaporation of the droplets, the dissolved NaCl remains on the surface in a manner which is unorganized compared to the epitaxial growth achieved by thermal sublimation. The example shows that not every substrate is suited for ESD. Limitations imposed by solvent effects generally have to be considered when deposition is performed on highly reactive surfaces. Furthermore, in order to prevent accumulation of solvent

residuals, ESD should not be carried out at sample temperatures that are below the adsorption temperature of the solvent molecules.

9 | Mn_{12} Single Molecule Magnets

The discovery of the mixed-valence manganese complex Mn_{12}-acetate in 1980 [9] and the disclosure of its unique magnetic properties 13 years later [10] have set the starting point of the field of single molecules magnets (SMMs). Although the number of known SMM compounds has grown considerably since then, derivatives of the Mn_{12} family are still in the focus of research. The great interest in this compound originates from several aspects. First, the blocking temperature of Mn_{12} is among the highest in the field of SMMs. Slow relaxation of magnetization and magnetic quantum phenomena are therefore accessible at experimentally available temperatures. Secondly, the material can be synthesized in good yield and with reasonable effort and expense. Purification is possible though the growth of single crystals, which is an essential requirement for many of the performed studies. Finally, Mn_{12} is stable in various solvents. Its organic ligand shell can therefore be easily modified by wet-chemical reaction schemes, which allows to provide the molecule with a rich variety of chemical functionalities.

While most information about Mn_{12} was obtained on poly- and single-crystalline material, the prospect to implement SMMs in future spintronic applications has also led to a large number of studies dealing with the deposition and investigation of Mn_{12} on surfaces. In order to bring the Mn_{12} molecules from bulk to substrate, a variety of different methods was applied. In the most simple case, the substrate was dipped into a solution of an unspecific Mn_{12} derivative and subsequently dried [177], or the solution was drop- or spin cast onto the native surface [178–181]. Alternatively, ligands with functional groups were used to chemisorb Mn_{12} via specific molecule-substrate interactions. In most cases, the strong Au-S bond was utilized to anchor sulfur containing Mn_{12} derivatives to gold surfaces [182–193], although a grafting of Mn_{12} on silicon was demonstrated to be possible as well [194–196]. In other studies, adaptions of the organic ligand shell were applied to tailor the adsorption behavior of Mn_{12} without formation of covalent bonds. As an example, multi-cationic Mn_{12} derivatives were electrostatically bound to surfaces which are functionalized by anionic self-assembled monolayers [204–206]. Furthermore, ligands with hydrophobic groups were used to enable a surface deposition of Mn_{12} via Langmuir-Blodgett films [178, 190, 197], or to influence the wetting behavior of Mn_{12} in microcontact

printing [198,199]. More recently, pulsed valve techniques [200,201] and electrospray ionization [162,202–204] were applied, allowing for a deposition of Mn_{12} in ultra-high vacuum (UHV).

Despite the great efforts that were made to deposit Mn_{12} on surfaces, no evidence was ever provided that the molecules retain their magnetic bistability when being in contact to a substrate. On the contrary, several studies report a loss of magnetic hysteresis in Mn_{12} monolayers [180,190,193,196,205]. The observed change in magnetic behavior was attributed by the authors to the interaction of Mn_{12} with the substrate. However, no systematic studies involving different surfaces were carried out in these cases, mainly because the preparation routines used by the authors were restricted to a deposition on gold or silicon.

Here, we report on the deposition of Mn_{12} on different substrates, using electrospray deposition (ESD) in UHV. In order to address the properties of the deposited molecules, we combine different experimental methods, including scanning tunneling microscopy and spectroscopy (STM/STS), X-ray photoelectron spectroscopy (XPS) and SQUID magnetometry. While our results indicate that the molecules stay structurally intact upon deposition, the electronic properties of Mn_{12} submonolayers on metallic surfaces are found to be significantly changed. Using an ultrathin layer of graphene as growth template is demonstrated to be a promising approach to electronically decouple Mn_{12} from the influence of the underlying substrate.

Some of the results presented in this chapter were obtained with the help of Sebastian Höll, Eva-Sophie Wilhelm and Nicole Barth as a part of their master theses [206–208].

9.1 Introduction to the Properties of Mn_{12}

Molecular Structure of Mn_{12}-ac

The molecular structure of the archetypical Mn_{12}-acetate cluster (in the following abbreviated Mn_{12}-ac) is shown in Figure 9.1a. The actual formula of the compound is $[Mn_{12}O_{12}(CH_3COO)_{16}(H_2O)_4] \cdot 2\,CH_3COOH \cdot 4\,H_2O$. Chemical synthesis and X-ray structure determination were first reported by Lis in 1980 [9].

The molecule has S_4 symmetry and crystallizes in the tetragonal space group $I\bar{4}$. It comprises an inner $Mn_{12}O_{12}$ core, which is surrounded by 16 acetate and four H_2O ligands. The twelve manganese ions are arranged in an inner tetrahedron of four ions in oxidation state +IV and an outer ring of eight ions in oxidation state +III. Each manganese ion is bound to six oxygens in octahedral coordination. The octahedral symmetry of the manganese(III) ions is distorted due to Jahn-Teller elongation.

The acetic acid molecules of crystallization are attached to the Mn_{12} cluster via hydrogen-bonds with the acetate and water ligands [19]. Since the attribution of the

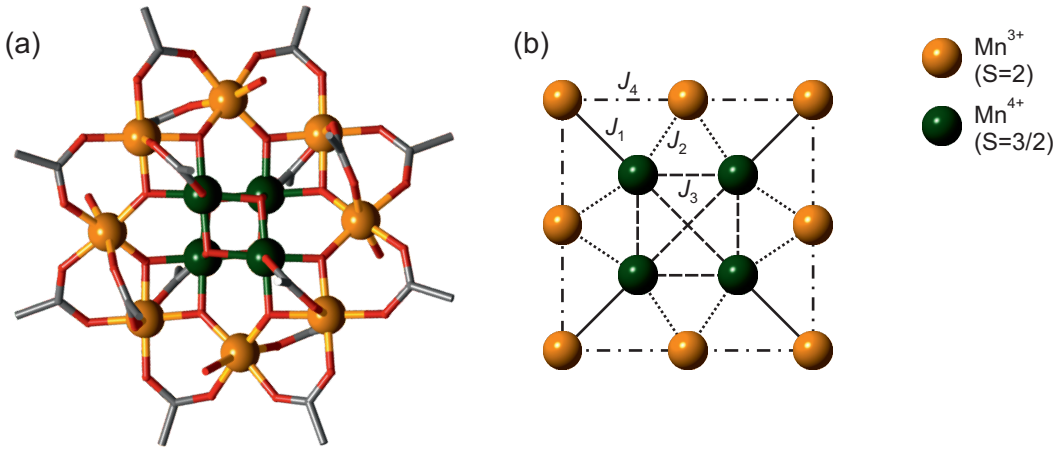

Figure 9.1 | **(a)** Molecular structure of Mn_{12}-ac. Color code: C = grey, O = red, Mn according to legend. Hydrogen atoms and solvent molecules of crystallization are omitted for clarity. Acquisition of X-ray diffraction data by Peter Schmitt. **(b)** Schematic representation of the exchange interaction between the twelve manganese spin centers.

acetic acid molecules to the adjacent Mn_{12} clusters is statistically distributed, most Mn_{12} clusters present in the crystal exhibit a local symmetry which is lower than fourfold. As already discussed in chapter 1.3, this finding has important implications for the magnetic quantum behavior.

Magnetic Properties of Mn_{12}-ac

Temperature dependent dc susceptibility and high field magnetization studies demonstrate a ferrimagnetic behavior with a ground spin state of $S = 10$ [209]. The ground spin state is easiest explained by assuming that the spins of the inner manganese(IV) tetrahedron are polarized antiparallel to the outer manganese(III) ring. Neutron diffraction experiments [210] and density functional theory calculations [211, 212] confirm this picture.

Magnetization measurements on Mn_{12}-ac single crystals provide evidence of a strong magnetic anisotropy with an easy axis parallel to the crystal c axis [19]. Theoretical calculations show that the main contribution to the magnetic anisotropy comes from the Jahn-Teller distortion of the manganese(III) ions. Other effects, such as intramolecular dipol interactions and anisotropic exchange, only play a minor role [19]. The first order magnetic anisotropy constant was calculated from EPR spectra to be $D = -0.47\,\mathrm{cm}^{-1}$ [213], corresponding to an anisotropy barrier of $\Delta E = |D|S^2 = 47\,\mathrm{cm}^{-1}$. Estimations of the effective barrier height from temperature dependent relaxation time measurements yield a slightly smaller value of $44.5\,\mathrm{cm}^{-1}$ [214], due to a bypassing of the topmost spin states in the relaxation process (see chapter 1.3).

At temperatures below 4 K, the relaxation time of the magnetization becomes long enough to induce an opening of a hysteresis loop [10]. Steps in the hysteresis curve at characteristic magnetic field values indicate quantum tunneling of magnetization (QTM) [6, 7]. Hysteresis and QTM in Mn_{12}-ac will be discussed in more detail in section 9.2.

For a calculation of the complete spin spectrum of Mn_{12}-ac, the exchange coupling between all twelve manganese ions must be taken into account. Considering the molecular symmetry, the number of different coupling constants is reduced to four (Figure 9.1b). Even though a reliable prediction of the coupling constants is difficult due to the high complexity of the system, consensus is reached that the values of J_1 and J_2 are both negative, indicating a strong antiferromagnetic exchange between the manganese(III) and manganese(IV) ions [19].

The Mn_{12} Family

The stability of the Mn_{12} cluster in organic solvents allows for a modification of its organic ligand shell by means of solution-based chemical reaction schemes. Compounds of general formula $[Mn_{12}O_{12}(R_1COO)_{16}(R_2OH)_x] \cdot Y$ are synthesized by substituting all 16 acetate ligands with other carboxylates, where Y denotes solvent molecules of crystallization. Mixed-ligand derivatives can be synthesized as well via am partial exchange of the axial and equatorial ligand sites [215]. Furthermore, variations of the carboxylate theme by incorporation of nitrate [216], phosphinate [217] and sulfonate ligands [218] are possible.

Notably, not every Mn_{12} derivative is characterized by an $S = 10$ ground state [219]. The possibility to modify the organic ligand shell, however, is most interesting with respect to the interaction of Mn_{12} with its surrounding, rather than because of the change of its intrinsic magnetic properties. As already mentioned before, ligands with additional functional groups have been extensively used to chemisorb Mn_{12} derivatives on different surfaces.

9.2 Synthesis and Characterization of the Mn_{12} Bulk Material

Two different Mn_{12} derivatives have been used for the deposition experiments presented in this work: Mn_{12}-ac and Mn_{12}-parafluorobenzoate (Mn_{12}-pfb), the latter one being introduced later in section 9.3. The chemical synthesis was performed by M. Burgert and S. Ambrus in the group of Prof. U. Groth (Department of Chemistry, University of Konstanz) and is described in their doctoral theses [220, 221]. In the following, we present a brief characterization of the Mn_{12}-ac bulk material, as it was used for most of the performed measurements.

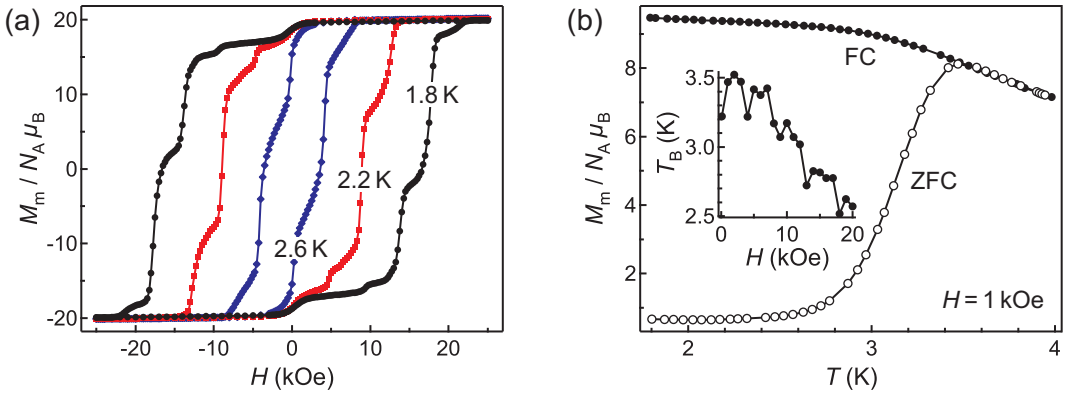

Figure 9.2 | SQUID magnetometry of an Mn_{12}-ac single crystal. Orientation of the magnetic field parallel to the crystal c axis. **(a)** Isothermal magnetization curves at 1.8, 2.2 and 2.6 K (field sweep rate $dH/dt = 0.12$ kOe/min). **(b)** Temperature dependence of the magnetization in a field of 1 kOe. Both zero-field-cooled (ZFC) and field-cooled (FC) curves are shown. Inset: Magnetic field dependence of the blocking temperature T_B as estimated from ZFC-FC curves up to $H = 20$ kOe.

9.2.1 SQUID Magnetometry

The DC magnetic properties of Mn_{12}-ac have already been reported in the 1990's [6, 7, 10] and are well understood. SQUID measurements were therefore utilized in the first place to verify the purity of the synthesized of Mn_{12}-ac bulk material. The results presented here were obtained on a single crystal with a mass of (0.8 ± 0.1) mg, which was glued to a plastic straw with its tetragonal axis oriented parallel to the external magnetic field. The diamagnetic background signal of the sample holder was corrected by subtracting a reference measurement and the diamagnetic contribution of Mn_{12}-ac was corrected based on an estimation of the susceptibility from Pascal's constants.

Figure 9.2a shows isothermal magnetization curves recorded at different temperatures between 1.8 and 2.6 K. Based on the weighed crystal mass, the saturation moment per molecule is $(18.6 \pm 2.3)\,\mu_B$, which is in agreement with an $S = 10$ ground state. The curves plotted in Figure 9.2 were renormalized in order to match the expected saturation moment of $20\,\mu_B$ per molecule.

The observed shape of the hysteresis loop is typical for Mn_{12}-ac in the regime of thermally assisted quantum tunneling of magnetization (QTM). On the one hand, the coercivity of Mn_{12}-ac increases as the temperature is decreased. This behavior can be explained by the slowdown of thermal excitation processes and is generally observed in superparamagnetic particles. On the other hand, the hysteresis loop comprises distinct steps at characteristic magnetic field values. Such steps are a fingerprint of QTM at level crossings and have been first reported for Mn_{12}-ac in [6, 7].

According to equation (1.13), the separation of the steps in the hysteresis loop

is proportional to the anisotropy constant D in first order approximation and is therefore a characteristic property of the Mn_{12}-ac compound. From the extrema of the derivatives $\mathrm{d}M/\mathrm{d}H$ of the magnetization curves, we measured an average separation of $\mu_0 \Delta H = (0.44 \pm 0.02)\,\mathrm{T}$. This value is in perfect agreement with the value of 0.44 T reported in [6].

In addition to the magnetization curves, we performed a measurement of the magnetic moment as a function of the temperature in constant magnetic field. Figure 9.2b shows zero-field-cooled (ZFC) and field-cooled (FC) curves obtained in the range of 1.8–4 K. The curves were recorded by first cooling the sample in zero field and measuring the magnetization at increasing temperature in a field of 1 kOe (ZFC) and then measuring the magnetization in the same field at decreasing temperature (FC). Both curves clearly diverge at low temperature, demonstrating that the magnetization dynamics become 'frozen' on the timescale of the experiment.

The blocking temperature T_B can be deduced from the measurement by estimating the local maximum of the ZFC curve. The inset of Figure 9.2b shows T_B as a function of the external magnetic field H. As H increases, the values of T_B oscillates with minima appearing at multiples of around 0.44 T. This peculiar behavior reflects the decrease in magnetic relaxation time at level crossings and is therefore another fingerprint of thermally assisted QTM.

9.2.2 ESI Mass Spectrometry

ESI mass spectrometry not only allows to study the chemical composition of the Mn_{12}-ac bulk material, but also gives insight into possible fragmentation processes that can occur during a deposition of the compound via ESD (since both procedures rely on electrospray ionization). The mass spectra presented here were recorded from a 1×10^{-4} M solution of Mn_{12}-ac in acetonitrile. The spectrometer was operated in positive ion mode at a source temperature of 150 °C.

The result of the measurement is shown in Figure 9.3. The mass spectrum exhibits five intense peaks, which are related to the cluster $Mn_{12}O_{12}(CH_3COO)_{16}$ (in the following abbreviated as M). According to the measurement, gas phase ions from Mn_{12}-ac in solution are most likely created by adduct formation with Na^+ ($[M + Na]^+$, 1818.9 Th). To a smaller extend, also the K^+ adduct ($[M + K]^+$, 1835.1 Th) is observed. Alternatively, the cluster can gain a positive charge by losing a single acetate ligand ($[M - Ac]^+$, 1736.9 Th).

A remarkable observation is that up to two of the 16 acetate ligands are replaced by formate ($HCOO^-$). The peaks of the corresponding Na^+ adducts are shifted to smaller m/z values by the respective mass of a CH_2 group ($[M - Ac + Fo + Na]^+$, 1804.9 Th and $[M - 2Ac + 2Fo + Na]^+$, 1790.9 Th). Formate is a common contamination in ESI-MS, since formic acid is a widely used additive. The occurrence of these peaks demonstrates how easily the Mn_{12} cluster can undergo a ligand exchange with

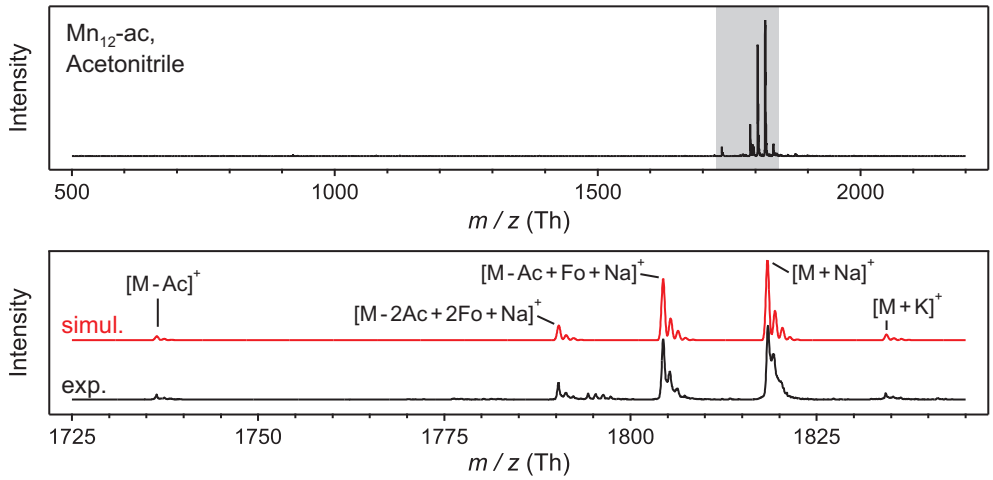

Figure 9.3 | Positive ion ESI-MS spectrum of Mn_{12}-ac from an acetonitrile solution. Top panel: Complete mass-to-charge range. Bottom panel: Detailed view of the mass-to-charge range that is marked by a grey background. The measured curve (black) is compared to a simulation of the isotopic pattern of the labeled ions (red). The peak series at $\sim$ 1795 Th does not match the isotope distribution of Mn_{12} and is therefore probably not related to the Mn_{12}-ac cluster.

other carboxylic acids. However, since no acid additives are used in the ESD setup, such ligand exchange reactions are not expected to take place in the deposition experiments.

In conclusion, ESI-MS proofs that intact Mn_{12} gas phase ions can be created by means of electrospray ionization. Fragmentation of the cluster can occur via loss of acetate ligands. While the number of absent ligands does not exceed one in the spectra shown here, ESI-MS measurements performed on another mass spectrometer in collaboration with S. Höll have shown that a loss of multiple ligands, associated with a breakup of the $Mn_{12}O_{12}$ core, is possible as well [206].

9.3 Preliminary Work: Deposition via Ligand Exchange

Preliminary experiments on Mn_{12} monolayers were carried out using a wet-chemical preparation routine, in which Mn_{12} is grafted on Au(111) by means of functional thiol groups in the carboxylate ligands. Since the Mn_{12} core is oxidatively unstable in the presence of free thiols, ligand exchange in solution prior to the deposition cannot be performed in a direct manner[1]. The sample preparation is therefore realized in a two step process, following a preparation protocol that was originally introduced by Voss *et al.* in 2006 [222,223]. First, the Au(111) surface is covered by a monolayer of thiol-carboxylate linkers, which are forming a strong bond to the gold surface via the sulfur atom of the thiol group. Subsequently, the Mn_{12} molecules are attached to the

[1]Synthesis of Mn_{12} derivatives that include thiol groups is possible by using acetyl-protected thiols for the ligand exchange and deprotecting the thiol group afterwards [182].

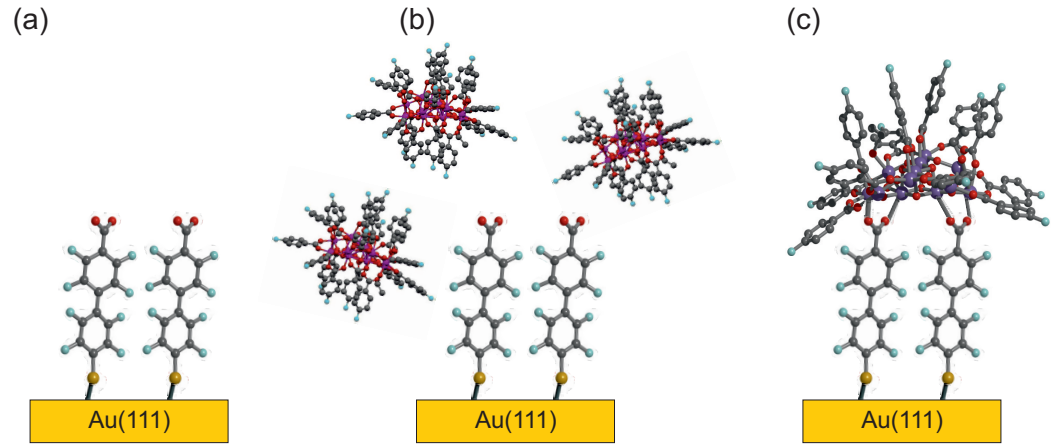

Figure 9.4 | Schematic illustration of the preparation process used for a wet-chemical grafting of Mn_{12}. **(a)** Functionalization of Au(111) with a layer of 4-MOBCA linkers. **(b)** Immersion of the functionalized surface in a solution of Mn_{12}-pfb. **(c)** Binding of Mn_{12}-pfb to Au(111) via ligand exchange with the 4-MOBCA linkers. Images by M. Fonin, S. Voss and M. Burgert.

prefunctionalized surface in a ligand exchange reaction, according to the following equation:

$$(Au_{sur}\text{–}S\text{–}R_3\text{–}COOH)_n + Mn_{12}O_{12}(R_1COO)_{16}(R_2OH)_x \longrightarrow$$
$$(Au_{sur}\text{–}S\text{–}R_3\text{–}COO)_n\text{–}Mn_{12}O_{12}(R_1COO)_{16-n}(R_2OH)_x + n \cdot R_1COOH.$$

Sample Preparation

Clean Au(111) surfaces were prepared as described in chapter 7.1. For the experiments presented here, the Au surface was prefunctionalized by immersing the gold single crystal in a 2 mM solution of 4′-mercapto-octafluorobiphenyl-4-carboxylic acid (4-MOBCA) in ethanol for 5–10 min. After removing the crystal from solution, the surface was rinsed with ethanol and dried in nitrogen gas. Deposition of Mn_{12} was then performed by dipping the functionalized surface in a 3×10^{-5} M solution of $Mn_{12}O_{12}(C_6H_4FCOO)_{16}(EtOH)_4$ (Mn_{12}-pfb) in dichloromethane (DCM) for 6 min. Finally, the surface was rinsed with DCM, dried in nitrogen atmosphere and introduced into the UHV chamber. The preparation process is schematically illustrated in Figure 9.4.

Results and Discussion

In order to validate the deposition process, STM measurements were performed both before and after immersing the prefunctionalized Au crystal in the Mn_{12}-pfb solution. After deposition of Mn_{12}, STM images reveal a homogeneous distribution of elliptically shaped objects that are separated by 2–3 nm (Figure 9.5c). In contrast,

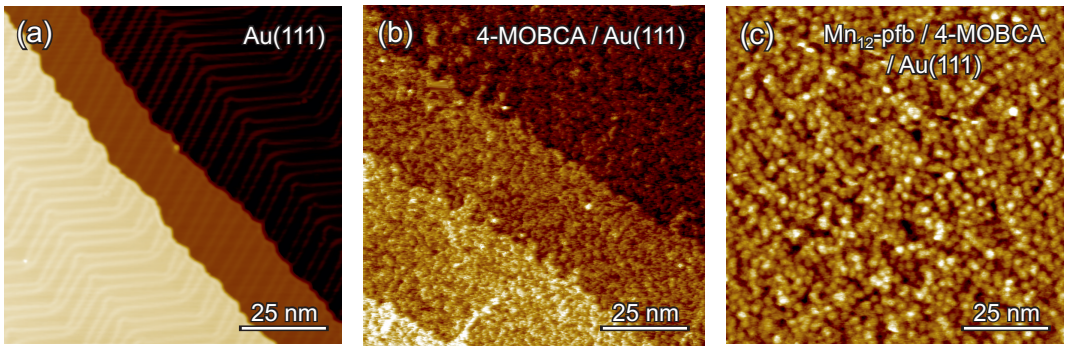

Figure 9.5 | STM images obtained on **(a)** the clean Au(111) substrate before deposition, **(b)** the 4-MOBCA functionalization layer and **(c)** the Mn_{12}-pfb monolayer. Scanning parameters: (a) $V = 0.5\,\mathrm{V}$, $I = 1\,\mathrm{nA}$, $T = 9\,\mathrm{K}$, (b) $V = 2\,\mathrm{V}$, $I = 20\,\mathrm{pA}$, room temperature, (c) $V = 3\,\mathrm{V}$, $I = 10\,\mathrm{pA}$, $T = 12\,\mathrm{K}$.

no objects of comparable size and shape were found on the prefunctionalized surface prior to Mn_{12} deposition (Figure 9.5b), or after immersion of the Au single crystal in pure solvents. The clusters are therefore attributed to the individual Mn_{12}-pfb molecules. No signs of fragmentation, such as significantly smaller objects or larger accumulations of material, are evident from the STM measurements.

Insight into the chemical composition of the Mn_{12}-pfb monolayer is provided by X-ray photoelectron spectroscopy. Figure 9.6a shows an XPS overview spectrum for binding energies in the range of 0–1000 eV. The measurement demonstrates that all elements expected to be observed in the system are present on the sample surface. Specifically, these are Au (from the substrate), C and O (from 4-MOBCA, Mn_{12}-pfb and organic impurities), F (from 4-MOBCA and Mn_{12}-pfb) and Mn (from Mn_{12}-pfb). The S atom of the 4-MOBCA linker is not resolved in the overview spectrum, due to the low abundance and the small photoelectron cross section [192]. Peaks labeled as *s.p.* arise from Mo and Ta contributions that are present in the sample plate.

The observation of strong Au peaks in the XPS overview indicates that the substrate is covered only by a relatively small amount of material. An inhomogeneous coverage of the sample, i.e. the occurrence of native Au(111) areas, can be excluded based on the STM measurements. Therefore, the XPS data support the assumption that only a single layer of Mn_{12} is formed during the preparation process.

High resolution measurements of the C 1s, F 1s and Mn 2p core level spectra are shown in Figure 9.6b–d. The C 1s spectrum comprises a complex structure, which is caused by a superposition of peaks from C atoms with different chemical environments. The individual contributions are ascribed to the phenyl rings and aliphatic carbon atoms (284.7 eV [119]), C−S species (286.0 eV [191]), C−OH species (286.4 eV [224]), carboxylate groups (288.6 eV [191]) and fluorinated carbon atoms (288.7 eV [119]). Adventitious carbon contaminations from the atmosphere are ex-

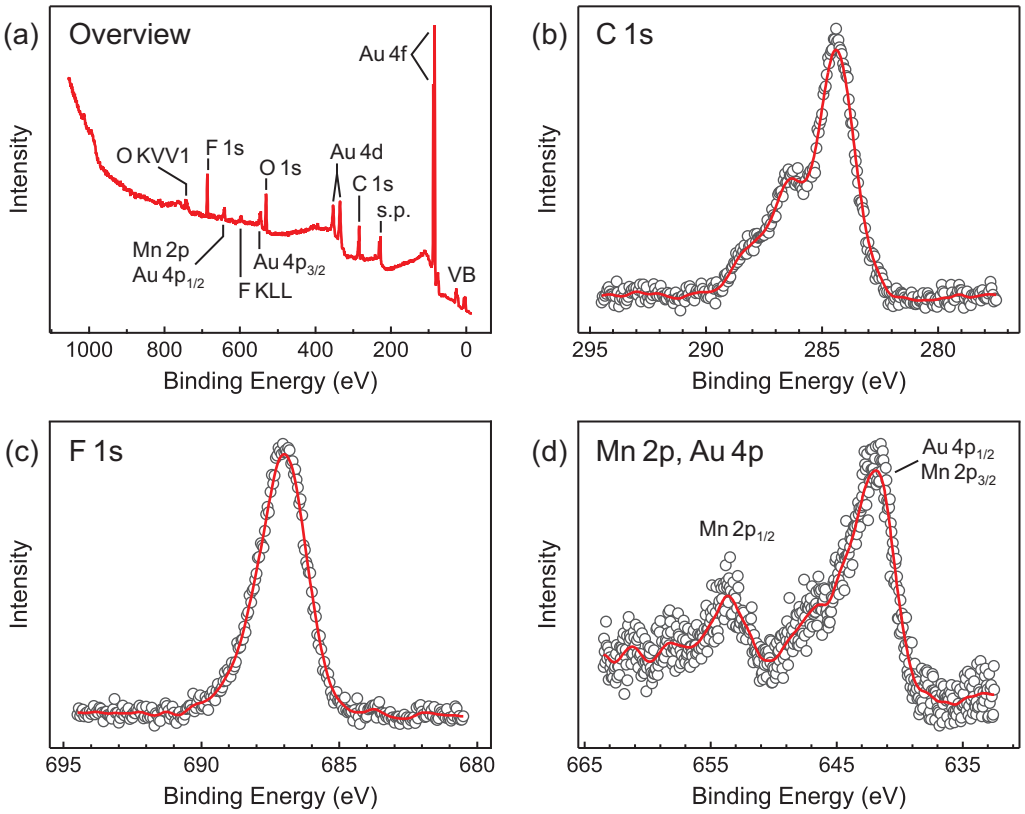

Figure 9.6 | XPS spectra (Mg K_α) obtained on Mn_{12}-pfb/4-MOBCA/Au(111). **(a)** Overview spectrum. **(b–d)** High resolution spectra of the C 1s, F 1s and Mn 2p core level contributions.

pected to contribute to the 284.7 eV peak. In contrast, the F 1s spectrum comprises a single peak structure, confirming the identical chemical environment of all F atoms in the 4-MOBCA linkers and Mn_{12}-pfb ligands. The spectral shape of the Mn 2p level is not discussed here, since a quantitative analysis is hampered by an overlap with the Au $4p_{1/2}$ peak.

In conclusion, both the STM and XPS measurements are in good agreement with previously published results [188, 223], demonstrating that the preparation routine of Voss *et al.* was successfully reproduced. It was originally planned to extend the available STM, XPS and XAS investigations by low temperature and magnetic field dependent STS measurements on individual Mn_{12}-pfb molecules. However, this goal turned out to be extremely challenging for several reasons. Since the deposition is performed *ex situ*, impurities on the sample surface result in frequent changes of the tip state during the measurement. Treating the tip after such contamination is difficult, since common procedures, such as application of voltage pulses or moderate ramping of the tip into the substrate, are hampered by the absence of clean metal spots. Furthermore, a characterization of the tip state via reference measurements on the metallic substrate is prevented the full monolayer coverage as well.

Because of the mentioned disadvantages, it was decided to change the preparation routine from wet-chemical grafting to electrospray deposition (ESD). The results obtained by means of ESD are described in the following section.

9.4 Study of Mn_{12}-ac Submonolayers and Individual Molecules

The implementation of a setup for electrospray deposition (see chapter 6) paved the way for an investigation of surface-supported Mn_{12} molecules without suffering from the disadvantages of wet-chemical preparation schemes. Since the deposition is performed *in situ*, samples prepared by ESD contain only a small number of impurities. The surface coverage can be easily controlled within the submonolayer regime by adjusting the deposition time. Furthermore, since ESD does not rely on specific molecule-substrate interactions, both the Mn_{12} derivative and the substrate can be freely chosen.

In the following, we present a study of Mn_{12}-ac submonolayers and individual molecules that were deposited by means of ESD. The molecules are studied on four different surfaces: Au(111), Ag(111), Cu(111) and graphene/Ir(111). The first substrate, Au(111), is used as a test bed for the deposition. STM and XPS data obtained on Mn_{12}-ac/Au(111) have already been published by two other groups [162,202,203], so that a reference for our measurements is available. As an extension of these studies, we provide the first observation of elastic charge transport though individual Mn_{12}-ac molecules on the Au(111) surface. Ag(111) was mainly utilized to address the electronic properties of the molecules via XPS. Unlike Au(111), the Ag surface allows for a measurement of the manganese XPS core level spectra, which provide direct information on the manganese oxidation state. The deposition of Mn_{12}-ac on Cu(111) is only briefly described in this chapter, since we observed a decomposition of the molecules on this surface. Finally, the intention of using a monatomic layer of graphene on Ir(111) was to electronically decouple the Mn_{12}-ac molecules from the influence of the metallic support.

9.4.1 Sample Preparation

Clean and atomically flat substrate surfaces were prepared as described in chapters 7.1 and 7.3. Mn_{12}-ac was deposited *in situ* via ESD in UHV from 2–6 $\times$ 10^{-5} M solutions of the compound in pure methanol. During the deposition, the sample was kept at room temperature. For STM/STS measurements, ion charges in the range of 20–30 pAh were deposited. For XPS studies, higher ion charges in the range of 35–133 pAh were accumulated by using longer deposition times in order to increase the signal to noise ratio.

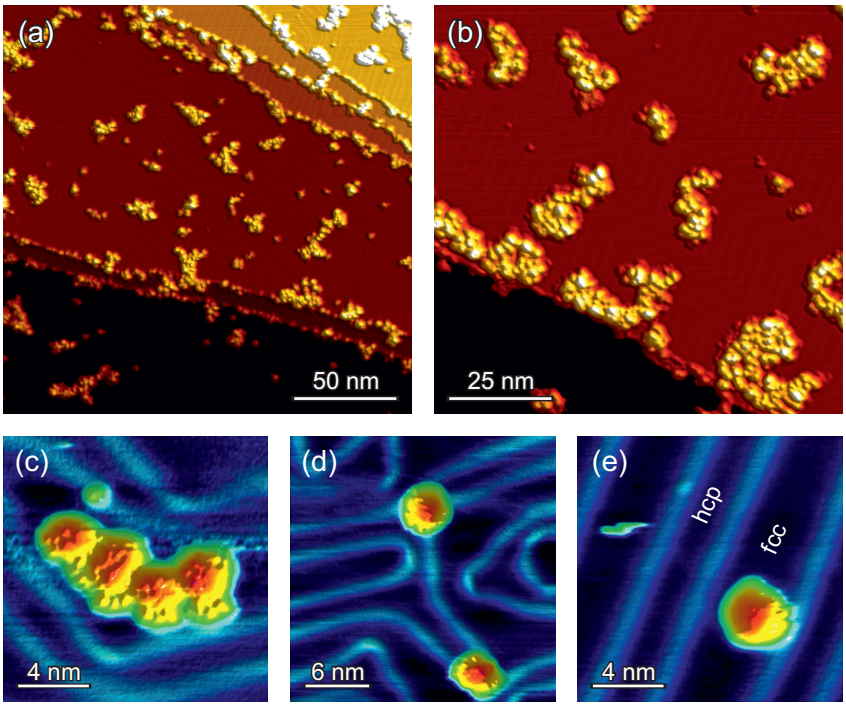

Figure 9.7 | STM images of Mn_{12}-ac on Au(111), showing aggregation to **(a,b)** islands, **(c)** chain-like structures, as well as **(d,e)** individual molecules. Scanning parameters: (a,d) $I = 20\,\text{pA}$, $T = 10\,\text{K}$, (b) $I = 10\,\text{pA}$, $T = 10\,\text{K}$, (c) $I = 40\,\text{pA}$, $T = 11\,\text{K}$, (e) $I = 20\,\text{pA}$, $T = 3.5\,\text{K}$. All measurements at $V = 2.5\,\text{V}$.

9.4.2 STM Imaging

Mn_{12}-ac on Au(111) and Ag(111)

STM images of Mn_{12}-ac on Au(111) and Ag(111) are depicted in Figure 9.7 and 9.8, respectively. The molecules appear as elliptically shaped objects with a voltage dependent apparent height of 400–700 pm. From the large scale images (Figure 9.7a,b and 9.8a), it is evident that the majority of the molecules is present on the surface in form of small aggregations and two-dimensional, unordered islands. However, individual molecules are observed on the surface as well (Figure 9.7d,e). On Au(111), we find that isolated clusters preferably occupy the elbow and fcc sites of the herringbone reconstruction.

The growth behavior of Mn_{12}-ac on Au(111) was subject to some controversy in recently published works. Using ESD as deposition method, Saywell *et al.* [202] report on unordered molecular assemblies similar to the aggregations and two-dimensional islands observed in our measurements. The herringbone reconstruction of the Au(111) surface was neither evident in the presented STM images, nor did it influence the adsorption of the molecules. In contrast, deposition of mass selected Mn_{12}-ac clusters via ES-IBD by Kahle *et al.* [162] clearly resulted in a preferred adsorption of Mn_{12}-ac on elbow and fcc sites and, resulting from this, in an observation

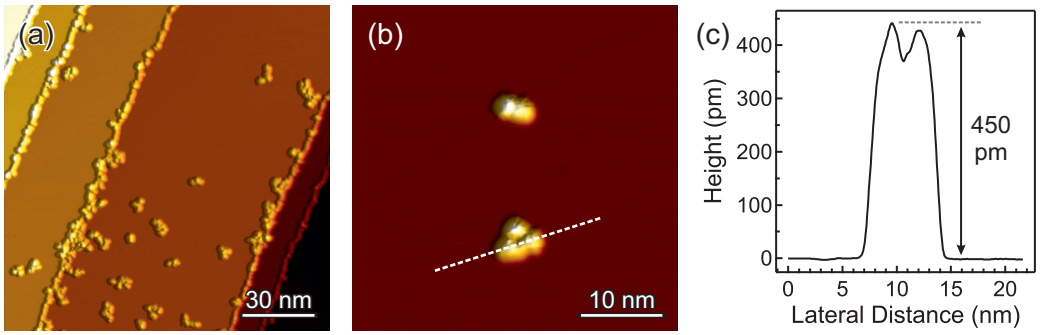

Figure 9.8 | **Mn_{12}-ac on Ag(111). (a)** Large scale STM image. **(b)** Detailed view of a molecular dimer and trimer. **(c)** Height profile along the dashed line in (b). Scanning parameters: $V = 2.5\,\mathrm{V}$, $I = 100\,\mathrm{pA}$, $T = 11\,\mathrm{K}$.

of isolated molecules at low coverage.

The different results were explained in [162] by a possible contamination of the Au(111) surface in the experiment of Saywell *et al.*. To support this argument, the authors pointed out that a contamination is indicated by the absence of the herringbone reconstruction in the data presented in [202]. However, this explanation does not apply to our measurements, as the herringbone reconstruction is clearly visible in our STM images. Instead, in our opinion, the different growth behavior is most likely related to the inherent properties of the different deposition methods. As it was discussed in chapter 6.2.2, sub-μm sized droplets containing at least some ten molecules in average are created in ESD. The unordered agglomerations observed by Saywell *et al.* and in our measurement therefore probably result from the solid residues that remain on the surface after evaporation of the deposited droplets. Apparently, a subsequent rearrangement of Mn_{12}-ac to energetically favored substrate sites is hindered by attractive intermolecular interactions. In contrast, Mn_{12}-ac is deposited as gas phase ions in ES-IBD, which explains the occurrence of individual molecules in the measurements of Kahle *et al.*.

The observation of individual molecules in addition to the molecular assemblies in our STM measurements can be well explained by taking into account the droplet size distribution created by the ESD setup. Although larger droplets account for the majority of the deposited material, a small number of molecules is expected to reach the surface either as gas phase ions or in form of droplets that contain only a single molecule. For such molecules, the same adsorption behavior as in ES-IBD is expected, which explains our finding that isolated molecules are trapped at the elbow and fcc sites of the herringbone reconstruction.

It was pointed out by Saywell *et al.* [202] that the elliptical cross section of the molecules in the STM topography can be linked to their rotational orientation, owing to the oblate geometry of the Mn_{12}-ac compound. This aspect is illustrated in Figure 9.9a. When projected on a plane perpendicular to the magnetic easy-axis,

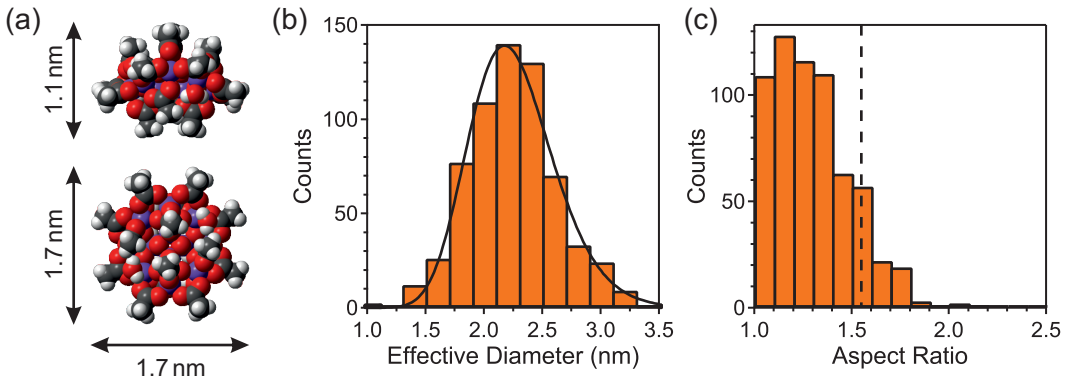

Figure 9.9 | **(a)** Space-filling model and lateral dimensions of Mn_{12}-ac. **(b,c)** Distribution of the effective diameter and aspect ratio of Mn_{12}-ac from STM images, based on a statistical analysis of 631 molecules on Au(111). The solid curve is a fit of the effective diameter with a log-normal distribution. The theoretical maximum of the aspect ratio of 1.55 is marked by a dashed line.

Mn_{12}-ac exhibits a circular cross section of around 1.7 nm diameter. In contrast, the height of the molecule measured along the easy-axis is only 1.1 nm.

In order to obtain quantitative information of the rotational orientation, we performed a statistical analysis of the major and minor semi-axes a and b of Mn_{12}-ac on Au(111), taking into account a total number of 631 molecules. The distributions of the effective diameter $2\sqrt{ab}$ and the aspect ratio a/b are shown in Figure 9.9b,c. Fitting the effective diameter with a log-normal distribution yields a mean of (2.2 ± 0.4) nm. The slightly larger value compared to the structural size of Mn_{12}-ac can be attributed to a broadening of the images due to the finite radius of the STM tip. As can be seen from Figure 9.9c, the abundance of the aspect ratio is almost constant for small a/b values and drops to zero around the theoretical maximum of $a/b = 1.7/1.1 \approx 1.55$. This indicates a random orientation of the Mn_{12}-ac molecules on the Au(111) surface.

Mn_{12}-ac on Graphene/Ir(111)

Figure 9.10 shows STM images of Mn_{12}-ac deposited on graphene/Ir(111). Depending on the voltage and tip state, the apparent height of the molecules is in the range of 300–700 pm, close to the values obtained on metallic surfaces. As already observed on Au(111) and Ag(111), most molecules are arranged in unordered islands that grow over step edges in a carpet-like manner (Figure 9.10a,b). However, a small number of molecules is found to either decorate the step edges, or to be organized in two-dimensional, periodic structures (Figure 9.10c–f). Compared to Au(111) and Ag(111), the observation of molecular self-assembly clearly indicates a decrease in molecule-substrate interaction.

The lattice parameters of the periodic assemblies were measured on a total

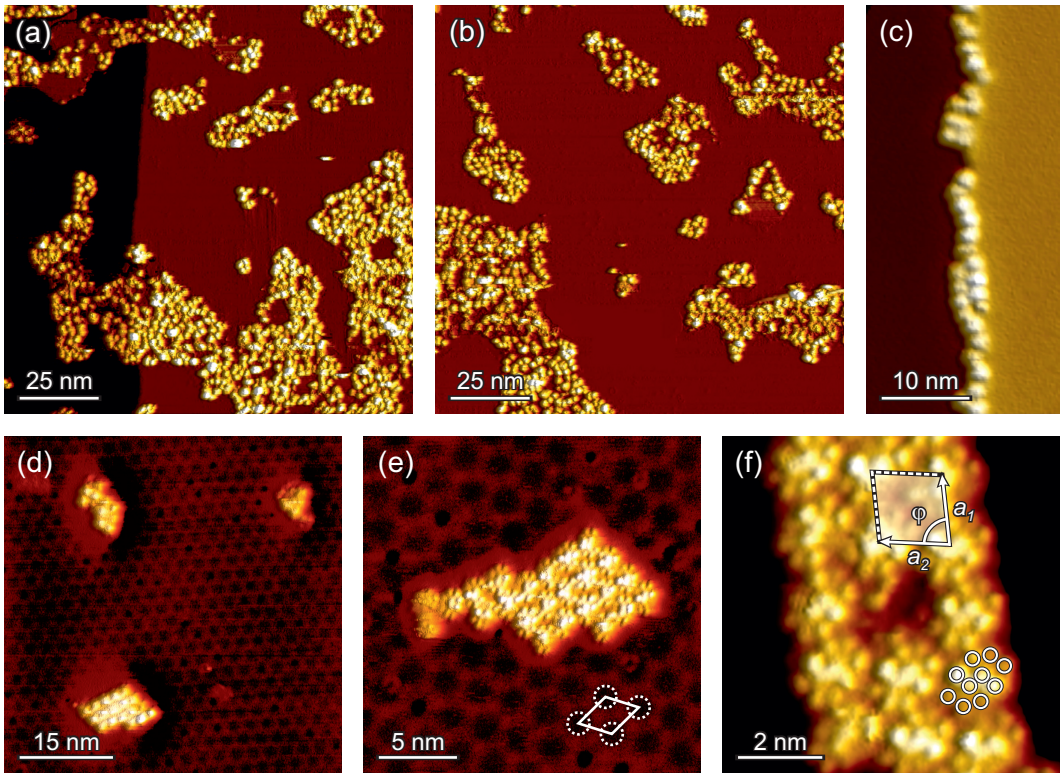

Figure 9.10 | STM measurements of Mn_{12}-ac on graphene/Ir(111). (a,b) Aggregation of molecules to unordered islands. **(c)** Adsorption of molecules at an Ir step edge. **(d-f)** Organization of molecules in periodic structures. The moiré unit cell of the underlying graphene layer is indicated in (e). Circles in (f) highlight the apparent intramolecular structure. Scanning parameters: (a,b) $V = 2.5\,\mathrm{V}$, $I = 500\,\mathrm{pA}$, $T = 21\,\mathrm{K}$, (c,d) $V = 2.5\,\mathrm{V}$, $I = 7\,\mathrm{pA}$, $T = 5.2\,\mathrm{K}$, (e,f) $V = 2.3\,\mathrm{V}$, $I = 10\,\mathrm{pA}$, $T = 9.9\,\mathrm{K}$.

number of 18 different islands, yielding average values of $a_1 = (1.75 \pm 0.07)\,\mathrm{nm}$, $a_2 = (1.84 \pm 0.08)\,\mathrm{nm}$ and $\varphi = (77 \pm 4)°$. As evident from Figure 9.10d,e, the internal structure of the islands and the moiré superstructure of the underlying graphene layer can be imaged simultaneously. No correlation was found between the position of the molecules and the moiré unit cell.

Further information on the orientation of the molecules within the periodic assemblies is provided by high resolution STM images. A clear intramolecular structure could be resolved in several measurements, comprising up to 10 protrusions which are assigned to the individual acetate units of the organic ligand shell (Figure 9.10f). The overall shape of the molecule is elliptical with an aspect ratio of 1.38 ± 0.02.

While the role of the aspect ratio was already discussed in the previous section, the relation between the number of imaged acetate ligands and the orientation of the molecules is best illustrated in Figure 9.9a. When Mn_{12}-ac is viewed along the magnetic easy axis, 12 acetate ligands are visible at the same time. In contrast, only 10 ligands point towards the spectator when the molecule is imaged perpendicular

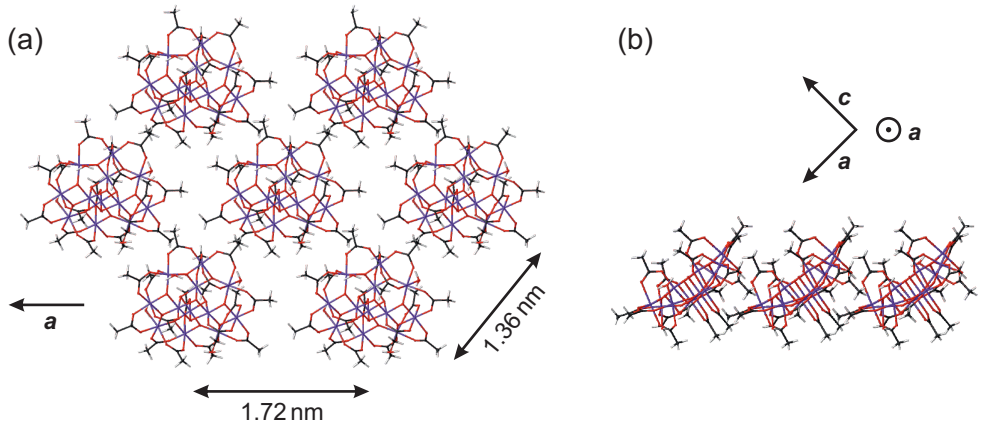

Figure 9.11 | Arrangement of Mn_{12}-ac molecules in crystalline bulk material. (a) View along the surface normal of the crystallographic (101) plane. **(b)** The same plane viewed perpendicular to the surface normal. Arrows indicate the orientation of the tetragonal a and c axes.

to the easy axis. Therefore, both the aspect ratio and the number of visible protrusions indicate that the molecules are sitting slantwise on the surface, i.e. the easy axis is rotated out of the surface normal. Since such an arrangement increases the contact area between adjacent molecules, but decreases the contact area between the molecules and the substrate, it becomes obvious that intermolecular van-der-Waals interactions play an important role for the surface self-assembly.

We note that the periodic structure observed on the surface does not reflect the intrinsic arrangement of the molecules in crystalline material. A comparison with the bulk is particularly interesting for the crystallographic planes of high molecular packing density. Since Mn_{12}-ac crystallizes in a body-centered tetragonal lattice, the highest density planes are the crystallographic (101) planes. The molecular arrangement in the (101) plane, as derived from X-ray diffraction measurements, is depicted in Figure 9.11.

Surface-Induced Dissociation of Mn_{12}-ac on Cu(111)

STM measurements performed after deposition of Mn_{12}-ac on Cu(111) reveal a significantly different picture compared to the substrates reported so far. Equally sized clusters with lateral dimensions in the range of 2–3 nm, as they were present on Au(111), Ag(111) and graphene/Ir(111), could not be observed on any of the prepared samples. Instead, the surface comprises islands of three different types, which can be clearly distinguished from each other by their shape, apparent height and inner structure (Figure 9.12a).

Objects resembling molecular entities could only be resolved in one of the three structures, which is labeled as ‘type 1’ in Figure 9.12a. High resolution STM images show that the units are arranged on a hexagonal lattice with a periodicity of

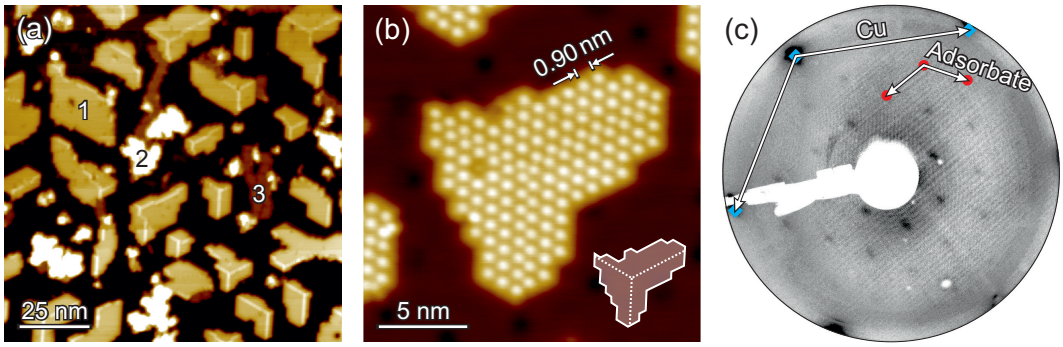

Figure 9.12 | Decomposition of Mn_{12}-ac after deposition on Cu(111). (a) Large scale STM image showing growth of three different types of structures, labeled as 1 to 3. **(b)** Detailed view of an island of type 1. The island comprises three different translational domains, whose positions are marked in the inset. Domain walls are clearly visible in (a) as bright lines on the islands of type 1. Note that almost every island exhibits a point at which three translational domains come together, indicating that these points are nucleation centers for the island growth. **(c)** LEED pattern of the surface measured at 40.2 eV. Scanning parameters: (a) $V = 2.5\,\mathrm{V}$, $I = 20\,\mathrm{pA}$, $T = 4.4\,\mathrm{K}$, (b) $V = -0.5\,\mathrm{V}$, $I = 500\,\mathrm{pA}$, $T = 4.0\,\mathrm{K}$.

(0.90 ± 0.02) nm (Figure 9.12b). LEED measurements further demonstrate that the objects form a commensurate $(2\sqrt{3} \times 2\sqrt{3})\mathrm{R}30°$ superstructure with respect to the underlying Cu(111) surface (Figure 9.12c). Based on the known lattice constant of copper, the periodicity of the superstructure, as derived from the LEED pattern, is 0.885 nm, which is in agreement with the STM measurements.

Notably, the periodicity is significantly smaller than the structural size of Mn_{12}-ac. The measurements therefore indicate that no intact Mn_{12}-ac molecules are present on the Cu(111) surface after electrospray deposition. Since the sample preparation was performed using identical deposition parameters for all substrates, we assume that the dissociation of Mn_{12}-ac is induced by the copper surface. The question arises why no such fragmentation is observed on Au(111) and Ag(111). A possible explanation is that the molecular decomposition is related to the high affinity of copper towards carboxylic acids. It is well known that acetic acid decomposes to acetate on various copper surfaces, which in turn is chemisorbed in a bidentate configuration via Cu−O bonds [225–227]. It therefore appears possible that acetate ligands are able to switch their binding partner from $Mn_{12}O_{12}$ to Cu(111), most likely resulting in a complete decomposition of the whole Mn_{12}-ac complex.

The identity of the clusters forming the $(2\sqrt{3} \times 2\sqrt{3})\mathrm{R}30°$ superstructure cannot be determined from the STM measurements. However, it can be excluded that the structure is formed solely by solvent (methanol) or acetate molecules for several reasons. First, methanol monolayers desorb from Cu(111) at 163 K and are therefore not expected to be present on the surface after room temperature deposition [228]. Moreover, no similar structures were reported in a low temperature STM study of

methanol/Cu(111) [228]. In contrast, acetate is bound to Cu(111) even at room temperature [227]. However, no periodic superstructure of acetate/Cu(111) is reported in literature [227]. Furthermore, STM and LEED measurements performed in our group on Cu(111) samples that were exposed to an acetic acid atmosphere did not show any sign of periodic ordering.

Since this work focuses on the investigation of intact Mn_{12} molecules, the properties of the observed superstructure are not further discussed here. More detailed information about the system is provided in the master thesis of S. Höll [206].

9.4.3 Elastic Charge Transport Through Individual Mn_{12}-ac Molecules

In order to get insight into the local electronic properties of the Mn_{12}-ac molecules, we utilized scanning tunneling spectroscopy. Current-voltage characteristics of individual molecules were obtained on Au(111) and on graphene/Ir(111). In the following, we first discuss some preliminary considerations concerning data acquisition and analysis. Thereafter, we compare both systems with regard to their elastic charge transport properties.

Possible Changes in the Molecular Geometry Induced by STS

Complex molecular objects like Mn_{12}-ac can easily undergo structural changes during STS measurements, as they are in close vicinity of the STM tip. The possibilities range from a displacement or rotation of the molecule to molecular fragmentation, which in the case of Mn_{12}-ac most likely involves a separation of acetate ligands. A typical example of STS induced fragmentation of Mn_{12}-ac is shown in Figure 9.13.

In order to ensure that STS measurements were obtained on intact molecules and under constant conditions, the molecular appearance was routinely checked by taking STM images before and after each STS measurement. Only data obtained on molecules whose STM topography stayed unchanged during data acquisition were used for further analysis.

The Role of the Set Point

Figure 9.14a shows exemplary current-voltage curves obtained on a single Mn_{12}-ac molecule on Au(111) at two different set points. It is evident that the ratio between the two curves is larger at positive bias voltages V compared to the negative bias voltage range, meaning that the shape of the curve is a function of the separation between tip and molecule. Consequently, tunneling spectra measured at different set points cannot be matched to one another by scaling with a single factor.

Several effects need to be be considered in order to explain the observed behavior. In another STS study of wet-chemically grafted Mn_{12} monolayers – as they were prepared in section 9.3 – Voss *et al.* [192] attributed a set point dependence of the

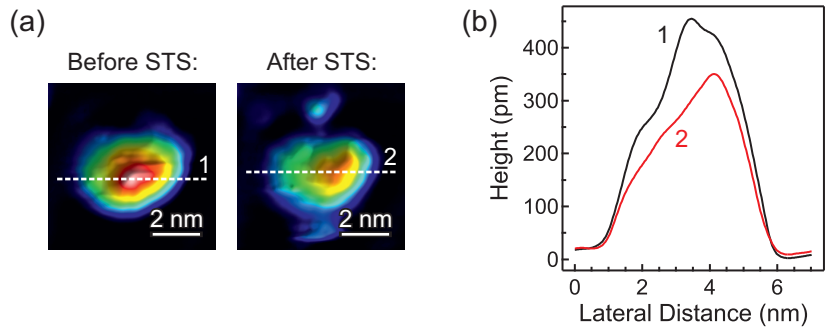

Figure 9.13 | STS induced fragmentation of Mn_{12}-ac on Au(111). (a) STM topography of a single molecule before and after performing an STS measurement. Both images are depicted in the same color scale. Note the difference in height, as well as the appearance of smaller objects at the top and bottom of the image after STS. **(b)** Height profiles along the dashed lines in (a). Scanning parameters: $V = 2.5\,\mathrm{V}$, $T = 3.6\,\mathrm{K}$, $I = 40\,\mathrm{pA}/20\,\mathrm{pA}$ (before/after STS).

spectroscopic features to a charging of the molecules induced by the tunnel current. Using a simple model for charge transport through a single energy level [102], the authors were able to simulate the behavior of the current-voltage curves based on the assumption that Mn_{12} is coupled to the two electrodes in an almost symmetric manner, i.e. the decrease in lifetime of a molecular state caused by the coupling of the molecule to the substrate and to the STM tip is of the same order of magnitude. While this might be a reasonable assumption for the sample geometry used in [192], where the Mn_{12} core is separated from the substrate by a full layer of linker molecules (compare Figure 9.4), it seems unlikely to apply in the present case, in which the molecules are in direct contact to the Au(111) surface.

The set voltage dependence of the curves shown in Figure 9.14a is therefore most likely explained by taking into account the energy and distance dependence of the tunneling matrix element T. This aspect was already discussed in detail in chapter 3.2.1 and it was pointed out that the impact of T on the shape of an STS measurement can be canceled out by normalizing the differential conductance $\mathrm{d}I/\mathrm{d}V$ to the total conductance I/V. The result of applying this normalization scheme to the present measurement is shown in Figure 9.14d. Indeed, both normalized curves overlap to a large extend, underlining that the observed behavior can be fully understood by assuming an asymmetric coupling geometry and considering the impact of the set point on the tunneling matrix element.

A particular obstacle arising from the normalization of $\mathrm{d}I/\mathrm{d}V$ in the present case is that the tunnel current is close to zero in the vicinity of E_F, meaning that the normalized conductance is diverging in this region. The origin of this problem and possible ways to overcome it have already been discussed in chapter 3.2.2. Here, the scheme of Prietsch *et al.* is applied, in which I/V is replaced by $\sqrt{(I/V)^2 + c^2}$ with a small offset constant c. The result shown in Figure 9.14d was calculated using a

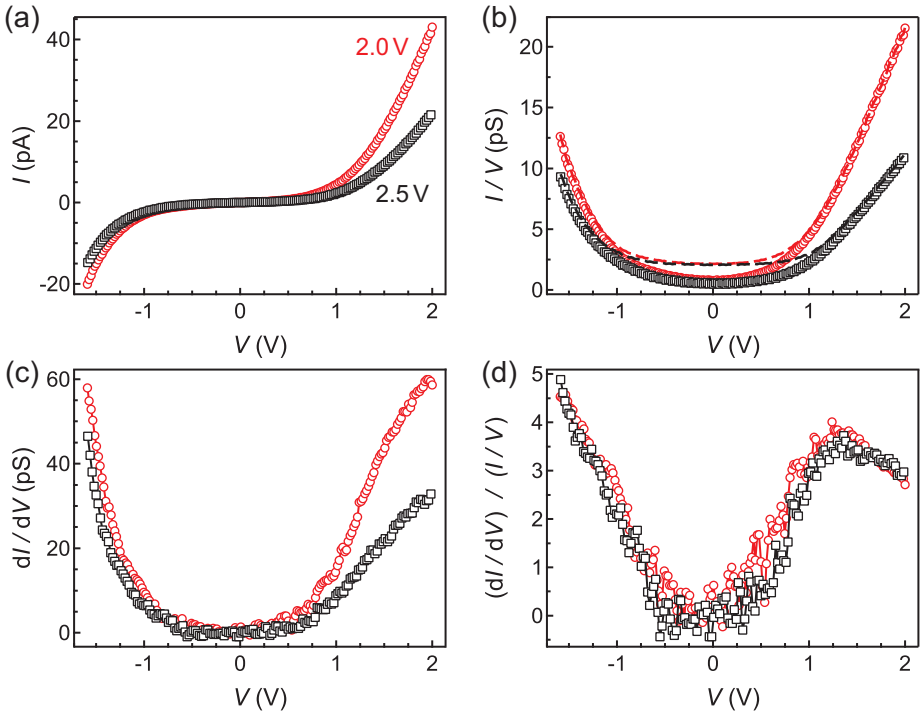

Figure 9.14 | Tunneling spectra of a single Mn_{12}-ac molecule on Au(111), obtained at two different set voltages. Red circles: $V_s = 2\,V$, black squares: $V_s = 2.5\,V$. Further parameters for spectroscopy: $I_s = 40\,pA$, $V_{mod} = 40\,mV$, $T = 11\,K$. **(a)** Tunnel current I. **(b)** Total conductance I/V. Dashed lines are obtained from the data by applying the method of Prietsch *et al.* with an offset constant of $c = 2\,pS$. **(c)** Differential conductance dI/dV. **(d)** Normalized differential conductance $(dI/dV)/(I/V)$.

value of $c = 2\,pS$.

Results

STS measurements performed at the center of 19 different Mn_{12}-ac molecules on Au(111) are shown in Figure 9.15a. All measurements were carried out using identical set parameters of $V_s = 2.5\,V$ and $I_s = 50\,pA$. In accordance with the previous section, all curves were normalized to I/V, using an offset constant of $c = 3\,pS$.

The most prominent feature evident from the data is a wide conductance gap that appears around zero bias voltage. The left and right onset energies of the gap E_l and E_r were estimated for each cluster by fitting the region of conductance onset with a linear function and calculating the intersection point of the fit with the conductance level inside the gap. From the obtained values, the width of the gap is calculated as $\Delta E_{gap} = E_r - E_l$. The distribution of the onset energies and gap widths of all 19 molecules is shown in Figure 9.15b. Taking the average over all molecules yields $\langle E_l \rangle = (-1.07 \pm 0.26)\,eV$, $\langle E_r \rangle = (1.13 \pm 0.24)\,eV$ and $\langle \Delta E_{gap} \rangle = (2.20 \pm 0.45)\,eV$, with the errors referring to the standard deviations.

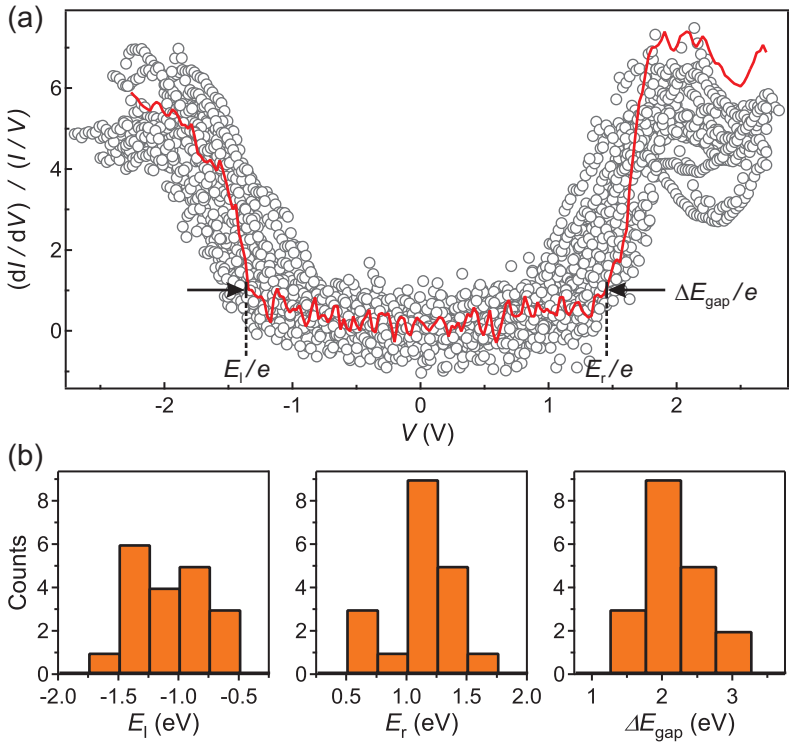

Figure 9.15 | Statistical analysis of elastic charge transport through Mn_{12}-ac on Au(111). (a) Normalized differential conductance curves obtained on 19 different molecules. Grey circles show the entirety of all measured data points. An exemplary conductance curve of one of the molecules is highlighted as a red line. Parameters for spectroscopy: $V_s = 2.5\,V$, $I_s = 50\,pA$, $V_{mod} = 30\,mV$, T: 5.7–8.1 K. All curves were normalized using an offset constant of $c = 3\,pS$. **(b)** Distributions of the left and right onset energies E_l and E_r and of the gap width ΔE_{gap}, as obtained from the data in (a).

As demonstrated in Figure 9.16 the existence of a conductance gap in Mn_{12}-ac on Au(111) is also evident from topographic STM images. When the molecules are scanned in the gap region, they become invisible to the STM tip and are consequently displaced along the scanning direction. As previously demonstrated by Voss *et al.* [223], this effect can be used to manipulate the spatial distribution of the molecules on the nanometer length scale.

In addition to Au(111), we performed STS measurements on individual Mn_{12}-ac molecules on graphene/Ir(111). Due to the high mobility of the molecules on the graphene layer, the measurements were hampered by a displacement of the molecules during data acquisition. Therefore, only a very limited amount of spectroscopic data is available on this system.

Figure 9.17 shows the result of an STS measurement performed at the center of a single Mn_{12}-ac cluster on graphene/Ir(111), which was located at a monatomic step edge. The measurement was carried out using the same set parameters, i.e. $V_s = 2.5\,V$ and $I_s = 50\,pA$. In contrast to the results obtained on Mn_{12}-ac/Au(111),

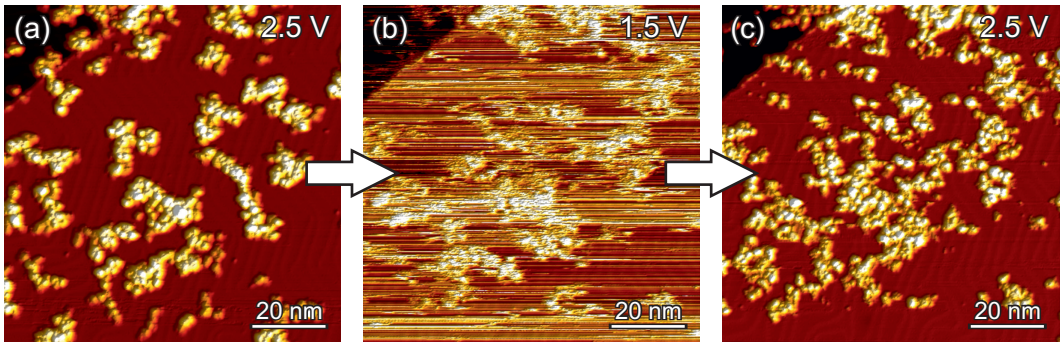

Figure 9.16 | Displacement of Mn_{12}-ac molecules on Au(111) by scanning within the edge region of the conductance gap. The STM images shown in **(a-c)** were subsequently measured at the same position, using bias voltages of 2.5, 1.5 and 2.5 V respectively. Note the unchanged position of the Au step edge in the top-left corner of all three images. Scanning parameters: $I = 10\,\text{pA}$, $T = 10\,\text{K}$.

two sharp peaks are visible in the normalized differential conductance curve. The maxima of the two peaks are estimated to be at -1.38 and 1.54 eV.

We note that the STS measurement presented in Figure 9.17a shows negative differential conductance (NDC) at $V \gtrsim 1.8\,\text{V}$. Due to the limited amount of data, it is not clear whether the observation of NDC is reproducible. The origin of this feature is therefore not further discussed.

Discussion

If we compare the STS measurements obtained on the two different substrates, the most striking difference is the appearance of sharp resonances in the conductance of Mn_{12}-ac on graphene/Ir(111). The observation of such resonances gives strong evidence that the corresponding molecular states do not hybridize with the electron gas of the substrate. Therefore, our STS data demonstrate that a monatomic layer of graphene can be used to electronically decouple Mn_{12}-ac from the influence the metallic support. This finding is consistent with the STM measurements reported in section 9.4.2, since the formation of periodic assemblies of Mn_{12}-ac on graphene/Ir(111) indicates a reduced molecule-substrate interaction compared to Au(111).

In accordance with the asymmetric geometry of the tunnel contact – the Mn_{12}-ac molecule being much stronger coupled to the substrate than to the STM tip – the observed resonances in conductance are interpreted in terms of charge transport through the highest occupied molecular orbital (HOMO) and the lowest unoccupied molecular orbital (LUMO). From the positions of the two resonances, the HOMO-LUMO gap of Mn_{12}-ac on graphene/Ir(111) is calculated to be $\Delta E_{\text{gap}} = 2.92\,\text{eV}$. Notably, the conductance gap of Mn_{12}-ac on Au(111) is of the same order, meaning that the interaction of the molecules with the bare metal surface results in a

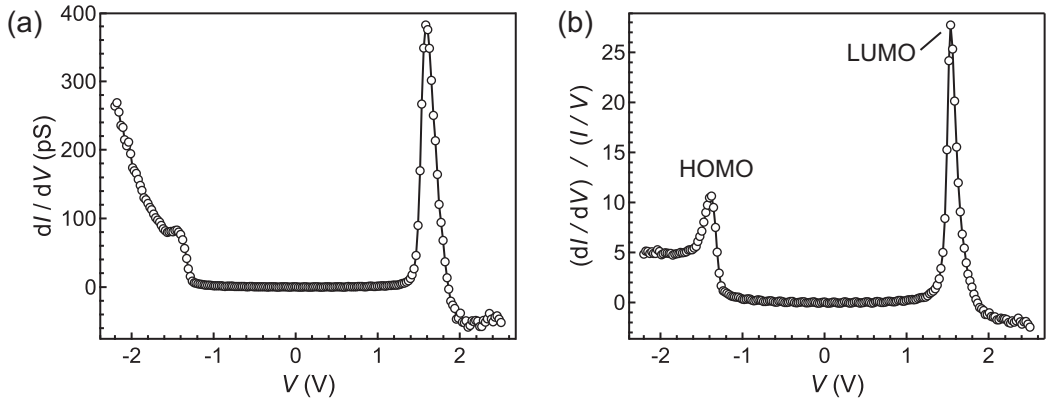

Figure 9.17 | STS spectrum of a single Mn_{12}-ac molecule on graphene/Ir(111). (a) Differential conductance $\mathrm{d}I/\mathrm{d}V$. **(b)** Normalization of $\mathrm{d}I/\mathrm{d}V$ to I/V ($c = 5\,\mathrm{pS}$). Parameters for spectroscopy: $V_\mathrm{s} = 2.5\,\mathrm{V}$, $I_\mathrm{s} = 50\,\mathrm{pA}$, $V_\mathrm{mod} = 10\,\mathrm{mV}$, $T = 5.1\,\mathrm{K}$.

broadening, but not in a significant shift of the molecular states.

In another STS study of Mn_{12}-ac on highly oriented pyrolytic graphite (HOPG) [181], a gap width of 2.34 eV is reported for measurements taken at the center of the Mn_{12} cluster. This value is in good agreement with the average gap width observed in our measurements on Mn_{12}-ac/Au(111). Furthermore, the value is in acceptable agreement with our result on Mn_{12}-ac/graphene/Ir(111), considering that no information on the molecular orientation is available.

A theoretical calculation of the HOMO-LUMO gap within density functional theory (DFT) is reported by Pederson *et al.* [211]. According to the calculation, the gap-width of Mn_{12}-ac is 2.08 and 0.45 eV for the minority and majority spin projection of the electrons, respectively. While a precise prediction of the absolute gap width is difficult in DFT, the result of the calculation indicates that charge transport in STS mainly takes place though the minority-spin states of the molecule. A possible explanation for this finding is that the wave functions of the majority states exhibit a shorter decay length in vacuum. Since the tunnel conductance generally depends on the local density of states at the apex of the tip, this would result in a discrimination of the majority-spin states in scanning tunneling spectroscopy. However, the vacuum decay is not addressed in [211], meaning that this aspect remains speculative.

9.4.4 Can Spin-Flip Excitations be Observed in STS?

Spin-flip excitations in tunneling spectroscopy obey selection rules that are imposed by the conservation of the total spin. Since the spin projection of the tunneling electron can only change by $\Delta M = 0, \pm 1$, the same holds for the adsorbate. Therefore, starting from the $|S, M\rangle = |10, \pm 10\rangle$ ground state, spin-flip transitions in Mn_{12}-ac

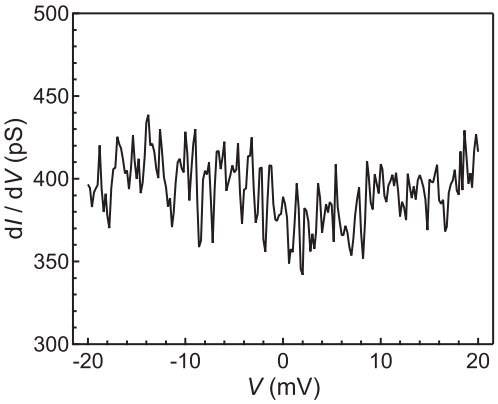

Figure 9.18 | Typical dI/dV spectrum of a single Mn_{12}-ac cluster on Au(111) in the mV bias voltage range. No signs of inelastic tunneling processes were found for any of the measured molecules. Spectroscopy parameters: $V_s = 100\,mV$, $I_s = 40\,pA$, $V_{mod} = 1\,mV$, $T = 6\,K$.

are expected to take place into the adjacent $|10, \pm 9\rangle$ levels of the ground state multiplet, and possibly into $|9, \pm 9\rangle$, $|11, \pm 9\rangle$, $|11, \pm 10\rangle$ and $|11, \pm 11\rangle$ states with excited spin quantum number S.

Taking into account only first order terms in magnetic anisotropy, the energy of the $|S, \pm S\rangle \rightarrow |S, \pm(S-1)\rangle$ transition is $|D|(2S-1)$. Based on the literature value of the anisotropy constant D of Mn_{12}-ac, the lowest energy excitation is therefore expected to be at 1.1 meV. In inelastic neutron scattering measurements on Mn_{12}-ac bulk material [229], higher energy excitations were observed at 5.0 and 9.1 meV.

In order to test whether inelastic excitations in the mentioned energy range can be observed in tunneling spectroscopy, extensive measurements on Mn_{12}-ac molecules on Au(111) were performed in the bias voltage range of $\pm 20\,mV$. A typical example of a dI/dV curve obtained on an individual molecule is shown in Figure 9.18. The spectrum is flat and exhibits no conductance steps that symmetrically appear at positive and negative bias voltage. Overall, no clear signs of spin-flip excitations were found in any of the measured Mn_{12}-ac molecules.

The absence of inelastic features in Mn_{12}-ac/Au(111) is in agreement with results reported in [162]. The authors of the work propose that no such features can be observed on bare metal surfaces due to a quenching of the spin caused by the molecule-substrate interaction. In this regard, it would be interesting to investigate whether spin-flip excitations are evident in Mn_{12}-ac/graphene/Ir(111). This question, however, was no longer pursued after spin-flip transitions in Mn_{12}-ac on h-BN/Rh(111) were reported by another group in the course of this work [162].

9.4.5 X-ray Photoelectron Spectroscopy

Further insight into the electronic properties of Mn_{12}-ac submonolayers deposited on Au(111) and Ag(111) was obtained by using X-ray photoelectron spectroscopy (XPS). In the following, we present a quantitative analysis of the C 1s, O 1s, Mn 2p and Mn 3s core level spectra.

C 1s and O 1s Core Level Spectra

Due to the similarity of the results achieved on both noble metal surfaces, the C 1s and O 1s core level spectra are discussed only for Mn_{12}-ac/Au(111). Figure 9.19a shows the spectral shape of the C 1s contribution at a surface coverage of 0.4 ML. The measurement exhibits a low binding energy peak at 285.2 eV and a high binding energy peak at 288.7 eV. According to the binding configuration, we attribute the two peaks to the C atoms of the methyl (CH_3) and carboxylate (COO) groups of the acetate ligands, respectively. The energy separation between both peaks is consistent with the range of 3.5–4 eV reported in literature [225].

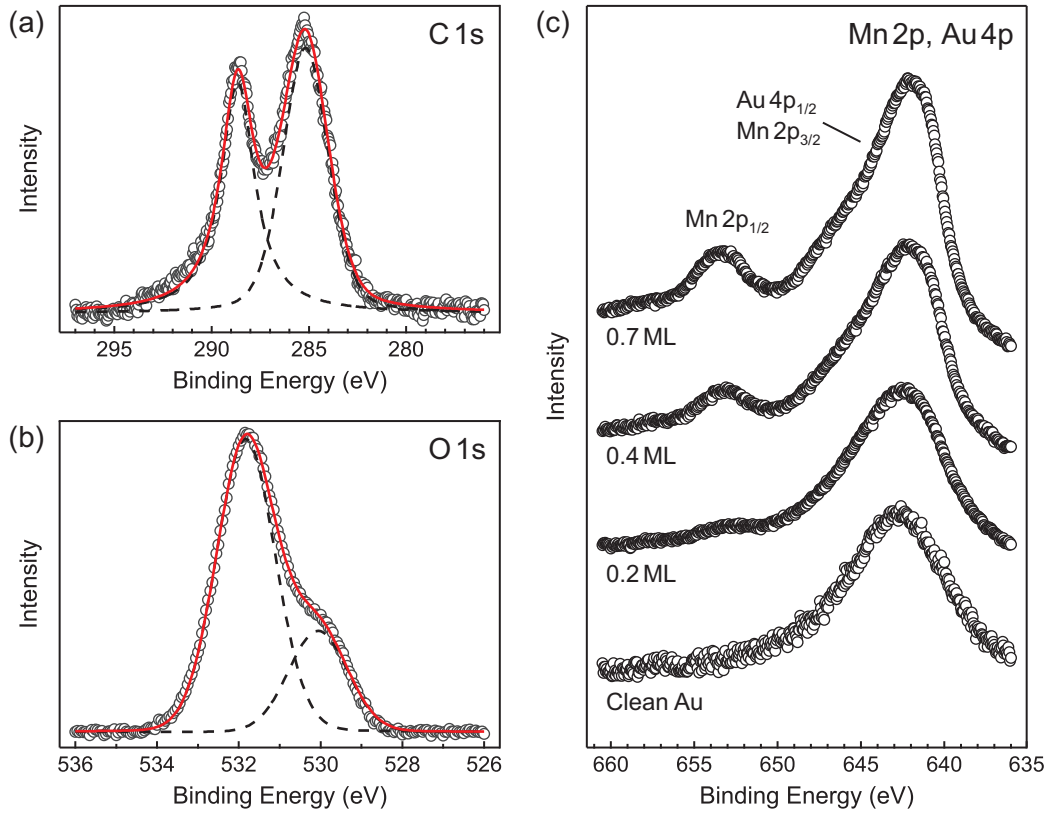

Figure 9.19 | X-ray photoelectron spectra (Mg K_α) of Mn_{12}-ac/Au(111). **(a)** C 1s and **(b)** O 1s core level spectra at 0.4 ML coverage. The data were corrected by subtracting a linear and a polynomial background, respectively. Solid red and dashed black lines are fits to the experimental data as described in the text. **(c)** The Mn 2p spectrum is superimposed by the Au $4p_{1/2}$ contribution. An increase of the Mn $2p_{1/2}$ peak is clearly visible as the coverage increases from 0 and 0.7 ML.

The peak areas were estimated by fitting the spectrum with a sum of pseudo-Voigt functions. The resulting area ratio of the methyl to carboxyl peak is 1.2, which is to be compared to a 1:1 ratio of the corresponding carbon atoms in Mn_{12}-ac. The slightly higher value of the area ratio can be explained by considering two different effects: First, the methyl groups of the upper-lying acetate ligands, which contribute

strongest to the signal, are closer to the top of the sample surface than their carboxyl groups, meaning that the methyl contribution is less attenuated. Secondly, organic contaminations present on the sample surface mainly contribute to the methyl peak. For the latter reason, significantly larger methyl to carboxyl ratios were reported in other experiments [200, 203]. In contrast to these former studies, the almost identical peak areas observed here demonstrate that only small amounts of impurities are present on the sample surface.

The O 1s core level spectrum, obtained on the same sample, is shown Figure 9.19b. The measurement exhibits a main peak at high binding energies, which is attributed to the oxygen atoms of the carboxylate groups and water molecules. An additional shoulder visible at smaller binding energies can be ascribed to the contribution of the $Mn_{12}O_{12}$ core [200]. Fitting the profile with two pseudo-Voigt functions yields peak positions of 531.8 eV and 530.1 eV, respectively. No attempts were made to separate the carboxylate and water contributions in the fit, as the spectral shape does not provide enough detail to reliably estimate the additional degrees of freedom that would result from a three-peaks fitting model.

From the best fit of the experimental spectrum, an area ratio of 3.0 between the high and low binding energy contribution is calculated. This value is in perfect agreement with the abundance of the different oxygen species when it is assumed that water and acetic acid molecules of crystallization are not present on the sample surface, i.e. only the cluster $Mn_{12}O_{12}(CH_3COO)_{16}(H_2O)_4$ is deposited.

The Mn Oxidation State

XPS allows for an identification of the Mn oxidation state based on three different parameters [230]. First, the binding energy of the Mn $2p_{3/2}$ peak is increasing as the oxidation state increases. Secondly, the position of the Mn 2p shake-up satellite with respect to the main peak is significantly different for Mn(II) compared to other oxidation states. Finally, the exchange splitting of the Mn 3s level is a decreasing function of the oxidation state. Reference values of all three parameters were reported for Mn_{12}-ac bulk material [231], as well as for different manganese oxides [230, 232] and are summarized in Table 9.1.

Unfortunately, in case of Mn_{12}-ac/Au(111) both the Mn 2p and Mn 3s core level contributions are superimposed by highly intensive substrate peaks, making a quantitative analysis of their structure impossible (see Figure 9.19c). The Mn oxidation state is therefore only discussed for Mn_{12}-ac/Ag(111). All data presented here were obtained on a sample with ~ 0.8 ML coverage.

The Mn 2p and Mn 3s core level spectra of the Mn_{12}-ac/Ag(111) submonolayer are depicted in Figure 9.20. The maximum of the Mn $2p_{3/2}$ peak is measured at a binding energy of 641.7 eV. Mn 2p shake-up satellites are clearly visible at around 5–6 eV with respect to the Mn $2p_{1/2}$ and Mn $2p_{3/2}$ main peaks. In order to estimate the

	Valency	**Mn $2p_{3/2}$ (eV)**	**ΔE sat. (eV)**	**ΔE Mn 3s (eV)**
MnO	2	640.4–641.7	5.4–5.7	5.8–6.2
Mn_3O_4	$2.\overline{6}$	641.4–641.5	10.5–11.3	5.3–5.6
Mn_2O_3	3	641.8–641.9	10.0–10.5	5.2–5.5
MnO_2	4	642.2–642.6	11.2–12.9	4.5–4.7
Mn_{12}-ac	$3.\overline{3}$	642.4 ± 0.2 [a]	10.6 ± 0.2 [a]	5.4 ± 0.15

Table 9.1 | Literature values of the Mn $2p_{3/2}$ binding energy, the Mn 2p shake-up satellite position and the Mn 3s exchange splitting, reported for manganese oxides with different Mn oxidation states and for Mn_{12}-ac bulk material. References: [230–232]. [a] Value estimated from the plot of the Mn 2p core level spectrum.

Mn 3s exchange splitting, great care was taken to perform an appropriate background correction. In detail, the background was described as a sum of a Shirley profile and four Doniach-Sunjic peaks, accounting for the nonlinear contributions of the adjacent Ag 4s, Ag $4p_{1/2}$ and Ag $4p_{3/2}$ levels, as well as for a Ag 4s satellite caused by the non monochromatic X-ray source. The data shown in Figure 9.20b were corrected for the background contribution. The best fit of the Mn 3s double-peak yields an exchange splitting of (5.7 ± 0.2) eV.

In comparison with the reference values reported for both Mn_{12}-ac bulk material and different manganese oxides, the observed position of the Mn 2p shake-up satellites clearly demonstrates a partial reduction of the manganese ions in the Mn_{12}-ac/Ag(111) submonolayer from +III/+IV to +II. This finding is corroborated by the binding energy of the Mn $2p_{3/2}$ peak, which is significantly smaller than the value expected for an Mn(III)/Mn(IV) mixed valence compound. The same trend is observed for the Mn 3s exchange splitting. Compared to manganese oxide reference materials, the exchange splitting of the Mn_{12}-ac submonolayer indicates a reduction the $Mn_{12}O_{12}$ core. However, we note that the deviation of the exchange splitting from the value reported for Mn_{12}-ac bulk material lies within the accuracy of our measurement.

In conclusion, the XPS Mn 2p and Mn 3s core level spectra indicate a reduction of manganese in Mn_{12}-ac/Ag(111). Two different effects need to be taken into account to explain this finding. First, a reduction of the manganese ions might result from a charge transfer between substrate and molecule. Secondly, a change of the oxidation state can generally be caused by radiation damage, i.e. a degradation or charging of the molecules caused by the X-ray radiation. From STM images reacord after X-ray photoelectron spectroscopy, we found no significant changes in the topographic appearance of the samples. Therefore, we consider a charge transfer process to be the most likely explanation.

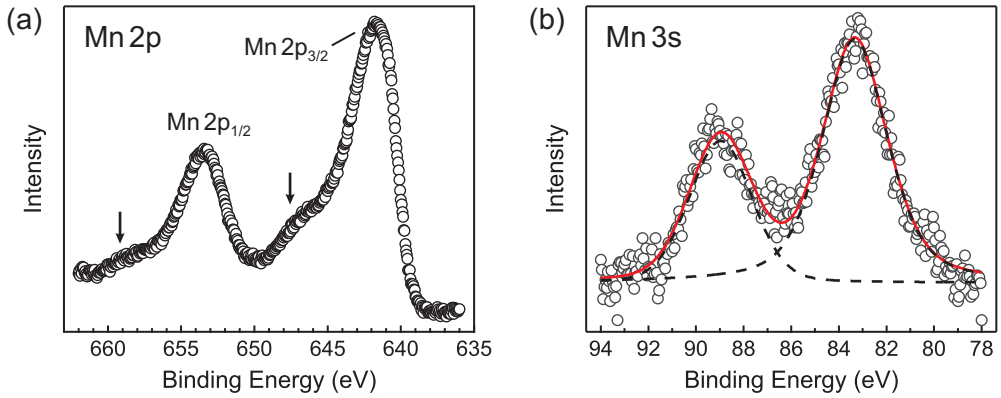

Figure 9.20 | X-ray photoelectron spectra (Mg K_α) of approximately 0.8 ML Mn_{12}-ac on Ag(111). (a) Mn 2p core level spectrum. Arrows indicate the positions of shake-up satellites. **(b)** Exchange splitting of the Mn 3s level. Data were background corrected as described in the text. Solid red and dashed black lines are fits to the data based on Voigt functions.

9.5 Study of Mn_{12}-ac Thick Films

The investigation of SMM films rather than submonolayers not only is of interest with regard to possible applications, but also allows for a direct measurement of the magnetic properties via bulk-sensitive SQUID magnetometry. In this section, the question is addressed whether the magnetic properties of Mn_{12}-ac thick films differ from bulk material or not. In order to account for the presumably random orientation of the molecules in the film material, the results are compared to the magnetic behavior of a polycrystalline powder sample.

9.5.1 Sample Preparation

The Mn_{12}-ac film was prepared by means of ESD, using an 0.5 mm thick sapphire plate covered with 75 nm gold as substrate. In contrast to the preparation of submonolayers for STM and XPS investigations, the deposition rate was strongly increased by placing the substrate in the first stage of the differential pumping system and increasing the concentration of the methanolic Mn_{12} solution to 2×10^{-4} M. For the results presented here, an ion charge of 114 nAh was deposited over a time period of 225 min. After deposition, the sample was transported to the SQUID magnetometer under ambient conditions.

The magnetometric measurements on Mn_{12}-ac polycrystalline powder were obtained on a sample with a mass of 9.4 mg. All SQUID measurements were background corrected as described in section 4.3.1.

9.5.2 Results and Discussion

Figure 9.21a shows isothermal magnetization curves obtained on the film and on the polycrystalline powder sample at 1.8 K. For comparison, a calculation of the magnetization curve of an ensemble of randomly oriented Mn_{12}-ac molecules in thermal equilibrium, i.e. without magnetic hysteresis, is plotted as well[2]. The calculation was carried out based on the ZFS Hamiltonian

$$\mathcal{H}_{\mathrm{ZFS}} = DS_z^2 + g\mu_{\mathrm{B}}\boldsymbol{S}\cdot\boldsymbol{H}. \tag{9.1}$$

In order to account for the random molecular orientation, the magnetization was averaged over all possible angles between $\boldsymbol{S}$ and $\boldsymbol{H}$. The first order anisotropy constant was set to the literature value $D = -0.47\,\mathrm{cm}^{-1}$ and the Landé-factor was estimated to be $g = 1.90$ from a fit of the calculation to the high magnetic field range of the polycrystalline powder measurement.

The differences observed in the magnetic behavior of the powder sample compared to single crystalline material (see Figure 9.2a) can be ascribed to the random orientation of the molecules. In particular, the magnetization curve of the powder sample is not saturated at 5 T, since high magnetic fields are required to rotate the magnetic moment of those molecules whose anisotropy axis is almost perpendicular to the external magnetic field. Furthermore, step-like magnetization changes, which are a signature of quantum tunneling of magnetization, are only observed at zero magnetic field. This is to be expected, since all QTM transitions other than the zero field resonance $|S, \pm M\rangle \rightarrow |S, \mp M\rangle$ depend on the angle between the anisotropy axis and the magnetic field and are therefore smeared out in the measurement.

Compared to the polycrystalline powder sample, the Mn_{12}-ac film exhibits a significantly different magnetic behavior. First, the coercive field of the film is strongly reduced. An opening of a hysteresis loop is visible only in a magnified view of the low magnetic field range, as shown in Figure 9.21b. Secondly, the hysteresis loop of the film shows no signs of QTM at zero magnetic field. Thirdly, the slope of the magnetization curve at zero magnetic field is considerably smaller than expected for an ensemble of randomly oriented Mn_{12}-ac molecules.

According to the Arrhenius law (1.9), the observed reduction of the coercive field can be explained by a decrease of either the pre-exponential factor τ_0, or the anisotropy barrier height ΔE. A smaller value of τ_0 is to be expected when going from crystalline to amorphous environment, due to an increased spin-phonon interaction [233]. For amorphous Mn_{12}-ac nanospheres, τ_0 was reported to be reduced by a factor of 3.5–4 compared to crystalline bulk material [233]. Since the relaxation

[2] The assumption of thermal equilibrium corresponds to an experimental situation in which the integration time of the measurement is chosen to be large compared to the magnetic relaxation time τ of Mn_{12}-ac. Since τ is of the order of years at 1.8 K, an experimental realization of this condition is not practicable.

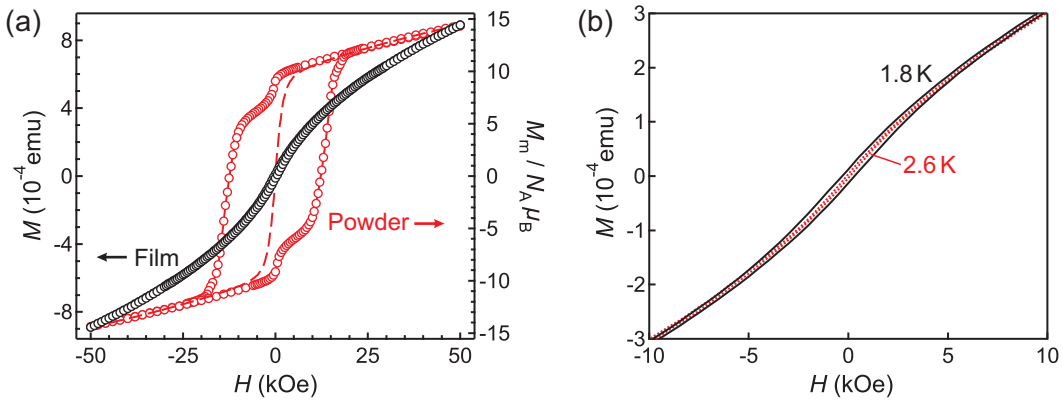

Figure 9.21 | **(a)** Isothermal magnetization curves of an Mn_{12}-ac film (black circles) and a polycrystalline powder sample (red circles) at $T = 1.8\,\mathrm{K}$. The dashed red line shows the magnetization calculated for an ensemble of randomly oriented Mn_{12}-ac molecules in thermal equilibrium. **(b)** Magnified view of the curve obtained on the film sample in the range of low magnetic fields. A temperature dependent opening of a hysteresis loop is visible.

time linearly depends on τ_0, a change of this magnitude cannot explain the drastic reduction of the coercive field observed here. We therefore assume that the small coercive field value is mainly caused by a reduction of the anisotropy barrier ΔE.

The reduced slope of the magnetization curve at zero magnetic field cannot be explained by this change in magnetic anisotropy. In general, for an ensemble of randomly oriented molecules with easy-axis type magnetic anisotropy, the slope of the magnetization curve at zero magnetic field increases when the anisotropy barrier is decreased. Clearly, the opposite trend is observed here. The shape of the magnetization curve therefore indicates that the magnetic moment of the molecules in the film, i.e. their spin quantum number S, is reduced as well.

Further insight into the magnetic properties of the film is provided by temperature dependent susceptibility measurements. As already discussed in section 9.2.1, slow magnetic relaxation due to easy-axis type magnetic anisotropy causes a difference between zero-field-cooled (ZFC) and field-cooled (FC) curves at low temperature. Figure 9.22a shows the result of a ZFC-FC measurement of film and powder sample in an external magnetic field of $H = 1\,\mathrm{kOe}$. The ZFC and FC curves measured on the film clearly diverge below 4 K, which is in accordance with the observed opening of a hysteresis loop in magnetic field dependent measurements. However, compared to the polycrystalline powder sample, the relative difference between both curves at 1.8 K is significantly smaller.

The blocking temperature T_B of the film can be deduced from the local maximum of the ZFC curve. The functional dependence of T_B on the external magnetic field H is depicted in Figure 9.22b. At $H = 0.1\,\mathrm{kOe}$, the value of T_B is around 3.9 K. By increasing H to 7 kOe, T_B continuously drops to around 2.4 K.

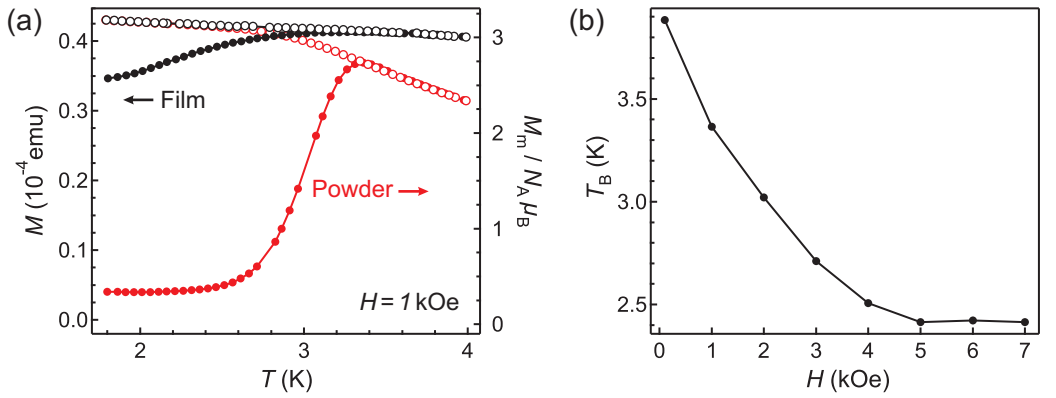

Figure 9.22 | **(a)** Temperature dependence of the magnetization of an Mn_{12}-ac film (black) and polycrystalline powder sample (red) in an external magnetic field of $H = 1\,\mathrm{kOe}$. Solid and open circles correspond to ZFC and FC curves, respectively. **(b)** Blocking temperature of the film as a function of the external magnetic field H.

Notably, the value of T_B is very close to that found for single crystalline material (compare Figure 9.2b). This is in apparent contradiction to the magnetization curves, since the decrease of both the magnetic anisotropy and the magnetic moment is expected to result in a significant reduction of T_B. It is therefore concluded that not all molecules are affected by the decrease in anisotropy and magnetic moment in the same way. Most likely, a large fraction of the molecules exhibits fast magnetic relaxation, whereas the magnetic properties of a smaller fraction, which is carrying the magnetic hysteresis, are almost unchanged. This explanation is in agreement with the observation that the relative difference between ZFC and FC curves at 1.8 K is significantly smaller for the film compared to the polycrystalline powder sample.

Conclusion

In conclusion, we observe a significant change of the magnetic properties of the molecules in the film compared to bulk material. Two different effects need to be taken into account in order to explain this finding. First, a part of the Mn_{12}-ac molecules is expected to be decomposed during the deposition process. As observed in the ESI-MS measurements reported in section 9.2.2, a loss of acetate ligands can occur in ESD, which is expected to severely influence the electronic and magnetic properties of the molecules. However, based on the small amount of fragments that is visible in STM measurements on Mn_{12}-ac submonolayers, it appears unlikely that molecular decomposition is responsible for the observed changes alone.

A second aspect to be considered is the impact of the changed molecular environment of the magnetic behavior. Various studies have shown that the electronic and magnetic properties of Mn_{12} SMMs are strongly modified when their crystalline order is broken. In amorphous material, around 45 % of all Mn_{12} clusters were found to

exhibit fast magnetic relaxation [234]. Isothermal magnetization curves of Mn_{12} films that were prepared by other techniques, such as evaporation of highly concentrated solutions [235] or deposition of Langmuir-Blodgett films [197], showed coercive fields values and slopes at zero magnetic field that are comparable to the results obtained here. Our finding of a changed magnetic behavior is therefore in line with a number of studies already reported in literature and is likely related to the redox instability of the Mn_{12} core.

10 | Fe_4 Ferric Stars

A second class of SMMs studied in this work are tetranuclear iron(III) complexes of formula $Fe_4L_2dpm_6$, where H_3L is a tripodal ligand of the general form R-$C(CH_2OH)_3$ and Hdpm = dipivaloylmethane. Great interest into this family of SMMs, also known as Fe_4 ferric stars, was raised by several studies who demonstrated a remarkable stability of its functional magnetic properties. As the only SMM to this day, Fe_4 was shown to retain its magnetic hysteresis when chemically grafted to a metallic substrate [11, 236]. Furthermore, the magnetic anisotropy of Fe_4 was found to be preserved when embedded into a three-terminal device geometry [237–239].

In previous studies, the deposition of the Fe_4 cluster was carried out either by forming a thiol bond between a sulfur containing tripodal ligand L^{3-} and a gold surface [11, 236], or by utilizing thermal sublimation in ultra-high vacuum (UHV), which up to now was shown to be possible only for R = phenyl [240–242]. However, the specific form of the tripodal ligand required for both deposition procedures is a limitation that restricts the free choice of the organic ligand shell as a tool to control the interaction of the molecule with its environment. In particular, the protruding size of these ligands forces Fe_4 to sit slantwise to the substrate, therefore resulting in an unfavorable angle between the molecular magnetic easy axis and the surface normal of up to 35° [11,242]. Furthermore, this hampers the assembly of the molecules in ordered two-dimensional superstructures [242].

Here, we present a successful fabrication of self-organized arrays of Fe_4 by using hexagonal boron nitride (*h*-BN) on Rh(111) and graphene on Ir(111) as templates. In order to achieve a preferably flat adsorption geometry of the Fe_4 molecule, we decided to use the smallest tripodal ligand possible, viz. R = H. The molecular structure of this specific derivative (Fe_4H) is depicted in Figure 10.1. Chemical synthesis and crystal structure characterization were performed by P. Schmitt in the group of Prof. U. Groth (Department of Chemistry, University of Konstanz) and are described elsewhere [243].

For the deposition of Fe_4H we use electrospray deposition (ESD), which has been shown to be capable of bringing complex and non-volatile molecules onto surfaces with only minor fragmentation [53]. The structural and electronic properties of Fe_4H

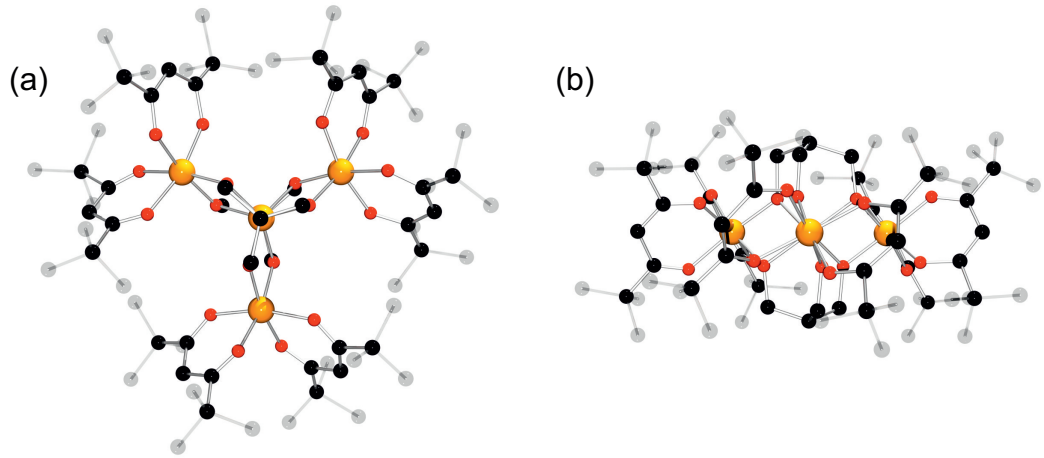

Figure 10.1 | Structure of the Fe_4H compound, viewed along the [001] **(a)** and [010] lattice direction **(b)** of the molecular crystal. Color code: Fe = orange, O = red, C = black. Outer C atoms of *tert*-butyl groups are translucent and H atoms are omitted for clarity.

sub-monolayers and individual molecules are studied by means of low temperature scanning tunneling microscopy and spectroscopy (STM/STS), as well as X-ray absorption spectroscopy (XAS) and X-ray magnetic circular dichroism (XMCD). Despite the complexity of the molecular structure, ordered arrays of Fe_4H are obtained. By comparison of STM images and density functional theory (DFT) calculations, we infer that the magnetic easy axis of the molecules is perpendicular to the surface. Furthermore, from the magnetic field dependence of the XMCD signal, we conclude that the magnetic anisotropy constant D is unaffected upon the deposition on graphene. The systems studied here therefore provide a promising playground to explore the magnetic properties of Fe_4 SMMs in a well-defined configuration.

A part of the following results have been published in Nano Letters in 2015 as an article named "Highly ordered surface self assembly of Fe_4 single molecule magnets" [243]. The STM and STS measurements presented in this chapter were performed together with Nicole Barth and Fabian Paschke in the context of their master theses [208].

10.1 Bulk Magnetic Properties of the Fe_4H Compound

Since the Fe_4H compound is not reported in literature so far, we first carried out a characterization of its bulk magnetic properties. The measurements were performed via SQUID magnetometry on a sample of 5.3 mg polycrystalline powder, dispersed in 21.4 mg of paraffin oil and cooled down in zero magnetic field to ensure a random orientation of the crystallites. The diamagnetic background consisting of the contributions of oil and sample holder was corrected by subtracting a reference

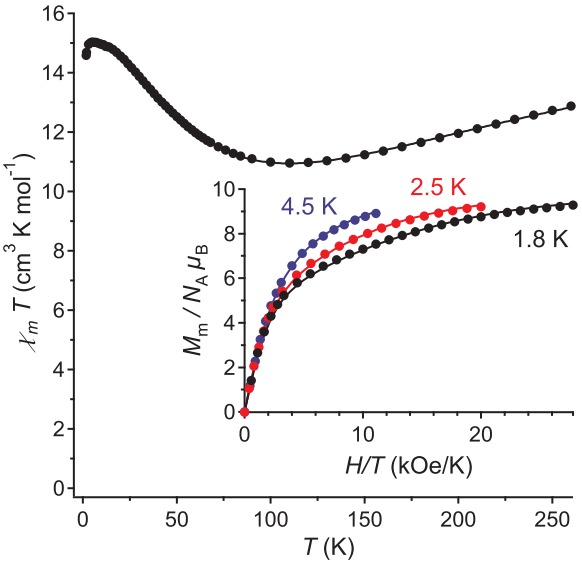

Figure 10.2 | DC magnetic properties of Fe_4H as polycrystalline material. Upper curve: Temperature dependence of the magnetic susceptibility. Inset: Isothermal magnetization curves, measured at different temperatures. Solid lines are fits to the data, based on the models described in the text.

measurement and the diamagnetic contribution of Fe_4H was subtracted by using a correction of -871×10^{-6} emu/mol, estimated from Pascals constants.

Results and Discussion

Figure 10.2 shows the temperature dependence of the molar susceptibility χ_m in the range of 1.8–260 K, measured in a magnetic field of $H = 1$ kOe. The $\chi_m T$ product at 260 K is around 12.9 $cm^3 K mol^{-1}$. By lowering the temperature, $\chi_m T$ reaches a broad minimum at around 110 K and finally increases to a maximum value of 15.0 $cm^3 K mol^{-1}$ at 5 K.

As pointed out in [244], the observed behavior of $\chi_m T$ is a fingerprint of the antiferromagnetic coupling in the star-like spin topology of Fe_4. A quantitative analysis of the data was carried out based on the Heisenberg Hamiltonian

$$\mathcal{H} = J_1 \boldsymbol{S}_1 \cdot (\boldsymbol{S}_2 + \boldsymbol{S}_3 + \boldsymbol{S}_4) + J_2(\boldsymbol{S}_2 \cdot \boldsymbol{S}_3 + \boldsymbol{S}_3 \cdot \boldsymbol{S}_4 + \boldsymbol{S}_2 \cdot \boldsymbol{S}_4) + g\mu_B \boldsymbol{S} \cdot \boldsymbol{H}. \quad (10.1)$$

Here, J_1 and J_2 denote the nearest-neighbor and next-nearest-neighbor exchange coupling constants, respectively, $\boldsymbol{S}_{i=1}$ and $\boldsymbol{S}_{i\neq 1}$ correspond to the spins of the central and the peripheral Fe atoms, $\boldsymbol{S}$ is the total spin and $\boldsymbol{H}$ is the applied magnetic field. The form of (10.1) implicates a threefold symmetry of the exchange interaction (see Figure 10.3) and was already used in previous studies of Fe_4 derivatives [244–247]. Fitting the experimental data based on (10.1) yields the best fit values $J_1 = 16.94(15)\,cm^{-1}$, $J_2 = 0.95(11)\,cm^{-1}$ and $g = 2.059(5)$. The corresponding $\chi_m T$ curve is shown in Figure 10.2 as a solid line. The values of J_1 and J_2 are in good agreement with values reported for other Fe_4 derivatives [245–247].

In addition, isothermal magnetization curves were recorded at 1.8, 2.5 and 4.5 K. The result is shown in the inset of Figure 10.2. The M_m vs. H/T curves do not coin-

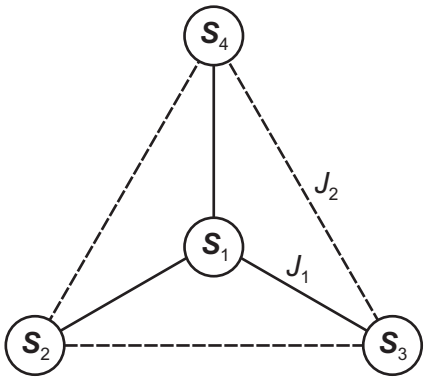

Figure 10.3 | Schematic illustration of the exchange interactions described by the Heisenberg Hamiltonian (10.1).

cide for different temperatures and approach a value of $10\,N_A\mu_B$ for high magnetic fields, indicating an $S = 5$ ground state with non-zero magnetic anisotropy. Good coincidence with the measured data can be achieved based on the simple zero-field splitting Hamiltonian

$$\mathcal{H} = DS_z^2 + g\mu_B \boldsymbol{S} \cdot \boldsymbol{H}, \tag{10.2}$$

where S_z is the component of the total spin in direction of the magnetic anisotropy axis. The magnetic moment is calculated from (10.2) by numerically diagonalizing the Hamiltonian as a function of the magnetic field orientation and subsequently integrating the result over all possible angles of the magnetic field with respect to the anisotropy axis, in order to account for the random orientation of the crystallites in the powder sample. Fitting the calculated magnetization curve to our data yields $D = -0.427(11)\,\mathrm{cm}^{-1}$ and $g = 1.994(8)$. The solid lines in the inset of Figure 10.2 show the magnetization curves that correspond to the best fit values. Again, the value of D is consistent with values reported for other Fe_4 derivatives [246].

10.2 Characterization of Fe_4H Thick Films

An important question regarding the surface deposition of Fe_4H is whether the molecular integrity of the compound is preserved during the ESD process. In order to address this aspect, preliminary measurements were performed on Fe_4H thick films that were grown by means of ESD. The magnetic properties of the films and their composition were studied via SQUID magnetometry and electrospray ionization mass spectrometry (ESI-MS). By comparing the results to those obtained on bulk material, insight is gained into possible fragmentation processes that can occur during the transfer of the molecules from solution onto the surface.

Film preparation: Solutions of Fe_4H with concentrations in the range of 7×10^{-5}–1×10^{-4} M in a mixture of tetrahydrofuran and methanol (volume ratio 6 : 1) were freshly prepared and immediately used for deposition. Gold-covered sapphire plates were used as substrate for the film growth. In order to achieve high deposition

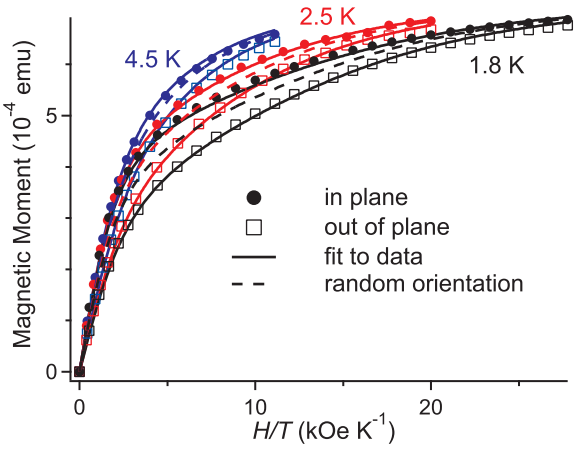

Figure 10.4 | Isothermal magnetization curves of an Fe_4H film, measured at different temperatures and with in-plane and out-of-plane magnetic field orientation. Solid lines are a fit to the data, based on a step-like angle distribution (10.4). Dashed lines are magnetization curves of a randomly oriented polycrystalline powder sample, scaled to the absolute magnetic moment of the film.

rates, the substrate was placed directly in front of the electrospray emitter tip at ambient conditions. The results presented herein were obtained on a film sample with an average thickness of around 1.5 μm, as estimated from the saturation value of its magnetic moment.

SQUID magnetometry: The diamagnetic background contribution of the substrate and the sample holder was corrected by subtracting a reference measurement of the substrate performed before the deposition of Fe_4H.

ESI-MS: Mass spectra were recorded from a solution generated by immersing the film into 3 ml of tetrahydrofuran (THF). A complete dissolution of the film by the solvent was observed to take place within several seconds. Reference spectra were obtained on a 7×10^{-5} M solution of crystalline material in the same solvent. All measurements were performed on a Bruker micrOTOF II electrospray ionization (ESI) time-of-flight system, using the following operating parameters of the ESI interface: source temperature 180 °C, desolvation gas flow 10 l/min, nebulizing gas pressure 1.2 bar.

10.2.1 DC Magnetic Properties

Figure 10.4 shows isothermal magnetization curves of the Fe_4H film, measured at temperatures of 1.8, 2.5 and 4.5 K and with the external magnetic field applied both along the in-plane and out-of-plane direction. For comparison, the magnetization curves that were obtained on polycrystalline bulk material are depicted in the same graph as dashed lines. It is evident that the measurement of the film resembles the curves taken on bulk material. However, a clear difference can be observed between the in-plane and out-of-plane geometry, the magnetic moment of the film being smaller in the latter case.

Two effects need to be taken into account in order to explain the observed dependence of the magnetization on the orientation of the magnetic field: shape anisotropy and a preferred orientation of the molecules in the film material. In case of a film

whose thickness is negligible compared to its lateral dimensions, the magnetization $M_\parallel$ measured with in-plane geometry is not affected by shape anisotropy, whereas the magnetization $M_\perp$ measured in out-of-plane geometry is reduced by the influence of the internal demagnetizing field. A quantitative estimation of this effect can be carried out in the limit $M_\perp \ll H$, which is a reasonable assumption for the Fe_4 complex due to its small volume magnetization. In this limit, the relative difference between both geometries is directly given by the differential volume susceptibility, i.e.

$$\frac{M_\parallel(H) - M_\perp(H)}{M_\perp(H)} = \frac{\mathrm{d}M_\parallel(H)}{\mathrm{d}H}. \tag{10.3}$$

In case of our measurement, an upper limit of $\mathrm{d}M_\parallel/\mathrm{d}H$ can be estimated by taking the volume susceptibility at the lowest temperature used and in zero magnetic field, which is $\chi(T = 1.8\,\mathrm{K}, H = 0) \approx 5 \times 10^{-3}$ (as obtained from the measurement on polycrystalline powder material – section 10.1). This value is much smaller than the relative difference between both geometries observed in our measurement. Therefore, we conclude that the impact of the magnetic field orientation on the magnetization of the film cannot be explained by shape anisotropy.

As a consequence, we ascribe the observed effect to a preferred orientation of the molecules within the film. In general, the distribution of the molecular orientations can be described by a probability density function $\rho(\vartheta, \varphi)$, where ϑ and φ are spherical coordinates giving the orientation of the anisotropy axis of Fe_4 with respect to the surface normal (see Figure 10.5a). For symmetry reasons, it holds that the probability density does not depend on the azimuth angle φ, i.e. $\rho(\vartheta, \varphi) = \rho(\vartheta)$. The exact functional dependence of $\rho(\vartheta)$ is not known a priori and is extremely difficult to deduce from the experimental magnetization curves[1]. We therefore propose a simple model with a step-like probability density function

$$\rho(\vartheta) = (2\pi \cos\vartheta_0)^{-1}\, \Theta(\vartheta - \vartheta_0). \tag{10.4}$$

Here, Θ is the Heaviside step function and ϑ_0 is a parameter describing the degree of orientation (random orientation for $\vartheta_0 = 0$, complete in-plane orientation for $\vartheta_0 \to \pi/2$). A schematic illustration of (10.4) is given in Figure 10.5b.

In order to estimate the value of ϑ_0, we calculate the temperature and magnetic field dependence of the in-plane and out-of-plane magnetization for an ensemble of Fe_4 SMMs with angle distribution (10.4) and refine ϑ_0 by fitting the result to our data. The projection of the magnetic moment onto the external field $\boldsymbol{H}$ can be

[1] This would require a numerical solution of a problem in calculus of variation.

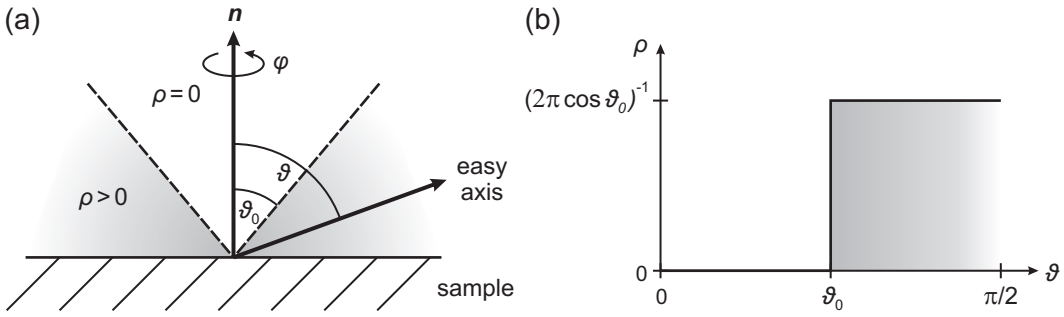

Figure 10.5 | Schematic illustration of the assumed distribution of molecular orientations. **(a)** Definition of ϑ, φ and ϑ_0. **(b)** Sketch of the angle distribution function (10.4).

calculated from

$$M(\boldsymbol{H}) = \int_0^{2\pi} d\varphi \int_0^{\pi/2} d\vartheta \sin\vartheta \, \rho(\vartheta) \boldsymbol{M}_{\vartheta,\varphi}(\boldsymbol{H}) \cdot \boldsymbol{e}_H, \tag{10.5}$$

where $\boldsymbol{M}_{\vartheta,\varphi}(\boldsymbol{H})$ is the magnetic moment of a molecule with orientation of the anisotropy axis given by (ϑ, φ) and $\boldsymbol{e}_H$ is the unit vector in direction of the magnetic field[2]. The calculation of $\boldsymbol{M}_{\vartheta,\varphi}$ was carried out within an $S = 5$ giant spin model based on the ZFS Hamiltonian (10.2). For the fitting routine, D and g were kept fixed to the values measured on polycrystalline material. All measured curved were fitted with a single set of parameters (besides ϑ_0, a prefactor was used in order to account for the unknown number of molecules in the film). The best fit is achieved for $\vartheta_0 = 35.0(5)°$. The corresponding in-plane and out-of-plane magnetization curves at 1.8, 2.5 and 4.5 K are shown as solid lines in Figure 10.4. For other film samples, the same analysis routine yielded ϑ_0 values in the range of 35–51°.

Despite the simplicity of our model, a good coincidence is achieved between the experimental data and the calculated curves. Considering that the calculation was carried out using the bulk values of the anisotropy constant D and spin quantum number S, our SQUID measurements provide strong evidence that the magnetic properties of the individual Fe_4H molecules do not change when being grown as film material.

10.2.2 Mass Spectrometry

Mass spectra measured on both the dissolved film and the bulk reference sample are depicted in Figure 10.6. Both spectra show a strong contribution at $m/z = 1530.2$ Th and two small peaks at $m/z = 1552.2$ and 1568.3 Th, which are assigned to $[M+H]^+$, $[M + Na]^+$ and $[M + K]^+$, respectively. Here, M denotes the intact Fe_4H molecule.

[2]Note that the magnetic moment depends on the azimuth angle φ when the magnetic field $\boldsymbol{H}$ is applied in-plane.

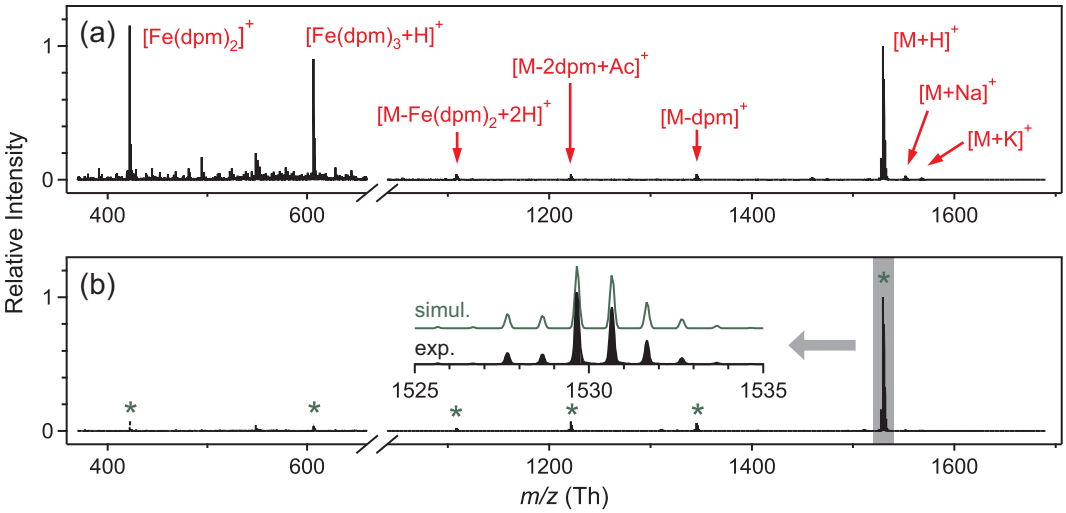

Figure 10.6 | Positive ion ESI-MS spectra of an Fe_4H film prepared by ESD **(a)** and of crystalline material of the Fe_4H complex **(b)**, both dissolved in THF. M denotes the intact Fe_4H molecule. Green asterisks are used to label peaks in (b) which also appear in (a). The two peaks assigned to $[M + Na]^+$ and $[M + K]^+$ are not visible in (b) at the scale of the graph, but are clearly apparent in the signal. The inset shows the $[M + H]^+$ peak in detail, together with the theoretical isotopic distribution (green line). The intensity is normalized to the height of the $[M + H]^+$ peak.

Several peaks at smaller m/z values can be attributed to fragments of Fe_4H. Peaks at $m/z = 1344.9$, 1221.7 and 1107.8 Th can be explained by the loss of either one or two dpm ligands, or of an $Fe(dpm)_2$ unit, resulting in $[M-dpm]^+$, $[M-2\,dpm+Ac]^+$ and $[M - Fe(dpm)_2 + 2\,H]^+$, respectively. The Ac^- adduct is present as an impurity in the mass spectrometer. Furthermore, peaks at $m/z = 606.7$ and 422.4 Th are assigned to the Fe monomers $[Fe(dpm)_3 + H]^+$ and $[Fe(dpm)_2]^+$.

The occurrence of a strong $[M + H]^+$ signal in the dissolved film gives evidence that a significant fraction of the Fe_4H molecules stays intact during the initial ESD process. Concerning fragmentation, two different processes have to be taken into account. The peaks attributed to $[M - dpm]^+$, $[M - 2\,dpm + Ac]^+$ and $[M - Fe(dpm)_2 + 2\,H]^+$ are of around the same height relative to the contribution of the intact complex in both spectra, indicating that these fragments are generated within the ionization process in the mass spectrometer. In contrast to this, the peaks attributed to $[Fe(dpm)_3 + H]^+$ and $[Fe(dpm)_2]^+$ are more dominant in the spectrum of the film compared to the reference sample and are therefore presumably related to fragmentation occurring during the deposition of the film.

It should be pointed out that no quantitative analysis of the ratio between fragments and intact molecules within the film is possible based on ESI-MS, due to different ionization efficiencies and transmission coefficients of the molecules involved. As will be shown in the following section based on STM measurements on Fe_4H sub-

monolayers, only a small percentage of the deposited material consists of molecular fragments.

10.3 Fe_4H on h-BN/Rh(111)

As already discussed in chapter 7.4, a monatomic layer of hexagonal boron nitride (h-BN) on Rh(111) forms a highly periodic moiré superstructure with a periodicity of around 3.2 nm, often referred to as "nanomesh". Here, we demonstrate that self-organized arrays of Fe_4H can be fabricated by using the h-BN/Rh(111) moiré pattern as template. The adsorption geometry and growth behavior of the molecules is addressed by means of high-resolution low temperature scanning tunneling microscopy (STM). Furthermore, insight into the electronic properties of the system is gained by combining scanning tunneling spectroscopy (STS) measurements and density functional theory (DFT) calculations.

Sample preparation: h-BN/Rh(111) was prepared as described in chapter 7.4. Fe_4H molecules were deposited *in situ* by ESD from freshly prepared solutions in tetrahydrofuran and methanol (volume ratio 6 : 1, concentration 7×10^{-5}–1×10^{-4} M) with the sample kept at room temperature.

DFT: Computational results within DFT were obtained by Andreas Irmler in the group of Fabian Pauly (Department of Physics, University of Konstanz) by employing version 6.5 of the TURBOMOLE program package[3] and using the PBE0 exchange-correlation functional [248, 249] with the TZVP basis set [250]. All shown results were determined from a relaxed isolated molecule.

10.3.1 STM Imaging

Figure 10.7 shows typical STM topographic images of Fe_4H molecules deposited on h-BN/Rh(111) at different coverages, ranging from 0.001 ML to 0.7 ML. At small coverage, the molecules appear as randomly distributed objects, occupying the pore sites of the moiré superstructure (Figure 10.7a,b). By increasing the coverage, formation of well-ordered islands is observed (Figure 10.7c,d). The hexagonal periodicity of the moiré pattern is visible on the islands as well. While the contrast of the moiré structure is inverted on clean h-BN for the bias voltage values typically used within this work ($V \geq 2.5$ V) [165], no inversion is observed on top of the islands. This results in different apparent height values of around 0.45 and 0.75 nm for molecules sitting at pore and wire sites, respectively (Figure 10.7e). A further increase of the coverage leads to the formation of an almost perfect monolayer of self-organized Fe_4H SMMs (Figure 10.7f,g).

[3]TURBOMOLE 6.5, TURBOMOLE GmbH Karlsruhe, http://www.turbomole.com. TURBOMOLE is a development of the University of Karlsruhe and Forschungszentrum Karlsruhe 1989-2007, TURBOMOLE GmbH since 2007.

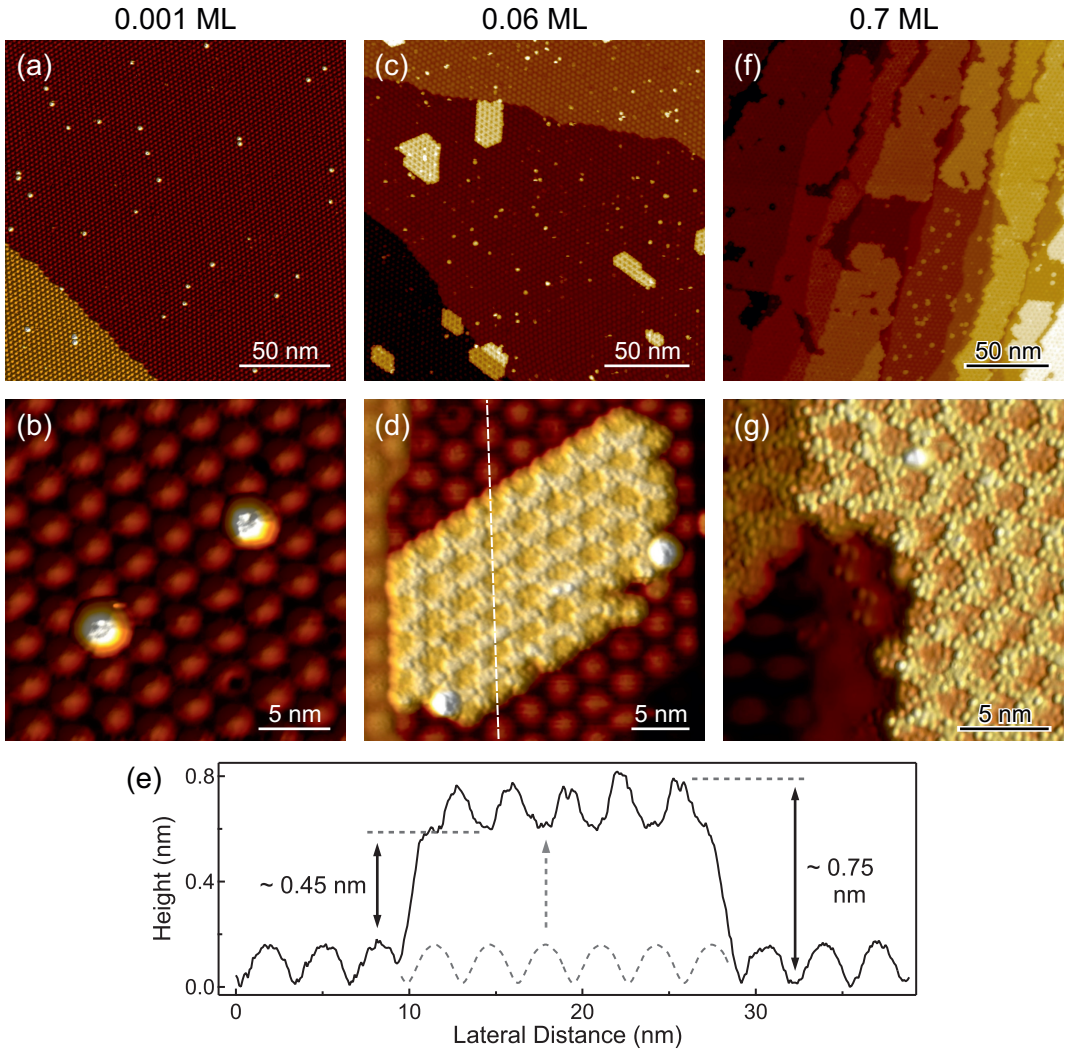

Figure 10.7 | Coverage dependent STM topographic images of Fe_4H on *h*-BN/Rh(111): **(a,b)** 0.001 ML, **(c,d)** 0.06 ML, **(f,g)** 0.7 ML. **(e)** Height profile along the dashed line in (d). An interpolation of the moiré pattern into the mid section is shown as a dashed line to point out the effect of contrast inversion. Scanning parameters: (a,b) $V = 2.5\,\mathrm{V}$, $I = 5\,\mathrm{pA}$, $T = 6.7\,\mathrm{K}$; (c-g) $V = 2.5\,\mathrm{V}$, $I = 10\,\mathrm{pA}$, $T = 1.9\,\mathrm{K}$.

As it can be seen in Figure 10.7, growth of islands begins prior to the complete occupation of pore sites by individual molecules. This finding elucidates the important role of intermolecular interactions in the system. While pore sites are energetically favored by molecule-substrate interaction, as concluded from the adsorption behavior in the low coverage regime and in accordance with studies of atoms and other molecules on *h*-BN/Rh(111) [157, 161–163], the additional energy necessary for the occupation of wire sites within islands is compensated by the decrease in energy through molecule-molecule interaction.

High resolution images of Fe_4H both as individual molecules and in islands re-

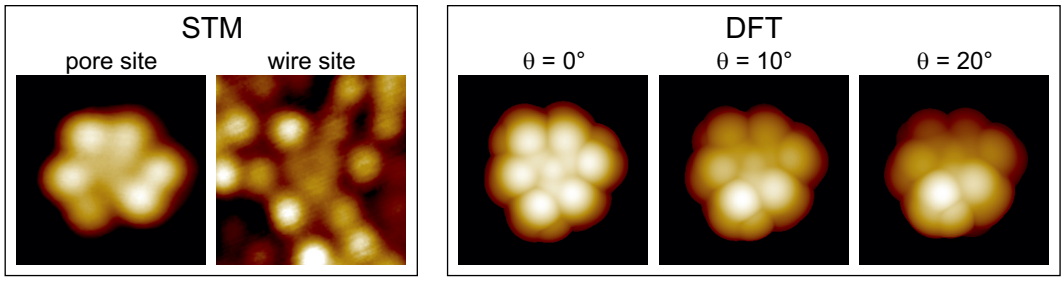

Figure 10.8 | **Left panel:** Experimental STM images of an individual Fe_4H molecule on a pore site and of an Fe_4H molecule embedded in an island on a wire site. Image size $2.4 \times 2.4\,nm^2$, scanning parameters: $V = 2.5\,V$, $I = 10\,pA$. **Right panel:** Simulated (DFT) STM images of Fe_4H determined from the density of states by considering all unoccupied molecular orbitals up to -1.5 eV (see later in Figure 10.12b). Different angles θ between anisotropy axis and surface normal are also shown. (The left image corresponds to the molecular orientation as depicted in Figure 10.1a. Rotation takes place around a horizontal axis through the central Fe atom.)

veal a clear intramolecular structure with an almost threefold rotational symmetry that comprises six protrusions, arranged in three pairs (Figure 10.8 left panel). In order to associate this structure with the molecular geometry, we compare our STM measurements to a DFT calculation of a free Fe_4H molecule. Simulated STM images were calculated for different angles θ between the scanning plane and the plane of the four Fe atoms (Figure 10.8 right panel). The simulation is in good agreement with our measurement for $\theta = 0$, whereas significant deviations are observed for $\theta > 10°$. We conclude that Fe_4H adsorbs on the substrate in a flat geometry, meaning that the plane of the four iron atoms is oriented almost parallel to the surface. The protrusions are therefore identified as the six dpm ligands of the organic ligand shell. Since the anisotropy axis of Fe_4 is perpendicular to the plane of the Fe atoms [11, 242, 251], the adsorption configuration corresponds to a perpendicular alignment of the magnetic easy axis of the molecule with respect to the surface.

Detailed imaging of the internal structure of the islands shows that the molecules can be arranged in two different hexagonal periodic lattices, forming either a $(1/2 \times 1/2)$ or a $(1/\sqrt{3} \times 1/\sqrt{3})R30°$ superstructure with respect to the h-BN moiré unit cell (Figure 10.9). For the $(1/\sqrt{3} \times 1/\sqrt{3})R30°$ superstructure, only one translational domain has been observed, in which Fe_4H molecules are occupying the pore sites of the moiré pattern (Figure 10.9d). In contrast to this, the majority of islands in $(1/2 \times 1/2)$ superstructure cannot be ascribed exclusively to one arrangement, but exhibits different translational domains. Two preferred arrangements have been observed, for which the pore positions coincide either with on top positions or with bridge positions of the hexagonal lattice of the molecules (Figure 10.9b,c). Due to the symmetry of the substrate, three different crystallographically equivalent translational domains

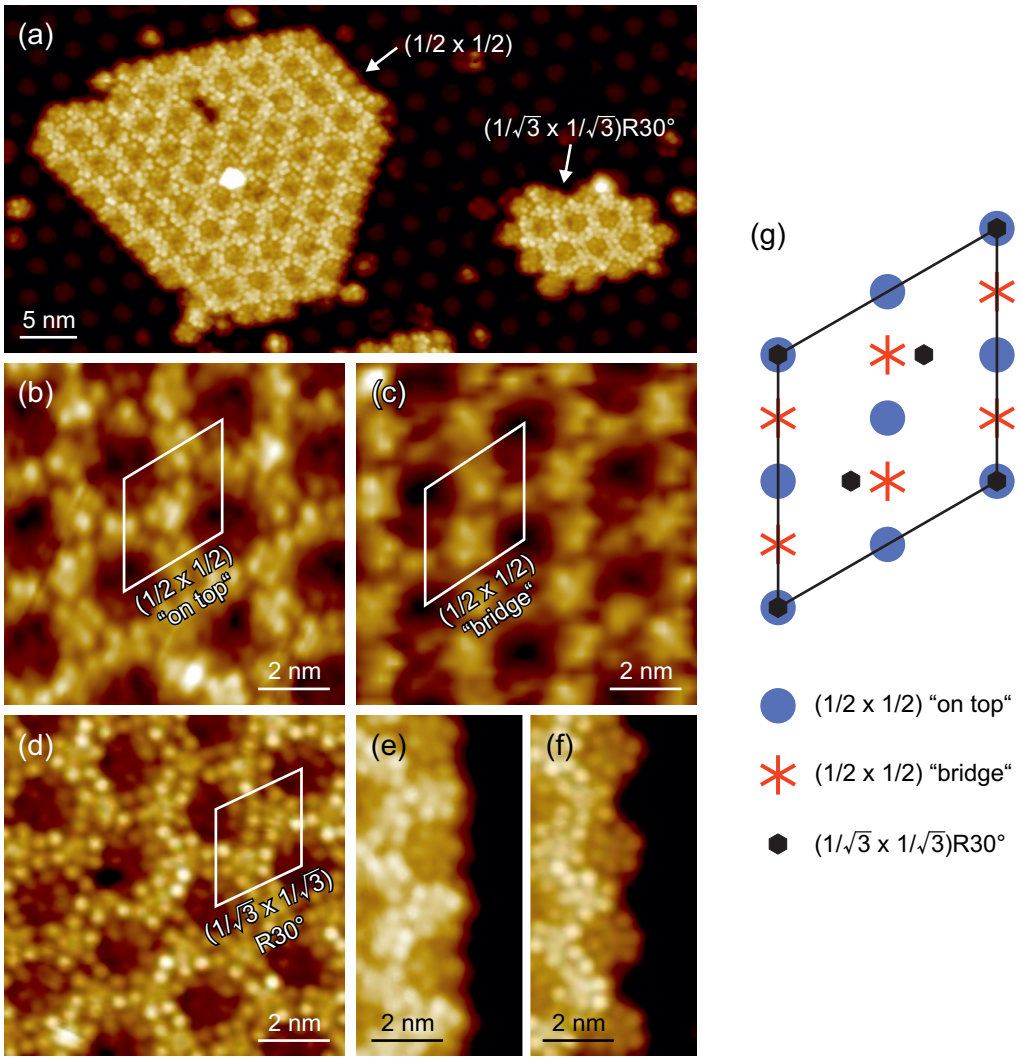

Figure 10.9 | **(a)** STM image of two Fe_4H islands with different superstructures. **(b-d)** Detailed views of the molecular arrangements for the observed superstructures. The white parallelogram marks the moiré unit cell with the pores being centered at the corners. **(e,f)** Detailed images of the edge structure for the $(1/2 \times 1/2)$ and $(1/\sqrt{3} \times 1/\sqrt{3})R30°$ superstructure, respectively. **(g)** Model of the exact positions of the molecules within the moiré unit cell. Scanning parameters for all STM images: $V = 2.5\,\mathrm{V}$, $I = 10\,\mathrm{pA}$ and $T = 1.9\,\mathrm{K}$.

exist for the bridge configuration, of which only one is shown in Figure 10.9.

The frequency of occurrence of both superstructures strongly depends on the angular rotation of the *h*-BN layer relative to the Rh(111) surface. While about 90% of all ordered islands were found in $(1/2 \times 1/2)$ superstructure on *h*-BN domains with R0 orientation, only the $(1/\sqrt{3} \times 1/\sqrt{3})R30°$ superstructure was observed on rotational *h*-BN domains.

The preferred abundance of the $(1/2 \times 1/2)$ superstructure on R0 *h*-BN can be explained by comparing the nearest-neighbor distance of both superstructures

to the structural size of the Fe_4H complex. The nearest-neighbor distance of the $(1/2 \times 1/2)$ and $(1/\sqrt{3} \times 1/\sqrt{3})R30°$ superstructure is 1.60(5) nm and 1.85(6) nm, respectively, based on an R0 h-BN moiré period of $a_m = 3.2(1)$ nm [160, 166]. The average intrinsic distance between two Fe_4H molecules within the plane of the four Fe atoms can be estimated from X-ray diffraction measurements on crystalline material to be $d = 1.63$ nm. Therefore, a $(1/2 \times 1/2)$ superstructure matches the crystalline molecule-molecule distance of Fe_4H within the limits of accuracy, whereas the larger periodicity of the $(1/\sqrt{3} \times 1/\sqrt{3})R30°$ superstructure leads to a significant mismatch of 13%, rendering the latter one unfavorable in terms of intermolecular interaction.

In contrast, the exclusive appearance of the $(1/\sqrt{3} \times 1/\sqrt{3})R30°$ superstructure on rotational h-BN domains is obviously caused by steric hindrance. A rotation of the h-BN layer with respect to the Rh(111) surface leads to a decrease of a_m. In our experiment, rotational h-BN domains with moiré periodicities in the range of 2.8–3.0 nm have been observed. Since this is significantly smaller than $2\,d = 3.26$ nm, but of the same order or even larger than $\sqrt{3}\,d = 2.82$ nm, a $(1/2 \times 1/2)$ superstructure is excluded due to steric reasons, while a $(1/\sqrt{3} \times 1/\sqrt{3})R30°$ superstructure is still possible.

A remarkable difference between both superstructures is observed concerning the edge structure of the corresponding islands. While the molecules are forming straight edges in islands with $(1/2 \times 1/2)$ superstructure (Figure 10.9e), a zigzag arrangement is found for the $(1/\sqrt{3} \times 1/\sqrt{3})R30°$ superstructure, in which the outmost molecules are occupying pore positions (Figure 10.9f).

In order to give a qualitative explanation for this finding, we compare the unit cells of both edge structures concerning their ratio η of occupied pore to wire sites, as well as their average coordination number Z. A precise definition of both quantities is given by

$$\eta = \frac{\sum\limits_{i \in \Omega_p} p_i}{\sum\limits_{i \in \Omega_w} p_i}, \quad Z = \frac{\sum\limits_{i \in \Omega} p_i Z_i}{\sum\limits_{i \in \Omega} p_i}. \tag{10.6}$$

Here, the index i is enumerating the adsorption sites within the unit cell of the edge structure, p_i is the occupation number of site i, Z_i is the coordination number of site i, Ω_p and Ω_w are the sets of all pore and wire sites, respectively, and $\Omega = \Omega_p \cup \Omega_w$. In terms of molecule-substrate interaction, a large value of η is favored, whereas intermolecular interaction tends to maximize the value of Z.

The occupation and coordination numbers for each of the observed super- and edge structures are depicted in Figure 10.10. For the $(1/\sqrt{3} \times 1/\sqrt{3})R30°$ superstructure, zigzag edges offer both a higher value of $\eta = 3/4$ and of $Z = 34/7 \approx 4.9$, compared to the respective values of $\eta = 1/2$ and $Z = 38/9 \approx 4.2$ for straight edges. Therefore, formation of zigzag edges is energetically favorable. In contrast to

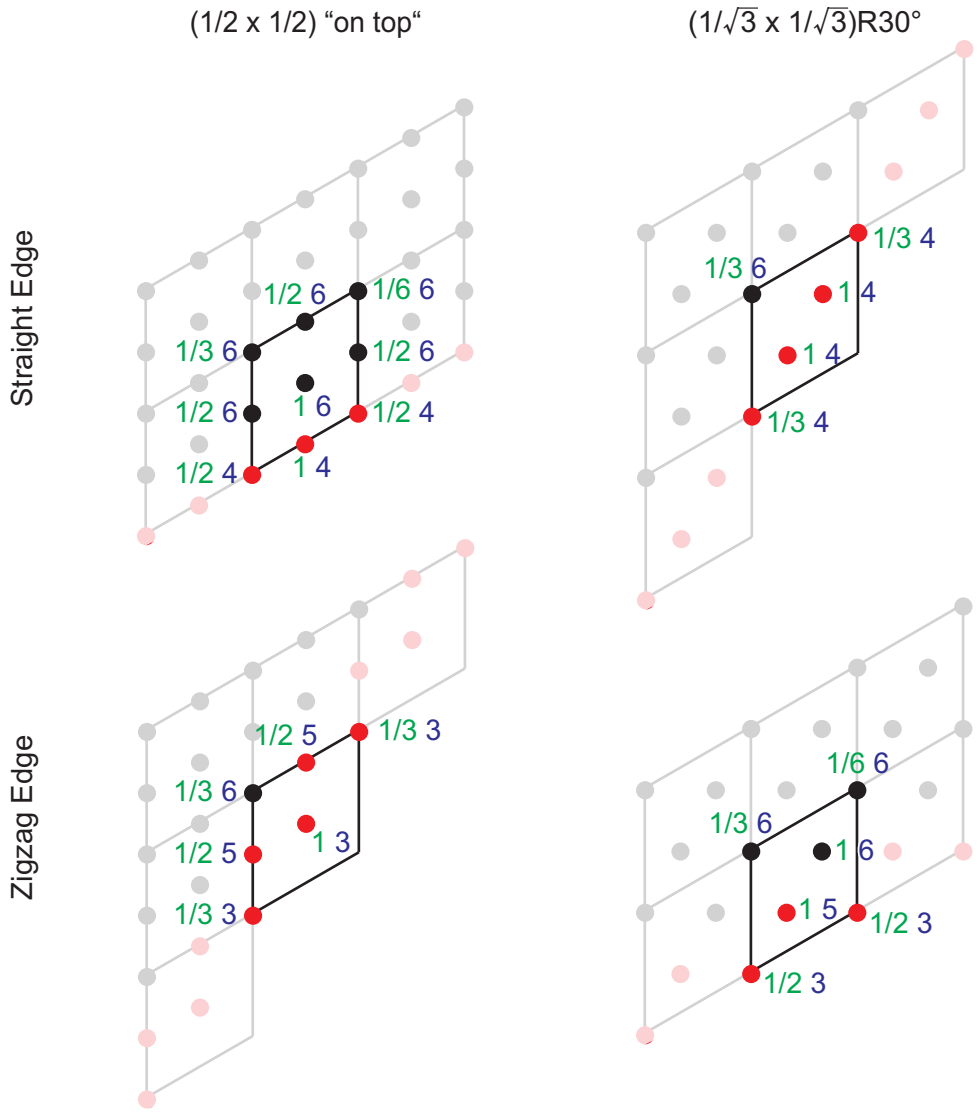

Figure 10.10 | Determination of η and Z for the observed super- and edge structures. Green and blue numbers refer to the occupation numbers p_i and coordination numbers Z_i of the individual adsorption sites within the edge structure unit cell, respectively.

this, the situation is not unambigious for the $(1/2 \times 1/2)$ superstructure. The argumentation can only be made for the "on top" configuration, for which zigzag edges ($\eta = 1/2$, $Z = 4$) are advantageous concerning the higher occupation of pore sites, while straight edges ($\eta = 3/7$, $Z = 5.2$) offer a larger coordination number. The formation of straight edges in the $(1/2 \times 1/2)$ superstructure is therefore obviously driven by intermolecular interactions.

10.3.2 Elastic Charge Transport

In order to investigate the electronic properties of the system, we performed differential conductance (dI/dV) measurements both on Fe_4H molecules and on clean h-BN/Rh(111) spots. All measurements were performed at $T = 1.9\,\mathrm{K}$ using a modulation voltage of $V_{\mathrm{mod}} = 40\,\mathrm{mV}$. To increase the dynamic range of the tunneling current, the separation between tip and sample was varied during the measurement, following a linear bias voltage dependence $z(V) = z_0 - \alpha|V - V_0|$. The starting distance z_0 was set by opening the feedback loop at $V = 3\,\mathrm{V}$ and $I = 20\,\mathrm{pA}$ and slopes of $\alpha = 0.8\,\mathrm{\AA V^{-1}}$ and $0.5\,\mathrm{\AA V^{-1}}$ were used for measurements on Fe_4H and on h-BN, respectively. Normalization of the spectra to I/V was carried out based on the method proposed by Prietsch et *al.* [101] with an offset constant of $2 \times 10^{-12}\,\mathrm{S}$.

Spectra of Fe_4H molecules were acquired both on the dpm ligands and on the center of Fe_4H. In addition, spectra were measured with respect to the position of the molecule within the moiré unit cell (pore or wire). Figure 10.11 compares the normalized spectra $(dI/dV)/(I/V)$ of these four cases. For negative bias voltages, the measurements do not show any significant features up to $-3\,\mathrm{V}$. On the other hand, all the investigated molecular spectra present a peak at positive bias voltages, while no such feature is observed in the reference measurement on the substrate next to the molecule. The location within the molecule (center/dpm ligand) affects both the position and the shape of the peak. A sharp resonance is observed on top of the dpm ligands, whereas a broader feature at higher energy is present when the measurement is performed above the center of the molecule. The respective peak positions are $1.56(3)\,\mathrm{V}$ and $1.84(5)\,\mathrm{V}$ for a molecule sitting on a pore site. When the spectrum is acquired on a molecule sitting on a wire site, the dpm ligand and center resonances are shifted by $0.35(4)\,\mathrm{V}$ and $0.40(5)\,\mathrm{V}$, respectively, while the overall shape of the spectrum is unaffected.

We assign the resonance measured at positive bias voltage to tunneling into the lowest unoccupied molecular orbital (LUMO) of Fe_4H. The shift of the LUMO resonance observed for different positions within the moiré unit cell can be attributed to the local work function difference between pore and wire sites. It was shown in a photoemission experiment that the work function on a pore is around $310(5)\,\mathrm{meV}$ lower than on a wire [157]. This work function difference is directly reflected in the local surface potential due to the build-up of electric dipole fields. The energy of the LUMO is defined by the electron affinity E_{A} with respect to the local vacuum level. Assuming that E_{A} is the same for both adsorption sites, the work function difference results in a shift of the LUMO with respect to the Fermi level of the Rh substrate and therefore enables tunneling into the LUMO at lower voltages on regions with lower work function. The same effect has been observed in recent STS studies of molecules adsorbed on a layer of h-BN on Ir(111) [252] and Cu(111) [253].

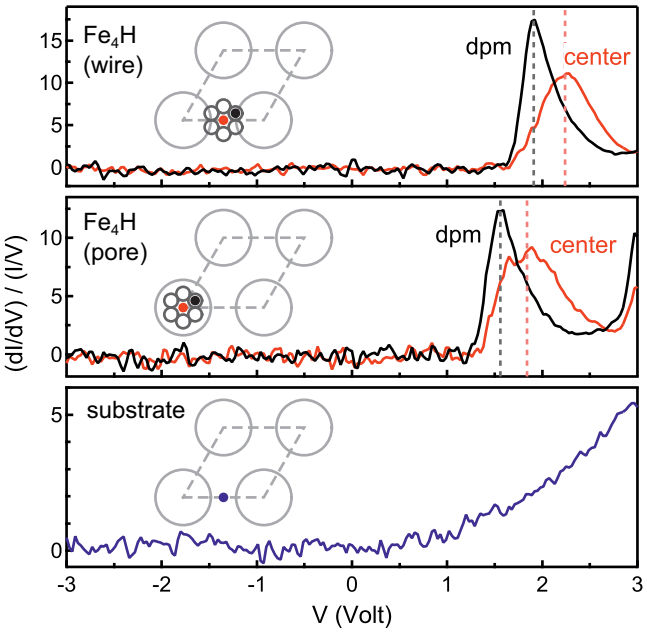

Figure 10.11 | Experimental $\mathrm{d}I/\mathrm{d}V$ spectra recorded on the dpm ligands (black lines) and on the center (red lines) of Fe_4H molecules, which occupy the h-BN wire sites (top panel) and pore sites (middle panel). A reference $\mathrm{d}I/\mathrm{d}V$ spectrum acquired on the clean h-BN/Rh(111) substrate is plotted for comparison (bottom panel). Spectroscopy parameters are given in the text.

It should be noted that spectra taken at center and dpm ligand positions of Fe_4H correspond to different points within the moiré unit cell. However, the observed dependence of the LUMO resonance on the position within the molecule cannot be explained by a work function variation of the substrate for several reasons: (1) The difference in surface potential cannot account for the different line widths of the resonances observed for both positions. (2) For a molecule sitting on a pore site, the surface potential will shift the LUMO resonance on the dpm ligand to larger voltages with respect to the center, whereas a shift to lower voltages will be the case when the molecule is sitting on a wire site. Clearly, such a change of sign is not observed. This effect however might account for the slightly different work function related shifts measured for the center and dpm ligand resonance.

In order to clarify the origin of the difference between the $\mathrm{d}I/\mathrm{d}V$ spectra obtained on the center and on the dpm ligand, we compare our measurements to the result of the spin-polarized first-principles calculation of a free Fe_4H molecule within DFT. Neglecting the influence of the substrate in the calculation is justified as the insulating h-BN layer effectively decouples adsorbed molecules from the metallic support. Experimental evidence for decoupling is given by the observation of a sharp resonance in the $\mathrm{d}I/\mathrm{d}V$ signal, as well as the measured adoption of the LUMO to the local vacuum level. Figure 10.12b shows the calculated spin-dependent projected density of states (PDOS) of Fe_4H. It is apparent that the LUMO of Fe_4H is spin split with an energy difference of 510 meV between minority and majority spin, the latter one being shifted to higher energy. The majority LUMO is mainly located at the central Fe atom with a small additional contribution coming from the two coordinating tripodal ligands L. In contrast to this, the minority LUMO can primarily

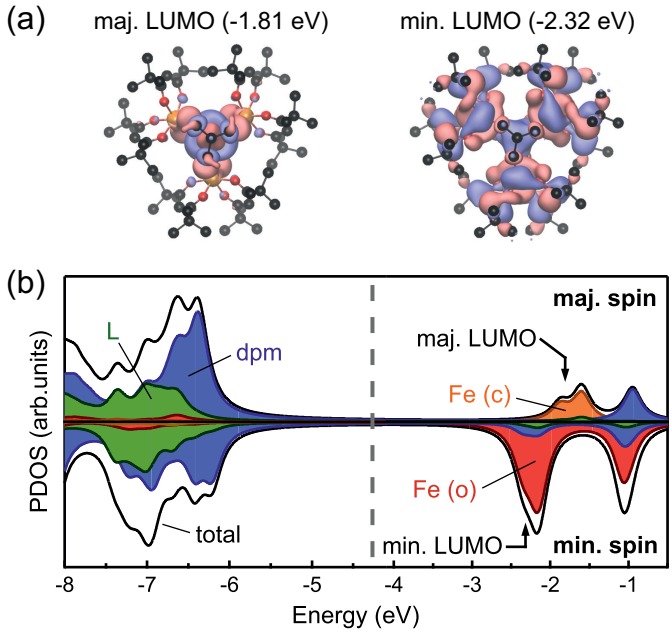

Figure 10.12 | DFT calculation of a free Fe_4H molecule. **(a)** Contour of the LUMOs for majority and minority spin electrons. **(b)** Spin-dependent total PDOS (black solid line) together with the projections on the central Fe (orange), outer Fe (red), dpm ligands (blue) and tripodal ligands L (green). The dashed line marks the center of the gap between the highest occupied molecular orbital (HOMO) and LUMO.

be allocated to the three outer Fe atoms with small additional fractions from the coordinating tripodal and dpm ligands. The majority LUMO is therefore located at the center of Fe_4H, while the minority LUMO can be mainly ascribed to the outer segments (Figure 10.12a).

Relying on both the distinctly different spatial distributions of the minority- and majority-spin LUMO predicted by DFT as well as the good agreement between the calculated spin splitting of the LUMO and the measured energy difference between the center and dpm ligand resonance, we attribute the spectral features observed at the center and at the dpm ligands to different spin projections. We therefore propose that electron transport within the used voltage range takes place mainly over the majority LUMO at the center of the Fe_4H molecule, whereas transport over the minority LUMO is dominating when the measurement is performed at the dpm ligands. These findings are a strong indication that the Fe_4 complex remains not only structurally intact upon the deposition on the *h*-BN surface, but also largely retains its electronic properties.

10.4 Fe_4H on Graphene/Ir(111)

We have demonstrated in the previous section that a single layer of hexagonal boron nitride can be used to electronically decouple Fe_4H molecules from the impact of the underlying metal substrate. At the same time, we have seen that the structural ordering of the molecules is influenced by the boron nitride layer itself, which is directly reflected in the formation of commensurate molecular superstructures. Here, we show that the impact of the substrate on the molecular assembly can be reduced by using graphene on Ir(111) as growth template. Like *h*-BN/Rh(111), graphene/Ir(111)

forms a highly periodic hexagonal moiré superstructure. In contrast to the strongly corrugated *h*-BN "nanomesh", the corrugation of the graphene layer on Ir(111) is relatively weak (see chapter 7). Furthermore, the electronic properties of both substrates are significantly different. While *h*-BN/Rh(111) is a wide-bandgap electric insulator, graphene/Ir(111) is electronically classified as a doped zero-gap semiconductor.

By means of low temperature scanning tunneling microscopy, we demonstrate that Fe_4H forms periodic self-assembled structures on graphene/Ir(111) as well. In contrast to *h*-BN/Rh(111), no correlation is observed between the order of these molecular assemblies and the moiré superstructure. The magnetic properties of the system are directly addressed by means of XMCD measurements. Furthermore, spin-flip excitations in individual molecules are observed using inelastic electron tunneling spectroscopy (IETS).

Sample preparation: Graphene/Ir(111) was prepared as described in chapter 7.3. Subsequent deposition of Fe_4H was carried out via ESD, using identical parameters as for *h*-BN/Rh(111) (see section 10.3).

10.4.1 STM Imaging

Figure 10.13a,b show overview STM images of the Fe_4H molecules on graphene/Ir(111) at submonolayer coverage. Islands of molecules are observed, which are located at step edges as well as on terraces of the substrate. A zoom on such an island is depicted in Figure 10.13c. In this image, the individual molecules are clearly resolved. The apparent height of the molecules is around 0.75 nm, which coincides with the value measured for Fe_4H on hBN/Rh(111) wire sites.

In contrast to *h*-BN/Rh(111), no isolated molecules are found on the surface. Some few isolated objects which are occasionally observed on the graphene terraces have neither the same apparent height nor the same lateral dimensions as the Fe_4H molecules that are organized in islands and are therefore ascribed to molecular fragments or impurities. This absence of isolated molecules already indicates the small impact of the graphene moiré structure on the adsorption behavior.

Although the topographic corrugation of the graphene/Ir(111) moiré structure is smaller than that of *h*-BN/Rh(111), the different trapping potential of both superstructures is most likely related to their electronic rather than their structural properties. For *h*-BN/Rh(111), it was shown that atoms and molecules are trapped by strong electric dipole fields that build up due to work function differences within the moiré unit cell [157]. As discussed in section 10.3.2, the lateral work function variation is directly reflected in STS measurements as a position dependent shift of the molecular levels. Since this bonding mechanism relies on a polarization of the molecule within the electrostatic landscape of the surface, it is chemically unspecific and therefore also applies to Fe_4H.

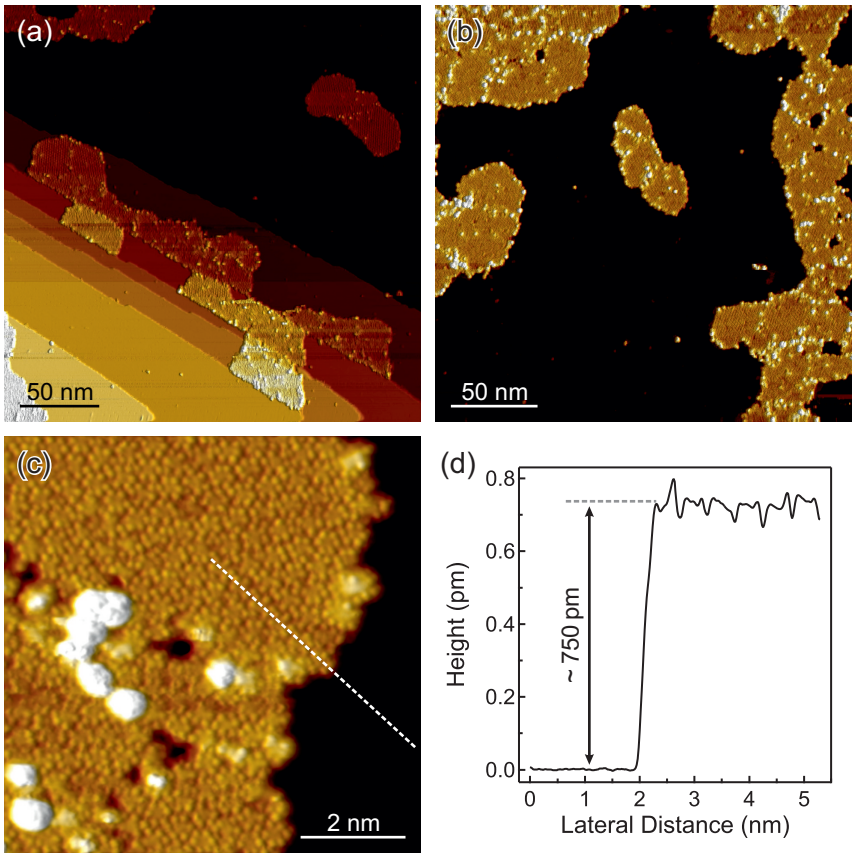

Figure 10.13 | **(a,b)** Overview STM images of Fe_4H on graphene/Ir(111). **(c)** Zoom on a molecular island, resolving the individual Fe_4H molecules. **(d)** Height profile along the dashed line in (c). Scanning parameters: (a) $V = 2.5\,\mathrm{V}$, $I = 20\,\mathrm{pA}$, $T = 6.9\,\mathrm{K}$; (b) $V = 2.5\,\mathrm{V}$, $I = 10\,\mathrm{pA}$, $T = 1.9\,\mathrm{K}$; (c) $V = 3\,\mathrm{V}$, $I = 10\,\mathrm{pA}$, $T = 1.8\,\mathrm{K}$.

It was shown by several authors that the graphene/Ir(111) moiré structure can serve as a template for the growth of atoms and molecules as well. For example, Ir atoms were reported to preferably adsorb on the fcc- and hcp regions of the graphene moiré structure [155]. The same positions – fcc and hcp – were found to be energetically favored for the adsorption of CoPc molecules [118]. The preference of these positions was explained by the authors with a covalent bonding mechanism. On fcc and hcp sites, three of the six C atoms in the carbon hexagon lie almost directly above an Ir atom of the Ir(111) surface and can therefore form a covalent bond to the substrate via hybridization of the C $2p_z$ with the Ir $3d$ orbitals. Since this induces a disturbance of the π-bonds in the carbon hexagon, it enables the remaining three C atoms to form a covalent bond to the adsorbed Ir atoms or CoPc molecules via hybridization with the $3d$ orbitals of the Ir adatoms and Co centers, respectively. However, in case of Fe_4H, the separation between the 3d metal sites and the graphene layer is much larger than for Ir atoms and CoPc molecules due to the protruding structure of the molecular ligand shell. It is therefore unlikely that a

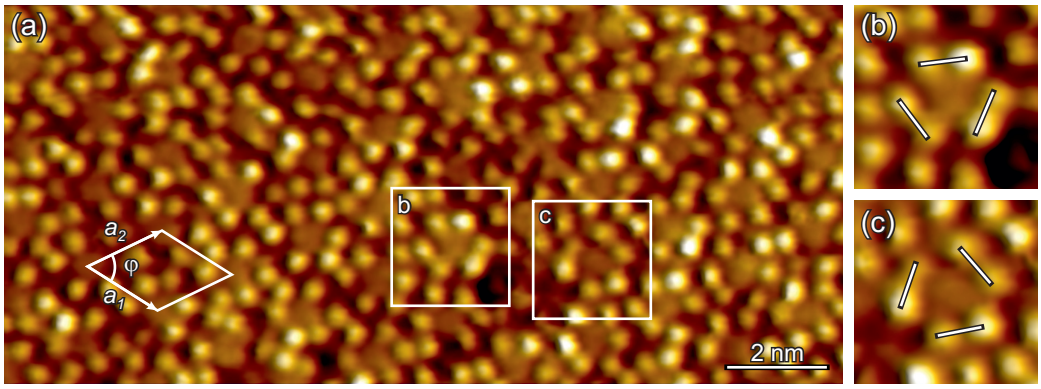

Figure 10.14 | **(a)** High resolution STM image showing the periodic assembly of the Fe_4H molecules in the observed islands. The unit cell of the periodic structure is indicated. **(b,c)** Magnification of the two individual molecules marked by white squares in (a). Pairs of adjacent dpm ligands are indicated by white lines. Scanning parameters: $V = 3\,\mathrm{V}$, $I = 10\,\mathrm{pA}$, $T = 1.8\,\mathrm{K}$.

hybridization takes place between the C $2p_z$ and Fe $3d$ orbitals, which explains our observation that Fe_4H is not trapped on the graphene moiré structure.

A high resolution STM image of the molecules in one of the self-assembled islands is shown in Figure 10.14a. The intramolecular structure is similar to that observed on *h*-BN/Rh(111), comprising six protrusions per molecule which are identified as the six dpm ligands. It is therefore concluded that Fe_4H adsorbs on graphene/Ir(111) in the same flat geometry, i.e. the magnetic easy axis of the molecule is oriented perpendicular to the surface, as in the case of *h*-BN/Rh(111). The arrangement of the molecules within the islands is found to be periodic with lattice parameters of $a_1 = (1.61 \pm 0.02)\,\mathrm{nm}$, $a_2 = (1.59 \pm 0.04)\,\mathrm{nm}$ and $\varphi = (58.1 \pm 1.8)°$. The given error intervals refer to the standard errors of the mean values estimated from a measurement on different islands. Additional systematic deviations in the values of all three lattice parameters due to drift effects generally cannot be ruled out.

We note that a hexagonal ordering of the molecules is possible within the accuracy of our measurement. However – apart from a possible influence of the substrate – there is no reason to expect a hexagonal structure to be more favorable than arrangements of lower symmetry, since the actual symmetry of the molecule is only C_3. Furthermore, we note that the lattice parameters are very close to the intrinsic ordering found in Fe_4H single crystals. As bulk material, Fe_4H crystallizes in the monoclinic system [243]. The arrangement of the molecules in the crystallographic (001) plane is depicted in Figure 10.15. The projection of the monoclinic unit cell on the (001) plane comprises a two-molecular basis. The nearest-neighbor distances are in the range of 1.622–1.632 nm and the angles to nearest-neighbors are the range of 59.8–60.4°.

The rotational orientation of the molecules with respect to the unit cell can be

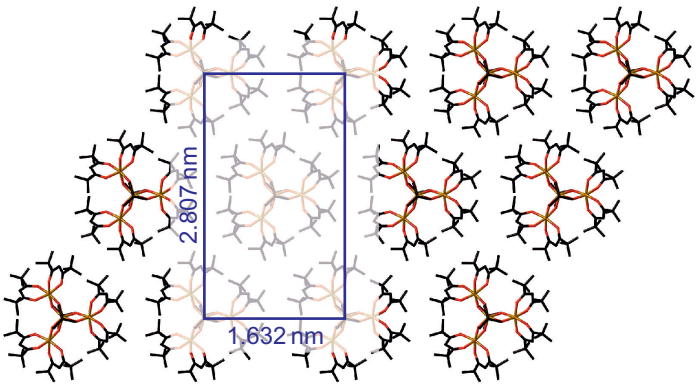

Figure 10.15 | Molecular arrangement in the (001) plane of an Fe_4H single crystal. The blue rectangle marks the projection of the monoclinic unit cell.

determined from the STM images by evaluating the position of the six dpm ligands. In accordance with the threefold molecular symmetry, the six ligands are arranged in three individual pairs that can be clearly identified for some of the molecules. We found that the self-assembled islands comprise a rotational disorder, in which the in-plane orientation of the molecules can differ by 60°. This peculiar aspect is demonstrated in Figure 10.14b,c. It shall be noted that the same disorder is observed on *h*-BN/Rh(111), as well as in Fe_4H bulk material. Detailed information about the latter case are provided elsewhere [243]. A possible explanation for the rotational disorder is that the symmetry of the outer ligand shell – from a steric point of view – is close to C_6. A rotation of individual molecules by 60° therefore results in only a small disturbance of the periodic structure.

The moiré pattern of the graphene layer is not visible on top of the islands, but can be imaged on uncovered graphene spots next to the islands simultaneously with the molecular assembly. From our STM images, we find no correlation between the ordering of the molecules and the moiré unit cell. This further corroborates the weak impact of the moiré superstructure on the adsorption behavior. In particular, no preferred orientation of the molecular unit cell with respect to the substrate is observed. As shown in detail in Figure 10.16a, most of the islands comprise multiple rotational domains. We assume that such multi-domain structures are formed from individual smaller islands that merge together during their growth process.

It is evident from Figure 10.16a that the domain boundaries and the edges of the islands act as pinning centers for objects that adsorb on top of the first Fe_4H layer. Magnified STM images, revealing the internal structure of these objects, are shown in Figure 10.16b,c. The lateral size of the objects typically is around 2 nm and their apparent height is in the range of 0.5–0.8 nm. The presence of these objects makes it easy to identify different rotational domains even in large scale STM images as Figure 10.13b. Based on the narrow size distribution and the overall topographic dimensions, it seems reasonable to suppose that the second layer objects are Fe_4H molecules. Since the intramolecular structure is not uniform and generally deviates from threefold rotational symmetry, we assume that the second layer molecules are

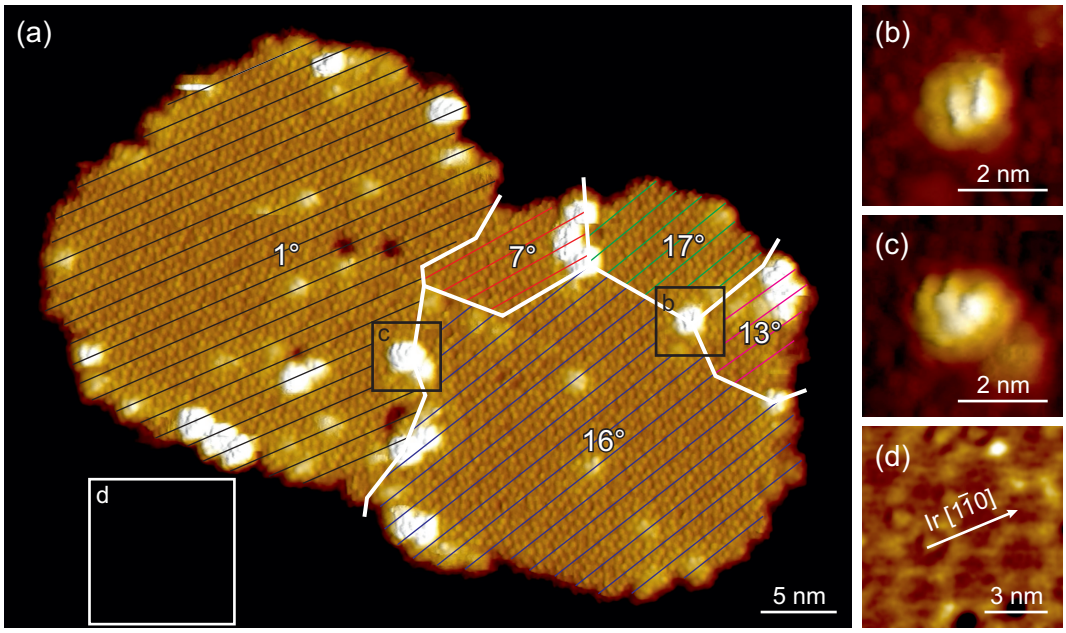

Figure 10.16 | **(a)** STM image showing rotational domains in an Fe_4H island on graphene/Ir(111). Colored lines inside the individual domains are drawn through the centers of adjacent molecules. The angle given for each domain refers to the orientation of these lines with respect to the particular [1$\bar{1}$0] direction of the Ir(111) substrate that is indicated in (d). Boundaries between the rotational domains are marked by white lines. **(b,c)** Magnified view of the areas that are marked by black squares in (a), showing the internal structure of second layer molecules. **(d)** The graphene moiré structure is clearly visible next to the island when adapting the color scale to its height range. Determination of the Ir [1$\bar{1}$0] direction was performed based the orientation of the moiré unit cell. Scanning parameters: $V = 3\,\mathrm{V}$, $I = 10\,\mathrm{pA}$, $T = 2.3\,\mathrm{K}$.

randomly oriented. This finding is most likely explained by the non-uniform adsorption geometry provided by the island edges and domain wall sites.

10.4.2 XAS and XMCD Measurements

In order to get insight into the electronic structure and magnetic properties of an Fe_4H submonolayer on graphene/Ir(111), we utilized X-ray absorption based techniques, namely X-ray absorption spectroscopy (XAS) and X-ray magnetic circular dichroism (XMCD). Both methods provide highly surface sensitive and element selective information about oxidation states and magnetic moments and are therefore considered to be key tools for studying electronic and magnetic phenomena at surfaces.

The measurements were performed at the X-Treme beamline of the Swiss Light Source (SLS) synchrotron radiation facility [254]. The end station of the beamline is equipped with a scanning tunneling microscope and contains a separate UHV

chamber that offers standard tools for sample preparation, including an Ar^+ sputter gun, a heating stage and leak valves for controlled gas inlet. Sample preparation was performed completely *in situ*. For the preparation of clean graphene/Ir(111) substrates, the procedure described in chapter 7.3 was adapted to lower substrate temperatures in order to comply with the restrictions of the experimental setup ($\sim$ 1100–1200 °C for cleaning of Ir(111) and 1100 °C for growth of graphene via CVD). A good quality of the graphene layers was verified by means of STM imaging. In order to allow for an *in situ* deposition of Fe_4H, the ESD setup was transported to the synchrotron facility and attached to the UHV system of the end station via a gate valve. The surface coverage was estimated by correlating XAS and STM data. All results presented here were obtained on a single sample with 0.55 ML coverage. Furthermore, an Fe_4H powder sample was used as a reference.

Measurements of the XAS signal were performed in the total electron yield (TEY) mode, using circularly polarized X-rays. Here, σ_+ and σ_- refer to a parallel and antiparallel alignment of the helicity and beam direction, respectively. The XMCD signal is calculated by taking the difference between both polarizations, i.e. $\sigma_+ - \sigma_-$. In order to prevent radiation damage (degradation of the molecules induced by X-ray radiation) the sample was placed out of focus of the X-ray beam, resulting in a spot size of around $0.5 \times 1.5\,\mathrm{mm}^2$. Furthermore, the photon flux was reduced as much as possible by setting the monochromator of the beamline to high energy resolution ($c_{\mathrm{ff}} = 10$, front end opening $0.25 \times 0.25\,\mathrm{mm}^2$, exit slit opening $5\,\mu$m - see [254] for details).

During the measurements, the sample was placed in a ^{4}He evaporation cryostat that provides magnetic fields of up to 7 T in beam direction. By rotating the sample around an axis perpendicular to the beam, signals were obtained at different angles θ of the magnetic field with respect to the surface normal. All measurements were performed at the lowest temperature possible. For this purpose, the 1-K pot of the cryostat was completely filled with liquid He in advance of the measurements and subsequently disconnected from the He bath, resulting in a single-shot mode. During this procedure, the 1-K pot reached a temperature of around 1.4 K and the sample reached a temperature of $T < 3\,\mathrm{K}$, depending on the sample and sample holder geometry (see below).

Figure 10.17 shows XAS and XMCD spectra taken at the Fe $L_{2,3}$ ($2p \rightarrow 3d$) absorption edges of both the powder sample and the Fe_4H submonolayer. On the timescale of our measurements[4], no change was observed in the shape of the XAS spectra, indicating that no radiation damage occurs. The spectral features observed in XAS are almost identical for both samples and coincide well with data reported for similar Fe_4 derivatives [11, 236, 242, 255]. Generally, the shape of the XAS spectrum is highly sensitive to the Fe oxidation state. Our measurements therefore indicate

[4]Taking a complete data set of a single sample takes several hours.

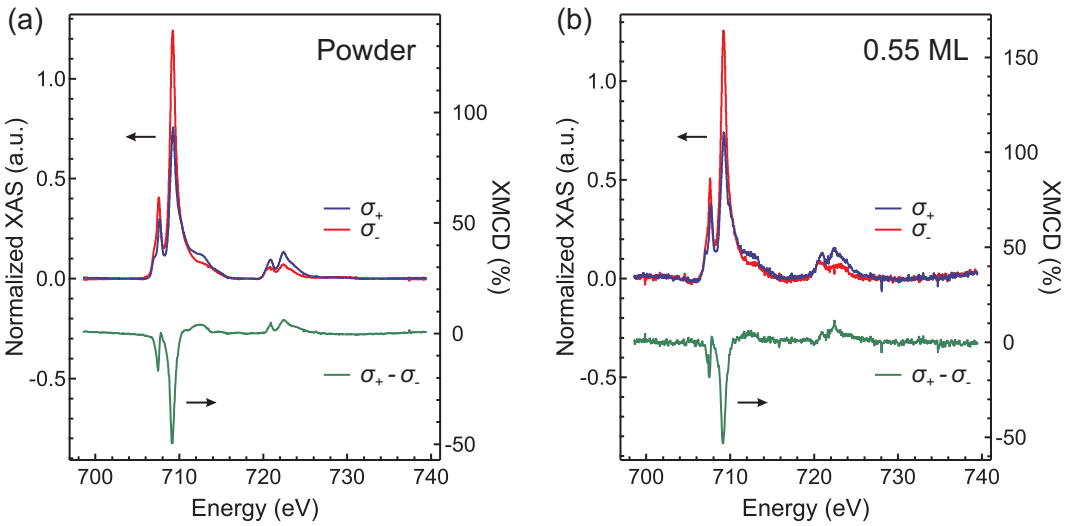

Figure 10.17 | XAS and XMCD spectra at the Fe $L_{2,3}$ edges, obtained on an Fe_4H powder sample **(a)** and on 0.55 ML Fe_4H on graphene/Ir(111) **(b)**. Data were acquired in a magnetic field of 6.8 T and at $T < 3$ K. All spectra are normalized to the intensity of $(\sigma_+ + \sigma_-)/2$ at the main peak of the L_3 edge (709.2 eV).

that the electronic structure of the molecule is largely unaffected by the deposition on graphene/Ir(111). The good coincidence of both samples is also reflected in their XMCD signals. Both the shape and the amplitude of the XMCD response agree well with data reported for other Fe_4 compounds [11,236,242,255]. It was demonstrated in [255] that the measured XMCD spectrum is reflecting the ferrimagnetic configuration of the central and the peripheral Fe sites. Our data therefore further corroborate that intact Fe_4H molecules are present on the sample surface.

Magnetization curves of both samples were obtained by measuring the magnetic field dependence of the XMCD signal at the energy of its highest intensity (709.2 eV). In case of the powder sample, no influence of the orientation of the magnetic field on the XMCD signal is expected since the sample is isotropic. The measurement shown here was obtained at $\theta = 20°$. In contrast, magnetization curves of the Fe_4H submonolayer were obtained both with out-of-plane ($\theta = 0°$) and partially in-plane ($\theta = 60°$) orientation of the magnetic field. The recorded magnetization curves are depicted in Figure 10.18.

For the Fe_4H submonolayer, the magnetization obtained at $\theta = 0°$ is significantly larger than for $\theta = 60°$, indicating an out-of-plane magnetic anisotropy of the sample. This is in well agreement with the STM measurements discussed in section 10.4.1, where Fe_4H was found to adsorb on graphene/Ir(111) in a flat geometry with the idealized C_3 axis pointing perpendicular to the sample surface.

In order to quantitatively analyze the recorded magnetization curves, we performed a fit of the experimental data based on the simple ZFS Hamiltonian (10.2). In accordance with the STM results, the magnetization of the Fe_4H/graphene sub-

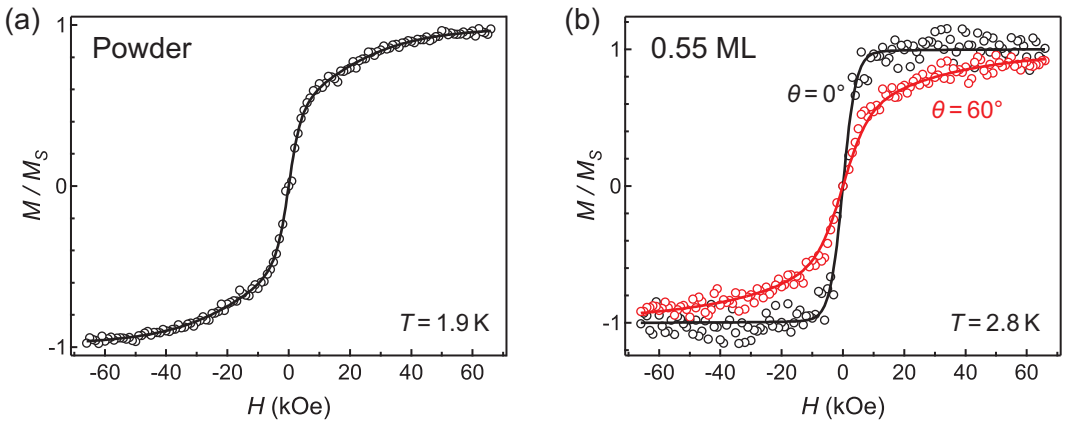

Figure 10.18 | Magnetization curves obtained by recording the magnetic field dependence of the XMCD signal at the Fe L_3 edge for the Fe_4H powder sample **(a)** and for 0.55 ML Fe_4H on graphene/Ir(111) **(b)**. Experimental data were symmetrized by replacing $M(H)$ with $(M(H) - M(-H))/2$. Solid lines represent fits to the data based on the models that are described in the text.

monolayer was calculated on the assumption that the anisotropy axes of all molecules are oriented along the surface normal, meaning that the angle θ directly reflects the orientation of the magnetic field with respect to the anisotropy axis. In contrast, for the powder sample, the calculated magnetization was averaged over all possible field orientations to account for the random orientation of the crystallites in the material. The fitting of the data was carried out by keeping the spin quantum number and Landé factor fixed to $S = 5$ and $g = 2$, respectively, and refining the temperature T and anisotropy constant D. The best-fit parameters so obtained are $T = (1.9 \pm 0.2)$ K, $D = -(0.44 \pm 0.03)\,\mathrm{cm}^{-1}$ for the powder sample and $T = (2.8 \pm 0.3)$ K, $D = -(0.51 \pm 0.07)\,\mathrm{cm}^{-1}$ for Fe_4H/graphene. The magnetization curves calculated from the best-fit results coincide well with our experimental data, as can be seen from Figure 10.18.

The good agreement between calculation and experiment corroborates the out-of-plane orientation of the magnetic easy axis and demonstrates that the assumption of an $S = 5$ spin ground state of Fe_4H on graphene/Ir(111) is justified. Notably, the anisotropy constant D of the Fe_4H/graphene submonolayer coincides with that of the powder sample within the accuracy of our measurement. Furthermore, both values are in agreement with the bulk value of D as obtained from SQUID magnetometry on polycrystalline material (see section 10.1). We therefore conclude that the magnetic anisotropy constant D of Fe_4H is unaffected upon the deposition on graphene/Ir(111).

The different temperature values obtained for the Fe_4H submonolayer and powder sample can be ascribed to the different mounting of both samples during the XMCD measurements. The Ir(111) crystal used for the preparation of the submono-

layer was mounted on an Omicron sample plate made of molybdenum, which in turn was clamped on a special sample holder that fits into the insert of the Cryostat. In contrast, the Fe_4H powder sample was in direct contact to that sample holder, resulting in a better thermal coupling to the 1-K pot of the cryostat and therefore in a lower temperature. We note that the best-fit value of the temperature obtained for the Fe_4H submonolayer is in good agreement with the value expected for this sample holder geometry, based on experiences with other experiments at the X-treme beamline[5].

In conclusion, the results presented in this chapter corroborate the outstanding stability of the magnetic properties of the Fe_4 complex. Due to the well defined orientation the magnetic easy-axis, Fe_4H on graphene/Ir(111) is demonstrated to be a promising system for further studies aiming at an implementation of SMMs in nanoscale spintronic devices.

10.4.3 Inelastic Electron Tunneling Spectroscopy

Inelastic electron tunneling spectroscopy (IETS) offers the possibility to extend the information provided by XMCD in several respects. First, IETS is capable of probing magnetic properties on the single molecule level. This is in contrast to XMCD, where a signal is acquired on a macroscopic area of the sample, therefore reflecting an average over a large number of molecules. Furthermore, IETS can give direct insight into the exchange coupling between the different spin centers in an individual molecule. Such information are difficult to attain by means of XMCD as they require temperature dependent measurements up to 300 K, which suffer from small signal amplitudes. Here, we present first preliminary results demonstrating that IETS is an appropriate method to detect spin-flip excitations in individual Fe_4H molecules on graphene/Ir(111).

Spectroscopic data were acquired by placing the STM tip above the center of the molecules and detecting the differential conductance $\mathrm{d}I/\mathrm{d}V$ as a function of the bias voltage V in the range of $\pm$10–20 mV. Figure 10.19 shows a conductance curve obtained on a single Fe_4H molecule, as well as a reference measurement performed on the clean graphene/Ir(111) substrate. Both curves were recorded at a temperature of 1.9 K and in a magnetic field of 1 T applied perpendicular to the sample surface. The spectrum acquired on Fe_4H shows symmetric steps around the Fermi energy, which are a fingerprint of inelastic excitations. In contrast, no such feature is observed on graphene/Ir(111). We note that the center of the two steps is slightly shifted with respect to the Fermi energy by around 660 μV. A shift of this magnitude can be attributed to the buildup of thermovoltages between tip and sample, as well as to a possible voltage offset of our STM preamplifier.

[5] Stefano Rusponi, private communication.

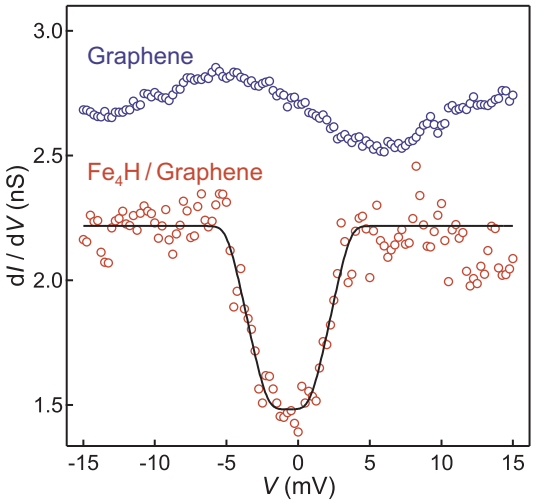

Figure 10.19 | Conductance spectra obtained on an individual Fe_4H molecule and on graphene/Ir(111). Spectroscopy parameters: $V_s = 25\,\mathrm{mV}$, $I_s = 50/250\,\mathrm{pA}$ (for Fe_4H and graphene, respectively), $V_{mod} = 1\,\mathrm{mV}$, $T = 1.9\,\mathrm{K}$. A magnetic field of 1 T was applied in out-of-plane direction. The conductance curve obtained on graphene is divided by a factor of 5 to account for the higher set current and shifted by 0.5 nS for clarity. The solid curve is a fit to the Fe_4H spectrum based on the model described in the text.

In order to determine the excitation energy, a fit of the Fe_4H spectrum is performed based on equation (3.19), describing the contribution of inelastic processes to the tunnel current. The elastic contribution to the current is assumed to be linear in the small bias voltage range of our measurement, therefore resulting in a simple offset constant in $\mathrm{d}I/\mathrm{d}V$. The broadening of the experimental spectrum caused by the modulation voltage of the lock-in amplifier is taken into account by convolving the calculated curve with a half circle of radius $\sqrt{2}V_{mod}$, according to equation (3.25). The best fit yields an excitation energy of 2.9 meV. The corresponding conductance curve is shown as a solid line in Figure 10.19.

Since vibrational excitations typically appear two orders of magnitude higher in energy, we attribute the inelastic feature observed in our measurement to a spin-flip excitation in the Fe_4H complex. An experimental proof of this interpretation can be provided by measuring the magnetic field dependence of the excitation energy, which is the aim of future work. To get insight into the exact origin of the excitation process, we quantitatively calculate the energies of possible spin-flip transitions in the Fe_4H complex. For a calculation of the complete spectrum of spin states, we consider the Hamiltonian

$$\mathcal{H} = J_1 \boldsymbol{S}_1 \cdot \sum_{i\neq 1} \boldsymbol{S}_i + \frac{J_2}{2} \sum_{i\neq j} \boldsymbol{S}_i \cdot \boldsymbol{S}_j + D S_z^2 + g\mu_B H S_z, \tag{10.7}$$

taking into account both exchange interactions and uniaxial magnetic anisotropy. Here, the same notation is used as in chapter 10.1, i.e. $\boldsymbol{S}_1$ is the spin of the central Fe atom, $\boldsymbol{S}_{i\neq 1}$ are the spins of the peripheral Fe atoms, S_z is the out-of-plane projection of the total spin $\boldsymbol{S} = \sum_{i=1}^{4} \boldsymbol{S}_i$, J_1 and J_2 are the nearest and next-nearest-neighbor exchange constants, D is the anisotropy constant, g is the Landé factor and H is the amplitude of the magnetic field. Higher order terms in magnetic anisotropy are neglected in (10.7) and the value of D is assumed to be the same for all spin

multiplets S.

As already discussed in chapter 9.4.4, spin excitations induced by tunneling electrons obey the selection rule $\Delta M = 0, \pm 1$. At 1.9 K, most likely the $|S, M\rangle = |5, 5\rangle$ ground spin state is initially occupied[6]. Therefore, the spin-flip excitation with the lowest energy is a transition between the adjacent $M = 5$ and $M = 4$ states of the $S = 5$ ground state multiplet. Transitions from $|5, 5\rangle$ into $|4, 4\rangle$, $|6, 4\rangle$, $|6, 5\rangle$ and $|6, 6\rangle$ states, involving a change of the spin quantum number S, are possible at higher excitation energies.

Since the lowest energy transition $|5, 5\rangle \rightarrow |5, 4\rangle$ takes place within the same spin multiplet, its excitation energy can be calculated from the anisotropy and Zeeman terms in (10.7) alone, yielding

$$\Delta E_{|5,5\rangle \rightarrow |5,4\rangle} = 9|D| + g\mu_B|H|. \tag{10.8}$$

Substituting the bulk values of $D = -0.427\,\mathrm{cm}^{-1}$ ($-52.9\,\mu$eV) and $g = 1.994$ into (10.8) and taking into account the value of the magnetic field used in our measurement, the expected excitation energy is 0.59 meV.

In contrast, spin-flip transitions into higher spin multiplets are energetically dominated by the Heisenberg terms in (10.7). As reported in [256], it is possible to diagonalize the Heisenberg Hamiltonian analytically. Using the notation $\boldsymbol{S}_{\mathrm{ext}} = \sum_{i=2}^{4} \boldsymbol{S}_i$ for the sum of the three peripheral spin operators and denoting the respective spin quantum number S_{ext}, the eigenvalues of the Heisenberg Hamiltonian are given by

$$E(S, S_{\mathrm{ext}}) = \frac{J_1}{2} S(S+1) + \frac{J_2 - J_1}{2} S_{\mathrm{ext}}(S_{\mathrm{ext}} + 1). \tag{10.9}$$

Figure 10.20a shows the exchange energy as a function of the total spin S, calculated for coupling constant values of $J_1 = 16.94\,\mathrm{cm}^{-1}$ (2.101 meV) and $J_2 = 0.95\,\mathrm{cm}^{-1}$ (0.12 meV) as measured on Fe_4H bulk material. The two lowest lying spin multiplets that can be addressed by spin-flip excitations are an $S = 4$ ($S_{\mathrm{ext}} = 13/2$) state, having an energy of $\frac{5}{2}J_1 - \frac{15}{2}J_2 = 4.37$ meV with respect to the ground state multiplet, followed by an $S = 6$ ($S_{\mathrm{ext}} = 15/2$) state at $6J_1 = 12.6$ meV. For a calculation of the energies of spin-flip transitions into these multiplets, the ZFS and Zeeman terms need to be taken into account in addition. In particular, the expected excitation energy of the $|5, 5\rangle \rightarrow |4, 4\rangle$ transition in a magnetic field of $H = 1$ T is 4.96 meV.

On the basis of the calculated energy values, we ascribe the inelastic excitation observed in our measurement to the transition into the $S = 4$ multiplet, i.e. $|5, 5\rangle \rightarrow |4, 4\rangle$. The low energy transition $|5, 5\rangle \rightarrow |5, 4\rangle$ is not observed in the spectroscopic signal, which can be well explained by taking into account the finite energy resolution of the measurement. From the temperature value and lock-in modulation

[6] The direction of the magnetic field is defined here so that the energy of $|S, |M|\rangle$ is lower than that of $|S, -|M|\rangle$.

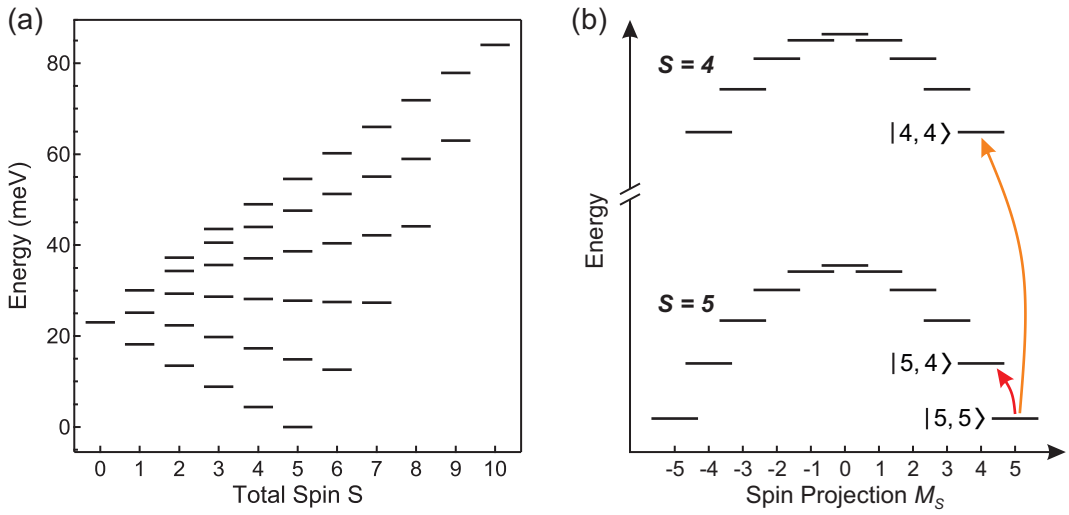

Figure 10.20 | **(a)** Eigenstates of the Heisenberg Hamiltonian as a function of the total spin S, calculated for Fe_4H bulk material (values of J_1 and J_2 given in the text). The ground state and the first excited state are an $S = 5$ and $S = 4$ multiplet, respectively. **(b)** Schematic sketch of the two lowest energy transitions $|5, 5\rangle \rightarrow |5, 4\rangle$ (red arrow) and $|5, 5\rangle \rightarrow |4, 4\rangle$ (orange arrow) in zero magnetic field. The degeneracy of the $S = 5$ and $S = 4$ multiplets is lifted due to magnetic anisotropy.

amplitude, the energy resolution of the spectrum shown in Figure 10.19 is calculated to be 2.6 meV, which is significantly larger than the expected energy separation of the two steps in $\mathrm{d}I/\mathrm{d}V$. As a result, the spectroscopic signal of the $|5, 5\rangle \rightarrow |5, 4\rangle$ transition is expected to be strongly smeared out and reduced in intensity. It shall be noted that no considerable improvement in energy resolution can be achieved by reducing the lock-in modulation amplitude, which was demonstrated by spectroscopic measurements previously performed in our group [118]. It therefore seems unlikely that the $|5, 5\rangle \rightarrow |5, 4\rangle$ transition can be resolved with our experimental setup.

We note that the measured value of the excitation energy is around 42 % smaller than the value calculated for the $|5, 5\rangle \rightarrow |4, 4\rangle$ transition from the anisotropy and exchange parameters of Fe_4H bulk material. A change of this magnitude cannot be explained by a reduction of the anisotropy parameter D, since the zero field splitting of the $M = 5$ and $M = 4$ levels only accounts for a contribution of $9|D| = 0.48$ meV to the excitation energy. Furthermore, a significant change in D can be ruled out based on the XMCD measurements that were reported in the previous section. Therefore, we ascribe the observed deviation in excitation energy to a reduction of the exchange coupling constant J_1. Generally, a change in J_2 is possible as well, but will only have a small impact on the excitation energy, since $J_2 \ll J_1$. For the sake of simplicity, we therefore neglect the next-nearest-neighbor exchange term in the following discussion by assuming $J_2 = 0$. The measured value of the excitation energy of 2.9 meV then corresponds to a nearest-neighbor constant of $J_1 = 7.5\,\mathrm{cm}^{-1}$ (0.93 meV), i.e. a

reduction of J_1 by around a factor of two.

Several effects must be taken into account in order to explain the observed change in J_1. According to a recent IETS and DFT study of another Fe_4 derivative on a Cu_2N surface [257], the structural and electronic influence of the substrate reduces the coupling constant by around 39 %. In order to clarify whether a reduction of the same order is expected for Fe_4H/graphene/Ir(111), additional DFT calculations of this system are required. Furthermore, a better experimental statistic is necessary to check if the inelastic excitation is observed at the same energy for all molecules on the surface. At the moment, a statistical IETS study is performed in our group by Fabian Paschke. First results indicate a distribution of different excitation energies with a mean corresponding well to the excitation energy expected for bulk material. A possible influence of the substrate might therefore result in either a decrease or increase in J_1, depending on the adsorption site.

Another important aspect is the influence of the STM tip on the molecular geometry. Generally, the exchange coupling is very sensitive towards a change in the Fe-O-Fe bond angles. In [257], it was shown that a 2 % compression of the molecular core parallel to the C_3 axis increases J_1 by a factor of 1.9. On the basis of this argument, the authors ascribed a too large value of the excitation energy measured by IETS to the confinement of the molecule in the substrate-tip junction. However, a tip induced compression of the molecule can be ruled out in our case, since it results in the opposite qualitative trend in J_1.

Summary and Outlook

Over the last decade, electrospray deposition (ESD) and electrospray ion beam deposition (ESIBD) have evolved into powerful tools for the transfer of nonvolatile compounds onto electrically conductive substrates in ultra-high vacuum (UHV). The development of these versatile techniques has opened up new perspectives for the implementation of functional molecules as building blocks in information technology. However, the possible impact of the substrate on the molecular functionality and the difficulty to contact individual molecules to metallic electrodes remain major challenges in this field.

Within this thesis, ESD has been applied to deposit single molecule magnets (SMMs) on atomically flat substrates and subsequently address the electronic and magnetic properties of the molecules by means of scanning tunneling microscopy and spectroscopy (STM/STS), X-ray photoelectron spectroscopy (XPS), X-ray absorption spectroscopy (XAS) and X-ray magnetic circular dichroism (XMCD). The experiments were carried out on two different molecular compounds: Mn_{12} and Fe_4. In the following, the main results are briefly summarized and a prospect for future research in the field is given.

Mn_{12}

In the first part of this thesis, the archetypical Mn_{12}-ac SMM has been studied on Au(111) and Ag(111) noble metal surfaces, as well as on a single layer of graphene on Ir(111). According to STM topographic images, structurally intact molecules are present on all of these substrates after deposition. In contrast, a fragmentation of Mn_{12}-ac is observed when the deposition is performed on Cu(111), which is ascribed to the high affinity of copper towards carboxylic acids.

On Au(111), Mn_{12}-ac mainly grows as unordered two-dimensional islands. To a smaller extent, individual molecules are observed at the fcc- and elbow-sites of the herringbone reconstruction, which is explained by the droplet size distribution generated by ESD. From a statistical analysis of the topographic appearance, the orientation of the molecules with respect to the substrate is found to be randomly distributed. STS measurements performed on individual Mn_{12}-ac molecules show a wide conductance gap around the Fermi energy with an average gap width of

$\langle \Delta E_{\mathrm{gap}} \rangle = (2.20 \pm 0.45)\,\mathrm{eV}$. No sharp resonances are evident from the recorded differential conductance curves, indicating a broadening of the molecular states caused by the interaction of the molecules with the Au(111) substrate. Furthermore, no inelastic features are present in charge transport measurements in the mV regime, indicating a quenching of the spin due to the molecule-substrate interaction.

XPS measurements performed on Mn_{12}-ac/Ag(111) further corroborate the strong impact of the metallic substrate on the properties of Mn_{12}-ac. From the position of the Mn $2p_{3/2}$ peak, the shift of the Mn 2p shake-up satellites and the value of Mn 3s exchange splitting, we infer that the manganese ions in Mn_{12}-ac are partially reduced from Mn(III)/Mn(IV) to Mn(II), indicating a charge transfer between the molecules and the Ag(111) substrate.

In contrast, STM and STS measurements performed on Mn_{12}-ac on graphene/Ir(111) provide strong evidence that a single layer of graphene is able to electronically decouple the molecules from the influence of the metallic support. This finding is supported by two observations: First, a part of the Mn_{12}-ac molecules self-assembles in highly ordered periodic structures. To the knowledge of the author, this is the first time that a periodic surface organization of Mn_{12} SMMs is reported. Secondly, sharp resonances at -1.38 and 1.54 eV are observed in the differential conductance, which are ascribed to a charge transport trough the highest occupied molecular orbital (HOMO) and the lowest unoccupied molecular orbital (LUMO), respectively.

Future experiments on Mn_{12}-ac could possibly address the magnetic properties of the molecules on graphene/Ir(111) via XMCD and inelastic spin-flip spectroscopy. However, a successful integration of Mn_{12} SMMs into more complex device geometries seems unlikely, as the redox instability of the $Mn_{12}O_{12}$ core makes the complex highly sensitive to the molecular surrounding. Despite its high blocking temperature, Mn_{12} therefore seems to be no suitable candidate for future studies aiming at a use of SMMs in technological applications.

Fe4

In the second part of this thesis, another SMM known as Fe_4 has been studied, which has raised great interest due to the remarkable stability of its magnetic functionality. We have demonstrated for the first time that Fe_4 can be organized in highly periodic surface structures with a well defined orientation of its magnetic easy-axis. This was achieved by the combination of three accurate choices: First, we modified the organic ligand shell of the Fe_4 complex, aiming for a flat molecular geometry. For this purpose, a new derivative (Fe_4H) was synthesized, comprising the shortest tripodal ligand possible. Secondly, we used ultrathin layers of *h*-BN and graphene grown on Rh(111) and Ir(111), respectively, to electronically decouple the molecules from the metallic substrate. Thirdly, we implemented electrospray deposition in UHV as

a suitable method for transferring the Fe_4H complex from solution to the surface, resulting in samples of high purity and with only minor fragmentation.

The bulk magnetic properties of the Fe_4H complex were characterized by means of superconducting quantum interference device (SQUID) magnetometry. The molecule has an $S = 5$ spin ground state with easy-axis type magnetic anisotropy. The values of the exchange constants describing the intramolecular coupling of the four Fe atoms and of the uniaxial anisotropy constant were found to be close to those of other Fe_4 derivatives.

On h-BN/Rh(111), the Fe_4H molecules assemble in $(1/2 \times 1/2)$ and $(1/\sqrt{3} \times 1/\sqrt{3})R30°$ superstructures with respect to the hexagonal moiré pattern of the substrate. As observed by high resolution STM imaging, the adsorption geometry of the molecules is such that their magnetic easy axis is aligned perpendicular to the surface plane. By STS measurements and accompanying DFT calculations, we infer that the minority- and majority-spin components of the spin-split LUMO can be addressed separately, depending on the energy and spatial position within the molecule.

On graphene/Ir(111), a periodic self-assembly of the molecules is observed with lattice parameters close to those found in Fe_4H bulk material. In contrast to h-BN/Rh(111), no correlation between the periodic ordering of the molecules and the moiré pattern of the substrate is found, which can be explained by the different nature of the molecule-substrate interaction (electric polarization on h-BN/Rh(111) vs. van-der-Waals interaction on graphene/Ir(111)). According to high resolution STM images, the magnetic easy axis of the molecules is oriented perpendicular to the sample surface as well. This finding is corroborated by XMCD measurements performed at different orientations of the magnetic field with respect to the surface normal. From a quantitative analysis of the magnetic field dependence of the XMCD spectra, we find that the uniaxial anisotropy constant of Fe_4H is unaffected upon the deposition on graphene/Ir(111). However, spin-flip excitations observed in inelastic electron tunneling spectroscopy (IETS) indicate that the interaction between Fe_4H and graphene might result in a reduction of the exchange constant J_1 by around a factor of 2.

The well defined adsorption geometry of the Fe_4H complex on different substrates, the superior stability of its functional magnetic properties and the versatility of the applied deposition method open up new and interesting perspectives for future research.

An intriguing experiment would be to study the tunnel transport through Fe_4H in between a superconducting tip and substrate. Due to the effect of the superconducting tip and sample density of states, inelastic excitations would occur as peaks rather than steps in $\mathrm{d}I/\mathrm{d}V$, which appear at threshold energies that are shifted by the sum

of the superconducting gaps of tip and sample, i.e. $|eV| = \Delta_{\text{tip}} + \Delta_{\text{sample}} + \epsilon$ [258]. It was shown that the energy resolution of the spectroscopic features in such a configuration is improved far beyond the Fermi-Dirac threshold [259]. Therefore, the low energy transition $|5,5\rangle \rightarrow |5,4\rangle$ would likely be resolved in IETS even at $T = 1.8\,\text{K}$, yielding direct information about the magnetic anisotropy of individual molecules.

A possible way to prepare the superconducting tunnel junction would be to deposit Fe_4H on a Pb(111) film or single crystal and to fabricate a Pb-covered superconducting tip by driving a regular tungsten-tip into the substrate. Alternatively, Pb could be intercalated underneath a layer of graphene and a bulk superconducting tip could be used to probe the molecules. This would provide the advantage of a better electronic decoupling of Fe_4H from the Pb surface.

A second interesting experiment would be to implement a ferromagnetic electrode into the tunnel junction, i.e. to either deposit Fe_4H on a ferromagnetic substrate (which again could be covered by a layer of graphene via intercalation or, if possible, direct growth of graphene on the ferromagnetic material) or to use a ferro- or antiferromagnetic tip, as is done in spin polarized STM. Since the two spin components of the LUMO of Fe_4H can be addressed separately in the tunnel transport, such an experiment could utilize a single Fe_4H molecule as a spin valve, whose resistance can be switched between two states, depending on the external magnetic field, the spatial position of the tunnel transport and the bias voltage.

Further Development of the Electrospray Deposition Setup

Finally, I would like to mention that a further development of the electrospray deposition setup is planned. In the current version of the setup, the generated particle beam consists of sub-μm sized droplets rather than gas-phase ions, which was shown by a measurement of the particle energy per unit charge (see chapter 6.2.2). Depending on the properties of the deposited molecules and the substrate, this might result in a partial agglomeration of the molecules on the surface (as observed for Mn_{12}-ac and the four-armed polyfluorene star polymer studied in chapter 8.2) or might not significantly affect the adsorption behavior (as in case of Fe_4H, CoPc and the triazatruxene derivative used in chapter 8.3).

The tools required for a complete desolvation of the charged droplets are already implemented in the ion source of the ESD setup. Specifically, the degree of desolvation can be controlled by the temperature of the inlet capillary and the temperature and flow rate of the N_2 counter gas flow. However, a deposition of completely desolved gas-phase ions is prevented in the current setup by the high pressure in the second differential pumping stage, which is associated with a high number of collisions between the particles and the background gas. For this reason, a new differential pumping system has been designed in the course of this thesis, which is expected to reduce the pressure in the second chamber to the $10^{-5}\,\text{mbar}$ range. In

future experiments, this modification of the setup might enable the deposition and investigation of isolated molecules even in the case of extremely large and complex molecular compounds.

Danksagung

Viele Personen haben auf unterschiedliche Weise zum erfolgreichen Abschluss dieser Arbeit beigetragen. Ich möchte mich an dieser Stelle bei einigen von ihnen besonders bedanken:

- Bei Herrn apl. Prof. Dr. Mikhail Fonin bedanke ich mich für die Betreuung der Arbeit und die Sicherstellung ihrer Finanzierung. Besonders bedanken möchte ich mich für das Vertrauen, das er mir während der Arbeit entgegen gebracht hat, für seine Unterstützung bei zahlreichen experimentellen Angelegenheiten und für die vielen hilfreichen Diskussionen und Anregungen.

- Prof. Dr. Elke Scheer möchte ich für die Übernahme des Zweitgutachtens zu dieser Arbeit danken. Ebenso danke ich Prof. Dr. Eva Weig und Prof. Dr. Peter Nielaba für die Abnahme der Prüfung.

- Für die Einweisung in zahlreiche Labortätigkeiten, die tolle Zusammenarbeit beim Umzug und Betrieb des Cryo-STM, die vielen interessanten Diskussionen und die schöne gemeinsame Zeit in Jülich und Konstanz möchte ich mich bei Dr. Samuel Bouvron bedanken.

- Dr. Stefan Ambrus und Dr. Peter Schmitt danke ich für die chemische Synthese und Bereitstellung von Mn_{12} und Fe_4 sowie für die Erklärung zahlreicher chemischer Sachverhalte.

- Andreas Irmler und Jun.-Prof. Fabian Pauly danke ich für die Durchführung der DFT Berechnungen zu Fe_4H und für die schnelle und unkomplizierte Zusammenarbeit bei der Publikation unserer Ergebnisse.

- Bei Dr. Luca Gragnaniello und Dr. Stefano Rusponi bedanke ich mich für die Zusammenarbeit bei der Durchführung der Synchrotronmessungen an Fe_4H.

- Dr. Holger Bußkamp danke ich für seine geduldige Unterstützung bei der Durchführung sämtlicher ESI-MS Messungen.

- Mein besonderer Dank gilt allen Studenten, die ich während der Arbeit betreuen durfte und die im Rahmen ihrer Diplom- und Masterarbeiten an der

Forschung zu Mn_{12} und Fe_4 mitgewirkt haben: Sebastian Höll, Eva-Sophie Wilhelm, Nicole Barth und Fabian Paschke. Ohne euch hätten die vielen Stunden im Labor nur halb so viel Spaß gemacht!

- Weiterhin danke ich allen Mitgliedern der Arbeitsgruppe Fonin für die Unterstützung und das tolle Arbeitsklima. Ganz speziell danke ich Dr. Philipp Leicht und Dr. Aleksej Laptev für die Einweisungen in das VT STM/AFM und das SQUID Magnetometer, Julia Tesch für das Korrekturlesen der Arbeit und Tobias Schosser für die großartige Unterstützung bei der Konstruktion und Modifikation des ESD-Setups. Außerdem danke ich Manfred Keil und Friederike Stuckenbrock für die Hilfe bei zahlreichen technischen und organisatorischen Angelegenheiten.

- Für die zuverlässige Versorgung mit flüssigem Helium möchte ich mich bei Ralf Sieber und Hartmut Görig bedanken.

- Der DFG danke ich für die finanzielle Förderung dieser Arbeit im Rahmen des Teilprojektes C5 des Sonderforschungsbereiches 767.

- Abschließend und ganz besonders danke ich meiner Familie für die fortwährende Unterstützung während der Arbeit.

Bibliography

[1] A. Aviram and M. A. Ratner: *Molecular rectifiers*. Chem. Phys. Lett. **29**, 277 (1974), doi:10.1016/0009-2614(74)85031-1.

[2] B. Behin-Aein, D. Datta, S. Salahuddin and S. Datta: *Proposal for an all-spin logic device with built-in memory*. Nature Nanotech. **5**, 266 (2010), doi:10.1038/nnano.2010.31.

[3] L. Bogani and W. Wernsdorfer: *Molecular spintronics using single-molecule magnets*. Nature Mater. **7**, 179 (2008), doi:doi:10.1038/nmat2133.

[4] M. Affronte: *Molecular nanomagnets for information technologies*. J. Mater. Chem. **19**, 1731 (2009), doi:10.1039/B809251F.

[5] M. N. Leuenberger and D. Loss: *Quantum computing in molecular magnets*. Nature **410**, 789 (2001), doi:10.1038/35071024.

[6] L. Thomas, F. Lionti, R. Ballou, D. Gatteschi, R. Sessoli and B. Barbara: *Macroscopic quantum tunneling of magnetization in a single crystal of nanomagnets*. Nature **383**, 145 (1996), doi:10.1038/383145a0.

[7] J. R. Friedman, M. P. Sarachik, J. Tejada and R. Ziolo: *Macroscopic measurement of resonant magnetization tunneling in high-spin molecules*. Phys. Rev. Lett. **76**, 3830 (1996), doi:http://dx.doi.org/10.1103/PhysRevLett.76.3830.

[8] W. Wernsdorfer and R. Sessoli: *Quantum phase interference and parity effects in magnetic molecular clusters*. Science **284**, 133 (1999), doi:10.1126/science.284.5411.133.

[9] T. Lis: *Preparation, structure, and magnetic properties of a dodecanuclear mixed-valence manganese carboxylate*. Acta Cryst. B **36**, 2042 (1980), doi:doi:10.1107/S0567740880007893.

[10] R. Sessoli, D. Gatteschi, A. Caneschi and M. A. Novak: *Magnetic bistability in a metal-ion cluster*. Nature **365**, 141 (1993), doi:10.1038/365141a0.

[11] M. Mannini, F. Pineider, C. Danieli, F. Totti, L. Sorace, P. Sainctavit, M.-A. Arrio, E. Otero, L. Joly, J. C. Cezar, A. Cornia and R. Sessoli: *Quantum tunnelling of the magnetization in a monolayer of oriented single-molecule magnets*. Nature **468**, 417 (2010), doi:10.1038/nature09478.

[12] M. R. Cheesman, V. S. Oganesyan, R. Sessoli, D. Gatteschi and A. J. Thomson: *Magnetically induced optical bi-stability of the molecular nanomagnet* $Mn_{12}O_{12}(OOCMe)_{16}(H_2O)_4$ *in an organic glass*. Chem. Commun. 1677 (1997), doi:10.1039/A703839I.

[13] E. J. L. McInnes, E. Pidcock, V. S. Oganesyan, M. R. Cheesman, A. K. Powell and A. J. Thomson: *Optical detection of spin polarization in single-molecule magnets [$Mn_{12}O_{12}(O_2CR)_{16}(H_2O)_4$].* J. Am. Chem. Soc. **124**, 9219 (2002), doi:10.1021/ja020456b.

[14] F. El Hallak, J. van Slageren, J. Gómez-Segura, D. Ruiz-Molina and M. Dressel: *High-frequency ESR and frequency domain magnetic resonance spectroscopic studies of single molecule magnets in frozen solution.* Phys. Rev. B **75**, 104403 (2007), doi:10.1103/PhysRevB.75.104403.

[15] L. Vergnani, A.-L. Barra, P. Neugebauer, M. J. Rodriguez-Douton, R. Sessoli, L. Sorace, W. Wernsdorfer and A. Cornia: *Magnetic bistability of isolated giant-spin centers in a diamagnetic crystalline matrix.* Chem. Eur. J. **18**, 3390 (2012), doi:10.1002/chem.201103251.

[16] N. Ishikawa, M. Sugita, T. Ishikawa, S.-Y. Koshihara and Y. Kaizu: *Lanthanide double-decker complexes functioning as magnets at the single-molecular level.* J. Am. Chem. Soc. **125**, 8697 (2003), doi:10.1021/ja029629n.

[17] G. L. Abbati, L.-C. Brunel, H. Casalta, A. Cornia, A. C. Fabretti, D. Gatteschi, A. K. Hassan, A. G. M. Jansen, A. L. Maniero, L. Pardi, C. Paulsen and U. Segre: *Single-ion versus dipolar origin of the magnetic anisotropy in iron(iii)-oxo clusters: a case study.* Chem. Eur. J. **7**, 1796 (2001), doi:10.1002/1521-3765(20010417)7:8<1796::AID-CHEM17960>3.0.CO;2-Y.

[18] K. W. H. Stevens: *Matrix elements and operator equivalents connected with the magnetic properties of rare earth ions.* Proc. Phys. Soc. A **65**, 209 (1952), doi:10.1088/0370-1298/65/3/308.

[19] D. Gatteschi, R. Sessoli and J. Villain: *Molecular nanomagnets.* Oxford University Press, New York (2006).

[20] Y. Gao, G.-F. Xu, L. Zhao, J. Tang and Z. Liu: *Observation of slow magnetic relaxation in discrete dysprosium cubane.* Inorg. Chem. **48**, 11495 (2009), doi:10.1021/ic901806g.

[21] J. Villain, F. Hartman-Boutron, R. Sessoli and A. Rettori: *Magnetic relaxation in big magnetic molecules.* Europhys. Lett. **27**, 159 (1994), doi:10.1209/0295-5075/27/2/014.

[22] E. C. Stoner and E. P. Wohlfarth: *A mechanism of magnetic hysteresis in heterogeneous alloys.* Phil. Trans. Roy. Soc. London A **240**, 599 (1948), doi:10.1098/rsta.1948.0007.

[23] L. Néel: *Théorie du trainage magnétique des ferromagnétiques en grains fins avec applications aux terres cuites.* Ann. géophys. **5**, 99 (1949).

[24] W. F. Brown: *Relaxational behaviour of fine magnetic particles.* J. Appl. Phys. **30**, 130S (1959), doi:10.1063/1.2185851.

[25] C. R. Ganivet, B. Ballesteros, G. de la Torre, J. M. Clemente-Juan, E. Coronado and T. Torres: *Influence of peripheral substitution on the magnetic behavior of single-ion magnets based on homo- and heteroleptic Tb^{III} bis(phthalocyaninate).* Chem. Eur. J. **19**, 1457 (2013), doi:10.1002/chem.201202600.

[26] A. M. Ako, I. J. Hewitt, V. Mereacre, R. Clérac, W. Wernsdorfer, C. E. Anson and A. K. Powell: *A ferromagnetically coupled Mn_{19} aggregate with a record $S = 83/2$ ground spin state.* Angew. Chem. Int. Ed. **45**, 4926 (2006), doi:10.1002/anie.200601467.

[27] J. D. Rinehart, M. Fang, W. J. Evans and J. R. Long: *Strong exchange and magnetic blocking in N_2^{3-}-radical-bridged lanthanide complexes.* Nature Chem. **3**, 538 (2011), doi:10.1038/NCHEM.1063.

[28] L. Thomas, A. Caneschi and B. Barbara: *Nonexponential dynamic scaling of the magnetization relaxation in Mn_{12} acetate.* Phys. Rev. Lett. **83**, 2398 (1999), doi:10.1103/PhysRevLett.83.2398.

[29] L. Landau: *Zur Theorie der Energieubertragung. II.* Phys. Z. Sowjetunion **2**, 46 (1932).

[30] C. Zener: *Non-adiabatic crossing of energy levels.* Proc. R. Soc. London A **137**, 696 (1932), doi:10.1098/rspa.1932.0165.

[31] E. C. G. Stückelberg: *Theorie der unelastischen Stösse zwischen Atomen.* Helv. Phys. Acta **5**, 24 (1932), doi:10.5169/seals-110177.

[32] W. Wernsdorfer, M. Murugesu and G. Christou: *Resonant tunneling in truly axial symmetry Mn_{12} single-molecule magnets: sharp crossover between thermally assisted and pure quantum tunneling.* Phys. Rev. Lett. **96**, 057208 (2006), doi:10.1103/PhysRevLett.96.057208.

[33] J. A. A. J. Perenboom, J. S. Brooks, S. Hill, T. Hathaway and N. S. Dalal: *Relaxation of the magnetization of Mn_{12} acetate.* Phys. Rev. B **58**, 330 (1998), doi:10.1103/PhysRevB.58.330.

[34] C. Sangregorio, T. Ohm, C. Paulsen, R. Sessoli and D. Gatteschi: *Quantum tunneling of the magnetization in an iron cluster nanomagnet.* Phys. Rev. Lett. **78**, 4645 (1997), doi:10.1103/PhysRevLett.78.4645.

[35] J. J. Henderson, C. Koo, P. L. Feng, E. del Barco, S. Hill, I. S. Tupitsyn, P. C. E. Stamp and D. N. Hendrickson: *Manifestation of spin selection rules on the quantum tunneling of magnetization in a single-molecule magnet.* Phys. Rev. Lett. **109**, 017202 (2009), doi:10.1103/PhysRevLett.103.017202.

[36] J. Zeleny: *The electrical discharge from liquid points, and a hydrostatic method of measuring the electric intensity at their surfaces.* Phys. Rev. **3**, 69 (1914), doi:10.1103/PhysRev.3.69.

[37] J. Zeleny: *Instability of electrified liquid surfaces.* Phys. Rev. **10**, 1 (1917), doi:10.1103/PhysRev.10.1.

[38] A. G. Bailey: *Electrostatic spraying of liquids.* Research Studies Press (1988).

[39] M. Dole, L. L. Mack, R. L. Hines, R. C. Mobley, L. D. Ferguson and M. B. Alice: *Molecular beams of macroions.* J. Chem. Phys. **49**, 2240 (1968), doi:10.1063/1.1670391.

[40] L. L. Mack, P. Kralik, A. Rheude and M. Dole: *Molecular beams of macroions II.* J. Chem. Phys. **52**, 4977 (1970), doi:10.1063/1.1672733.

[41] M. Yamashita and J. B. Fenn: *Electrospray ion source. Another variation of the free jet theme.* J. Phys. Chem. **88**, 4451 (1984), doi:10.1021/j150664a002.

[42] J. B. Fenn, M. Mann, C. K. Meng, S. F. Wong and C. M. Whitehouse: *Electrospray ionization for mass spectrometry of large biomolecules.* Science **246**, 64 (1989), doi:10.1126/science.2675315.

[43] A. Premstaller, H. Oberacher and C. G. Huber: *High-performance liquid chromatography-electrospray ionization mass spectrometry of single- and double-stranded nucleic acids using monolithic capillary columns.* Anal. Chem. **72**, 4386 (2000), doi:10.1021/ac000283d.

[44] S. D. Fuerstenau, W. H. Benner, J. J. Thomas, C. Brugidou, B. Bothner and G. Siuzdak: *Mass spectrometry of an intact virus.* Angew. Chem. **113**, 560 (2001), doi:10.1002/1521-3757(20010202)113:3<559::AID-ANGE559>3.0.CO;2-%23.

[45] C. J. McNeal, R. D. Macfarlane and E. L. Thurston: *Thin film deposition by the electrospray method for Californium-252 plasma desorption studies of involatile molecules.* Anal. Chem. **51**, 2036 (1979), doi:10.1021/ac50048a032.

[46] V. N. Morozov and T. Y. Morozova: *Electrospray deposition as a method to fabricate functionally active protein films.* Anal. Chem. **71**, 1415 (1999), doi:10.1021/ac9808775.

[47] V. N. Morozov and T. Y. Morozova: *Electrospray deposition as a method for mass fabrication of mono- and multicomponent microarrays of biological and biologically active substances.* Anal. Chem. **71**, 3110 (1999), doi:10.1021/ac981412h.

[48] R. Saf, M. Goriup, T. Steindl, T. E. Hamedinger, D. Sandholzer and G. Hayn: *Thin organic films by atmospheric-pressure ion deposition.* Nature Mater. **3**, 323 (2004), doi:10.1038/nmat1117.

[49] Z. Ouyang, Z. Takáts, T. A. Blake, B. Gologan, A. J. Guymon, J. M. Wiseman, J. C. Oliver, V. J. Davisson and R. G. Cooks: *Preparing protein microarrays by soft-landing of mass-selected ions.* Science **301**, 1351 (2003), doi:10.1126/science.1088776.

[50] B. Gologan, Z. Takáts, J. Alvarez, J. M. Wiseman, N. Talaty, Z. Ouyang and R. G. Cooks: *Ion soft-landing into liquids: Protein identification, separation, and purification with retention of biological activity.* J. Am. Soc. Mass. Spectrom. **15**, 1874 (2004), doi:10.1016/j.jasms.2004.09.005.

[51] M. Volný, W. T. Elam, A. Branca, B. D. Ratner and F. Turecek: *Preparative soft and reactive landing of multiply charged protein ions on a plasma-treated metal surface.* Anal. Chem. **77**, 4890 (2005), doi:10.1021/ac0507136.

[52] O. Hadjar, P. Wang, J. H. Futrell, Y. Dessiaterik, Z. Zhu, J. P. Cowin, M. J. Iedema and J. Laskin: *Design and performance of an instrument for soft landing of biomolecular ions on surfaces.* Anal. Chem. **79**, 6566 (2007), doi:10.1021/ac070600h.

[53] S. Rauschenbach, F. L. Stadler, E. Lunedei, N. Malinowski, S. Koltsov, G. Costantini and K. Kern: *Electrospray ion beam deposition of clusters and biomolecules.* Small **2**, 540 (2006), doi:10.1002/smll.200500479.

[54] S. Rauschenbach: *Electrospray ion beam deposition and mass spectrometry of non-volatile molecules and nanometerials.* Ph.D. thesis, École Polytechnique Fédérale de Lausanne (2007).

[55] S. Rauschenbach, R. Vogelgesang, N. Malinowski, J. W. Gerlach, M. Benyoucef, G. Costantini, Z. Deng, N. Thontasen and K. Kern: *Electrospray ion beam deposition: soft-landing and fragmentation of functional molecules at solid surfaces.* ACS Nano **3**, 2901 (2009), doi:10.1021/nn900022p.

[56] J. C. Swarbrick, J. B. Taylor and J. N. O'Shea: *Electrospray deposition in vacuum.* Appl. Surf. Sci. **252**, 5622 (2006), doi:10.1016/j.apsusc.2005.12.025.

[57] C. J. Satterley, L. M. A. Perdigão, A. Saywell, G. Magnano, A. Rienzo, L. C. Mayor, V. R. Dhanak, P. H. Beton and J. N. O'Shea: *Electrospray deposition of fullerenes in ultra-high vacuum: in situ scanning tunneling microscopy and photoemission spectroscopy.* Nanotechnology **18**, 455304 (2007), doi:10.1088/0957-4484/18/45/455304.

[58] C. Hamann, R. Woltmann, I.-P. Hong, N. Hauptmann, S. Karan and R. Berndt: *Ultrahigh vacuum deposition of organic molecules by electrospray ionization.* Rev. Sci. Instr. **82**, 033903 (2011), doi:10.1063/1.3553010.

[59] V. Corradini, C. Cervetti, A. Ghirri, R. Biagi, U. del Pennino, G. A. Timco, R. E. P. Winpenny and M. Affronte: *Oxo-centered carboxylate-bridged trinuclear complexes deposited on Au(111) by a mass-selective electrospray.* New J. Chem. **35**, 1683 (2011), doi:10.1039/c1nj20080a.

[60] T. Yamada, H. Suzuki, H. Miki, G. Maofa and S. Mashiko: *High-resolution scanning tunneling microscopy images of molecular overlayers prepared by a new molecular beam deposition apparatus with spray-jet technique.* J. Phys. Chem. B **109**, 3183 (2005), doi:10.1021/jp046389k.

[61] L. Vitali, S. Fabris, A. M. Conte, S. Brink, M. Ruben, S. Baroni and K. Kern: *Electronic structure of surface-supported bis(phtalocyanito)terbium(III) single molecular magnets.* Nano Lett. **8**, 3364 (2008), doi:10.1021/nl801869b.

[62] G. Taylor: *Disintegration of water drops in an electric field.* Proc. R. Soc. London A **280**, 383 (1964), doi:10.1098/rspa.1964.0151.

[63] J. F. de la Mora and I. G. Loscertales: *The current emitted by highly conducting Taylor cones.* J. Fluid Mech. **260**, 155 (1994), doi:10.1017/S0022112094003472.

[64] M. Cloupeau and B. Prunet-Foch: *Electrostatic spraying of liquids in cone-jet mode.* J. Electrostat. **22**, 135 (1989), doi:10.1016/0304-3886(89)90081-8.

[65] A. Gomez and K. Tang: *Charge and fission of droplets in electrostatic sprays.* Phys. Fluids **6**, 404 (1994), doi:10.1063/1.868037.

[66] M. Wilm and M. Mann: *Analytical properties of the nanoelectrospray ion source.* Anal. Chem. **68**, 1 (1996), doi:10.1021/ac9509519.

[67] M. S. Wilm and M. Mann: *Electrospray and Taylor-cone theory, Dole's beam of macromolecules at last?* Int. J. Mass Spectrom. **136**, 167 (1994), doi:10.1016/0168-1176(94)04024-9.

[68] J. W. Thompson, J. W. Eschelbach, R. T. Wilburn and J. W. Jorgenson: *Investigation of electrospray ionization and electrostatic focusing devices using a three-dimensional electrospray current density profiler.* J. Am. Soc. Mass. Spectrom. **16**, 312 (2005), doi:10.1016/j.jasms.2004.11.012.

[69] P. Kebarle: *A brief overview of the present status of the mechanisms involved in electrospray mass spectrometry.* J. Mass Spectrom. **35**, 804 (2000), doi:10.1002/1096-9888(200007)35:7<804::AID-JMS22>3.0.CO;2-Q.

[70] Lord Rayleigh: *On the equilibrium of liquid coducting masses charged with electricity.* Phil. Mag. **14**, 184 (1882), doi:10.1080/14786448208628425.

[71] D. Duft, T. Achtzehn, R. Müller, B. A. Huber and T. Leisner: *Coulomb fission: Rayleigh jets from levitated microdroplets.* Nature **421**, 128 (2003), doi:10.1038/421128a.

[72] J. V. Iribarne and B. A. Thomson: *On the evaporation of small ions from charged droplets.* J. Chem. Phys. **64**, 2287 (1976), doi:10.1063/1.432536.

[73] R. Campargue: *Progress in overexpanded supersonic jets and skimmed molecular beams in free-jet zones of silence.* J. Phys. Chem. **88**, 4466 (1984), doi:10.1021/j150664a004.

[74] J. M. Hayes: *Analytical spectroscopy in supersonic expansions.* Chem. Rev. **87**, 745 (1987), doi:10.1021/cr00080a004.

[75] P. Milani and S. Iannotta: *Cluster beam synthesis of nanostructured materials.* Springer (1999).

[76] J. B. Anderson, R. P. Anders and J. B. Fenn: *Supersonic nozzle beams.* In J. Ross (ed.), *Molecular Beams*, chapter 8, 275, Interscience Publishers (1966).

[77] S. A. Shaffer, D. C. Prior, G. A. Anderson, H. R. Udseth and R. D. Smith: *An ion funnel interface for improved ion focusing and sensitivity using electrospray ionization mass spectrometry.* Anal. Chem. **70**, 4111 (1998), doi:10.1021/ac9802170.

[78] S. A. Shaffer, A. Tolmachev, D. C. Prior, G. A. Anderson, H. R. Udseth and R. D. Smith: *Characterization of an improved electrodynamic ion funnel interface for electrospray ionization mass spectrometry.* Anal. Chem. **71**, 2957 (1999), doi:10.1021/ac990346w.

[79] R. T. Kelly, A. V. Tolmachev, J. S. Page, K. Tang and R. D. Smith: *The ion funnel: theory, implementations, and applications.* Mass Spectrom. Rev. **29**, 294 (2010), doi:10.1002/mas.20232.

[80] N. B. Cech and C. G. Enke: *Practical implications of some recent studies in electrospray ionization fundamentals.* Mass. Spectrom. Rev. **20**, 362 (2001), doi:10.1002/mas.1000.

[81] G. Binnig, H. Rohrer, C. Gerber and E. Weibel: *Tunneling through a controllable vacuum gap.* Appl. Phys. Lett. **40**, 178 (1982), doi:10.1063/1.92999.

[82] G. Binnig, H. Rohrer, C. Gerber and E. Weibel: *Surface studies by scanning tunneling microscopy.* Phys. Rev. Lett. **49**, 57 (1982), doi:10.1103/PhysRevLett.49.57.

[83] G. Binnig, H. Rohrer, C. Gerber and E. Weibel: 7×7 *Reconstruction on Si(111) resolved in real space.* Phys. Rev. Lett. **50**, 120 (1983), doi:10.1103/PhysRevLett.50.120.

[84] A. Zusan: *Local electronic properties of graphene nanodots.* Master's thesis, Universität Konstanz (2011).

[85] P. Leicht: *Local electronic properties of graphene flakes on noble metal surfaces*. Ph.D. thesis, Universität Konstanz (2014).

[86] C. J. Chen: *Introduction to scanning tunneling microscopy*. Oxford University Press, New York, 2nd edition (2008).

[87] R. Wiesendanger: *Scanning probe microscopy and spectroscopy*. Cambridge University Press (1994).

[88] J. A. Stroscio and W. J. Kaiser (eds.): *Scanning tunneling microscopy*. Academic Press (1993).

[89] J. Bardeen: *Tunneling from a many body point of view*. Phys. Rev. Lett. **6**, 57 (1961), doi:10.1103/PhysRevLett.6.57.

[90] I. Giaever: *Energy gap in superconducters measured by electron tunneling*. Phys. Rev. Lett. **5**, 147 (1960), doi:10.1103/PhysRevLett.5.147.

[91] I. Giaever: *Electron tunneling between two superconductors*. Phys. Rev. Lett. **5**, 464 (1960), doi:10.1103/PhysRevLett.5.464.

[92] J. Tersoff and D. R. Hamann: *Theory and application for the scanning tunneling microscope*. Phys. Rev. Lett. **50**, 1998 (1983), doi:10.1103/PhysRevLett.50.1998.

[93] J. Tersoff and D. R. Hamann: *Theory of the scanning tunneling microscope*. Phys. Rev. B. **31**, 805 (1985), doi:10.1103/PhysRevB.31.805.

[94] A. Selloni, P. Carnevali, E. Tosatti and C. D. Chen: *Voltage-dependent scanning-tunneling microscopy of a crystal surface: graphite*. Phys. Rev. B **31**, 2602 (1985), doi:10.1103/PhysRevB.31.2602.

[95] C. J. Chen: *Tunneling matrix elements in three-dimensional space: the derivative rule and the sum rule*. Phys. Rev. B **42**, 8841 (1990), doi:10.1103/PhysRevB.42.8841.

[96] C. J. Chen: *Origin of atomic resolution on metal surfaces in scanning tunneling microscopy*. Phys. Rev. Lett. **65**, 448 (1990), doi:10.1103/PhysRevLett.65.448.

[97] J. A. Stroscio, R. M. Feenstra and A. P. Fein: *Electronic structure of the Si(111)* 2×1 *surface by scanning-tunneling microscopy*. Phys. Rev. Lett. **57**, 2579 (1986), doi:10.1103/PhysRevLett.57.2579.

[98] R. Feenstra, J. A. Stroscio and A. Fein: *Tunneling spectroscopy of the Si(111)*2×1 *surface*. Surf. Sci. **181**, 295 (1987), doi:10.1016/0039-6028(87)90170-1.

[99] N. D. Lang: *Spectroscopy of single atoms in the scanning tunneling microscope*. Phys. Rev. B **34**, 5947 (1986), doi:10.1103/PhysRevB.34.5947.

[100] P. Mårtensson and R. M. Feenstra: *Geometric and electronic structure of antimony on the GaAs(110) surface studied by scanning tunneling microscopy*. Phys. Rev. B. **39**, 7744 (1989), doi:10.1103/PhysRevB.39.7744.

[101] M. Prietsch, A. Samsavar and R. Ludeke: *Structural and electronic properties of the Bi/GaP(110) interface*. Phys. Rev. B **43**, 11850 (1991), doi:10.1103/PhysRevB.43.11850.

[102] M. Paulsson, F. Zahid and S. Datta: *Resistance of a molecule*. In W. A. Goddard, D. W. Brenner, S. E. Lyshevski, and G. J. Iafrate (eds.), *Handbook of nanoscience, engineering and technology*, CRC Press, Boca Raton (2003).

[103] Y. Selzer and D. L. Allara: *Single-molecule electrical junctions*. Annu. Rev. Phys. Chem. **57**, 593 (2006), doi:10.1146/annurev.physchem.57.032905.104709.

[104] J. C. Cuevas and E. Scheer: *Molecular electronics: an Introduction to theory and experiment*. World Scientific Publishing Company (2010).

[105] R. C. Jaklevic and J. Lambe: *Molecular vibration spectra by electron tunneling*. Phys. Rev. Lett. **17**, 1139 (1966), doi:10.1103/PhysRevLett.17.1139.

[106] J. Lambe and R. C. Jaklevic: *Molecular vibration spectra by inelastic electron tunneling*. Phys. Rev. **165**, 821 (1968), doi:10.1103/PhysRev.165.821.

[107] W. Ho: *Single-molecule chemistry*. J. Chem. Phys. **117**, 11033 (2002), doi:10.1063/1.1521153.

[108] G. Binnig, N. Garcia and H. Rohrer: *Conductivity sensitivity of inelastic scanning tunneling microscopy*. Phys. Rev. B **32**, 1336 (1985), doi:10.1103/PhysRevB.32.1336.

[109] B. N. J. Persson and J. E. Demuth: *Inelastic electron tunneling from a metal tip*. Solid State Commun. **57**, 769 (1986), doi:10.1016/0038-1098(86)90856-2.

[110] B. N. J. Persson and A. Baratoff: *Inelastic electron tunneling from a metal tip: the contribution from resonant processes*. Phys. Rev. Lett. **59**, 339 (1987), doi:10.1103/PhysRevLett.59.339.

[111] M. A. Gata and P. R. Antoniewicz: *Resonant tunneling through adsorbates in scanning tunneling microscopy*. Phys. Rev. B **47**, 13797 (1993), doi:10.1103/PhysRevB.47.13797.

[112] B. C. Stipe, M. A. Rezaei and W. Ho: *Single-molecule vibrational spectroscopy and microscopy*. Science **280**, 1732 (1998), doi:10.1126/science.280.5370.1732.

[113] A. J. Heinrich, J. A. Gupta, C. P. Lutz and D. M. Eigler: *Single-atom spin-flip spectroscopy*. Science **306**, 466 (2004), doi:10.1126/science.1101077.

[114] C. F. Hirjibehedin, C. P. Lutz and A. J. Heinrich: *Spin coupling in engineered atomic structures*. Science **312**, 1021 (2006), doi:10.1126/science.1125398.

[115] C. F. Hirjibehedin, C.-Y. Lin, A. F. Otte, M. Ternes, C. P. Lutz, B. A. Jones and A. J. Heinrich: *Large magnetic anisotropy of a single atomic spin embedded in a surface molecular network*. Science **317**, 1199 (2007), doi:10.1126/science.1146110.

[116] J. A. Gupta, C. P. Lutz, A. J. Heinrich and D. M. Eigler: *Strongly coverage-dependent excitations of adsorbed molecular hydrogen*. Phys. Rev. B **71**, 115416 (2005), doi:10.1103/PhysRevB.71.115416.

[117] L. Müller: *Untersuchung von Metall-Supraleiter Tunnelkontakten mittels Rastertunnelmikroskopie*. Bachelor thesis, Universität Konstanz (2011).

[118] S. Bouvron: *Gate-controlled scanning tunneling spectroscopy of CoPc molecules on graphene*. Ph.D. thesis, Universität Konstanz (2014).

[119] J. F. Moulder, W. F. Stickle, P. E. Sobol and K. D. Bomben: *Handbook of x-ray photoelectron spectroscopy: A reference book of standard spectra for identification and interpretation of XPS data*. Physical Electronics (1995).

[120] S. Hüfner: *Photoelectron spectroscopy*. Springer, 3rd edition (2003).

[121] Omicron Nanotechnology: *EA 125 energy analyzer user's guide*. 2nd edition (2002).

[122] H. Lüth: *Solid surfaces, interfaces and thin films*. Springer, 5th edition (2010).

[123] M. Henzler and W. Göpel: *Oberflächenphysik des Festkörpers*. B. G. Teubner, 2nd edition (1994).

[124] J. Clarke and A. I. Braginski (eds.): *The SQUID handbook: Fundamentals and technology of SQUIDs and SQUID systems (1st volume)*. Wiley-VCH (2004).

[125] E. du Trémolet de Lacheisserie, D. Gignoux and M. Schlenker (eds.): *Magnetism: Materials & applications (2nd volume)*. Springer (2005).

[126] Quantum Design: *MPMS application note 1014-213* (2002).

[127] G. A. Bain and J. F. Berry: *Diamagnetic corrections and Pascal's constants*. J. Chem. Educ. **85**, 532 (2008), doi:10.1021/ed085p532.

[128] B. B. Schneider, D. J. Douglas and D. D. Y. Chen: *An atmospheric pressure ion lens to improve electrospray ionization at low solution flow-rates*. Rapid Commun. Mass Spectrom. **15**, 2168 (2001), doi:10.1002/rcm.481.

[129] L. Zhou, L. Zhai, B. Yue, E. D. Lee and M. L. Lee: *New interface plate for microspray ionization mass spectrometry*. Anal. Bioanal. Chem. **385**, 1087 (2006), doi:10.1007/s00216-006-0523-1.

[130] L. Zhou, B. Yue, D. V. Dearden, E. D. Lee, A. L. Rockwood and M. L. Lee: *Incorporation of a venturi device in electrospray ionization*. Anal. Chem. **75**, 5978 (2003), doi:10.1021/ac020786e.

[131] A. M. Hawkridge, L. Zhou, M. L. Lee and D. C. Muddiman: *Analytical performance of a venturi device integrated into an electrospray ionization fourier transform ion cyclotron resonance mass spectrometer for analysis of nucleic acids*. Anal. Chem. **76**, 4118 (2004), doi:10.1021/ac049677l.

[132] A. D. Appelhans and D. A. Dahl: *SIMION ion optics simulations at atmospheric pressure*. Int. J. Mass Spectrom. **244**, 1 (2005), doi:10.1016/j.ijms.2005.03.010.

[133] B. Lin and J. Sunner: *Ion transport by vicious gas flow through capillaries*. J. Am. Soc. Mass. Spectrom. **5**, 873 (1994), doi:10.1016/1044-0305(94)87012-8.

[134] J. A. Simpson: *Design of retarding field energy analyzers*. Rev. Sci. Instr. **32**, 1283 (1961), doi:10.1063/1.1717235.

[135] S. Zhou and M. Hamburger: *Formation of sodium cluster ions in electrospray mass spectrometry*. Rapid Commun. Mass Sp. **10**, 797 (1996), doi:10.1002/(SICI)1097-0231(199605)10:7<797::AID-RCM550>3.0.CO;2-7.

[136] D. Zhang and R. G. Cooks: *Doubly charged cluster ions* $[(NaCl)_m(Na)_2]^{2+}$*: magic numbers, dissociation, and structure.* Int. J. Mass Spectrom. **195**, 667 (2000), doi:10.1016/S1387-3806(99)00184-0.

[137] C. Hao, R. E. March, T. R. Croley, J. C. Smith and S. P. Rafferty: *Electrospray ionization tandem mass spectrometric study of salt cluster ions. Part 1: Investigations of alkali metal chloride and sodium salt cluster ions.* J. Mass Spectrom. **36**, 79 (2001), doi:10.1002/jms.107.

[138] J. V. Barth, H. Brune, G. Ertl and R. J. Behm: *Scanning tunneling microscopy observations on the reconstructed Au(111) surface: atomic structure, long-range superstructure, rotational domains, and surface defects.* Phys. Rev. B **42**, 9307 (1990), doi:10.1103/PhysRevB.42.9307.

[139] N. Takeuchi, C. T. Chan and K. M. Ho: *Au(111): A theoretical study of the surface reconstruction and the surface electronic structure.* Phys. Rev. B **43**, 13899 (1991), doi:10.1103/PhysRevB.43.13899.

[140] S. Narasimhan and D. Vanderbilt: *Elastic stress domains and the herringbone reconstruction on Au(111).* Phys. Rev. Lett. **69**, 1564 (1992), doi:10.1103/PhysRevLett.69.1564.

[141] W. Chen, V. Madhavan, T. Jamneala and M. F. Crommie: *Scanning tunneling microscopy observation of an electronic superlattice at the surface of clean gold.* Phys. Rev. Lett. **80**, 1469 (1998), doi:10.1103/PhysRevLett.80.1469.

[142] J. Li, W.-D. Schneider and R. Berndt: *Local density of states from spectroscopic scanning-tunneling-microscope images: Ag(111).* Phys. Rev. B **56**, 7656 (1997), doi:10.1103/PhysRevB.56.7656.

[143] M. F. Crommie, C. P. Lutz and D. M. Eigler: *Imaging standing waves in a two-dimensional electron gas.* Nature **363**, 524 (1993), doi:10.1038/363524a0.

[144] X. Sun, M. P. Felicissimo, P. Rudolf and F. Silly: *NaCl multi-layer islands grown on Au(111)-(*$22 \times \sqrt{3}$*) probed by scanning tunneling microscopy.* Nanotechnology **19**, 495307 (2008), doi:10.1088/0957-4484/19/49/495307.

[145] K. Lauwaet, K. Schouteden, E. Janssens, C. van Haesendonck and P. Lievens: *Dependence of the NaCl/Au(111) interface state on the thickness of the NaCl layer.* J. Phys. Cond. Mat. **47**, 475507 (2012), doi:10.1088/0953-8984/24/47/475507.

[146] L. Ramoino, M. von Arx, S. Schintke, A. Baratoff, H.-J. Güntherodt and T. A. Jung: *Layer-selective epitaxial self-assembly of porphyrins on ultrathin insulators.* Chem. Phys. Lett. **417**, 22 (2006), doi:10.1016/j.cplett.2005.10.006.

[147] R. Bennewitz, V. Barwich, M. Bammerlin, C. Loppacher, M. Guggisberg, A. Baratoff, E. Meyer and H.-J. Güntherodt: *Ultrathin films of NaCl on Cu(111): a LEED and dynamic force microscopy study.* Surf. Sci. **438**, 289 (1999), doi:10.1016/S0039-6028(99)00586-5.

[148] C. Loppacher, M. Bammerlin, M. Guggisberg, F. Battiston, R. Bennewitz, S. Rast, A. Baratoff, E. Meyer and H.-J. Güntherodt: *Phase variation experiments in non-contact dynamic force microscopy using phase locked loop techniques.* Appl. Surf. Sci. **140**, 287 (1999), doi:10.1016/S0169-4332(98)00542-X.

[149] J. Repp, G. Meyer, F. E. Olsson and M. Persson: *Controlling the charge state of individual gold adatoms*. Science **305**, 493 (2004), doi:10.1126/science.1099557.

[150] K. Glöckler, M. Sokolowski, A. Soukopp and E. Umbach: *Initial growth of insulating overlayers of NaCl on Ge(100) observed by scanning tunneling microscopy with atomic resolution*. Phys. Rev. B **54**, 7705 (1996), doi:10.1103/PhysRevB.54.7705.

[151] W. Hebenstreit, M. Schmid, J. Redinger, R. Podloucky and P. Varga: *Bulk terminated NaCl(111) on aluminum: A polar surface of an ionic crystal?* Phys. Rev. Lett. **85**, 5376 (2000), doi:10.1103/PhysRevLett.85.5376.

[152] J. Repp: *Rastertunnelmikroskopie und -spektroskopie an Adsorbaten auf Metall- und Isolatoroberflächen*. Ph.D. thesis, Freie Universität Berlin (2002).

[153] J. Wintterlin and M.-L. Bocquet: *Graphene on metal surfaces*. Surf. Sci. **603**, 1841 (2009), doi:10.1016/j.susc.2008.08.037.

[154] A. T. N'Diaye, J. Coraux, T. N. Plasa, C. Busse and T. Michely: *Structure of epitaxial graphene on Ir(111)*. New J. Phys. **10**, 043033 (2008), doi:10.1088/1367-2630/10/4/043033.

[155] A. T. N'Diaye, S. Bleikamp, P. J. Feibelman and T. Michely: *Two-dimensional Ir cluster lattice on a graphene moire on Ir(111)*. Phys. Rev. Lett. **97**, 215501 (2006), doi:10.1103/PhysRevLett.97.215501.

[156] C. Busse, P. Lazić, R. Djemour, J. Coraux, T. Gerber, N. Atodiresei, V. Caciuc, R. Brako, A. T. N'Diaye, S. Blügel, J. Zegenhagen and T. Michely: *Graphene on Ir(111): physisorption with chemical modulation*. Phys. Rev. Lett. **107**, 036101 (2011), doi:10.1103/PhysRevLett.107.036101.

[157] H. Dil, J. Lobo-Checa, R. Laskowski, P. Blaha, S. Berner, J. Osterwalder and T. Greber: *Surface trapping of atoms and molecules with dipole rings*. Science **319**, 1824 (2008), doi:10.1126/science.1154179.

[158] F. D. Natterer, F. Patthey and H. Brune: *Ring state for single transition metal atoms on boron nitride on Rh(111)*. Phys. Rev. Lett. **109**, 066101 (2012), doi:10.1103/PhysRevLett.109.066101.

[159] I. Brihuega, C. Heinrich Michaelis, J. Zhang, S. Bose, V. Sessi, J. Honolka, M. A. Schneider, A. Enders and K. Kern: *Electronic decoupling and templating of Co nanocluster arrays on the boron nitride nanomesh*. Surf. Sci. **602**, L95 (2008), doi:10.1016/j.susc.2008.04.040.

[160] M. Corso, W. Auwärter, M. Muntwiler, A. Tamai, T. Greber and J. Osterwalder: *Boron nitride nanomesh*. Science **303**, 217 (2004), doi:10.1126/science.1091979.

[161] S. Berner, M. Corso, R. Widmer, O. Groening, R. Laskowski, P. Blaha, K. Schwarz, A. Goriachko, H. Over, S. Gsell, M. Schreck, H. Sachdev, T. Greber and J. Osterwalder: *Boron nitride nanomesh: functionality from a corrugated monolayer*. Angew. Chem. Int. Ed. **46**, 5115 (2007), doi:10.1002/anie.200700234.

[162] S. Kahle, Z. Deng, N. Malinowski, C. Tonnoir, A. Forment-Aliaga, N. Thontasen, G. Rinke, D. Le, V. Turkowski, T. S. Rahman, S. Rauschenbach, M. Ternes and

K. Kern: *The Quantum Magnetism of Individual Manganese-12-Acetate Molecular Magnets Anchored at Surfaces*. Nano Lett. **12**, 518 (2012), doi:10.1021/nl204141z.

[163] M. Iannuzzi, F. Tran, R. Widmer, T. Dienel, K. Radican, Y. Ding, J. Huttera and O. Gröning: *Site-selective adsorption of phthalocyanine on h-BN/Rh(111) nanomesh*. Phys. Chem. Chem. Phys. **16**, 12374 (2014), doi:10.1039/c4cp01466a.

[164] R. Laskowski, P. Blaha, T. Gallauner and K. Schwarz: *Single-layer model of the hexagonal boron nitride nanomesh on the Rh(111) surface*. Phys. Rev. Lett. **98**, 106802 (2007), doi:10.1103/PhysRevLett.98.106802.

[165] R. Laskowski and P. Blaha: *Unraveling the structure of the h-BN/Rh(111) nanomesh with ab initio calculations*. J. Phys. Cond. Mat. **20**, 064207 (2008), doi:10.1088/0953-8984/20/6/064207.

[166] A. B. Preobrajenski, A. S. Vinogradov, M. L. Ng, E. Ćavar, R. Westerström, A. Mikkelsen, E. Lundgren and N. Mårtensson: *Influence of chemical interaction at the lattice-mismatched h-BN/Rh(111) and h-BN/Pt(111) interfaces on the overlayer morphology*. Phys. Rev. B **75**, 245412 (2007), doi:10.1103/PhysRevB.75.245412.

[167] A. Zhao, Q. Li, L. Chen, H. Xiang, W. Wang, S. Pan, B. Wang, X. Xiao, J. Yang, J. G. Hou and Q. Zhu: *Controlling the Kondo effect of an adsorbed magnetic ion through Its chemical bonding*. Science **309**, 1542 (2005), doi:10.1126/science.1113449.

[168] L. Gao, W. Ji, Y. B. Hu, Z. H. Cheng, Z. T. Deng, Q. Liu, N. Jiang, X. Lin, W. Guo, S. X. Du, W. A. Hofer, X. C. Xie and H.-J. Gao: *Site-specific Kondo effect at ambient temperatures in iron-based molecules*. Phys. Rev. Lett. **99**, 106402 (2007), doi:10.1103/PhysRevLett.99.106402.

[169] C. Iacovita, M. V. Rastei, B. W. Heinrich, T. Brumme, J. Kortus, L. Limot and J. P. Bucher: *Visualizing the spin of individual cobalt-phtalocyanine molecules*. Phys. Rev. Lett. **101**, 116602 (2008), doi:10.1103/PhysRevLett.101.116602.

[170] J. Brede, N. Atodiresei, S. Kuck, P. Lazić, V. Caciuc, Y. Morikawa, G. Hoffmann, S. Blügel and R. Wiesendanger: *Spin- and energy-dependent tunneling through a single molecule with intramolecular spatial resolution*. Phys. Rev. Lett. **105**, 047204 (2010), doi:10.1103/PhysRevLett.105.047204.

[171] Y. Wang, K. Wu, J. Kröger and R. Berndt: *Review Article: Structures of phthalocyanine molecules on surfaces studied by STM*. AIP Advances **2**, 041402 (2012), doi:10.1063/1.4773458.

[172] Z. H. Cheng, L. Gao, Z. T. Deng, Q. Liu, N. Jiang, X. Lin, X. B. He, S. X. Du and H.-J. Gao: *Epitaxial growth of iron phthalocyanine at the initial stage on Au(111) surface*. J. Phys. Chem. C **111**, 2656 (2007), doi:10.1021/jp0660738.

[173] Z. H. Cheng, L. Gao, Z. T. Deng, N. Jiang, Q. Liu, D. X. Shi, S. X. Du, H. M. Guo and H.-J. Gao: *Adsorption behavior of iron phthalocyanine on Au(111) surface at submonolayer coverage*. J. Phys. Chem. C **111**, 9240 (2007), doi:10.1021/jp070388l.

[174] C. S. Fischer, C. Jenewein and S. Mecking: *Conjugated star polymers from multidirectional Suzuki-Miyaura polymerization for live cell imaging*. Macromolecules **48**, 483 (2015), doi:10.1021/ma502294n.

[175] E. M. García-Frutos and B. Gómez-Lor: *Synthesis and self-association properties of functionalized C_3-symmetric hexakis(p-substituted-phenylethynyl)triindoles*. J. Am. Chem. Soc. **130**, 9173 (2008), doi:10.1021/ja8025399.

[176] G. E. Poirier and E. D. Pylant: *The self-assembly mechanism of alkanethiols on Au(111)*. Science **272**, 1175 (1996), doi:10.1126/science.272.5265.1145.

[177] D. Seo, V. Meenakshi, W. Teizer, H. Zhao and K. Dunbar: *Enhanced magnetic anisotropy of Mn_{12}-acetate*. J. Magn. Magn. Mater **301**, 31 (2006), doi:10.1016/j.jmmm.2005.06.005.

[178] M. Clemente-León, E. Coronado, A. Forment-Aliaga and F. M. Romero: *Organized assemblies of magnetic clusters*. C. R. Chimie **6**, 683 (2003), doi:10.1016/S1631-0748(03)00121-8.

[179] J. Gómez-Segura, O. Kazakova, J. Davies, P. Josephs-Franks, J. Veciana and D. Ruiz-Molina: *Self-organization of Mn_{12} single-molecule magnets into ring structures induced by breath-figures as templates*. Chem. Commun. 5615 (2005), doi:10.1039/b509282e.

[180] N. Grumbach, A. Barla, L. Joly, B. Donnio, G. Rogez, E. Terazzi, J.-P. Kappler and J.-L. Gallani: *Loss of single-molecule-magnet behavior of a Mn_{12}-based compound assembled in a monolayer*. Eur. Phys. J. B **73**, 103 (2010), doi:10.1140/epjb/e2009-00430-x.

[181] L. Meng, B.-F. Lin, J.-Y. Yang, Y. Sun, R.-F. Dou, L.-X. Ma, C.-M. Xiong and J.-C. Nie: *Detection of the intrinsic two energy gaps in individual Mn_{12} single molecule magnets*. Chem. Phys. Lett. **542**, 81 (2012), doi:10.1016/j.cplett.2012.05.068.

[182] A. Cornia, A. C. Fabretti, M. Pacchioni, L. Zobbi, D. Bonacchi, A. Caneschi, D. Gatteschi, R. Biagi, U. del Pennino, V. de Renzi, L. Gurevich and H. S. J. van der Zant: *Direct observation of single-molecule magnets organized on gold surfaces*. Angew. Chem. Int. Ed. **42**, 1645 (2003), doi:10.1002/anie.200350981.

[183] A. Nait Abdi, J. P. Bucher, P. Rabu, O. Toulemonde, M. Drillon and P. Gerbier: *Magnetic properties of bulk $Mn_{12}pivalates_{16}$ single molecule magnets and their self assembly on functionnalized gold surface*. J. Appl. Phys. **95**, 7345 (2004), doi:10.1063/1.1689191.

[184] J. S. Steckel, N. S. Persky, C. R. Martinez, C. L. Barnes, E. A. Fry, J. Kulkarni, J. D. Burgess, R. B. Pacheco and S. L. Stoll: *Monolayer and multilayer films of $[Mn_{12}O_{12}(O_2CMe)_{16}]$*. Nano Lett. **4**, 399 (2004), doi:10.1021/nl0343553.

[185] S. Phark, Z. G. Khim, B. J. Kim, B. J. Suh, S. Yoon, J. Kim, J. M. Lim and Y. Do: *Atomic force microscopy study of $Mn_{12}O_{12}(O_2CC_4H_3S)_{16}(H_2O)_4$ single-molecule magnet adsorbed on Au surface*. Jap. J. Appl. Phys. **43**, 8273 (2004), doi:10.1143/JJAP.43.8273.

[186] L. Zobbi, M. Mannini, M. Pacchioni, G. Chastanet, D. Bonacchi, C. Zanardi, R. Biagi, U. del Pennino, D. Gatteschi, A. Cornia and R. Sessoli: *Isolated single-molecule magnets on native gold*. Chem. Commun. 1640 (2005), doi:10.1039/B418072K.

[187] A. Nait Abdi, J.-P. Bucher, P. Gerbier, P. Rabu and M. Drillon: *Self-assembly and magnetism of Mn_{12} nanomagnets on native and functionalized gold surfaces*. Adv. Mater. **17**, 1612 (2005), doi:10.1002/adma.200401623.

[188] M. Burgert, S. Voss, S. Herr, M. Fonin, U. Groth and U. Rüdiger: *Single-molecule magnets: a new approach to investigate the electronic structure of Mn_{12} molecules by scanning tunneling spectroscopy.* J. Am. Chem. Soc. **129**, 14362 (2007), doi:10.1021/ja074884z.

[189] S. Voss, M. Fonin, U. Rüdiger, M. Burgert, U. Groth and Y. S. Dedkov: *Electronic structure of Mn_{12} derivatives on the clean and functionalized Au surface.* Phys. Rev. B **75**, 045102 (2007), doi:10.1103/PhysRevB.75.045102.

[190] L. Bogani, L. Cavigli, M. Gurioli, R. L. Novak, M. Mannini, A. Caneschi, F. Pineider, R. Sessoli, M. Clemente-León, E. Coronado, A. Cornia and D. Gatteschi: *Magneto-optical investigations of nanostructured materials based on single-molecule magnets monitor strong environmental effects.* Adv. Mater. **19**, 3906 (2007), doi:10.1002/adma.200700594.

[191] F. Pineider, M. Mannini, R. Sessoli, A. Caneschi, D. Barreca, L. Armelao, A. Cornia, E. Tondello and D. Gatteschi: *Solvent effects on the adsorption and self-organization of Mn_{12} on Au(111).* Langmuir **23**, 11836 (2007), doi:10.1021/la7016837.

[192] S. Voss, O. Zander, M. Fonin, U. Rüdiger, M. Burgert and U. Groth: *Electronic transport properties and orientation of individual Mn_{12} single-molecule magnets.* Phys. Rev. B **78**, 155403 (2008), doi:10.1103/PhysRevB.78.155403.

[193] M. Mannini, P. Sainctavit, R. Sessoli, C. Cartier dit Moulin, F. Pineider, M.-A. Arrio, A. Cornia and D. Gatteschi: *XAS and XMCD investigation of Mn_{12} monolayers on gold.* Chem. Eur. J. **14**, 7530 (2008), doi:10.1002/chem.200800693.

[194] G. G. Condorelli, A. Motta, I. L. Fragalà, F. Giannazzo, V. Raineri, A. Caneschi and D. Gatteschi: *Anchoring molecular magnets on the Si(100) surface.* Angew. Chem. Int. Ed. **43**, 4081 (2004), doi:10.1002/anie.200453933.

[195] B. Fleury, L. Catala, V. Huc, C. David, W. Z. Zhong, P. Jegou, L. Baraton, S. Palacin, P.-A. Albouy and T. Mallah: *A new approach to grafting a monolayer of oriented Mn_{12} nanomagnets on silicon.* Chem. Commun. 2020 (2005), doi:10.1039/B419271K.

[196] Z. Salman, K. H. Chow, R. I. Miller, A. Morello, T. J. Parolin, M. D. Hossain, T. A. Keeler, C. D. P. Levy, W. A. MacFarlane, G. D. Morris, H. Saadaoui, D. Wang, R. Sessoli, G. G. Condorelli and R. F. Kiefl: *Local magnetic properties of a monolayer of Mn_{12} single molecule magnets.* Nano Lett. **7**, 1551 (2007), doi:10.1021/nl070366a.

[197] M. Clemente-León, H. Soyer, E. Coronado, C. Mingotaud, C. J. Gómez-García and P. Delhaès: *Langmuir-Blodgett films of single-molecule nanomagnets.* Angew. Chem. Int. Ed. **37**, 2842 (1998), doi:10.1002/(SICI)1521-3773(19981102)37:20<2842::AID-ANIE2842>3.0.CO;2-B.

[198] M. Cavallini, F. Biscarini, J. Gomez-Segura, D. Ruiz and J. Veciana: *Multiple length scale patterning of single-molecule magnets.* Nano Lett. **3**, 1527 (2003), doi:10.1021/nl034630l.

[199] M. Mannini, D. Bonacchi, L. Zobbi, F. M. Piras, E. A. Speets, A. Caneschi, A. Cornia, A. Magnani, B. J. Ravoo, D. N. Reinhoudt, R. Sessoli and D. Gatteschi: *Advances in single-molecule magnet surface patterning through microcontact printing.* Nano Lett. **5**, 1435 (2005), doi:10.1021/nl0508016.

[200] R. Moroni, R. Buzio, A. Chincarini, U. Valbusa, F. Buatier de Mongeot, L. Bogani, A. Caneschi, R. Sessoli, L. Caviglid and M. Gurioli: *Optically addressable single molecule magnet behaviour of vacuum-sprayed ultrathin films.* J. Mater. Chem. **18**, 109 (2008), doi:10.1039/b712913k.

[201] K. Reaves, K. Kim, K. Iwaya, T. Hitosugi, H. G. Katzgraber, H. Zhao, K. R. Dunbar and W. Teizer: *STM studies of isolated Mn_{12}-ph single-molecule magnets.* SPIN **3**, 1350004 (2013), doi:10.1142/S2010324713500045.

[202] A. Saywell, G. Magnano, C. J. Satterley, L. M. A. Perdigão, A. J. Britton, N. Taleb, M. del Giménez-López, N. R. Champness, J. N. O'Shea and P. H. Beton: *Self-assembled aggregates formed by single-molecule magnets on a gold surface.* Nat. Commun. **1**, 75 (2010), doi:10.1038/ncomms1075.

[203] A. Saywell, A. J. Britton, N. Taleb, M. d. C. Giménez-López, N. R. Champness, P. H. Beton and J. N. O'Shea: *Single molecule magnets on a gold surface: in situ electrospray deposition, x-ray absorption and photoemission.* Nanotechnology **22**, 075704 (2011), doi:10.1088/0957-4484/22/7/075704.

[204] K. Handrup, V. J. Richards, M. Weston, N. R. Champness and J. N. O'Shea: *Single molecule magnets with protective ligand shells on gold and titanium dioxide surfaces: in situ electrospray deposition and x-ray absorption spectroscopy.* J. Chem. Phys. **139**, 154708 (2013), doi:10.1063/1.4825382.

[205] F. Moro, R. Biagi, V. Corradini, M. Evangelisti, A. Gambardella, V. de Renzi, U. del Pennino, E. Coronado, A. Forment-Aliaga and F. M. Romero: *Electronic and magnetic properties of Mn_{12} molecular magnets on sulfonate and carboxylic acid prefunctionalized gold surfaces.* Phys. Chem. C **116**, 14936 (2012), doi:10.1021/jp3031896.

[206] S. Höll: *Untersuchung von molekularen Magneten auf Oberflächen mittels Tieftemperatur-Rastertunnelmikroskopie.* Master's thesis, Universität Konstanz (2013).

[207] E.-S. Wilhelm: *Microscopic and spectroscopic investigations of Mn_{12}-acetate on different substrates.* Master's thesis, Universität Konstanz (2014).

[208] N. Barth: *Tieftemperatur Rastertunnelmikroskopie an Fe_4 Einzelmolekülmagneten auf Oberflächen.* Master's thesis, Universität Konstanz (2015).

[209] A. Caneschi, D. Gatteschi and R. Sessoli: *Alternating current susceptibility, high field magnetization, and millimeter band EPR evidence for a ground S = 10 State in $[Mn_{12}O_{12}(CH_3COO)_{16}(H_2O)_4]\cdot 2CH_3COOH\cdot 4H_2O$.* J. Am. Chem. Soc. **113**, 5873 (1991), doi:10.1021/ja00015a057.

[210] R. A. Robinson, P. J. Brown, D. N. Argyriou, D. N. Hendrickson and S. M. J. Aubin: *Internal magnetic structure of Mn_{12} acetate by polarized neutron diffraction.* J. Phys. Cond. Mat. **12**, 2805 (2000), doi:10.1088/0953-8984/12/12/318.

[211] M. R. Pederson and S. N. Khanna: *Magnetic anisotropy barrier for spin tunneling in $Mn_{12}O_{12}$ molecules.* Phys. Rev. B **60**, 9566 (1999), doi:10.1103/PhysRevB.60.9566.

[212] Z. Zeng, D. Guenzburger and D. E. Ellis: *Electronic structure, spin couplings, and hyperfine properties of nanoscale molecular magnets*. Phys. Rev. B **59**, 6927 (1999), doi:10.1103/PhysRevB.59.6927.

[213] S. Hill, J. A. A. J. Perenboom, N. S. Dalal, T. Hathaway, T. Stalcup and J. S. Brooks: *High-sensitivity electron paramagnetic resonance of Mn_{12}-acetate*. Phys. Rev. Lett. **80**, 2453 (1998), doi:10.1103/PhysRevLett.80.2453.

[214] M. A. Novak, R. Sessoli, A. Caneschi and D. Gatteschi: *Magnetic properties of a Mn cluster organic compound*. J. Magn. Magn. Mater. **146**, 211 (1995), doi:10.1016/0304-8853(94)00860-4.

[215] M. Fonin, S. Voss, S. Herr, G. de Loubens, A. D. Kent, M. Burgert, U. Groth and U. Rüdiger: *Influence of the ligand shell on the surface orientation of Mn_{12} single molecule magnets*. Polyhedron **28**, 1977 (2009), doi:10.1016/j.poly.2008.11.028.

[216] P. Artus, C. Boskovic, J. Yoo, W. E. Streib, L.-C. Brunel, D. N. Hendrickson and G. Christou: *Single-molecule magnets: Site-specific ligand abstraction from $[Mn_{12}O_{12}(O_2CR)_{16}(H_2O)_4]$ and the preparation and properties of $[Mn_{12}O_{12}(NO_3)_4(O_2CCH_2Bu^t)_{12}(H_2O)_4]$*. Inorg. Chem. **40**, 4199 (2001), doi:10.1021/ic010252g.

[217] C. Boskovic, M. Pink, J. C. Huffman, D. N. Hendrickson and G. Christou: *Single-molecule magnets: Ligand-induced core distortion and multiple Jahn-Teller isomerism in $[Mn_{12}O_{12}(O_2CMe)_8(O_2PPh_2)_8(H_2O)_4]$*. J. Am. Chem. Soc. **123**, 9914 (2001), doi:10.1021/ja016341+.

[218] N. E. Chakov, W. Wernsdorfer, K. A. Abboud, D. N. Hendrickson and G. Christou: *Single-molecule magnets. A Mn_{12} complex with mixed carboxylate-sulfonate ligation: $[Mn_{12}O_{12}(O_2CMe)_8(O_3SPh)_8(H_2O)_4]$*. Dalton Trans. **43**, 5919 (2003), doi:10.1039/B301785K.

[219] R. Sessoli, H.-L. Tsai, A. R. Schake, S. Wang, J. B. Vincent, K. Folting, D. Gatteschi, G. Christou and D. N. Hendrickson: *High-spin molecules: $[Mn_{12}O_{12}(O_2CR)_{16}(H_2O)_4]$*. J. Am. Chem. Soc. **115**, 1804 (1993), doi:10.1021/ja00058a027.

[220] M. Burgert: *Synthese, Charakterisierung und Oberflächenpräparation von Mn_{12} Single Molecule Magnets*. Ph.D. thesis, Universität Konstanz (2008).

[221] S. C. Ambrus: *Darstellung und Charakterisierung von einzelmolekular magnetischen Molekülen*. Ph.D. thesis, Universität Konstanz (2012).

[222] S. Voss: *Rastertunnelmikroskopie und -spektroskopie an monomolekularen Schichten molekularer Magnete*. Master's thesis, Universität Konstanz (2006).

[223] S. Voss: *Structural and spectroscopic characterization of monolayers of Mn_{12} single molecule magnets*. Ph.D. thesis, Universität Konstanz (2009).

[224] H. G. Jenniskens, P. W. F. Dorlandt, M. F. Kadodwala and A. W. Kleyn: *The adsorption of methanol on Ag(111) studied with TDS and XPS*. Surf. Sci. **357**, 624 (1996), doi:10.1016/0039-6028(96)00234-8.

[225] K.-U. Weiss, R. Dippel, K.-M. Schindler, P. Gardner, V. Fritzsche, A. M. Bradshaw, A. L. D. Kilcoyne and D. P. Woodruff: *Chemical shift photoelectron diffraction from molecular adsorbates*. Phys. Rev. Lett. **69**, 3196 (1992), doi:10.1103/PhysRevLett.69.3196.

[226] M. Sambi, G. Granozzi, M. Casarin, G. A. Rizzi, A. Vittadini, L. Caputi and G. Chiarello: *Surface carboxylate species on Cu(100) studied by angle-scanned photoelectron diffraction and LCAO-LDF calculations*. Surf. Sci. **315**, 309 (1994), doi:10.1016/0039-6028(94)90135-X.

[227] S. M. Johnston, G. Rousseau, V. Dhanak and M. Kadodwala: *The structure of acetate and trifluoroacetate on Cu(111)*. Surf. Sci. **477**, 163 (2001), doi:10.1016/S0039-6028(01)00808-1.

[228] A. E. Baber, T. J. Lawton and E. C. H. Sykes: *Hydrogen-bonded networks in surface-bound methanol*. J. Phys. Chem. C **115**, 9157 (2011), doi:10.1021/jp201465d.

[229] M. Hennion, L. Pardi, I. Mirebeau, E. Suard, R. Sessoli and A. Caneschi: *Neutron study of mesoscopic magnetic clusters:* $Mn_{12}O_{12}$. Phys. Rev. B **56**, 8819 (1997), doi:10.1103/PhysRevB.56.8819.

[230] V. di Castro and G. Polzonetti: *XPS study of MnO oxidation*. J. Electron. Spectrosc. **48**, 117 (1989).

[231] D. W. Boukhvalov, M. Al-Saqer, E. Z. Kurmaev, A. Moewes, V. R. Galakhov, L. D. Finkelstein, S. Chiuzbaian, M. Neumann, V. V. Dobrovitski, M. I. Katsnelson, A. I. Lichtenstein, B. N. Harmon, K. Endo, J. M. North and N. S. Dalal: *Electronic structure of a* Mn_{12} *molecular magnet: theory and experiment*. Phys. Rev. B **75**, 014419 (2007), doi:10.1103/PhysRevB.75.014419.

[232] V. R. Galakhov, M. Demeter, S. Bartkowski, M. Neumann, N. A. Ovechkina, E. Z. Kurmaev, N. I. Lobachevskaya, Y. M. Mukovskii, J. Mitchell and D. L. Ederer: *Mn 3s exchange splitting in mixed-valence manganites*. Phys. Rev. B **65**, 113102 (2002), doi:10.1103/PhysRevB.65.113102.

[233] C. Carbonera, I. Imaz, D. Maspoch, D. Ruiz-Molina and F. Luis: *Magnetic behaviour of* Mn_{12} *single-molecule magnet nanospheres*. Inorg. Chim. Acta **361**, 3951 (2008), doi:10.1016/j.ica.2008.03.037.

[234] C. Carbonera, F. Luis, J. Campo, J. Sánchez-Marcos, A. Camón, J. Chaboy, D. Ruiz-Molina, I. Imaz, J. van Slageren, S. Dengler and M. González: *Effect of crystalline disorder on quantum tunneling in the single-molecule magnet* Mn_{12} *benzoate*. Phys. Rev. B **81**, 014427 (2010), doi:10.1103/PhysRevB.81.014427.

[235] D. Seo: *Alignment of micro-crystals of* Mn_{12}*-acetate and direct observation of single molecules thereof*. Ph.D. thesis, Texas A&M University (2007).

[236] M. Mannini, F. Pineider, P. Sainctavit, C. Danieli, E. Otero, C. Sciancalepore, A. M. Talarico, M.-A. Arrio, A. Cornia, D. Gatteschi and R. Sessoli: *Magnetic memory of a single-molecule quantum magnet wired to a gold surface*. Nature Mater. **8**, 194 (2009), doi:10.1038/NMAT2374.

[237] A. S. Zyazin, J. W. G. van den Berg, E. A. Osorio, H. S. J. van der Zant, N. P. Konstantinidis, M. Leijnse, M. R. Wegewijs, F. May, W. Hofstetter, C. Danieli and A. Cornia: *Electric field controlled magnetic anisotropy in a single molecule.* Nano Lett. **10**, 3307 (2010), doi:10.1021/nl1009603.

[238] E. Burzurí, A. S. Zyazin, A. Cornia and H. S. J. van der Zant: *Direct observation of magnetic anisotropy in an individual Fe_4 Single-Molecule Magnet.* Phys. Rev. Lett. **109**, 147203 (2012), doi:10.1103/PhysRevLett.109.147203.

[239] E. Burzurí, R. Gaudenzi and H. S. J. van der Zant: *Observing magnetic anisotropy in electronic transport through individual single-molecule magnets.* J. Phys. Cond. Mat. **27**, 113202 (2015), doi:10.1088/0953-8984/27/11/113202.

[240] L. Margheriti, M. Mannini, L. Sorace, L. Gorini, D. Gatteschi, A. Caneschi, D. Chiappe, R. Moroni, F. B. de Mongeot, A. Cornia, F. M. Piras, A. Magnani and R. Sessoli: *Thermal deposition of intact tetrairon(III) single-molecule magnets in high-vacuum conditions.* Small **5**, 1460 (2009), doi:10.1002/smll.200801594.

[241] L. Rigamonti, M. Piccioli, L. Malavolti, L. Poggini, M. Mannini, F. Totti, B. Cortigiani, A. Magnani, R. Sessoli and A. Cornia: *Enhanced vapor-phase processing in fluorinated Fe_4 single-molecule magnets.* Inorg. Chem. **52**, 5897 (2013), doi:10.1021/ic400037c.

[242] L. Malavolti, V. Lanzilotto, S. Ninova, L. Poggini, I. Cimatti, B. Cortigiani, L. Margheriti, D. Chiappe, E. Otero, P. Sainctavit, F. Totti, A. Cornia, M. Mannini and R. Sessoli: *Magnetic bistability in a submonolayer of sublimated Fe_4 single-molecule magnets.* Nano Lett. **15**, 535 (2015), doi:10.1021/nl503925h.

[243] P. Erler, P. Schmitt, N. Barth, A. Irmler, S. Bouvron, T. Huhn, U. Groth, F. Pauly, L. Gragnaniello and M. Fonin: *Highly ordered surface self-assembly of Fe_4 single molecule magnets.* Nano Lett. **15**, 4546 (2015), doi:10.1021/acs.nanolett.5b01120.

[244] A. L. Barra, A. Caneschi, A. Cornia, F. Fabrizi de Biani, D. Gatteschi, C. Sangregorio, R. Sessoli and L. Sorace: *Single-molecule magnet behavior of a tetranuclear iron(III) complex. The origin of slow magnetic relaxation in iron(III) clusters.* J. Am. Chem. Soc. **121**, 5302 (1999), doi:10.1021/ja9818755.

[245] A. Cornia, A. C. Fabretti, P. Garrisi, C. Mortalò, D. Bonacchi, D. Gatteschi, R. Sessoli, L. Sorace, W. Wernsdorfer and A.-L. Barra: *Energy-barrier enhancement by ligand substitution in tetrairon(iii) single-molecule magnets.* Angew. Chem. Int. Ed. **43**, 1136 (2004), doi:10.1002/anie.200352989.

[246] S. Accorsi, A.-L. Barra, A. Caneschi, G. Chastanet, A. Cornia, A. C. Fabretti, D. Gatteschi, C. Mortalò, E. Olivieri, F. Parenti, P. Rosa, R. Sessoli, L. Sorace, W. Wernsdorfer and L. Zobbi: *Tuning anisotropy barriers in a family of tetrairon(III) single-molecule magnets with an $S = 5$ ground state.* J. Am. Chem. Soc. **128**, 4742 (2006), doi:10.1021/ja0576381.

[247] A.-L. Barra, F. Bianchi, A. Caneschi, A. Cornia, D. Gatteschi, L. Gorini, L. Gregoli, M. Maffini, F. Parenti, R. Sessoli, L. Sorace and A. M. Talarico: *New single-molecule magnets by site-specific substitution: incorporation of alligator clips into Fe_4 complexes.* Eur. J. Inorg. Chem. **2007**, 4145 (2007), doi:10.1002/ejic.200700382.

[248] C. Adamo and V. Barone: *Toward reliable density functional methods without adjustable parameters: the PBE0 model.* J. Chem. Phys. **110**, 6158 (1999), doi:10.1063/1.478522.

[249] J. P. Perdew, K. Burke and M. Ernzerhof: *Generalized gradient approximation made simple.* Phys. Rev. Lett. **77**, 3865 (1996), doi:10.1103/PhysRevLett.77.3865.

[250] A. Schäfer, C. Huber and R. Ahlrichs: *Fully optimized contracted Gaussian basis sets of triple zeta valence quality for atoms Li to Kr.* J. Chem. Phys. **100**, 5829 (1994), doi:10.1063/1.467146.

[251] J. Ribas-Arino, T. Baruah and M. R. Pederson: *Density-functional study of two Fe_4-based single-molecule magnets.* J. Chem. Phys. **123**, 044303 (2005), doi:10.1063/1.1961367.

[252] F. Schulz, R. Drost, S. K. Hämäläinen and P. Liljeroth: *Templated self-assembly and local doping of molecules on epitaxial hexagonal boron nitride.* ACS Nano **7**, 11121 (2013), doi:10.1021/nn404840h.

[253] S. Joshi, F. Bischoff, R. Koitz, D. Ecija, K. Seufert, A. P. Seitsonen, J. Hutter, K. Diller, J. I. Urgel, H. Sachdev, J. V. Barth and W. Auwärter: *Control of molecular organization and energy level alignment by an electronically nanopatterned boron nitride template.* ACS Nano **8**, 430 (2014), doi:10.1021/nn406024m.

[254] C. Piamonteze, U. Flechsig, S. Rusponi, J. Dreiser, J. Heidler, M. Schmidt, R. Wetter, M. Calvi, T. Schmidt, H. Pruchova, J. Krempasky, C. Quitmann, H. Brune and F. Nolting: *X-Treme beamline at SLS: X-ray magnetic circular and linear dichroism at high field and low temperature.* J. Synchrotron Rad. **19**, 661 (2012), doi:10.1107/S0909049512027847.

[255] M. Mannini, F. Pineider, P. Sainctavit, L. Joly, A. Fraile-Rodriguez, M.-A. Arrio, C. Cartier dit Moulin, W. Wernsdorfer, A. Cornia, D. Gatteschi and R. Sessoli: *X-Ray magnetic circular dichroism picks out single-molecule magnets suitable for nanodevices.* Adv. Mater. **21**, 167 (2009), doi:10.1002/adma.200801883.

[256] S. Carretta, P. Santini, G. Amoretti, T. Guidi, R. Caciuffo, A. Candini, A. Cornia, D. Gatteschi, M. Plazanet and J. A. Stride: *Intra- and inter-multiplet magnetic excitations in a tetrairon(III) molecular cluster.* Phys. Rev. B **70**, 214403 (2004), doi:10.1103/PhysRevB.70.214403.

[257] J. A. J. Burgess, L. Malavolti, V. Lanzilotto, M. Mannini, S. Yan, S. Ninova, F. Totti, S. Rolf-Pissarczyk, A. Cornia, R. Sessoli and S. Loth: *Magnetic fingerprint of individual Fe_4 molecular magnets under compression by a scanning tunnelling microscope.* Nat. Commun. **6**, 8216 (2015), doi:10.1038/ncomms9216.

[258] B. W. Heinrich, L. Braun, J. I. Pascual and K. J. Franke: *Protection of excited spin states by a superconducting energy gap.* Nature Phys. **9**, 765 (2013), doi:10.1038/NPHYS2794.

[259] B. W. Heinrich, L. Braun, J. I. Pascual and K. J. Franke: *Tuning the Magnetic Anisotropy of Single Molecules.* Nano Lett. **15**, 4024 (2015), doi:10.1021/acs.nanolett.5b00987.